Dynamics of colloids in molecular glass forming liquids studied via X-ray photon correlation spectroscopy

Dissertation zur Erlangung des Doktorgrades

an der Fakultät für Mathematik, Informatik und Naturwissenschaften
Fachbereich Physik
der Universität Hamburg

vorgelegt von Heiko Conrad
aus Burg

Hamburg
2014

Gutachter der Dissertation: Prof. Dr. Gerhard Grübel
Prof. Dr. Joachim Wagner

Gutachter der Disputation: Prof. Dr. Gerhard Grübel
Prof. Dr. Wilfried Wurth

Datum der Disputation: 23.01.2014

Vorsitzender des Prüfungsausschusses: Dr. Michael Martins

Vorsitzender des Promotionsausschusses: Prof. Dr. Peter Hauschildt

Leiterin des Fachbereichs Physik: Prof. Dr. Daniela Pfannkuche

Dekan der Fakultät für Mathematik,
Informatik und Naturwissenschaften: Prof. Dr. Heinrich Graener

Abstract

In this work the static and dynamical properties of the glass formers polypropylene glycol and dibutyl phthalate are studied in the supercooled state. Colloidal tracer particles suspended in these glass formers allow the investigation of their dynamics with coherent synchrotron radiation by means of X-ray photon correlation spectroscopy. The static structure factors, the relaxation times and the dispersion relations of the tracer particles were determined as function of the solvent temperature. The results show that the nature of the particles dynamics in the glass former changes close to the glass transition temperature (T_g) between $1.08 - 1.12\ T_\mathrm{g}$. While the static structure factor remains unchanged in this temperature range, the particle dynamics changes from free diffusion at $T > 1.12\ T_\mathrm{g}$ to hyper diffusive and correlated particle motion at $T < 1.08\ T_\mathrm{g}$. By comparing samples of different particle sizes and concentrations it becomes evident that this change in the dynamics is related to changes of the solvent properties. These changes are accompanied by an increasing heterogeneity in the dynamics of the tracer particles. The findings are in agreement with an interpretation that domains of correlated dynamics in the supercooled glass formers grow in size with decreasing temperature.

Zusammenfassung

In der vorliegenden Arbeit wurden die statischen und dynamischen Eigenschaften der Glasbildner Polypropylenglycol und Dibutylphthalate im unterkühlten Zustand untersucht. Dazu wurden kolloidale Partikel in den Glasbildnern suspendiert, um deren Dynamik mit kohärenter Synchrotronstrahlung mittels Röntgen-Photonen-Korrelations-Spektroskopie untersuchen zu können. Aus der Analyse wurden Strukturfaktoren, Relaxationszeiten und Dispersionsrelationen der kolloidalen Suspensionen in Abhängigkeit der Lösungsmitteltemperatur bestimmt. Die Ergebnisse zeigen, dass sich die Natur der Dynamik der kolloidalen Partikel in den Glasbildnern nahe der Glasübergangstemperatur (T_g) zwischen $1.08 - 1.12\ T_\mathrm{g}$ verändert. Während in diesem Temperaturbereich die Struktur der Partikel unverändert bleibt, erfolgt ein Wechsel der Partikeldynamik von freier Diffusion bei $T > 1.12\ T_\mathrm{g}$ hin zu einer "Hyperdiffusion" mit korrelierter Teilchenbewegung bei $T < 1.08\ T_\mathrm{g}$. Diese Veränderungen sind zudem mit einer zunehmenden Heterogenität der Partikeldynamik verbunden. Durch den Vergleich unterschiedlicher Proben mit verschiedenen Partikelkonzentrationen und Partikelgrößen kann dieser Übergang in der Dynamik auf Änderungen der Charakteristika der Glasbildner in diesem Temperaturbereich zurückgeführt werden. Insgesamt deuten die Ergebnisse auf Domänen korrelierter Bewegung in den unterkühlten Glasbildnern hin, die mit sinkender Temperatur anwachsen.

Contents

1 Introduction

Since glasses are easily designed with desired mechanical or optical properties on industrial scales, it might be assumed that the glassy state is a well-known state of matter. A large number of theories have been developed to describe the underlying microscopic processes causing the vitrification from the supercooled liquid state to the glassy state. However, a microscopic understanding of glassy materials still remains a challenge for condensed matter physics.[1] In general it is difficult to gain a unified description of the glass transition from results of different model glass formers due to additional dependencies of the results on the thermal history and the chosen experimental approach. For this reason, the glass transition of supercooled liquids is still subject to many investigations, both theoretically and experimentally. Supercooling of glass formers, e.g. polymers, metallic glass former or molecular liquids, leads to a dramatic change of the molecular dynamics until vitrification sets in around the glass transition temperature T_{g}. A dramatic increase of the viscosity and a non-exponential relaxation towards equilibrium are common features for all glass formers upon approaching T_{g}. Experimental methods, that investigate these features directly by probing molecular dynamics, lack either spatial or temporal resolution to observe the structural arrest which is believed to be accompanied by dynamical heterogeneities near T_{g}.

This can be overcome by using larger tracer particles suspended in a glass forming solvent (colloidal suspension) to probe the solvent dynamics at different time- and length scales. Colloidal systems have been the subject of intense research efforts in the past decades and colloid chemistry has progressed to make well-defined model systems available, such as monodisperse silica or latex spheres in the nanometer regime. These can be stabilized against aggregation. This includes in particular dilute colloidal suspensions where the particle dynamics is almost only driven by the thermal excitation of the suspension and the particle-solvent interactions. Moreover, the characteristics of colloidal systems are experimentally accessible via scattering methods, such as small angle X-ray scattering or X-ray photon correlation spectroscopy. In experiments of hard sphere tracer particles suspended in a molecular glass former a transition from free diffusive to hyper-diffusive particle motion around $T = 1.2\ T_{\mathrm{g}}$ was found.[2] This was accompanied by a change from a

---

[1] Berthier, L. (2011). *Rev. Mod. Phys.* **83**, 587.

[2] Caronna, C. (2008). "Glassy systems studied by X-ray photon correlation spectroscopy." PhD thesis.

stretched to a compressed exponential shape of the correlation functions that evidenced cooperative particle dynamics below $T = 1.2\ T_\mathrm{g}$, especially at higher concentrations.

In this context, the subject of the presented study is to investigate the effect of the size and the concentration of the tracer particles on the probed dynamics and to learn more about the dynamics in supercooled liquids at temperatures between $T_\mathrm{g} < T < 1.2\ T_\mathrm{g}$. Furthermore, it will be investigated to what extent the dynamic susceptibility[3] obtained from the instantaneous intensity autocorrelation function can be used to quantify dynamic heterogeneities.[4] These are assumed to grow with decreasing temperature in this temperature regime. Silica tracer particles suspended in polypropylene glycol and dibutyl phthalate are chosen as model system due to their simple molecular structure and high glass forming ability.

The thesis is organized as follows: After giving a general introduction about glasses, supercooled liquids and the glass transition in **Chapter 2**, an overview on colloidal systems follows in **Chapter 3**. **Chapter 4** presents the theoretical basis of the experimental methods, in particular small angle X-ray scattering (SAXS) and X-ray photon correlation spectroscopy (XPCS), which is followed by **Chapter 5** describing the scattering from model systems. **Chapter 6** is dedicated to the experimental methods that includes the synthesis of the samples and the presentation of the experimental setups. The structural properties of the samples are discussed in **Chapter 7** followed by the discussion on their dynamics in **Chapter 8**. Finally, a summary of the results is given in **Chapter 9**.

Palermo, Italy: University Palermo.

[3] Cipelletti, L. and Weitz, D. A. (1999). *Rev. Sci. Instrum.* **70**, 3214.

[4] Trappe, V. et al. (2007). *Phys. Rev. E* **76**, 51404.

2 Glasses and the glass transition

When a liquid is cooled below its melting temperature T_m it may undergo a first-order phase transition to a crystalline state or with sufficiently high cooling rate it stays in a metastable liquid state, the so called supercooled state. While the viscosity η of the liquid increases with cooling, the molecular dynamics in the liquid slows down. That usually results in a reduction of the specific volume.[1] If the cooling rate is high enough, the molecules will move so slow at a certain temperature, that they cannot explore this equilibrium specific volume within the time scale of the cooling. The experimentally observed specific volume therefore deviates from its equilibrium value. With further cooling the time scales of molecular rearrangements become so long compared to the time scale of the experimental observations, that the liquid appears to be frozen. This characterizes the glassy state. All liquids can in principle undergo a glass transition and form a glass. In Figure 2.1 a schematic phase diagram of a glass former is shown, where the specific volume (respectively the enthalpy) is plotted as function of temperature for two different cooling rates c_1 and c_2 with $c_1 < c_2$. The different cooling rates lead to different glass transition temperatures $T_{\mathrm{g}_1} < T_{\mathrm{g}_2}$.[2] The glass transition temperature T_g defines the point of intersection of the extrapolation of the specific volume in the glassy state with that of the supercooled liquid line assuming infinite small cooling rates. Furthermore, the Kauzmann temperature T_k which is assumed to define a thermodynamic phase transition is given by the extrapolation of the liquid entropy to the entropy of the crystal.[3] For most materials T_k is similar to the Vogel temperature T_0, a hypothetic temperature where the relaxation times τ_c of the glass former diverges.[4] The transition between the supercooled and the glassy state is not instantaneous as the crystallization process, but is extended over a certain temperature interval. According to the Ehrenfest classification scheme the formation of the glass is neither a first- nor a second-order phase transition.[5] It is assumed to be a dynamical transition characterized by the scaling between experimental and molecular dynamics time

---

[1] It is noted that for example water is an exception of that.

[2] While this effect is in the order of 3 to 5 K and deviations of the cooling rates were small, T_g can be considered to be not dependent of the cooling rates in the experiments.

[3] Kauzmann, W. (1948). *Chem. Rev.* **43**, 219.

[4] Angell, C. A. (1997). *J. Res. Natl. Inst. Stand. Technol.* **102**, 171.

[5] Hansen, J. P. and McDonald, I. R. (2005). *Theory of simple liquids.* 3rd Edition. Academic Press, Waltham, USA.

scales.

It was found in various experiments, that the structure in the supercooled state is similar to the glassy state while the dynamics is dramatically slowed down close to T_g.[6] This is commonly interpreted as an increase of the effective activation energy E. This is illustrated in Figure 2.2 for various liquids, where the logarithm of the viscosity η is shown as a function of the inverse temperature scaled by T_g (Angell-plot). The curves clearly exhibit a change of η for more than 15 orders of magnitude in a relatively small temperature interval. The various glass formers exhibit different temperature dependencies, e.g., the viscosity of $\mathrm{SiO_2}$ has almost an Arrhenius type dependence given by

$$\eta \propto \exp\left(\frac{E}{k_\mathrm{B} \cdot T}\right), \tag{2.1}$$

while the viscosity for o-terphenyl is characterized by a super-Arrhenius dependence given by

$$\eta \propto \exp\left(\frac{E}{k_\mathrm{B} \cdot (T - T_0)}\right), \tag{2.2}$$

where k_B denotes the Boltzmann constant. Most of the liquids fall in between these two extreme cases. The temperature dependence can be used to classify supercooled liquids as so-called strong (Arrhenius) or fragile (super-Arrhenius) glass formers. Based on the evolution of η versus the temperature, a classification was introduced by Angell[7] with the fragility index

$$m\left(T_\mathrm{g}\right) = -\left.\frac{\mathrm{d}\left(\log_{10}\left[\eta\left(T\right)\right]\right)}{\mathrm{d}\left(\ln\left[T\right]\right)}\right|_{T=T_\mathrm{g}}. \tag{2.3}$$

The value of m ranges from 15 (strong liquids) up to 200 (fragile liquids). In this context, strong glass formers typically reveal three-dimensional network structures of covalent bonds, whereas fragile glass formers are typically characterized by non-directional, non-covalent molecule interactions.[8] While an Arrhenius dependence describes the slowing down of the dynamics in a wide temperature range that diverges at $T = 0$ K, super-Arrhenius behavior describes dynamics that is characterized by a temperature dependent activation energy and diverge at a finite temperature, the Vogel temperature.

In addition to the change of the dynamical time scales, measurements of the excess entropy, that quantifies the entropy difference between the supercooled liquid and the

---

[6] Berthier, L. (2011). *Rev. Mod. Phys.* **83**, 587.

[7] Angell, C. A. (1988). *J. Non-Cryst. Solids* **102**, 205.

[8] Ediger, M. D. et al. (1996). *J. Phys. Chem.* **100**, 13200.

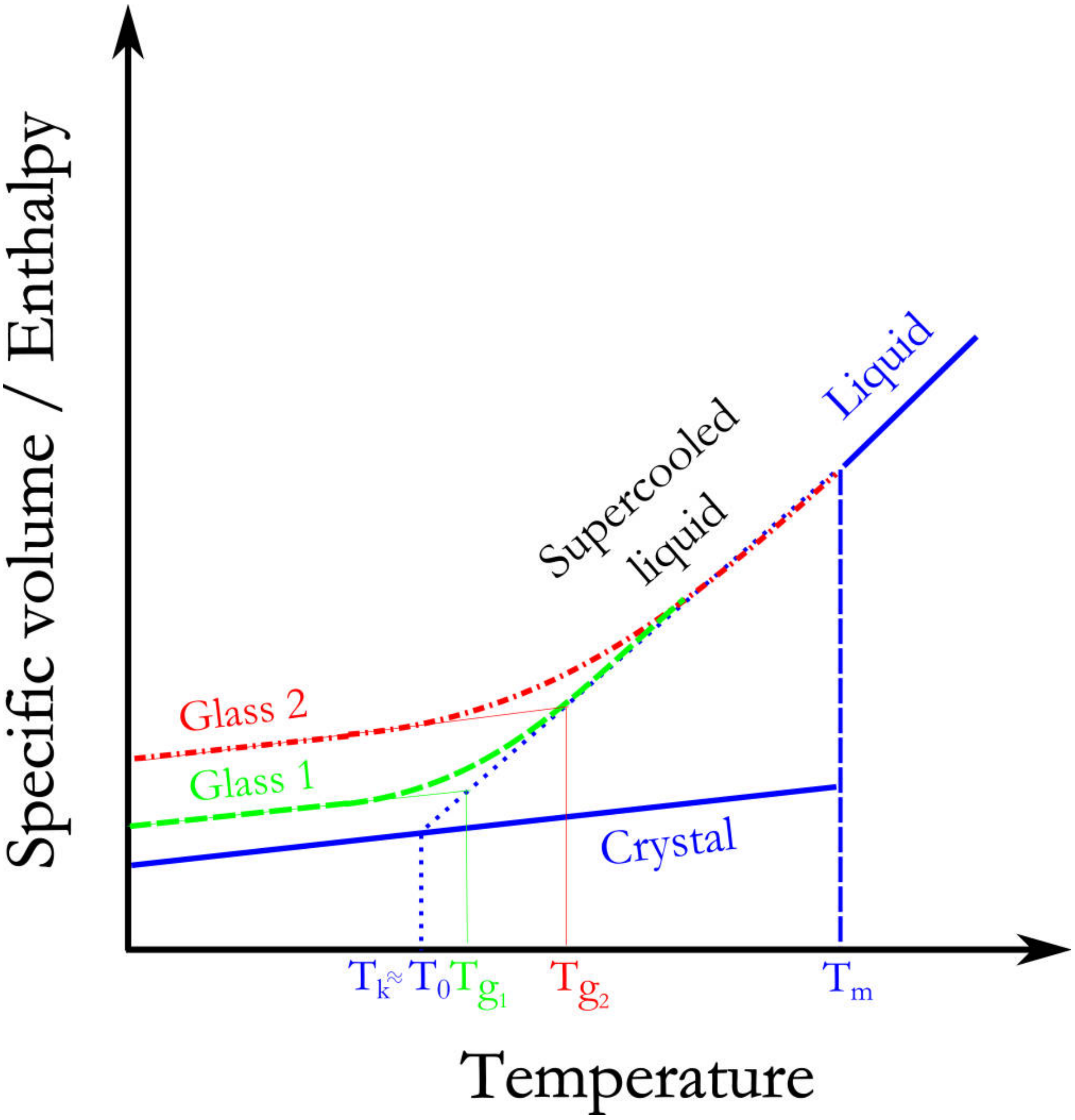

Figure 2.1: Schematic phase diagram of a glass former in the vicinity of the glass transition. The specific volume (respectively the enthalpy) is shown at constant pressure as a function of temperature. Depending on the cooling rate c the cooling of the glass former below its melting temperature T_m can lead to a crystalline or supercooled state. Below T_{g_1} or T_{g_2} corresponding to cooling rates c_1 or c_2 the supercooled liquid is in the glassy state. The Kauzmann temperature T_k, similar to the Vogel temperature T_0, corresponds to the hypothetical transition for $c \to 0$. (Picture taken and adapted from: Ediger, M. D. et al. (1996). *J. Phys. Chem.* **100**, 13200.)

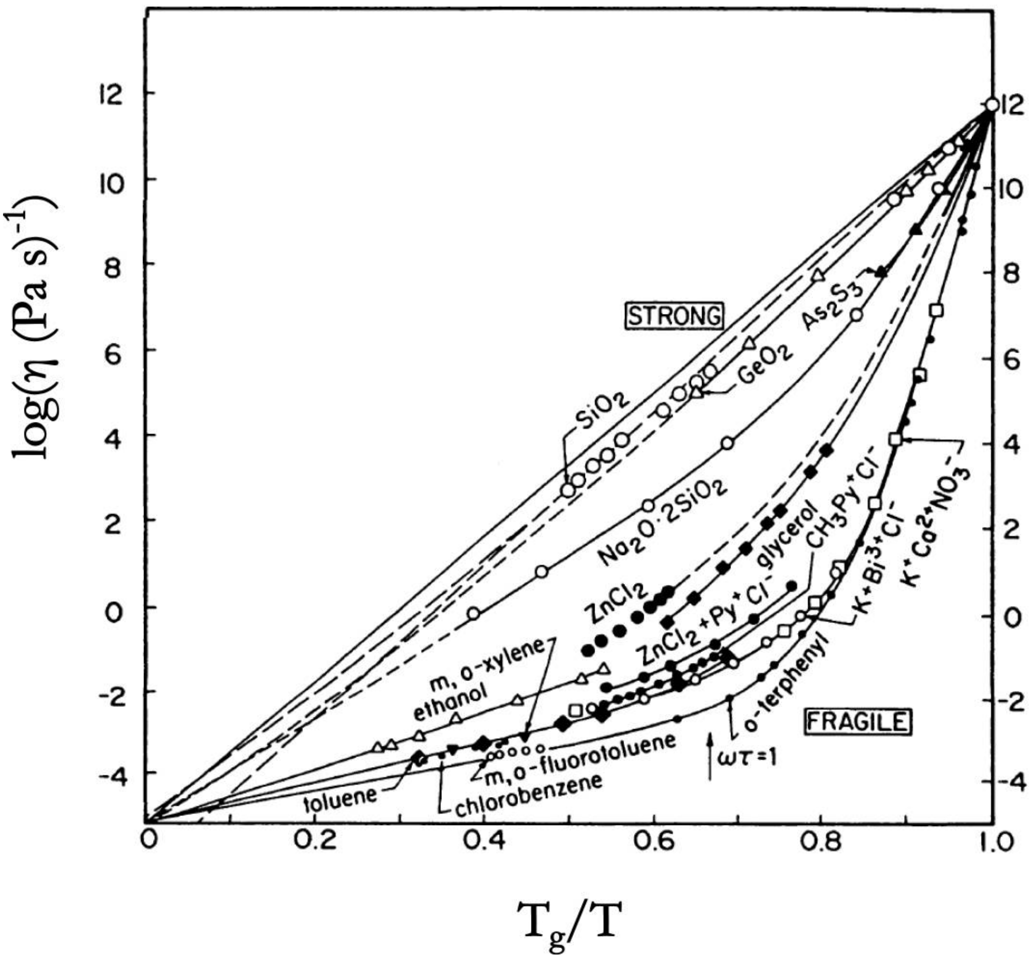

Figure 2.2: Angell-plot (T_g-scaled Arrhenius representation of liquid viscosities): In this illustration a Arrhenius behavior is characterized by a straight line which is the typical behavior of strong glass formers while fragile liquids show a super-Arrhenius behavior. (Picture taken and adapted from: Angell, C. A. (1988). *J. Non-Cryst. Solids* **102**, 205.)

crystal state, suggested a decreasing configurational space with supercooling[9]. The first attempt to explain this phenomenon was given by Adam and Gibbs[10] (AG), who introduced a concept of cooperatively rearranging regions (CRR). CRR are assumed to arise in a very dense medium, when particles or molecules are not able to move independently from their surrounding and a simultaneous change in the position of larger volumes is necessary. Although the size of the CRR is not specified within this model, it is considered to be a function of temperature, which changes according to the dynamics at T_g. Within the AG model the temperature dependence of the relaxation time $\tau_\mathrm{c}(T)$ is given by

$$\tau(T)_\mathrm{c} \propto \exp\left(\frac{C}{T \cdot S_\mathrm{c}}\right), \tag{2.4}$$

where S_c is the excess entropy and C is a constant incorporating the change in the chemical potential and the configurational entropy of the CRR. With an approximation for S_c at T_g one can obtain the Vogel-Fulcher-Tammann (VFT) equation[11]

$$\tau(T)_\mathrm{c} \propto \exp\left(\frac{A}{T - T_0}\right) \propto \eta(T), \tag{2.5}$$

where A is an empirical parameter. The VFT equation describes the temperature dependence of the relaxation time for many fragile liquids above T_g.[12] However, there are also exceptions[13]. Several assumptions of the AG model were proven to be in disagreement with experimental results. On the one hand, the size of CRR was observed to grow in confinement although the AG model predicts the opposite. On the other hand, the distribution of molecular relaxation times $G\left(\frac{\tau}{\tau_\mathrm{c}}\right)$ was found to be more complex as predicted by the AG model. In this context, the results of broadband dielectric spectroscopy experiments on glassy systems interpreted via the Kohlrausch-Williams-Watts (KWW) function suggests that $G\left(\frac{\tau}{\tau_\mathrm{c}}\right)$ is broader as described by a Gaussian. The KWW function is a phenomenological description of relaxations in disordered systems[14] given by $f_\gamma(t, \tau_\mathrm{c}) = \mathrm{e}^{-\left[\frac{t}{\tau_\mathrm{c}}\right]^\gamma}$ that for $\gamma = 1$ is interpreted as a linear superposition of relaxation processes. For $\gamma \neq 1$ different spectra of relaxation times $G\left(\frac{\tau}{\tau_\mathrm{c}}\right)$ are attributed to the decay process described by the KWW function.[15] It can either be an indication of a homogeneous ($\gamma > 1$) or

---

[9] Kauzmann, W. (1948). *Chem. Rev.* **43**, 219.

[10] Adam, G. and Gibbs, J. H. (1965). *J. Chem. Phys.* **43**, 139.

[11] Richert, R. and Angell, C. A. (1998). *J. Chem. Phys.* **108**, 9016.

[12] For details see Trachenko, K. (2008). *J. Non-Cryst. Sol.* **354**, 3903 and references within.

[13] Arndt, M. et al. (1997). *Phys. Rev. Lett.* **79**, 2077.

[14] It was first applied to describe a capacitor discharge by Kohlrausch (Kohlrausch, F. (1863). *Ann. Phys* **195**, 337) and later to model dielectric relaxations by Williams and Watts (Williams, G. and Watts, D. C. (1970). *Trans. Farad. Soc.* **66**, 80).

[15] Philipse, A. P. and Vrij, A. (1989). *J. Coll. Inter. Sci.* **128**, 121.

a heterogeneous ($\gamma < 1$) decay process.[16] For many glasses the stretched exponential form ($\gamma < 1$) of the KWW function was found. Thus, glassy dynamics is assumed to be governed by dynamical heterogeneities including dynamics ranging from slow to fast relaxations.[17] Since clusters of molecules are indistinguishable in the AG model, it is incapable to explain dynamical heterogeneities. Moreover, the AG model does not provide direct predictions for the dynamics of structural relaxations. Even though, cooperative motion is considered as one of the possible mechanisms causing dynamical heterogeneities and the structural arrest in the glassy phase. Furthermore, broadband dielectric spectroscopy, neutron scattering and nuclear magnetic resonance spectroscopy experiments on supercooled liquids reveal a separation of dynamical time scales at the transition from liquid to supercooled liquid state.[18] Typically, the temporal fluctuation of the density is obtained within the experiments, which allows to determine the characteristic relaxation times via autocorrelation functions. A typical result is illustrated in Figure 2.3 for a simple (a) and a supercooled liquid (b). While the density autocorrelation function (DAC) has a single relaxation time τ_c for (a), two relaxation times τ_α and τ_β evolve in case of (b). These exhibit a different temperature dependence that implies a complex connection between dynamical and thermodynamical properties. Moreover, this supports the idea that dynamics in supercooled liquids might be spatially heterogeneous.[19] It was found that the dynamics in some regions of a supercooled liquid can be orders of magnitude faster than dynamics in other regions only a few nanometers away. A description of this remained a big challenge also for more advanced approaches to supercooled liquids, in particular the Mode Coupling Theory[20] (MCT) and the Potential Energy Landscape Approach[21] (PELA).[22]

Initially, MCT has been used to describe the dynamics of molecules in simple liquids by density-density correlation functions and was extended to describe the freezing at the glass transition temperature. The theory derives a critical density corresponding to the mode coupling critical temperature T_c at which density fluctuations become localized. Thus, marking the transition from the liquid to the glass, T_c is predicted to be well above T_g. Above T_c molecules are completely free to diffuse and the density autocorrelation function

---

[16] For example, the spectrum of relaxation times broadens with decreasing γ or narrows vice versa. See Lindsey, C. P. and Patterson, G. D. (1980). *J. Chem. Phys.* **73**, 3348 and Hansen, E. W. et al. (2013). *Macromolecular Chemistry and Physics* **214**, 844.

[17] Colin, R. et al. (2011). *Soft Matter* **7**, 4504.

[18] Debenedetti, P. G. and Stillinger, F. H. (2001). *Nature* **410**, 259.

[19] Clear evidence for this emerged only during the last decade. See Ediger, M. D. (2000). *Annu. Rev. Phys. Chem.* **51**, 99.

[20] Götze, W. (2008). *Complex Dynamics of glass forming liquids. A mode-coupling theory.* 1st Edition. Oxford University Press, Oxford, UK.

[21] Stillinger, F. H. (1995). *Science* **267**, 1935.

[22] For a review to the MCT see Reichman, D. R. and Charbonneau, P. *J. Stat. Mech.* **2005**, P05013, and for the PELA see Sciortino, F. (2005). *J. Stat. Mech.* P05015.

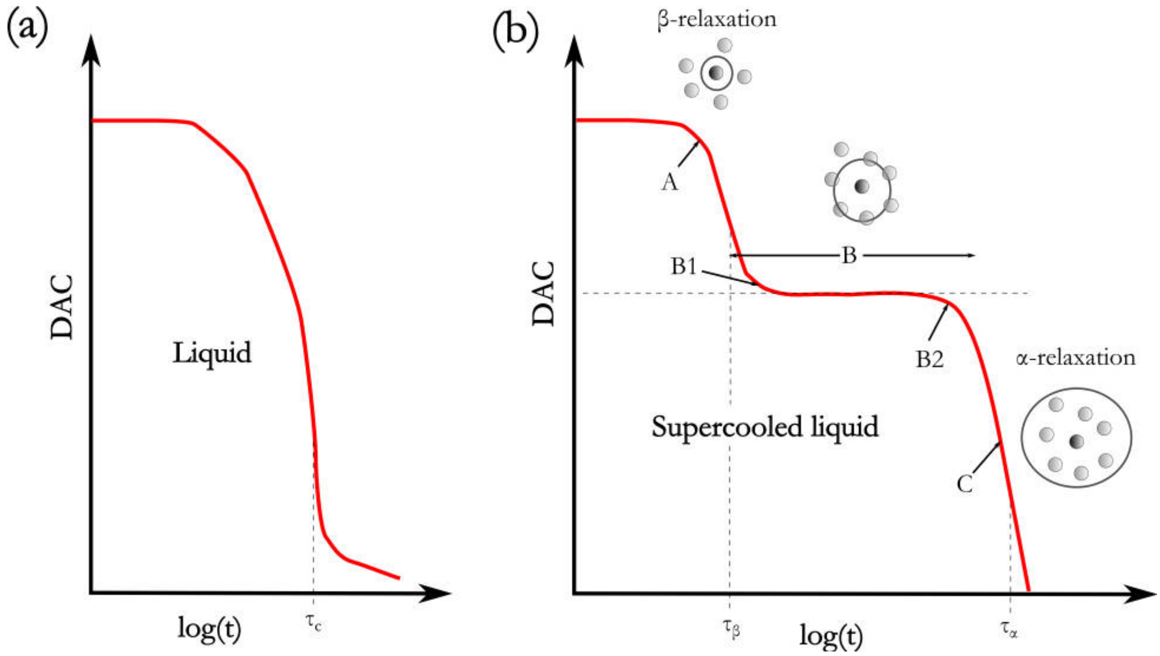

Figure 2.3: Density autocorrelation functions (DAC) of a simple (a) and a supercooled (b) liquid. The simple liquid shows only a single decay characterized by τ_c while the supercooled liquid exhibits two decays characterized by τ_α and τ_β. The β-relaxation decay describes the short-time relaxation processes in a cage, while the α-relaxation decay time describes the diffusion of the molecules out of the cage for longer times. (Picture taken and adapted from: Reichman, D. R. and Charbonneau, P. *J. Stat. Mech.* **2005**, P05013.)

(Figure 2.3(a)) decays due to the motion of molecules. The characteristic relaxation time τ_c specifies the averaged time scale for the molecules to move their own diameter. Upon approaching T_c dynamics splits into a slow α-relaxation and a fast β-relaxation (Figure 2.3(b)). While the β-relaxation decay originates from microscopic intermolecular collisions (A), the α-relaxation decay is attributed to the localized motion of molecules trapped in cages formed by the surrounding liquid. This causes the correlation function to settle (B1) at a plateau (B). The decay of the plateau is characterized by the escape from the cages (B2) and the movement of the cages (C). While the β-relaxation decay can be described by a simple power law, the α-relaxation decay is described typically by a stretched exponential KWW function suggesting increasing dynamical heterogeneities with supercooling. The β-relaxation has been studied frequently, while the investigation of the much slower α-relaxation is experimentally hard to probe, especially at dimensions above the molecular length scale where the structural arrest becomes significant in the glassy phase. Nevertheless, the relaxation times of the α-relaxation was found to increase upon cooling.[23] According to ideal MCT, the diffusion constant vanishes and the viscosity

---

[23] Binder, K. and Kob, W. (2005). *Glassy Materials and Disordered Solids.* World Scientific Publishing Co., Singapore, Republic of Singapore.

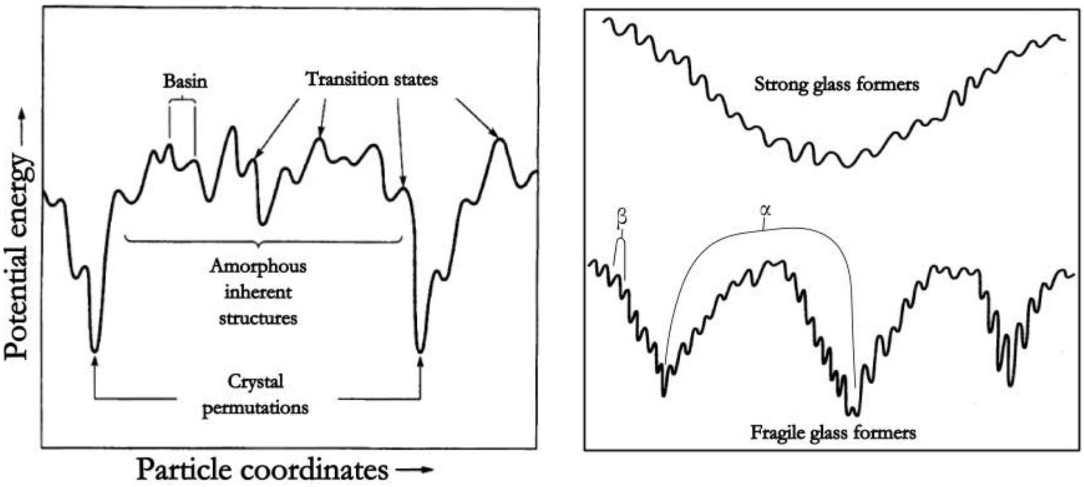

Figure 2.4: Left: Schematic illustration of an energy landscape. Right: Energy landscapes of strong and fragile glass formers. The x-axis represents all configurational coordinates. (Picture taken and adapted from: Stillinger, F. H. (1995). *Science* **267**, 1935.)

diverges below T_c. This is in contradiction to experimental findings and leads to a more advanced MCT.[24] Still, the MCT does not define the role of the interplay between dynamic and thermodynamic processes, which is nowadays assumed to be essential at the glass transition.

For this reason the complementary PELA has incorporated the thermodynamical point of view to the theory of supercooled liquids. The configurational space of a system is partitioned into basins surrounding local energy minima, termed 'inherent structures', to a multi-dimensional rugged surface called PEL. The minima correspond to mechanically stable particle packings statistically described by their depth. It was shown, that α-relaxations can arise from rearrangements between larger minima and β-relaxations are due to transitions between neighboring minima.[25] In the same way, the glass transition can be described as the result of a second order dynamical transition represented by the appearance of an unique global minimum corresponding to the glassy state. While the shape of the PEL does not change with temperature, the sampling of the PEL does. These differences of the PEL explain why fragile and strong glass formers have a different temperature dependence. In Figure 2.4 the PEL of strong and fragile glass forming liquids are shown. In case of strong glass formers, the height of the energy barrier between two minima is uniform. Since this is proportional to the activation energy (E), E occurs to be temperature independent (Arrhenius behavior). For fragile glass formers the PEL is extremely heterogeneous which is the reason for the super-Arrhenius behavior.

Although MCT and PELA are two complementary approaches, there are results which

---

[24] Götze, W. and Sjögren, L. (1995). *Transp. Theory. Stat. Phys.* **24**, 801.

[25] Stillinger, F. H. (1995). *Science* **267**, 1935.

strengthen the arguments of the PELA for a connection between the PEL of the system and the exploration of their configurations. For example, an increasing amount of simultaneous rearrangements is required to explore a fragile PEL with very deep energy minima separated by high energy barriers, which support the formation of the CRR. A study on a fragile glass former with hard sphere colloidal tracer particles showed evidence of such cooperative effects on the particle dynamics especially at larger volume fractions.[26] This was attributed to the heterogeneous PEL of the fragile glass formers as the viscoelastic properties change when approaching T_{g}. However, due to the limited comparability of the investigated colloidal samples the study could not provide a conclusive explanation.

---

[26] Caronna, C. (2008). "Glassy systems studied by X-ray photon correlation spectroscopy." PhD thesis. Palermo, Italy: University Palermo.

3 Colloidal systems

In the framework of this thesis, the influences of the particle size and the particle volume fraction on the appearance of correlated particle motion in suspensions of colloidal tracer particles in fragile glass formers are investigated, especially for temperatures above the glass transition temperature T_g. In this chapter, physical properties will be derived to describe the particle dynamics on the basis of inter-particle and particle-solvent interactions.

3.1 Introduction to colloidal systems

A dispersion is a mixture of phases where one phase (particles) is dispersed in one or more continuous ones. The phases can be gaseous, liquid or solid. Colloidal systems represent a class of dispersions. Therein, particles of intermediate size ($1 - 1000$ nm) are intermixed in a liquid phase. Thus, colloidal systems are typical mesoscopic systems which can be often described within the framework of classical physics. Colloidal systems comprise many natural systems, e.g. fog as a system of small water droplets in air[1], milk as an emulsion of fat and other substances in water, or foams which are gas enclosures in a liquid. Colloidal systems have attracted scientific and economic interest, especially during the last decades.[2]

This work focuses on colloidal suspensions composed of mesoscopic solid particles suspended in a background fluid. The particles can be designed with specific interaction potentials, and thus their solutions exhibit a rich phase behavior including liquid and crystals phases.[3] Since the associated time and length scales are larger than common for atomic systems, they are easier to access experimentally. Thus, colloids are often used as model systems to study fundamental problems in statistical mechanics on mesoscopic length scales.[4]

Due to the large time and length scale differences between colloidal particles and the solvent molecules, the dispersion phase is assumed as a continuum and the colloidal

---

[1] Gultepe, I. (2007). *Pure and Applied Geophysics* **164**, 1126.

[2] Tadros, T. F. (2008). *Colloids in Cosmetics and Personal Care.* 1st Edition. Wiley-VCH, Weinheim, Germany.

[3] Pusey, P. N. and van Megen, W. (1986). *Nature* **320**, 340; Ilett, S. M. et al. (1995). *Phys. Rev. E* **51**, Van Megen, W. and Underwood, S. M. (1993). *Nature* **362**, 616.

[4] Dhont, J. K. G. (1996). *An Introduction to the Dynamics of Colloids.* 1st Edition. Elsevier, Amsterdam, Netherlands.

suspension can be treated within a coarse-grained approach. The resulting effective interaction can be described by a potential of mean force $U\left(\vec{r}^N\right)$ between N colloidal particles in the suspension. Generally, this potential is complicated and depends on the center-of-mass positions $\vec{r}^N$ of all particles. Usually, pairwise additivity is assumed, i.e. the interaction potential can be expressed as a sum over pair-potentials $u\left(|\vec{r}_i - \vec{r}_j|\right)$. For spherically symmetric particles it is given by

$$U\left(\vec{r}^N\right) = \frac{1}{2}\sum_{i}^{N}\sum_{j\neq i}^{N} u\left(|\vec{r}_i - \vec{r}_j|\right). \tag{3.1}$$

$U\left(\vec{r}^N\right)$ depends only on the distance between two particles given by the modulus of the vector difference $r_{ij} = |\vec{r}_i - \vec{r}_j|$. Such systems are determined by the pair correlation function $g\left(r\right)$ defined as

$$g\left(r\right) = \frac{V}{4\pi r^2 N^2}\left\langle \sum_{i}^{N}\sum_{j\neq i}^{N} \delta\left(r - r_{ij}\right)\right\rangle, \tag{3.2}$$

where $\langle\cdot\rangle$ is the ensemble average equivalent to the averaging over distances.[5] This function describes the relative probability to find a particle at distance r from another particle. For example, the average number of particles which can be found within a spherical shell $\left(r + \mathrm{d}r, r\right)$ around a particle is given by $4\pi r^2 g\left(r\right)\mathrm{d}r$ (Figure 3.1). $g\left(r\right)$ describes the spatial correlation of particles. It becomes unity for long distances in the absence of a long range order.

3.2 Stability of colloidal suspensions

The stability of colloidal suspensions is defined as the ability of the colloidal particles to remain dispersed in the solvent. Colloidal particles in suspension exhibit so-called Brownian motion. This is a random motion of the larger particles solved in the fluid caused by interactions with the medium and with each other. Between the particles either attractive or repulsive interactions are present. These determine the stability of the colloidal suspensions. If attractive interactions dominate, the particles adhere to each other and finally form aggregates of increasing size which may settle due to gravity. If repulsive interactions dominate, the particles remain in a dispersed state. In general, dispersion forces like van der Waals forces cause attraction between colloidal particles because these forces are always present between particles of similar composition. For

---

[5] Hansen, J. P. and McDonald, I. R. (2005). *Theory of simple liquids*. 3rd Edition. Academic Press, Waltham, USA.

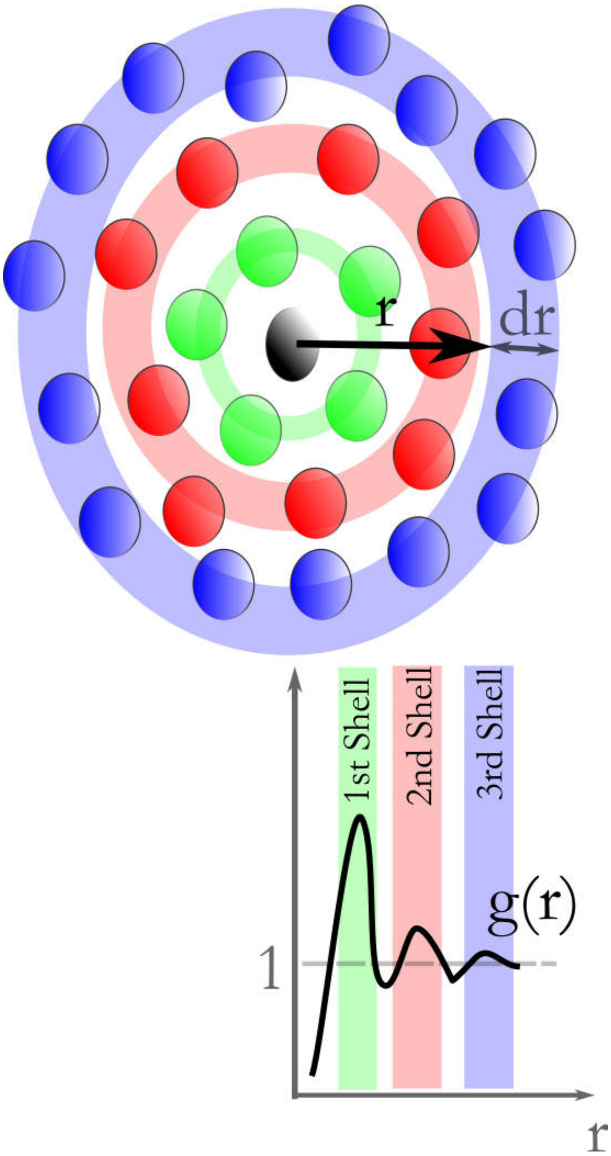

Figure 3.1: The pair distribution function $g(r)$ shown for an ensemble of particles. $g(r)$ peaks at distance where the next neighbor particles form a coordination shell around the particle. For amorphous materials the peak height of $g(r)$ decreases with distance due to a missing long range order.

equally sized spherical particles of radius R_P, the van der Waals interaction potential is given by[6]

$$U_\mathrm{H}\left(\bar{r}\right) = -\frac{H}{6}\left[\frac{2R_\mathrm{P}^2}{\bar{r}^2 - 4R_\mathrm{P}^2} + \frac{2R_\mathrm{P}^2}{\bar{r}^2} + \ln\left(1 - \frac{4R_\mathrm{P}^2}{\bar{r}^2}\right)\right], \tag{3.3}$$

where $\bar{r} = r + 2R_\mathrm{P}$ is the center-to-center distance of the particles and H is the Hamaker constant[7], a parameter that describes the strength of the interactions and depends on the polarizabilities of the compounds. For many colloidal suspensions, the range of significant attractive van der Waals forces is around 10 nm. If the mean particle distance is below this size, that system becomes instable. Therefore, stable colloidal suspensions introduce a sufficiently strong repulsive force, which counteracts the van der Waals attraction. This can be achieved either by polymeric or electrostatic stabilization.[8]

3.2.1 Polymeric stabilization

Polymeric stabilization of colloids involves polymeric molecules either attached to the surface of the particles (steric stabilization) or added to the solvent to prevent the aggregation of colloidal particles (depletion stabilization). In both cases the compressibility of the polymeric molecules as well as the osmotic pressure induces a repulsive force, which counterbalances the attractive van der Waals force of the particles. Steric stabilization of colloidal particles is achieved by attaching polymer molecules to the particle surface. The polymers form a coating which induces a repulsive force leading to the separation of particles. The stabilization of colloidal particles due to depletion is achieved by adding unanchored polymers to the solution which impose repulsive forces between approaching particles. These mechanisms of stabilization are illustrated in Figure 3.2. The effective particle interaction potential U_PS is given as sum of the van der Waals interaction potential U_H and the repulsive potential U_S due to polymeric stabilization. U_S contributes significantly only if the particles are close to each other and rises to infinity at the contact distance of the particles. A simple model for such a stabilized colloidal suspension was developed by Asakura and Oosawa[9] and by Vrij[10]. The authors describe these systems via the short-range

---

[6] Russel, W. B. et al. (1989). *Colloidal dispersions.* 1st Edition. Cambridge University Press, Cambridge, UK.

[7] Hamaker, H. C. (1937). *Physica* **4**, 1058.

[8] The stability of colloidal systems are of great importance in order to use them as model system or as industrial applications such as pharmaceutics, ceramics, paints or pigments. A detailed overview can be found in: Norde, W. (2011). *Colloids and Interfaces in Life Sciences and Bionanotechnology.* 2nd Edition. CRC Press, Boca Raton, USA.

[9] Asakura, S. and Oosawa, F. (1954). *J. Chem. Phys.* **22**, 1255; Asakura, S. and Oosawa, F. (1958). *J. Polym. Sci.* **33**, 183.

[10] Vrij, A. (1976). *Pure and Appl. Chem.* **48**, 471.

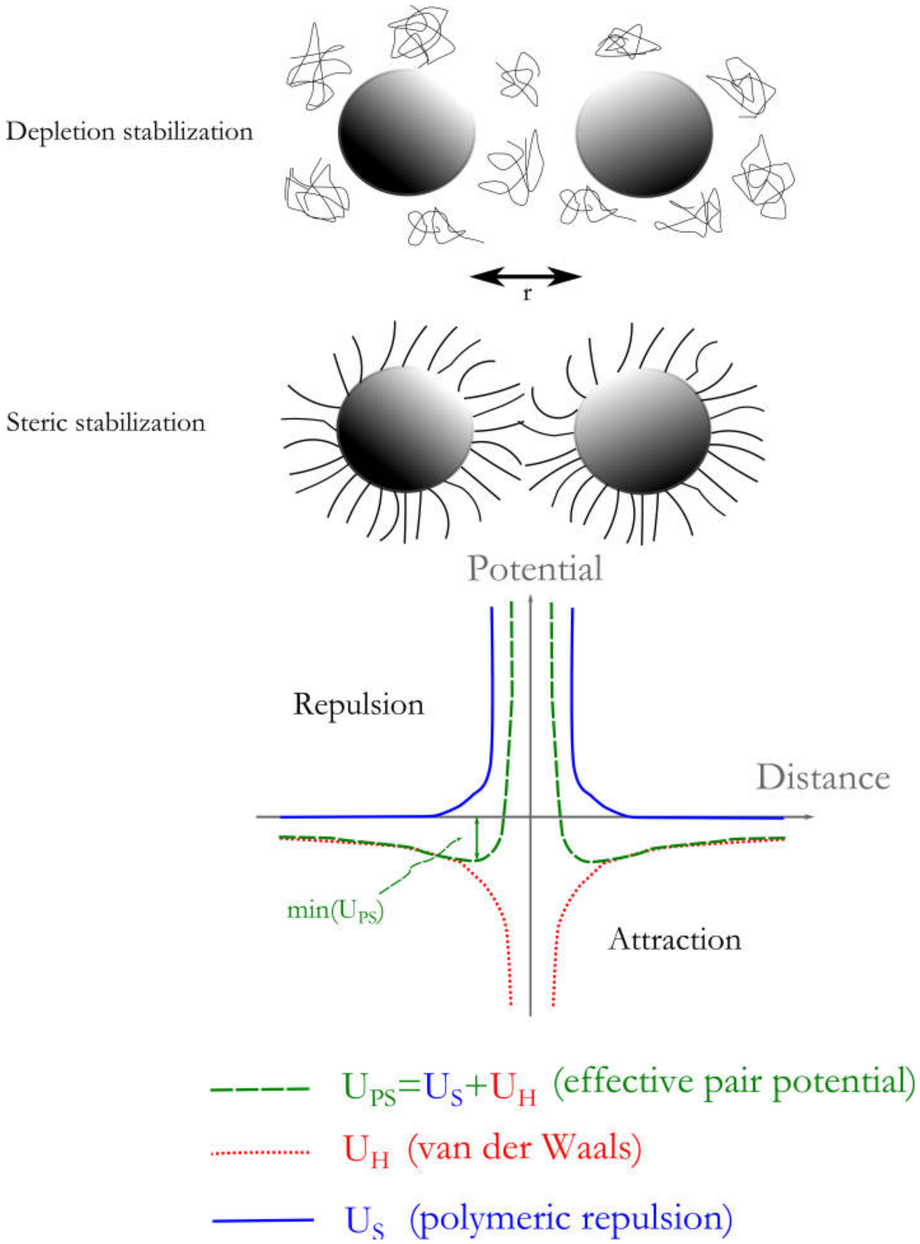

Figure 3.2: Top: Schematic of depletion stabilization. Middle: Schematic of steric stabilization. Bottom: The effective interaction potential U_{PS} between two particles is the sum of the van der Waals potential U_{H} and a repulsive potential U_{S} due to polymeric stabilization. Polymeric stabilization leads to a stable colloidal suspension when the effective particle attraction is smaller than the kinetic energy of the particles: $|\min(U_{\mathrm{PS}})| \ll k_{\mathrm{B}}T$.

interactions of hard spheres[11] leading to a phase behavior, which only depends on the particle volume fraction defined by

$$\phi = \frac{4}{3}\pi R_{\mathrm{P}}^{3} n, \tag{3.4}$$

where n is the number density of the colloidal particles. For instance, hard sphere systems exhibit a phase behavior ranging from a liquid phase below a volume fraction of $\phi = 49.4$ vol.% to a crystal phase above $\phi = 54.5$ vol.% and a liquid-crystal coexistence in between.[12]

3.2.2 Electrostatic stabilization

The electrostatic stabilization of colloidal particles is based on the repulsive Coulomb force counterbalancing the attractive van der Waals force. Typically, this is achieved by attaching charged ions on the surface of the colloidal particles. Dispersed in a polar solvent these particles are surrounded by counter-ions and establish an electric double layer (Figure 3.3). Such an electric double layer consists of the so-called Stern layer[13] followed by a diffuse layer. The Stern layer includes the ions on the particle surface and the closely surrounding counter-ions. The diffuse layer includes the volume of increased counter-ion concentration affected by the screened Coulomb force of the particle surface charge. In this context, the DLVO theory[14] provides a good explanation of the interaction between electrostatic stabilized particles. The DLVO theory is based on the assumptions that the particles are well separated and that the liquid behaves as a simple electrolyte in equilibrium[15]. The stability of such systems is determined by the interaction potential of the particles U_{ES} given by the sum of the repulsive electrical double layer potential U_{DL} and attractive van der Waals potential U_{H} as illustrated in Figure 3.4. Within the DLVO theory, the particles are assumed as spherical macroions with radii R_i, R_j, effective charges Z_i, Z_j, solved in an electrolyte with a permittivity $\epsilon = \epsilon_0 \epsilon_r$, and the ionic strength[16] I.

---

[11] Hansen, J.P. et al. *Liquids, freezing and the glass transition.* Elsevier, Amsterdam, Netherlands.

[12] For a detailed discussion on hard sphere systems see: Pusey, P. N. and van Megen, W. (1986). *Nature* **320**, 340, and references within.

[13] Stern, O. (1924). *Z. Electrochem.* **30**, 508.

[14] The theory is named after Derjaguin, Landau [Derjaguin, B. and Landau, L. (1941). *Acta Physico Chemica URSS* **14**, 633.], Verwey, and Overbeek [Verwey, E. J. W. and Overbeek, J. T. G. (1948). *Theory of the stability of lyophobic colloids.* 1st Edition. Elsevier, Amsterdam, Netherlands.]. A coherent derivation can be found in Hunter, R. J. (2000). *Foundations of colloid science.* 2nd Edition. Oxford University Press, New York, USA, Hansen, J. P. and McDonald, I. R. (2005). *Theory of simple liquids.* 3rd Edition. Academic Press, Waltham, USA, and Nägele, G. (1996). *Physics Reports* **272**, 215.

[15] Debye, P. and Hückel, E. (1923). *Physikalische Zeitschrift* **24**, 185.

[16] The ionic strength of a fluid is given by $I = \frac{1}{2}\sum n_k c_k^2$, where n_k is the concentration of the ion species k with valency c_k. A high concentration of the charged colloidal particles leads to a high concentration

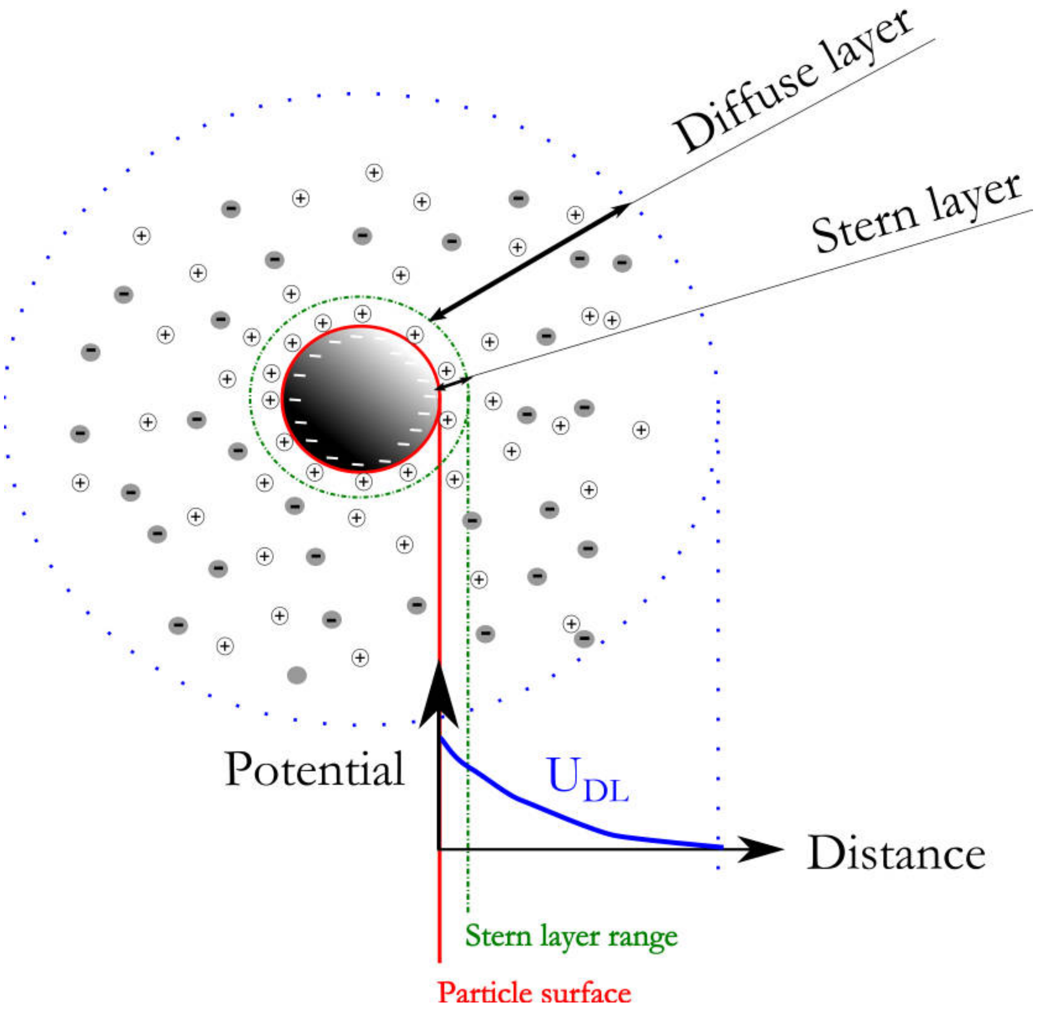

Figure 3.3: Illustration of an electric double layer around a charged particle. U_{DL} the double layer potential that has its maximum at the particle surface, drops within the Stern layer and reaches zero at the end of the diffuse layer.

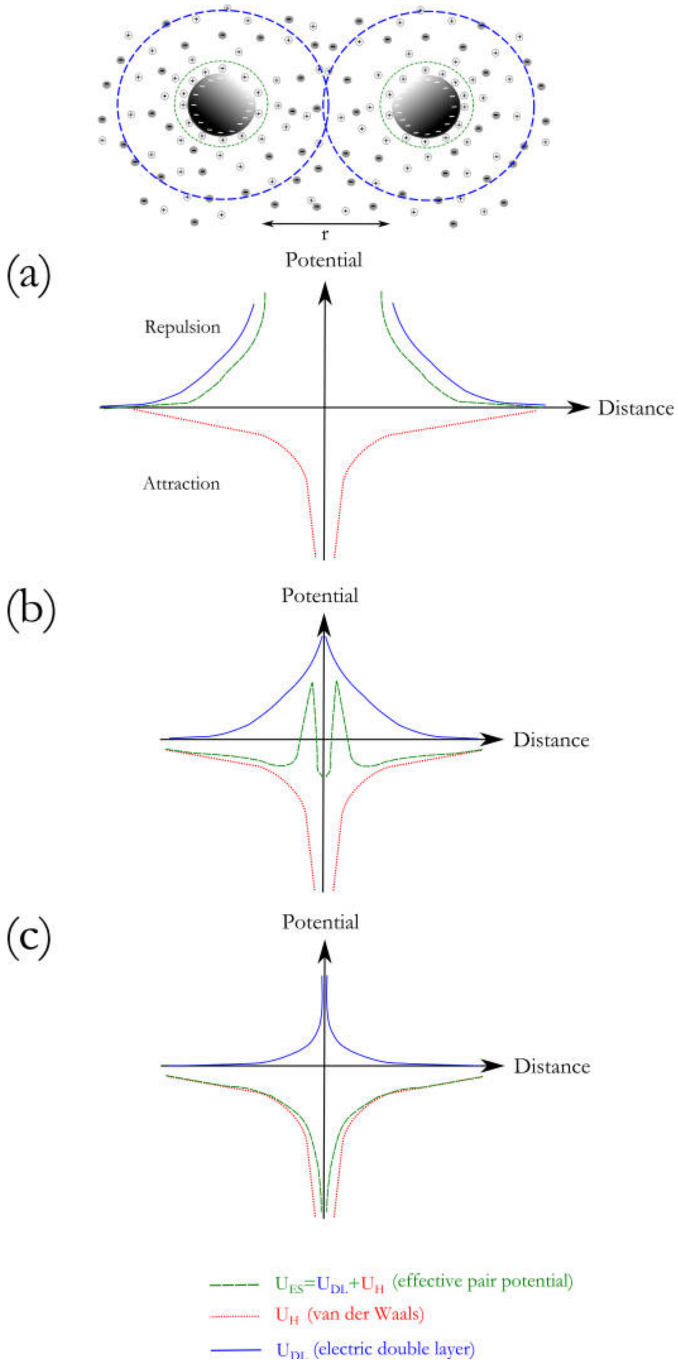

Figure 3.4: Top: Two electrostatically stabilized particles interact with each other. (a) In the case that the ionic strength of the liquid is small, the effective interaction potential becomes repulsive without aggregation. (b) For an intermediate ionic strength of the liquid, the interaction potential is attractive at long and short distances with a repulsive barrier in between. In this case the particle barrier-transition determines the particle aggregation rate. (c) For a large ionic strength, the particle charge is effectively screened and the effective interaction potential becomes completely attractive. This leads to aggregation which is only governed by the diffusion of particles.

The interaction potential is given by a screened Coulomb (Yukawa) potential[17]

$$U_{\mathrm{ES}}\left(r\right)_{ij} = \begin{cases} \infty, & r \leq (R_i + R_j) \\ \frac{e}{4\pi\epsilon}\left(Z_i \frac{\exp(\kappa\cdot R_i)}{1+\kappa\cdot R_i}\right)\left(Z_j \frac{\exp(\kappa\cdot R_j)}{1+\kappa\cdot R_j}\right)\frac{\exp(-\kappa\cdot r)}{\kappa\cdot r}, & r > (R_i + R_j) \end{cases}, \tag{3.5}$$

where κ is the inverse of the Debye-Hückel decay length (defining the range of the electrical double layer force) given by $\kappa^2 = \frac{2e^2}{\epsilon\cdot k_{\mathrm{B}}T}\cdot I$. At a low I, the range of the Debye-Hückel screening length is longer than the attraction by the van der Waals force and the particle interaction is characterized by a potential barrier as shown in Figure 3.4(a). Since the interaction is fully repulsive, this type of colloidal suspension is stable. At an intermediate ionic strength I, the surface charge is not fully screened which results in a particle interaction characterized by a deep primary minimum at short distances, by a maximum at intermediate distances and by a secondary minimum at longer distances. This case is shown in 3.4(b) and describes a non-stable colloidal suspension at long terms, where the aggregation rate is determined by the potential barrier transition rate of the particles. Finally, if the charge repulsion is effectively removed for a large I, the attractive term dominates the particle interaction (Figure 3.4(c)) and the aggregation rate is only governed by the particle diffusion.

3.3 Dynamics of colloidal particles in suspension

The dynamics of colloidal particles in suspension follows the theory of Brownian motion which describes a random particle motion based on the interaction with the solvent molecules and with other particles in the absence of external forces. Brownian motion was first discovered in 1827 by Brown[18], theoretically developed for the free diffusion of particles by Einstein, Smoluchowski, and Langevin[19] and was generalized by Fokker, Planck and many others[20] to describe the diffusion of particles directly by particle and hydrodynamic interactions[21].

---

of counter-ions and the effective ionic strength is reduced. It can be found that I depends on the volume fraction $\phi = \frac{V_{\mathrm{Particle}}}{V}$ by $I \propto \frac{1}{1-\phi}$. Details can be found in: Russel, W. B. et al. (1989). *Colloidal dispersions.* 1st Edition. Cambridge University Press, Cambridge, UK.

[17] Nägele, G. (1996). *Physics Reports* **272**, 215.

[18] Brown, R. R. (1866). *The miscellaneous botanical works of Robert Brown.* 1st Edition. The Ray society, London, UK.

[19] Einstein, A. (1905). *Ann. Phys.* **322**, 549; Smoluchowski, M. (1906). *Ann. Phys.* **14**, 756; Langevin, P. (1908). *C. R. Acad. Sci.* **146**, 530.

[20] An overview to the theory can be found in: Nägele, G. (1996). *Physics Reports* **272**, 215, and Snook, I. (2007). *The Langevin and Generalised Langevin Approach to the Dynamics of Atomic, Polymeric and Colloidal Systems.* 1st Edition. Elsevier, Amsterdam, Netherlands.

[21] Ermak, D. R. and McCammon, J. A. (1978). *J. Chem. Phys.* **69**, 1352.

3.3.1 Free diffusion

Brownian motion of particles in diluted solutions can be quantitatively described by free diffusion neglecting inter-particle interactions. A quantitative expression for the free diffusion was first given by the Einstein-Smoluchowski relation[22] as

$$D_0 = \mu k_\mathrm{B} T, \tag{3.6}$$

which describes the relation between the macroscopic diffusion constant D_0, the kinetic energy and the mobility μ of the particles. μ is given by the ratio of the particles drift velocity v and the friction ζ of the solvent to the particle motion ($\zeta = \nu v$). With the friction coefficient for spherical particles given by $\nu = 6\pi\eta R_\mathrm{P}$ (Stokes law) this leads to the Stokes-Einstein relation

$$D_0 = \frac{k_\mathrm{B} T}{6\pi\eta R_\mathrm{P}}, \tag{3.7}$$

which connects the diffusion of particles D_0 to the viscosity η of the solvent. The equations of motion for a free diffusing particle with the radius R_P, mass m, and position $\vec{r}\,(t)$ are given by the Langevin equations[23]

$$m\frac{\mathrm{d}\vec{v}\,(t)}{\mathrm{d}t} = -\nu\vec{v}\,(t) + \vec{\xi}\,(t)\,. \tag{3.8}$$

Here $\nu\vec{v}\,(t)$ is the effective friction force and $\vec{\xi}\,(t)$ a random force determining the motion of the particle. The solution of the Langevin equations for an Ornstein-Uhlenbeck process[24] in equilibrium implicates that the relaxation time of the particle velocity is $\tau_\mathrm{B} \approx \frac{m}{\nu}$ and that the normalized mean square displacement $W\,(t) = \frac{1}{6}\left\langle \left|\vec{r}\,(t) - \vec{r}\,(0)\right|^2 \right\rangle$ of the particles is given by

$$W\,(t) = D_0\tau_\mathrm{B}\left[\frac{t}{\tau_\mathrm{B}} - 1 + \exp\left(-\frac{t}{\tau_\mathrm{B}}\right)\right]. \tag{3.9}$$

---

[22] Einstein, A. (1905). *Ann. Phys.* **322**, 549.

[23] The chosen formulation for a single particle is only a simplification of the $3N$ equations which characterize the motion of $i = 1, \cdots, N$ particles, given by

$$m_i\frac{\mathrm{d}\vec{v}_i\,(t)}{\mathrm{d}t} = -\sum_{j=1}^{N}\nu_{ij}\vec{v}_i\,(t) + \vec{\xi}_i\,(t)\,.$$

Langevin, P. (1908). *C. R. Acad. Sci.* **146**, 530.

[24] This is a special stochastic process which describes the velocity of Brownian motion particles. See: Uhlenbeck, G. E. and Ornstein, L. S. (1930). *Phys. Rev.* **36**, 823.

The corresponding short- and long-time asymptotic limits of $W(t)$ are

$$W(t) = \begin{cases} \frac{1}{2}\frac{k_\mathrm{B}T}{m}t^2 & \text{, for } t \to 0 \\ \frac{k_\mathrm{B}T}{\nu}t = D_0 t & \text{, for } t \to \infty \end{cases}, \tag{3.10}$$

which implies that the motion of the particles between their collisions ($t \ll \tau_\mathrm{B}$) is similar to a ballistic flight[25] and that the crossover from ballistic to diffusive motion sets in for times $t \approx \tau_\mathrm{B}$.

3.3.2 Diffusion of interacting colloidal particles

If interactions between colloidal particles are not negligible, two additional forces have to be considered in the Langevin equations for a single particle. On the one hand, there is the force due to the particle interaction $-\nabla U$, which induces a drift velocity to the Brownian motion of the particle. On the other hand, particle motion induces a flow field which influences the motion of other particles. These two influences are summarized as hydrodynamic interactions. Accounting for both, the effective Langevin equation for a single particle is given by[26]

$$\begin{aligned} m\frac{\mathrm{d}\vec{v}(t)}{\mathrm{d}t} = &- \nu\vec{v}(t) + \vec{\xi}(t) \\ &+ \int \left[\nabla_r U\left(\left|\vec{r} - \vec{r}'\right|\right)\right] \delta\vec{n}(\vec{r}, t)\,\mathrm{d}r^3 \\ &- \int \breve{\nu}\left(\vec{r} - \vec{r}'\right)\vec{j}(\vec{r}, t)\,\mathrm{d}r^3, \end{aligned} \tag{3.11}$$

where $\breve{\nu}$ is the effective friction tensor, $\vec{j}(\vec{r}, t)$ the local particle current and $\delta\vec{n}(\vec{r}, t)$ the fluctuation of the particle concentration.

Within X-ray photon correlation spectroscopy (XPCS) mainly self-diffusion properties in the short-time regime $t \ll \tau_\mathrm{R}$ are accessible. Here, τ_R is the time a colloidal particle needs to diffuse the mean particle distance estimated by $\tau_\mathrm{R} \approx \frac{n^{-\frac{2}{3}}}{D_0}$.[27] Neglecting hydrodynamic interactions in equation 3.11, $n(\vec{r}, t)$ can be considered as static for $t \ll \tau_\mathrm{R}$, which leads to an ordinary diffusion process described by

$$W(t) = D_\mathrm{S}^\mathrm{s} t \quad (\tau_\mathrm{B} \ll t \ll \tau_\mathrm{R}), \tag{3.12}$$

where D_S^s is the short-times self-diffusion coefficient. D_S^s is similar to the diffusion constant

---

[25] Einstein, A. (1908). *Z. Elektrochem. Angew. Phys. Chem.* **14**, 235.

[26] Medina-Noyola, M. (1987). *Faraday Discuss. Chem. Soc.* **83**, 21.

[27] It has to be noted, that this short-time regime is much longer than the typical relaxation time τ_B of the particle velocity.

of non-interacting colloidal particles and depends only on the particle volume fraction ϕ. It is given by

$$D_{\mathrm{S}}^{\mathrm{s}} = \alpha D_0 \left(1 - \beta\phi\right), \tag{3.13}$$

where α and β are empirical parameters covering the effect of the hydrodynamic interactions.[28] For $t \gg \tau_{\mathrm{R}}$ the particles have experienced many collisions, which allows to express the second component in equation 3.11 by a time dependent friction force $\int \Delta\vec{\nu}\left(t - t\,'\right)\vec{v}\left(t\,'\right)\mathrm{d}t\,'$ within the generalized Langevin equations.[29] As the particle motion is distorted by many particle interactions, the diffusion described by the long-time self-diffusion coefficient $D_{\mathrm{L}}^{\mathrm{s}}$ via

$$W\left(t\right) = D_{\mathrm{L}}^{\mathrm{s}} t \quad \left[t \gg \tau_{\mathrm{R}}\right], \tag{3.14}$$

is in general smaller than $D_{\mathrm{S}}^{\mathrm{s}}$.[30]

---

[28] This is described in: Beenakker, C. W. J. and Mazur, P. (1984). *Physica A* **126**, 349.

[29] Medina-Noyola, M. (1988). *Phys. Rev. Lett.* **60**, 2705.

[30] A detailed calculation for $D_{\mathrm{L}}^{\mathrm{s}}$ can be found in: Hemández-Contreras, M. et al. (1996). *Physica A* **234**, 271.

4 Scattering Methods

This chapter contains a short introduction to the X-ray scattering methods used in this work. First, terms and definitions regarding general principles of small angle X-ray scattering (SAXS) are defined, followed by an introduction into X-ray photon correlation spectroscopy (XPCS) and coherence properties of X-ray sources. Due to the different foci of the methods, the SAXS section deals more with time averaged properties of the scatterers[1] whereas the XPCS section covers their dynamical properties.[2]

4.1 Small angle X-ray scattering

When X-ray photons penetrate matter they can interact via absorption or scattering processes depending on their energy.[3] Due to the photon energy used in this study the interactions are sufficiently described by scattering processes. Within a scattering process, the scattered photon is characterized by the interference of re-emitted secondary waves from electrons in the sample, which are accelerated by the oscillating electric field of the incident photon. A typical scattering geometry for such a process is shown in Figure 4.1, where an incident photon with wavelength λ_i is scattered by the sample. The scattered photon with wavelength λ_s is detected at a scattering angle 2θ at a distance D behind the sample. The wave vectors $\vec{k}_\mathrm{i}$ and $\vec{k}_\mathrm{s}$ specify the incident and scattered propagation directions. The scattering process is characterized by the wave vector transfer $\vec{q} = \vec{k}_\mathrm{s} - \vec{k}_\mathrm{i}$. At small angles incoherent or Compton scattering processes are basically nonexistent. Thus, the quasi-elastic approximation is valid, i.e. the wavelength λ_i does not change during the scattering process, yielding $\lambda_i = \lambda_s =: \lambda$ (Thompson scattering). This leads to

---

[1] Details on the theory described in the referring subsections can be found in: Als-Nielsen, J. W. and McMorrow, D. (2001). *Modern X-Ray Physics.* 2nd Edition. Wiley, Hoboken, USA; Glatter, O. and Kratky, O. (1982). *Small-Angle X-ray Scattering.* 1st Edition. Academic Press, London, UK; Hansen, J. P. and McDonald, I. R. (2005). *Theory of simple liquids.* 3rd Edition. Academic Press, Waltham, USA. In addition, a very well done introduction to SAXS can be found here: Schroer, M. A. (2011). “Small angle X-ray scattering studies on proteins under extreme conditions.” PhD thesis. Dortmund, Germany: Technical University of Dortmund.

[2] Details can be found in: Grübel, G. et al. (2008). “Soft-Matter Characterization.” 1st Edition. Springer, New York, USA, 954–995.

[3] James, R. W. (1948). *The optical principles of the diffraction of X-rays.* 1st Edition. Bell and sons, London, UK.

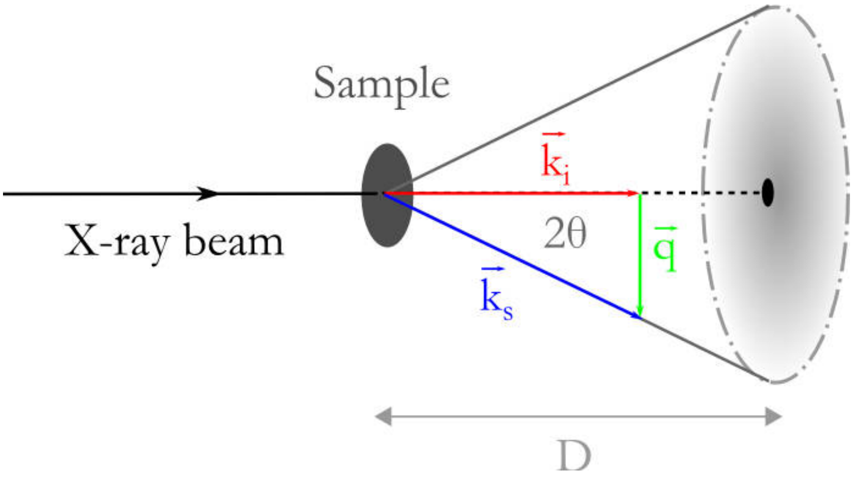

Figure 4.1: Schematic of the scattering process: A plane wave with wave vector $\vec{k}_\mathrm{i}$ is scattered by the sample at an angle 2θ and is detected at a distance D. The difference of the incident to the scattered wave vector is defined by the wave vector transfer $\vec{q}$.

$\left|\vec{k}\right| = k = \frac{2\pi}{\lambda}$, which yields:

$$|\vec{q}| = q = \frac{4\pi}{\lambda} \sin\left(\frac{2\theta}{2}\right). \tag{4.1}$$

First, the scattering of X-rays of a free electron is considered. The scattered intensity $I_\mathrm{S}(\theta)$ detected at a scattering angle 2θ within the solid angle increment $\Delta\Omega$ is given by the Thompson formula[4]

$$I_\mathrm{S}(\theta) = I_0 \cdot \frac{\mathrm{d}\sigma(\theta)}{\mathrm{d}\Omega}\Delta\Omega. \tag{4.2}$$

Here

$$\frac{\mathrm{d}\sigma(\theta)}{\mathrm{d}\Omega} = r_\mathrm{e}^2 \cdot \left(\frac{1+\cos^2(2\theta)}{2}\right) \tag{4.3}$$

is the Thompson differential scattering cross-section, $r_\mathrm{e} = 2.818 \cdot 10^{-15}$ m the classical electron radius, and I_0 the incident beam intensity per unit area. The term $\frac{1+\cos^2(2\theta)}{2}$ is the polarization factor of the incident beam which simplifies to unity for small scattering angles 2θ.

In general, the differential scattering cross-section $\frac{\mathrm{d}\sigma(\vec{q})}{\mathrm{d}\Omega}$ describes the angular distribution of the scattered photons, given by

$$\frac{\mathrm{d}\sigma(\vec{q})}{\mathrm{d}\Omega} = A(\vec{q}) \cdot A^*(\vec{q}), \tag{4.4}$$

---

[4] Als-Nielsen, J. W. and McMorrow, D. (2001). *Modern X-Ray Physics*. 2nd Edition. Wiley, Hoboken, USA.

where $A\left(\vec{q}\right)$ is the scattering amplitude and $A^{*}\left(\vec{q}\right)$ its complex conjugate. Equation 4.3 implies that the scattering amplitude of a single electron is r_e.

4.1.1 Scattering from a colloidal particle

Within the Thompson scattering approximation the electrons are considered to be free. In this case, the scattering amplitude of an atom can be expressed by $A_{\text{Atom}} = r_{\text{e}} \cdot \tilde{f}$, where $\tilde{f}$ denotes the atomic scattering factor. The atomic scattering factor is a complex function depending on the wave vector transfer $\vec{q}$ and the photon energy $\hbar\omega$ given by[5]

$$\tilde{f}\left(\vec{q}, \hbar\omega\right) = \tilde{f}_0\left(\vec{q}\right) + \tilde{f}'\left(\hbar\omega\right) + i \cdot \tilde{f}''\left(\hbar\omega\right), \tag{4.5}$$

where $\tilde{f}_0\left(\vec{q}\right)$ is the atomic form factor that corresponds to the Fourier transform of the atomic electron density, $\tilde{f}'\left(\hbar\omega\right)$ is the dispersion correction, and $\tilde{f}''\left(\hbar\omega\right)$ describes the absorption of photons. As the photon energy used here was far away from the atomic absorption edges of typical light elements, e.g. hydrogen H, carbon C, nitrogen N, and oxygen O, the contribution to the last two terms in equation 4.5 can be considered as not significant.[6]

The scattering amplitude of a colloidal particle can be described by the so-called particle form factor. It is given in the far-field[7] and first Born approximation[8] by the sum over all electrons with their corresponding phase shifts $\exp(i\vec{q} \cdot \vec{r})$. This is identical to the Fourier integral of the continuous charge distribution $\rho\left(\vec{r}\right)$ over the illuminated sample volume[9] V_{s}, given by

$$\tilde{f}_{\text{P}}\left(q\right) = \int_{V_{\text{s}}} \rho\left(\vec{r}\right) \exp\left(i\vec{q} \cdot \vec{r}\right) \mathrm{d}^3 r, \tag{4.6}$$

where $\rho\left(\vec{r}\right)$ is the electron density at position $\vec{r}$. Therefore, the scattering intensity of a particle within the solid angle $\Delta\Omega$ is given by

$$I\left(q\right) = I_0 \cdot r_e^2 \left|\tilde{f}_{\text{P}}\left(q\right)\right|^2. \tag{4.7}$$

---

[5] Feigin, L. A. and Svergun, D. I. (1987). *Structure analysis by small angle X-ray and neutron scattering.* 1st Edition. Plenum Press, London, UK.

[6] Schurtenberger, P. (2002). "Neutrons, X-ray and light: Scattering methods applied to soft condensed matter." 1st Edition. Elsevier, Amsterdam, Netherlands, 145ff.

[7] This is the case when the sample system is much smaller than the sample-detector distance.

[8] The first Born approximation is identical to the kinematic approximation, neglecting multiple scattering, i.e. electrons in the sample are not effected by secondary waves and waves scattered by two electrons separated by a distance $|\vec{r}|$ only differ by a phase factor $\exp(i\vec{q} \cdot \vec{r})$. See: Pietsch, U. et al. (2004). *High resolution X-ray scattering.* 2nd Edition. Springer, Berlin, Germany; and Dawydow, A. S. (1999). *Quantenmechanik.* 8th Edition. Wiley-VCH, Weinheim, Germany.

[9] The illuminated sample volume V_{s} is in the following abbreviated as scattering volume.

4.1.2 Scattering from colloidal particles in suspension

For the case of identical and spherical colloidal particles with the volume $V_\mathrm{P} = \frac{4}{3}\pi \cdot {R_\mathrm{P}}^3$ which are suspended in an isotropic medium, the particles can be characterized by an uniform[10] electron density ρ_P while the suspending medium has an average electron density ρ_S. Here, an isotropic distribution of the particles without a specific long range order is assumed. In this case, the scattering medium can be described by an effective scattering electron density defined by $\Delta\rho = \rho_\mathrm{P} - \rho_\mathrm{S}$ within $0 \leq |\vec{r} - \vec{r}_n| \leq R_\mathrm{P}$ and zero for $|\vec{r} - \vec{r}_n| > R_\mathrm{P}$, where R_P is the radius of the particles with its center located at $\vec{r}_n$. Hence, with equation 4.6 the scattering amplitude for N particles is given by [11]

$$\begin{aligned} A(q,t) &= r_\mathrm{e} \sum_{n=1}^{N} \left(\int_{V_\mathrm{P}} \Delta\rho \cdot \exp\left(i\vec{q} \cdot \vec{r}\right) \mathrm{d}^3 r \right) \exp\left(i\vec{q} \cdot \vec{r}_n(t)\right) \\ &= r_\mathrm{e} \sum_{n=1}^{N} f_n(q) \cdot \exp\left(i\vec{q} \cdot \vec{r}_n(t)\right). \end{aligned} \tag{4.8}$$

This leads to the differential scattering cross-section[12],

$$\frac{\mathrm{d}\sigma(q,t)}{\mathrm{d}\Omega} = {r_\mathrm{e}}^2 \cdot \sum_{n,m=1}^{N} \exp\left(i\vec{q} \cdot \left(\vec{r}_n(t) - \vec{r}_m(t)\right)\right) f_n(q) \cdot f_m^*(q). \tag{4.9}$$

The double sum in equation 4.9 can be decomposed by separation of terms with the same index $n = m$ corresponding to scattering from the same particle and cross-terms $n \neq m$ corresponding to the interference from different particles. Assuming ergodicity for the system, it follows for the temporal average[13]

$$\begin{aligned} \frac{d\sigma(q)}{d\Omega} &= \left\langle \frac{d\sigma(q,t)}{d\Omega} \right\rangle_t \\ &= {r_\mathrm{e}}^2 \cdot N \left\langle |f(q)|^2 \right\rangle + {r_\mathrm{e}}^2 \cdot \left\langle \sum_{n=1}^{N} \sum_{m \neq n}^{N} \exp\left(i\vec{q} \cdot \left(\vec{r}_n(t) - \vec{r}_m(t)\right)\right) f_n(q) \cdot f_m^*(\vec{q}) \right\rangle. \end{aligned} \tag{4.10}$$

---

[10] This is applicable since the internal structure of the particles is small compared to their size ($R_\mathrm{P} \gg$ 0.1 nm) and because SAXS is more sensitive to larger structures.

[11] The contribution of the solvent $\int_{V_\mathrm{P}} \rho_\mathrm{S} \cdot \exp\left(-i\vec{q} \cdot \vec{r}\right) \mathrm{d}^3\vec{r}$ is neglected for the calculation of the intensity. It is later considered as background intensity. See: Carpenter, D. K. and Mattice, W. L. (1977). *Biopolymers* **16**, 67.

[12] For a detailed derivation see: Glatter, O. and Kratky, O. (1982). *Small-Angle X-ray Scattering.* 1st Edition. Academic Press, London, UK; and Brumberger, H (1995). *Modern Aspects of Small Angle Scattering.* 1st Edition. Kluwer Academic Publishers, Dordrecht, Netherlands.

[13] The brackets $\langle\rangle$ denotes the statistical average over different particle configurations. Ergodicity implies here that the statistical average equals the temporal average $\langle\rangle_t$.

For dilute solutions, equation 4.10 can be further simplified within the so-called decoupling approximation[14] to

$$\frac{d\sigma\left(q\right)}{d\Omega} = {r_{\mathrm{e}}}^{2} \cdot N \left\langle \left|f\left(q\right)\right|^{2} \right\rangle + {r_{\mathrm{e}}}^{2} \cdot \left\langle f\left(q\right)\right\rangle^{2} \left\langle \sum_{n=1}^{N} \sum_{m\neq n}^{N} \exp\left(i\vec{q}\cdot\left(\vec{r}_{n}\left(t\right) - \vec{r}_{m}\left(t\right)\right)\right) \right\rangle . \tag{4.11}$$

By applying the pair distribution function $g\left(r\right)$, defined for a suspension of colloidal particles in equation 3.2, the double sum in equation 4.11 can be substituted for the isotropic case by[15]

$$\left\langle \sum_{n=1}^{N} \sum_{m\neq n}^{N} \exp\left(i\vec{q}\cdot\left(\vec{r}_{n}\left(t\right) - \vec{r}_{m}\left(t\right)\right)\right) \right\rangle =$$

$$\begin{aligned} &= \left\langle \sum_{n=1}^{N} \sum_{m\neq n}^{N} \int\limits_{V} \int\limits_{V'} \exp\left(i\vec{q}\cdot\left(\vec{r} - \vec{r}'\right)\right) \delta\left(\vec{r} - \vec{r}_{n}\left(t\right)\right) \delta\left(\vec{r}\,' - \vec{r}_{m}\left(t\right)\right) \mathrm{d}^{3}r\mathrm{d}^{3}r' \right\rangle \qquad (4.12) \\ &= 4\pi\frac{N^{2}}{V} \int\limits_{0}^{\infty} r^{2}\left(g\left(r\right) - 1\right) \frac{\sin\left(qr\right)}{qr}\mathrm{d}r, \end{aligned}$$

leading to the differential scattering cross section

$$\frac{d\sigma\left(q\right)}{d\Omega} = {r_{\mathrm{e}}}^{2} \cdot N \left\{ \left\langle \left|f\left(q\right)\right|^{2} \right\rangle + \left|\left\langle f\left(q\right)\right\rangle\right|^{2} \cdot 4\pi\frac{N}{V} \int_{0}^{\infty} r^{2}\left(g\left(r\right) - 1\right) \frac{\sin\left(qr\right)}{qr}\mathrm{d}r \right\} . \tag{4.13}$$

Since the shape of the particles is described by the $f\left(\vec{q}\right)$-term, one can define the electron density contrast dependent particle form factor $P\left(q\right)$ by

$$P\left(q\right) = \left\langle \left|f\left(q\right)\right|^{2} \right\rangle . \tag{4.14}$$

This allows the separation from the static structure factor $S\left(q\right)$ of the particles, containing the distribution of the inter-particle distances, via

$$S\left(q\right) = 1 + 4\pi\frac{N}{V} \int_{0}^{\infty} r^{2}\left(g\left(r\right) - 1\right) \frac{\sin\left(qr\right)}{qr}\mathrm{d}r. \tag{4.15}$$

With $\kappa\left(q\right) = \frac{\left|\left\langle f\left(q\right)\right\rangle\right|^{2}}{\left\langle \left|f\left(q\right)\right|^{2}\right\rangle}$, equation 4.13 thus becomes

$$\frac{d\sigma}{d\Omega}\left(q\right) = {r_{\mathrm{e}}}^{2} \cdot NP\left(q\right) \cdot \underbrace{\left(1 + \kappa\left(q\right)\left\{S\left(q\right) - 1\right\}\right)}_{S_{\mathrm{eff}}\left(q\right)}, \tag{4.16}$$

---

[14] Kotlarchyk, M. and Chen, S. H. (1983). *J. Chem. Phys.* **79**, 2461.

[15] Details can be found in: Hansen, J. P. and McDonald, I. R. (2005). *Theory of simple liquids.* 3rd Edition. Academic Press, Waltham, USA.

where $S_{\mathrm{eff}}(q)$ is the effective static structure factor. In the case of monodisperse and spherical particles $\left(\left|\langle f(q)\rangle\right|^2 = \left\langle \left|f(\vec{q})\right|^2\right\rangle\right)$, $\kappa(q)$ becomes unity and $S_{\mathrm{eff}}(q)$ is identical to the static structure factor $S(q)$. The static structure factor oscillates around unity in the limit of large momentum transfers, $\lim_{q\to\infty} S(q) = 1$. At length scales much smaller than the particle radius ($r \ll R_{\mathrm{P}}$) inter-particle correlations are negligible. The static structure factor is connected to macroscopic thermodynamical properties for $q \to 0$ via

$$S(0) = \tilde{n} k_{\mathrm{B}} T \Xi_T, \tag{4.17}$$

where Ξ_T is the isothermal compressibility and $\tilde{n}$ is the particle number density. For small wave vector transfers it can be expanded yielding $S(\vec{q}) = S(0) + \tilde{O}(\vec{q}^{\,2})$.[16]

In the case of monodisperse spherical particles, the electron density contrast dependent particle form factor $P(q)$ can be expressed by

$$P(q) \quad = \quad \left\langle \left| \int_{V_{\mathrm{P}}} \Delta\rho \cdot \exp(i\vec{q}\cdot\vec{r})\,\mathrm{d}^3 r \right|^2 \right\rangle = \Delta\rho^2 V_{\mathrm{P}}^2 \cdot F(q, R_{\mathrm{P}}), \tag{4.18}$$

with $F(q, R_{\mathrm{P}})$ denoting the particle form factor of spheres. It is given by[17]

$$F(q, R_{\mathrm{P}}) = \left[\frac{3\left[\sin(q\cdot R_{\mathrm{P}}) - q\cdot R_{\mathrm{P}}\cdot\cos(q\cdot R_{\mathrm{P}})\right]}{(q\cdot R_{\mathrm{P}})^3} \right]^2. \tag{4.19}$$

Incorporating absorption by the sample, the scattered intensity detected in a solid angle increment $\Delta\Omega$ becomes

$$I(q) = I_0 \cdot T \cdot d \cdot N \cdot r_{\mathrm{e}} \cdot \Delta\rho^2 \cdot V_{\mathrm{P}}^2(R_{\mathrm{P}}) \cdot F(q, R_{\mathrm{P}}) \cdot S(q). \tag{4.20}$$

where N is the number of illuminated colloidal particles, T is the transmission and d the thickness of the sample.

---

[16] Denev, A. et al. (2005). *Phys. Rev. E* **71**, 11105.

[17] Glatter, O. and Kratky, O. (1982). *Small-Angle X-ray Scattering.* 1st Edition. Academic Press, London, UK.

4.2 X-ray photon correlation spectroscopy

X-ray photon correlation spectroscopy (XPCS) is the analogue to the photon correlation spectroscopy technique of visible light used to study slow dynamics in soft matter systems.[18] Thus, XPCS can be used to study dynamical properties of disordered systems utilizing the properties of coherent X-rays. When a quasi static disordered sample is exposed to coherent light the scattering pattern shows grainy structures, so-called speckles, as the scattered photons interfere in the far-field. Due to coherent illumination such a speckle pattern reflects the exact spatial particle arrangement in the sample. Fluctuations of the intensity of individual speckles are related to the dynamic properties of the sample. In an XPCS experiment these temporal fluctuations are studied. It has become a powerful technique to measure the dynamics of condensed matter systems, such as colloidal suspensions[19], gels[20], ferrofluids[21], and surface dynamics[22]. The shorter wavelength of X-rays allows the investigation of dynamics on the nanometer length scale, which is essential to study liquid surfaces[23]. In addition, X-rays are not subject to multiple scattering, which seriously limits studies of opaque samples using visible light.[24] In the following, the coherence properties of X-rays are described in comparison to visible light.

4.2.1 Coherence properties of synchrotron radiation

In this chapter 'coherent illumination' is assumed, equivalent to the scattering by a perfect monochromatic and plane wave front. In reality this is valid only to a certain extend. A real X-ray source has a finite size and a non-zero energy bandwidth, which leads to emitted photons of slightly different energies and phases. In this context, the coherence lengths define the coherence volume. In this volume, the scattering can be assumed as

---

[18] Therefore, the theory of XPCS outlined here, follows mainly: Berne, B. J. and Pecora, R. (2000). *Dynamic Light Scattering: With Applications to Chemistry, Biology, and Physics.* 1st Edition. Dover Publications, New York, USA.

[19] Robert, A. (2007). *J. Appl. Cryst.* **40**, 34; Burghardt, W. R. et al. (2012). *Phys. Rev. E* **85**, 21402.

[20] Papagiannopoulos, A. et al. (2005). *J. Phys.: Condens. Matter* **17**, 279; Duri, A. and Cipelletti, L. (2006). *Europhys. Lett.* **76**, 972; Roshi, A. et al. (2006). *Phys. Rev. E* **74**, 31404; Fluerasu, A. et al. (2007). *Phys. Rev. E* **76**, 10401; Trappe, V. et al. (2007). *Phys. Rev. E* **76**, 51404; Madsen, A. et al. (2010). *New Journal of Physics* **12**, 55001.

[21] Lal, J. et al. (2001). *Eur. Phys. J. E* **4**, 263; Robert, A. et al. (2006). *Europhys. Lett.* **75**, 764; Robert, A. et al. (2005b). *J. Chem. Phys.* **122**, 84701; Robert, A. et al. (2005a). *Journal of Magnetism and Magnetic Materials* **289**, 47; Autenrieth, T. et al. (2007). *J. Appl. Cryst.* **40**, 250.

[22] Madsen, A. et al. (2001). *Phys. Rev. E.* **64**, 61406; Madsen, A. et al. (2005). *J. Synchotron Rad.* **12**, 786; Seydel, T. et al. (2003). *Rev. Sci. Instrum.* **74**, 4003; Duri, A. et al. (2009). *Phys. Rev. Lett.* **102**, 145701.

[23] Sikorski, M. (2008). "Glass transition near the free surface studied by synchrotron radiation." PhD thesis. Hamburg, Germany: University of Hamburg.

[24] A comparison regarding multiple scattering can be found in appendix A.1.

coherent.[25] Two different types of coherent lengths are distinguished.[26] The longitudinal (or temporal) coherence length ξ_l takes into account the energy distribution of the photons. The transverse (or spatial) coherence length ξ_t is related to the finite size of the source.

In Figure 4.2(a) a conceptional definition of the longitudinal coherence is illustrated. It is characterized by two plane waves, propagating in the same direction, but with slightly different wavelengths λ and $\lambda - \Delta\lambda$. After propagating a distance equal to the longitudinal coherence length $\xi_\mathrm{l} = \frac{1}{2}N\lambda = \frac{1}{2}(N+1)(\lambda - \Delta\lambda)$ the two waves are completely out of phase, corresponding to a phase difference of π. Using the wavelength relationship $N\lambda = (N+1)(\lambda - \Delta\lambda)$ it follows that $N \approx \frac{\lambda}{\Delta\lambda}$ as a result of considerations in Figure 4.2(a). Thus, the longitudinal coherence length is given by

$$\xi_\mathrm{l} = \frac{1}{2}\frac{\lambda^2}{\Delta\lambda}. \tag{4.21}$$

It is dominated by the energy resolution of the source $\frac{\Delta\lambda}{\lambda}$, which is for synchrotron radiation sources usually given by the energy bandwidth of the monochromator. For example, the [111] reflection of a perfect silicon crystal has an energy resolution of $\frac{\Delta\lambda}{\lambda} \approx 10^{-4}$, leading to a longitudinal coherence length in the order of $\xi_\mathrm{l} = 0.75$ µm for a typical wavelength of $\lambda = 0.15$ nm.

A conceptional definition of the transverse coherence is shown in Figure 4.2(b), where two plane waves with the same wavelength λ are emitted from opposing ends of a finite-sized source of size L. The sample is positioned at a distance D from the source. After the scattering process, the waves can be considered out of phase at a distance $\xi_\mathrm{t} = \frac{\lambda}{2}\frac{1}{\tan(\Delta\lambda)}$ perpendicular to the radiation. With the simplification $\tan(\Delta\lambda) \approx \frac{L}{D}$, the transverse coherence length is given by

$$\xi_\mathrm{t} = \frac{\lambda}{2}\frac{D}{L}, \tag{4.22}$$

which is dominated by the ratio $\frac{D}{L}$. For example, the coherence beamline P10, where most of the experiments were carried out, has a source-sample distance of $D^{\mathrm{P10}} \geq 90$ m and

---

[25] The coherence volume of a source limits the scattering volume which can be studied according to the 'coherent illumination'. For example, only scatterers within the dimensions of the coherent volume contribute to the same sum in the expression for the differential scattering cross-section

$$\frac{\mathrm{d}\sigma(q,t)}{\mathrm{d}\Omega} = {r_\mathrm{e}}^2 \cdot \sum_{n,m=1}^{N} \exp\left(i\vec{q}\cdot\left(\vec{r}_n(t) - \vec{r}_m(t)\right)\right) f_n(q) \cdot f_m^*(q).$$

Scatterers outside this volume contribute to another sum. In consequence, if one considers the scattering volume n times larger than the coherence volume, the wave fronts originating from scatterers inside the nth volume will interfere and give rise to $I_n(\vec{q}, t)$. In this case, the total intensity is averaged over n ensembles, and therefore is similar to the case of incoherent scattering.

[26] Grübel, G. et al. (2008). “Soft-Matter Characterization.” 1st Edition. Springer, New York, USA, 954–995.

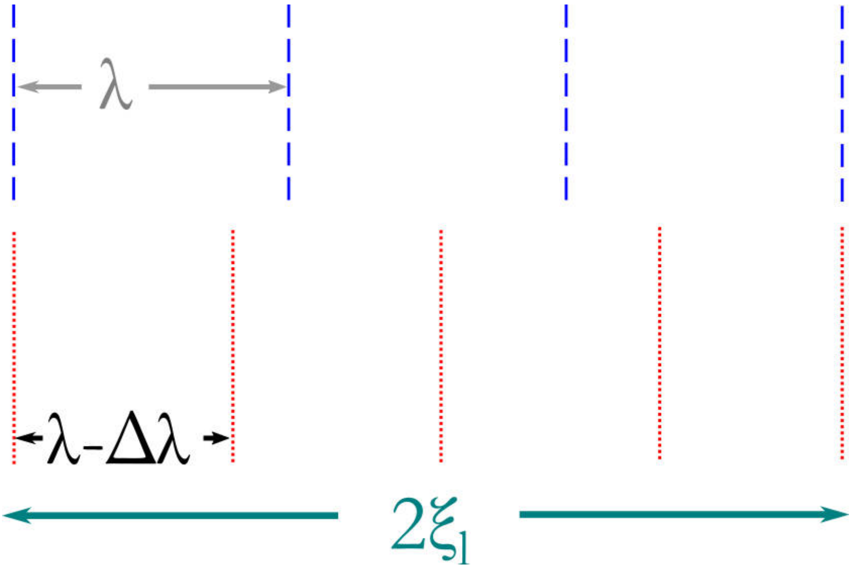

(a) Longitudinal coherence length ξ_l defined by the energy bandwidth.

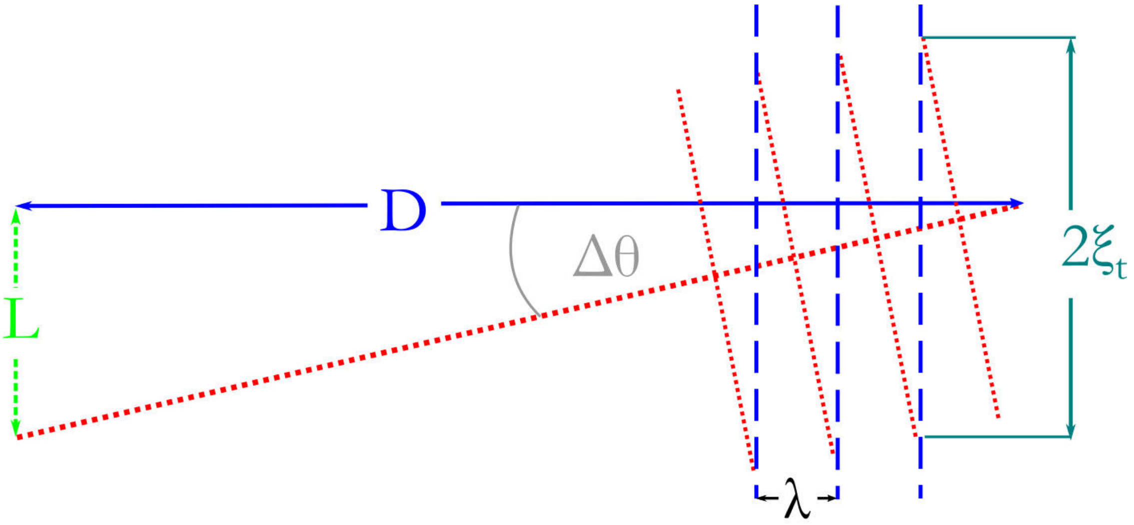

(b) Transverse coherence length ξ_l defined by the beam divergence.

Figure 4.2: Conceptional illustration of coherence lengths.

a source dimension of 14×84 µm^2 $[h \times v]$, resulting in transverse coherence lengths of $\xi_{\mathrm{t_v}}^{\mathrm{P10}} \approx 450$ µm and $\xi_{\mathrm{t_h}}^{\mathrm{P10}} \approx 75$ µm.[27] The transverse coherence lengths limits the size of the illuminated area which can assumed to be coherently illuminated. Therefore, the part of the beam which illuminates the sample has to be smaller than 450×75 µm^2 in this example. Typically, this is achieved by using two or more pairs of slits in front of the sample.

The longitudinal coherence length ξ_l limits the path length difference (PLD) of two scattered waves, which can be accepted as coherently illuminated. Thus, this defines the maximum wave vector transfer $q_{\max}\left(\theta_{\mathrm{PLD}<\xi_\mathrm{l}}\right)$ for which full coherence can be assumed. The PLD for a scattering process from a sample with thickness w illuminated by a beam with the size L in transmission geometry is given by[28]

$$\mathrm{PLD}\,(\theta) \approx 2 \cdot w \cdot \sin^2(\theta) + L \cdot \sin(2\theta)\,. \tag{4.23}$$

In consequence full coherence can only be achieved for wave vector transfers $q < 0.16$ nm^{-1}, assuming $L = 20$ µm, and $w = 1$ mm as typical experimental parameter for XPCS at the P10 beamline. It has to be noted, that the coherence lengths are proportional to λ and λ^2 respectively, so that the requirements for 'coherent illumination' in the X-ray regime ($\lambda \approx 0.1$ nm) are much more demanding than at wavelengths in the optical regime ($\lambda \approx 500$ nm). This is even more pronounced for the coherent flux, especially with respect to the beam size limitations due to the coherence lengths. For example, the spatially coherent flux F_c of an undulator based X-ray source is given by[29]

$$F_\mathrm{c} = \frac{\Delta\lambda}{\lambda} \cdot B \cdot \left(\frac{\lambda}{2}\right)^2. \tag{4.24}$$

Here, B is the so-called spectral brilliance given by[30]

$$B = \frac{F}{\left(\Delta\alpha_h \Delta\alpha_v\right)\left(\alpha_h \alpha_v\right)\left(\frac{\Delta\lambda}{\lambda}\right)}. \tag{4.25}$$

It describes the photon flux per area, per solid angle and per wavelength interval of 0.1%. In equation 4.25 F denotes the total photon flux, $\Delta\alpha_{h,v}$ is the horizontal and vertical beam divergence, $\alpha_h \cdot \alpha_v$ is the beam size, and $\frac{\Delta\lambda}{\lambda}$ is the bandwidth. Using the coherence

---

[27] See: DESY, Photon Science (Oct. 2013). *P10: Beamline layout/specifications.* URL: `http://photon-science.desy.de/facilities/petra_iii/beamlines/p10_coherence_applications/index_eng.html`; and Balewski, K., ed. (2010). *Comissioning of Petra III.* International Particle Accelerator Conference 1. Kyoto University. Kyoto: IPAC'10/ACFA.

[28] Grübel, G. et al. (2008). "Soft-Matter Characterization." 1st Edition. Springer, New York, USA, 954–995.

[29] Kim, K. (1986). *Nuclear Instruments and Methods in Physics Research* **A246**, 71.

[30] Thompson, A. C., ed. *X-ray data booklet.* 3rd Edition. Lawrence Berkeley National Laboratory, Berkeley, USA.

time defined by the longitudinal coherence length $t_\mathrm{c} = \frac{\xi_\mathrm{l}}{c}$, it follows that the number of photons n_c in the coherence volume is given by the expression

$$n_\mathrm{c} = F_\mathrm{c} \cdot t_\mathrm{c} = \left(\frac{\lambda}{2}\right)^3 \frac{B}{c}. \tag{4.26}$$

As a result, the number of coherent photons of a source is proportional to λ^3. This is why a significant coherent flux is much easier achievable at longer wavelengths and thus at lower energies.

4.2.2 Principles of X-ray photon correlation spectroscopy

In the following a suspension of N particles with time depending positions $\vec{r}_n(t)$ for $n = 1, \ldots, N$ is considered. As result of the previous section, the total scattering amplitude $A(\vec{q}, t)$ of such a system within 'coherent illumination' is given by the sum over the scattering amplitudes A_0 for each particle with respect to the position dependent phase shift $\exp(-i\vec{q} \cdot \vec{r}_n(t))$,

$$A(\vec{q}, t) = \sum_{n=1}^{N} A_0 \cdot e^{-i\vec{q}\cdot\vec{r}_n(t)}. \tag{4.27}$$

Due to Brownian motion, the particles' positions change and thus their phases are time dependent. As a result, the total scattering amplitude fluctuates in time. If one considers $A(\vec{q}, t)$ at two different times t and $t + \Delta t$ with a time delay Δt smaller than the characteristic time τ_c of the particle dynamics ($\Delta t \ll \tau_\mathrm{c}$), the scattering amplitude $A(\vec{q}, t + \Delta t)$ does change significantly compared to $A(\vec{q}, t)$. For larger time delays the scattering amplitudes become uncorrelated. This can be described by the normalized temporal field correlation function

$$g_1(\vec{q}, \Delta t) = \frac{\langle A(\vec{q}, t)\, A^*(\vec{q}, t + \Delta t)\rangle}{\langle A(\vec{q}, t)\, A^*(\vec{q}, t)\rangle}, \tag{4.28}$$

wherein the brackets denotes the average, defined by

$$\langle A(\vec{q}, t)\, A^*(\vec{q}, t + \Delta t)\rangle = \lim_{T\to\infty} \frac{1}{T} \int_0^T A(\vec{q}, t)\, A^*(\vec{q}, t + \Delta t)\, \mathrm{d}t. \tag{4.29}$$

As only the intensity $I\left(\vec{q},t\right) = \left|A\left(\vec{q},t\right)\right|^2$ is accessible in an experiment, the normalized intensity autocorrelation function $g_2\left(\vec{q},\tau\right)$ has to be defined as

$$g_2\left(\vec{q},\Delta t\right) = \frac{\langle I(\vec{q},t)I(\vec{q},t+\Delta t)\rangle}{\langle I(\vec{q},t)\rangle^2}. \tag{4.30}$$

It can contain similar information on the particle dynamics as $g_1\left(\vec{q},\Delta t\right)$. If $A\left(\vec{q},t\right)$ is a Gaussian variable, $g_1\left(\vec{q},\Delta t\right)$ and $g_2\left(\vec{q},\Delta t\right)$ are related by the Siegert relation[31]

$$g_2(\vec{q},\Delta t) = 1 + \beta \cdot \left|g_1\left(\vec{q},\Delta t\right)\right|^2. \tag{4.31}$$

Here, β is the so-called speckle contrast which is determined by the spatial coherence of the scattered photons.[32]

By resolving the time correlation of the particles' scattering amplitudes, the normalized field correlation function $g_1\left(\vec{q},\Delta t\right)$ can be expressed by the static structure factor $S\left(q\right)$ via

$$g_1\left(\vec{q},\Delta t\right) = \frac{1}{S\left(q\right)} \cdot \underbrace{\frac{1}{N}\sum_{n,m}^{N} \left\langle \exp\left(i\vec{q}\cdot\left[\vec{r}_n\left(t\right) - \vec{r}_m\left(t+\Delta t\right)\right]\right)\right\rangle_t}_{\tilde{S}(\vec{q},\Delta t)} = \frac{\tilde{S}\left(\vec{q},\Delta t\right)}{S\left(q\right)}, \tag{4.32}$$

where $\langle\rangle_t$ is the time average and $\tilde{S}$ the dynamic structure factor which contains information on the evolution of inter-particle correlations. Using the Siegert relation, $\tilde{S}$ is connected to g_2. Since the Siegert relation assumes ergodic systems, g_2 is sensitive to the degree of ergodicity in the system.[33] In principle, the slowing down of the particle dynamics near the glass transition temperature T_g leads to a non-ergodic state. Proper statistics for a g_2 function can be obtained either by measuring long enough and applying the temporal average or by using multiple speckles within an azimuthal average of the scattering pattern (multi-speckle technique)[34]. While the temporal average limits the study of time dependent dynamics, e.g. heterogeneous dynamics, it becomes unfeasible for non-ergodic systems like glasses. This favors the multi-speckle technique which offers proper statistics while enabling the access to the time dependent features of the dynamics.[35]

In order to measure speckle intensity correlations, it is essential that a single speckle

---

[31] Berne, B. J. and Pecora, R. (2000). *Dynamic Light Scattering: With Applications to Chemistry, Biology, and Physics.* 1st Edition. Dover Publications, New York, USA.

[32] The contrast ranged between $\beta = 0.3 - 0.6$, due to the partially coherent light of synchrotron radiation sources, whereas β is close to unity for almost fully coherent laser sources.

[33] Non-ergodic systems cannot evolve through a representative fraction of possible spatial configuration for a certain time.

[34] Lumma, D. et al. (2000). *Rev. Sci. Instrum.* **71**, 3274.

[35] It is noted that the multi-speckle technique requires 2D-detection of speckles which is accompanied by additional technical constraints.

can be resolved by the detector. This means that the size of the detector pixel p has to match or to be smaller than the speckles size s, $p \leq s$. With the speckle size given by the formula[36],

$$s = \frac{\lambda D}{L}, \tag{4.33}$$

where λ is the wavelength, D the sample-detector distance and L the lateral extension of the effective scattering volume, the requirement becomes $p \leq \frac{\lambda D}{L}$.[37]

4.2.3 Multi-speckle technique

The adaptation of the intensity autocorrelation function to the multiple-speckle detection scheme is given by

$$g_2\left(q, \Delta t\right) = \frac{\left\langle \left\langle I_p\left(\vec{q}, t\right) I_p\left(\vec{q}, t + \Delta t\right)\right\rangle_\psi \right\rangle_t}{\left\langle \left\langle I_p\left(\vec{q}, t\right)\right\rangle_\psi^2 \right\rangle_t}, \tag{4.34}$$

where I_p is the intensity measured by a detector pixel p, $\langle\rangle_\psi$ denotes the azimuthal average of the pixel-ensemble corresponding to the same range of wave vector transfers $[q, q + \Delta q]$ with a negligible phase difference, and $\langle\rangle_t$ is the temporal average.[38] To study the time dependent out-of-equilibrium behavior, which is an important feature of glassy systems[39], one defines the instantaneous intensity autocorrelation function C_I as[40]

$$C_\mathrm{I}\left(q, t_1, t_2\right) = \frac{\left\langle I_p\left(\vec{q}, t_1\right) I_p\left(\vec{q}, t_2\right)\right\rangle_\psi}{\left\langle I_p\left(\vec{q}, t_1\right)\right\rangle_\psi \left\langle I_p\left(\vec{q}, t_2\right)\right\rangle_\psi}. \tag{4.35}$$

Here, the multi-speckle time correlation scheme[41] is essential to overcome the time averaging in g_2. An example of C_I for equilibrium dynamics is shown in Figure 4.3. C_I measures the time evolution of the intensity autocorrelation function $g_2(q, \bar{t})$ along the absolute experimental time $t = \left(t_1 + t_2\right)/2$ for a delay time $\bar{t} = t_2 - t_1$. In the case that the

---

[36] Goodman, J. W. (2000). *Statistical optics*. 1st Edition. Wiley, Hoboken, USA.

[37] For example, the speckle size s for a sample illuminated with a beam of the size $L^2 = 20$ µm × 20 µm at a photon energy of $E = 8$ keV ($\lambda \approx 0.154$ nm) measured at a distance $D = 2$ m is $s \approx 15.4$ µm. Thus, a speckle can be resolved in this configuration by an Andor detector with a pixel size of $p_\mathrm{Andor} = 13$ µm × 13 µm (see chapter 6.2).

[38] 2D-detection is typically achieved by an X-ray sensitive chip which is segmented in a 2D-array of pixels detecting the incoming photons.

[39] Struik, L. C. E. (1978). *Physical aging in amorphous polymers and other materials*. 1st Edition. Elsevier, Amsterdam, Netherlands.

[40] Malik, A. et al. (1998). *Phys. Rev. Lett.* **81**, 5832.

[41] Cipelletti, L. and Weitz, D. A. (1999). *Rev. Sci. Instrum.* **70**, 3214.

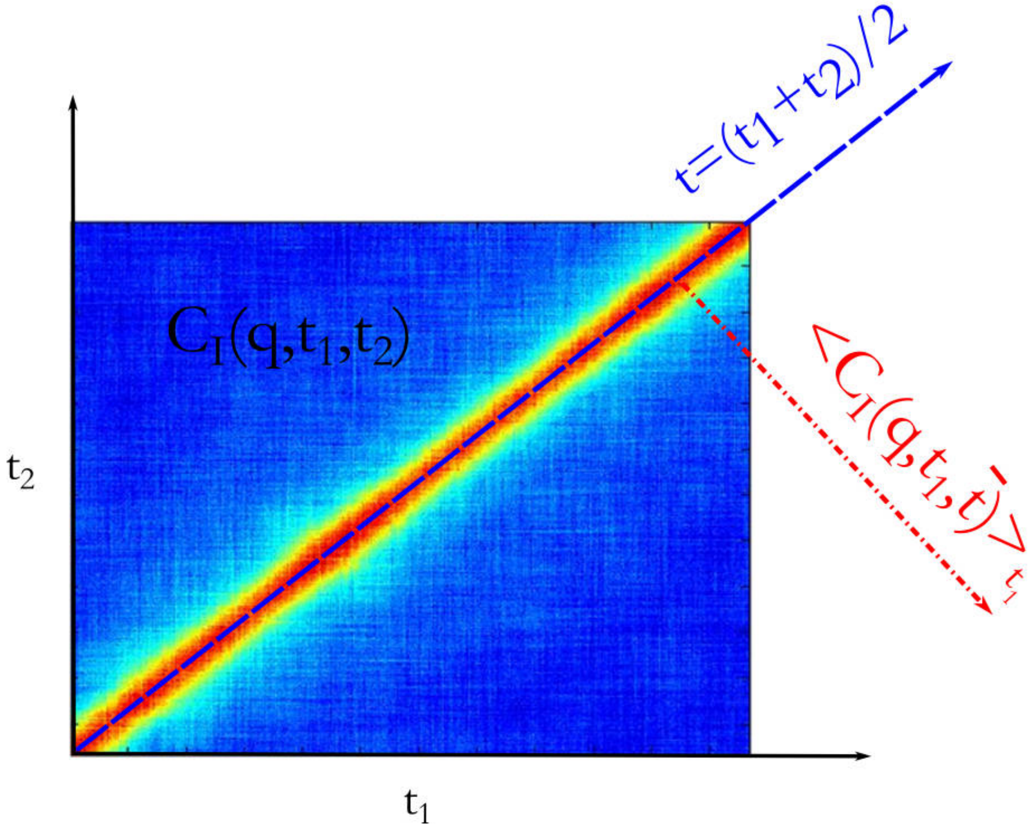

Figure 4.3: The instantaneous intensity autocorrelation function $C_{\mathrm{I}}\left(q, t_1, t_2\right)$ in a given interval $[q, q+\Delta q]$ for equilibrium dynamics. The colors represent the scaling of C_{I} from large (red) to low (blue) values.

dynamics does not change with t, the time average of C_{I} is equal to g_2:

$$g_2(q, t)=\left\langle C_{\mathrm{I}}\left(q, t_1, t\right)\right\rangle_{t_1} . \tag{4.36}$$

In addition to the investigation of non-equilibrium dynamics (Figure 4.4), C_{I} can be used to quantify temporal fluctuations in equilibrium dynamics which are assumed to play a key role in the dynamics of supercooled glass formers near T_{g}.[42] A quantity for the fluctuations of C_{I} is given by its normalized variance[43]

$$\chi_{\mathrm{T}}(q, t)=\frac{\left\langle C_{\mathrm{I}}^2\left(q, t_1, t\right)\right\rangle_{t_1}-\left\langle C_{\mathrm{I}}\left(q, t_1, t\right)\right\rangle_{t_1}^2}{\left\langle C_{\mathrm{I}}\left(q, t_1, t=0\right)\right\rangle_{t_1}^2} . \tag{4.37}$$

χ_{T} quantifies temporal fluctuations and peaks typically around the inflection point of g_2. The height of the peak is proportional to the variance of the characteristic relaxation

---

[42] Berthier, L. (2011). *Rev. Mod. Phys.* **83**, 587.

[43] Duri, A. and Cipelletti, L. (2006). *Europhys. Lett.* **76**, 972.

time $\left(\frac{\Delta\tau_\mathrm{c}}{\tau_\mathrm{c}}\right)$ which is related to the width of the relaxation time distribution $G\left(\frac{\tau}{\tau_\mathrm{c}}\right)$ in the system. Thus, an increase of the peak height $\chi_{\mathrm{T}_\mathrm{max}}$ can be related to increasing dynamical heterogeneities. This interpretation is only valid if $G\left(\frac{\tau}{\tau_\mathrm{c}}\right)$ is sufficiently explored by the system during the measurement. This is not the case for non-equilibrium dynamics, e.g. a 'speed-up' (Figure 4.4(a)) or a 'slow-down' (Figure 4.4(c)), where $\chi_{\mathrm{T}_\mathrm{max}}$ can be a function of the experimental time t_e.

The increase of spatial heterogeneity as a result of correlated motion is assumed to be the origin of the increasing dynamical heterogeneity near T_g.[44] Spatial heterogeneity is quantified via the four-point susceptibility χ_4. Its increase has been identified as a signature for growing dynamical correlation lengths, e.g. in supercooled liquids.[45] More precisely, χ_4 is a measure for the correlation of the dynamics between two points in space within a given time window. It is defined by

$$\chi_4\left(t\right) \propto \int G_4\left(\vec{r},t\right)\mathrm{d}\vec{r}, \tag{4.38}$$

where

$$G_4\left(\vec{r},t\right) = \left\langle \rho\left(0,0\right)\rho\left(0,t\right)\rho\left(\vec{r},0\right)\rho\left(\vec{r},t\right)\right\rangle - \left\langle \rho\left(0,0\right)\rho\left(0,t\right)\right\rangle\left\langle \rho\left(\vec{r},0\right)\rho\left(\vec{r},t\right)\right\rangle \tag{4.39}$$

is the four-point density correlator. Here, $\rho\left(\vec{r},\tau\right)$ is the electron density at a certain point in space-time.[46]

The theory predicts a direct relation between spatial and dynamical heterogeneities.[47] While χ_4 is difficult to measure in experiments, χ_T has been studied in glassy materials to characterize dynamical correlation lengths.[48] Likewise, studies of χ_T in glassy systems reported a peaking around $t = \tau^* \approx \frac{\tau_\mathrm{c}}{\mathrm{e}}$. It was found that the height of the χ_T-peak has a distinct q-related scaling $\propto q^p$ at small q, with $1 < p < 2$.[49] This scaling can be related to the q-dependence of $\tau_\mathrm{c}\left(T,q\right)$. Thus, $\chi_\mathrm{T}^* = \chi_\mathrm{T}\cdot\left(\frac{q}{q_0}\right)^p$ can be used to compare temporal fluctuations of the dynamics at different temperatures q-independently.[50]

Two restrictions limit the investigation of χ_T^* as quantity of temporal fluctuations for colloidal particle dynamics in supercooled liquids. First, the requirements concerning the statistics to obtain C_I is much more demanding, as e.g. for g_2. This prohibits the evaluation of χ_T^* for larger q or for very dilute suspensions of colloids where the signal-to-noise ratio is too low. The effect of the statistics is demonstrated on the example of a dilute suspension

---

[44] Richert, R. (2002). *J. Phys.: Condens. Matter* **14**, R703.

[45] Berthier, L. et al. (2005). *Science* **310**, 1797.

[46] Lačević, N. et al. (2003). *J. Chem. Phys.* **119**, 7372.

[47] Carré, A. et al. (2007). *J. Chem. Phys.* **127**, 114512.

[48] Trappe, V. et al. (2007). *Phys. Rev. E* **76**, 51404.

[49] Wandersman, E. et al. (2008). *J. Phys.: Condens. Matter* **20**, 155104.

[50] The measurable q-range changes with temperature which leads to barely comparable values of $\chi_\mathrm{T}\left(T,q\right)$.

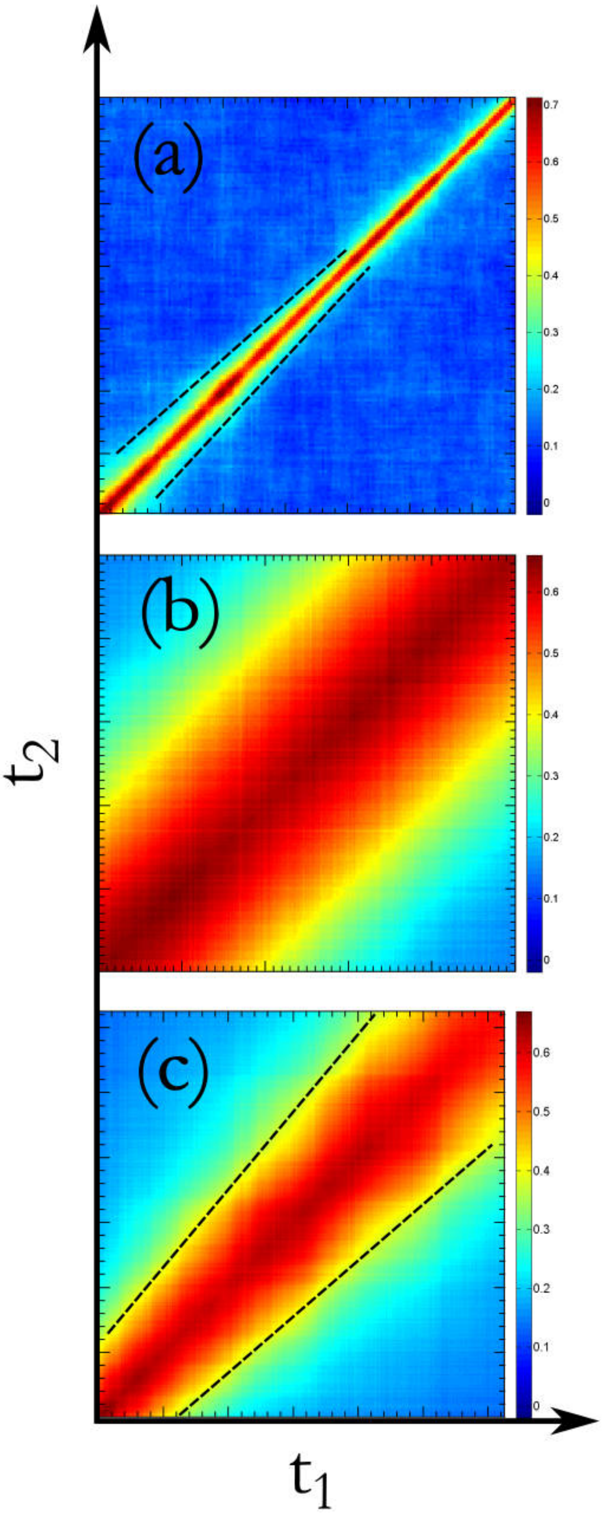

Figure 4.4: C_{I} of equilibrium and non-equilibrium dynamics: (a) 'speed-up' dynamics, (b) equilibrium dynamics and (c) 'slow-down' dynamics. The color bar represents the scaling of C_{I}.

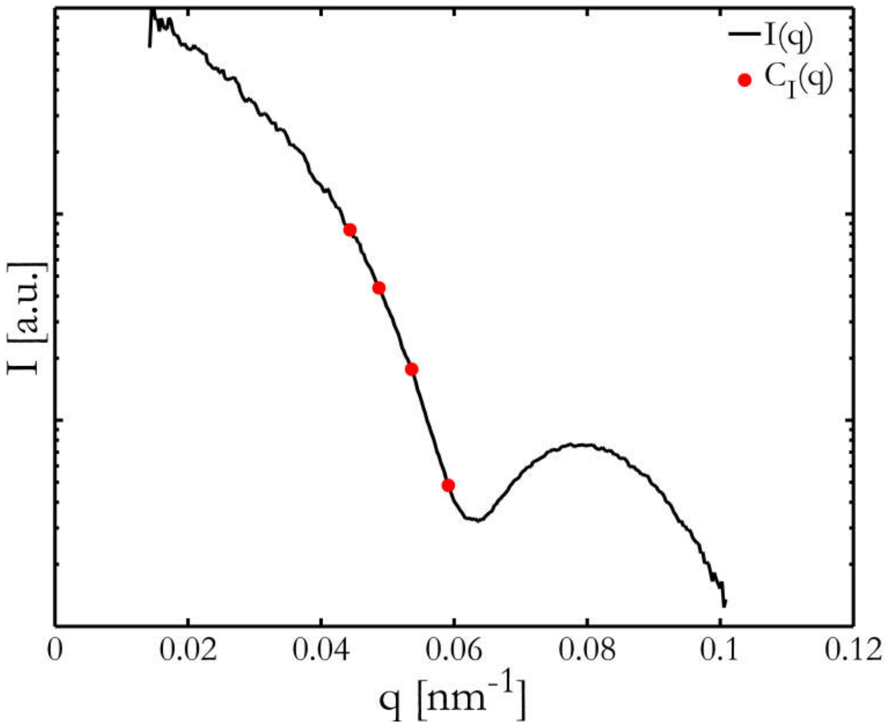

Figure 4.5: The scattered intensity $I\,(q)$ of a speckle pattern from a dilute suspension of colloidal particles with radius $R = 71$ nm at $T = 220$ K. The marked q-values were evaluated for $C_{\mathrm{I}}\,(q)$.

of colloidal particles with radius $R = 71$ nm at $T = 220$ K, for which the intensity is shown in Figure 4.5. Here, the azimuthal averaged scattered intensity $I\,(q)$ of a speckle pattern decreases about an order of magnitude for the q-values at which $C_{\mathrm{I}}\,(q)$ was obtained. $C_{\mathrm{I}}\,(q)$, shown in Figure 4.6, exhibits a strong blurring with decreasing intensity. This blurring causes a strong increase of χ^*_{T} for $q > 0.0486$ nm^{-1} that is not related to temporal fluctuations. This is illustrated in Figure 4.7, where the results of χ^*_{T} are shown for these q-values. It is obvious, that for $q \leq 0.0486$ nm^{-1}, χ^*_{T} collapse to a master curve while for larger q-values χ^*_{T} appears much larger.

Second, near T_{g} the characteristic time τ_{c} exceed the accessible experimental time t_{e} and χ^*_{T} become statistically insufficient to quantify the temporal fluctuations of g_2.[51] Due to an experimental limitation of t_{e}, the information on dynamical heterogeneities obtained by χ^*_{T} is restricted to the case of $\tau_{\mathrm{c}} \ll t_{\mathrm{e}}$. The effect when τ_{c} approaches t_{e} is demonstrated in Figure 4.8. Here, $C_{\mathrm{I}}\,(q = 0.0279\text{ nm}^{-1})$ is shown for $\tau_{\mathrm{c}} \ll t_{\mathrm{e}}$ (see Figure 4.8(a)) and shorter time segments which for A indicates 'slow-down' (see Figure 4.8(b)) and for F 'speed-up' (see Figure 4.8(c)) dynamics. The results of τ^* and $\chi^*_{\mathrm{T_{max}}}$ for these time sections

---

[51] For details see: Richert, R. (2002). *J. Phys.: Condens. Matter* **14**, R703; Dalle-Ferrier, C. et al. (2007). *Phys. Rev. E* **76**, 041510; and Berthier, L. et al. (2005). *Science* **310**, 1797.

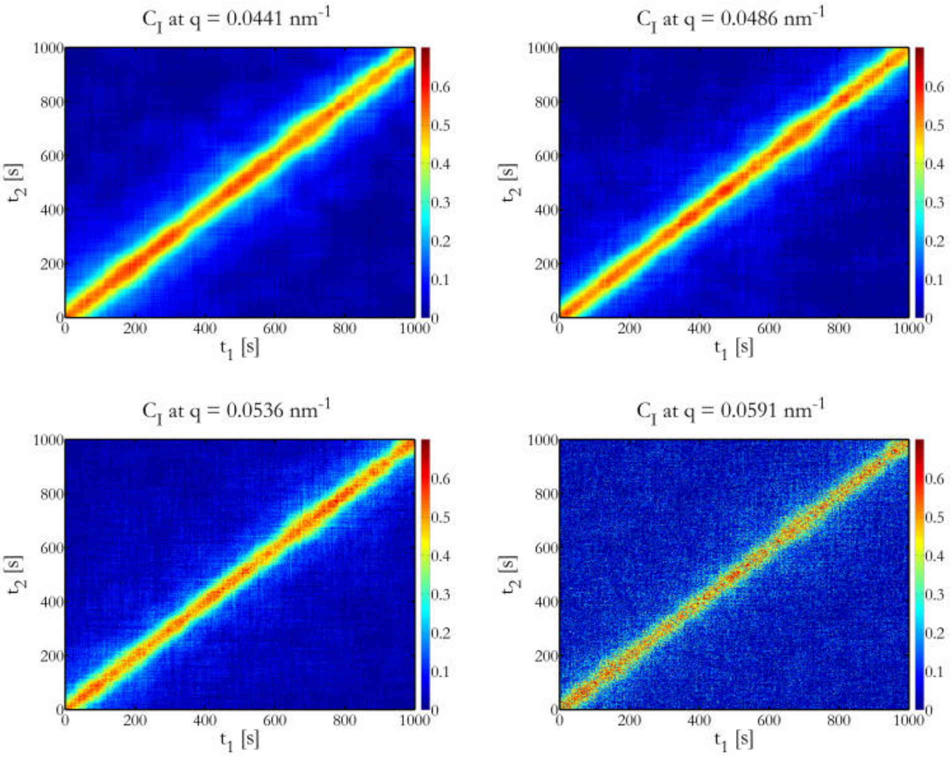

Figure 4.6: The effect of the scattered intensity on $C_{\mathrm{I}}(q)$ demonstrated for a dilute suspension of colloidal particles with radius $R = 71$ nm at $T = 220$ K. With increasing q, $C_{\mathrm{I}}(q)$ becomes noisy due to the low scattered intensity.

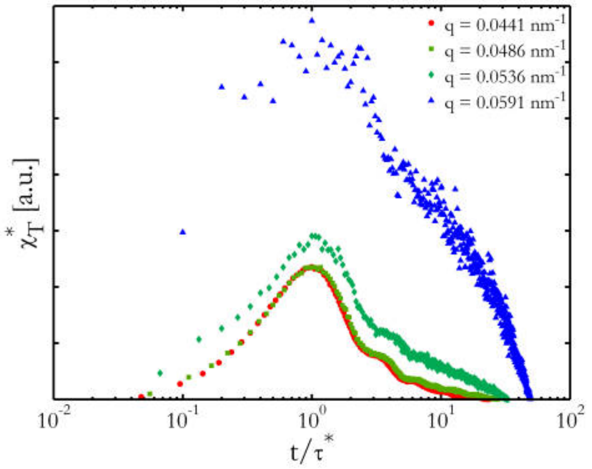

Figure 4.7: The effect of the scattered intensity on $\chi_{\mathrm{T}}(q)$. Shown are the corresponding results of $\chi^*_{\mathrm{T}}(q, t/\tau^*)$ for a dilute suspension of colloidal particles with radius $R = 71$ nm at $T = 220$ K.

are shown in Figure 4.9. It is clearly visible, that the peak times τ^* appear shorter (see Figure 4.9(a)) and $\chi^*_{\mathrm{T_{max}}}$ much larger (see Figure 4.9(b)) for the shorter sections A and F in comparison to the case of $\tau_c \ll t_e$. In particular, the artificial increase of χ^*_{T} limits the interpretation as measure of dynamical heterogeneity at temperatures near T_g when τ_c approaches t_e.

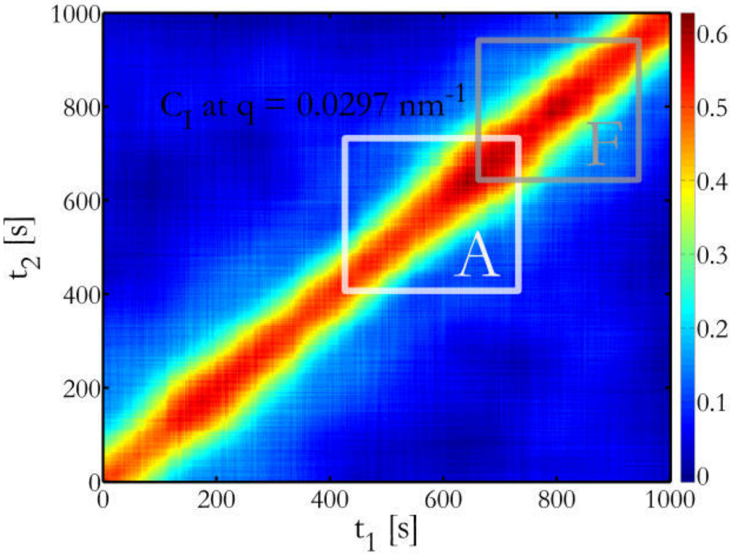

(a) $C_{\mathrm{I}}\left(q = 0.0279\ \mathrm{nm}^{-1}\right)$ for the full experimental time t_e.

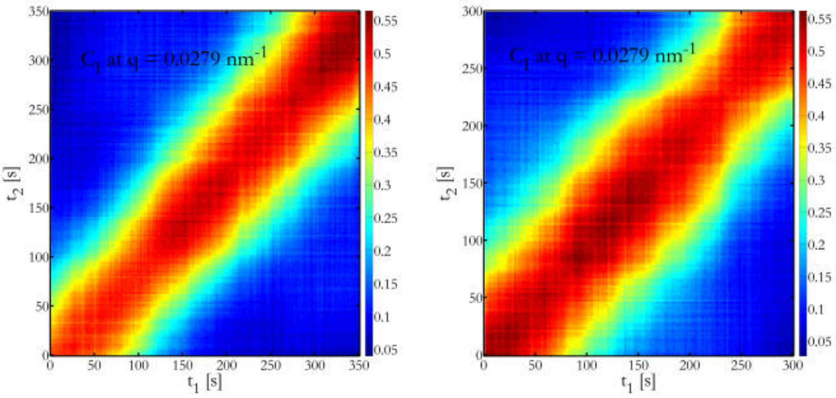

(b) $C_{\mathrm{I}}\left(q = 0.0279\ \mathrm{nm}^{-1}\right)$ of subsection A.

(c) $C_{\mathrm{I}}\left(q = 0.0279\ \mathrm{nm}^{-1}\right)$ of subsection F.

Figure 4.8: Experimental time dependence of C_{I}, demonstrated for a dilute suspension of colloidal particles with radius $R = 71$ nm at $T = 220$ K for (a) the full experimental time and subsections (b) A and (c) F.

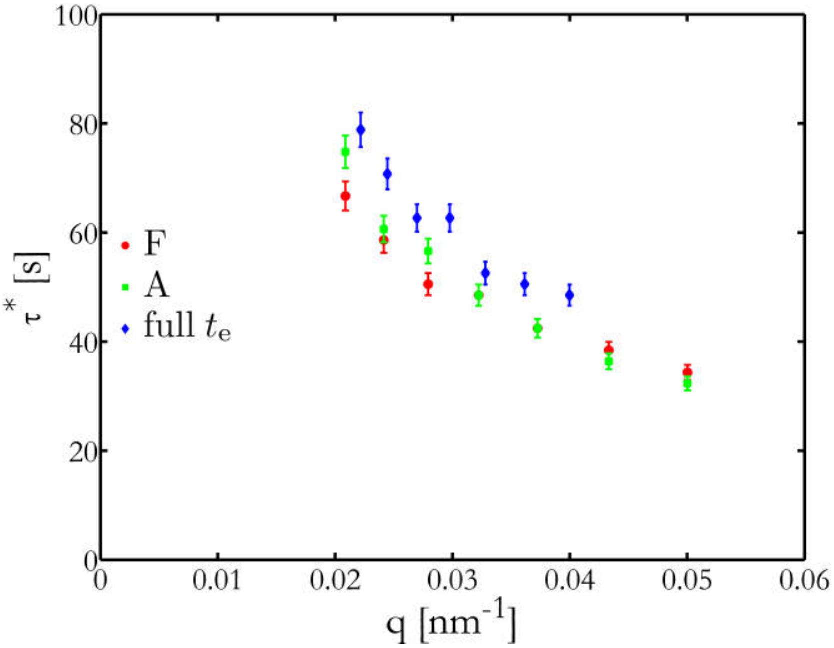

(a) Results of τ^* for different experimental times.

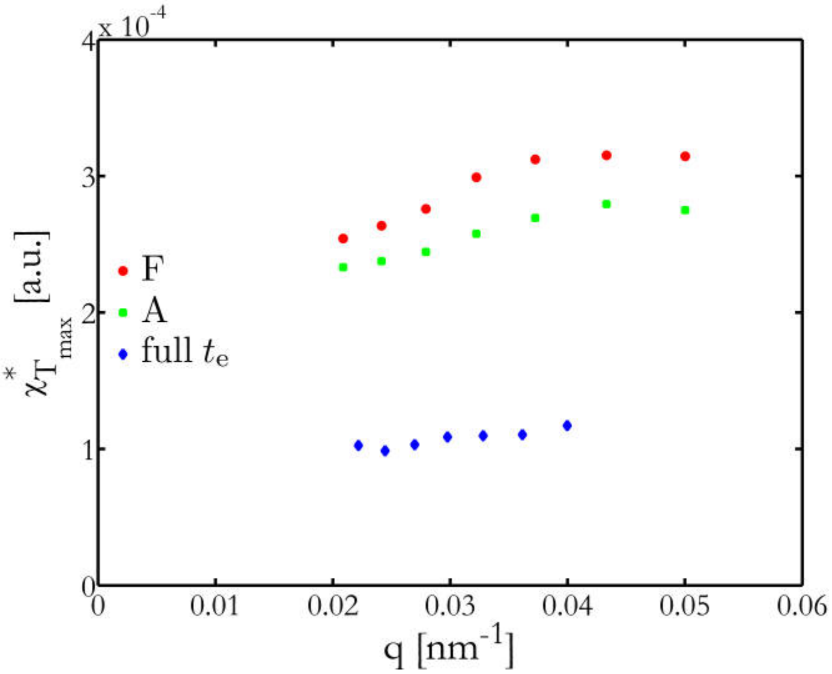

(b) Results of $\chi^*_{\mathrm{T_{max}}}$ for different experimental times.

Figure 4.9: Results of (a) τ^*, and (b) $\chi^*_{\mathrm{T_{max}}}$ for different experimental times demonstrated at a dilute suspension of colloidal particles with radius $R = 71$ nm at $T = 220$ K.

5 Scattering from colloidal particles

In this chapter, the static and dynamic properties of charge-stabilized and spherical particles suspended in a viscous liquid will be presented in connection to the observables obtained via small angle X-ray scattering (SAXS) and X-ray photon correlation spectroscopy (XPCS) measurements.

5.1 The particle form factor

In dilute and screened systems of charge-stabilized and spherical particles, inter-particle correlations are negligible and the static structure factor $S\left(q\right)$ in equation 4.20 becomes unity. Therefore, measurements of dilute samples are appropriate to determine the particle form factor. As real colloidal systems show a notable size distribution, equation 4.19 for the particle form factor $\tilde{F}$ has to be adapted. Typically, the Schulz-Flory[1] distribution a_{sf} is used to describe the size distribution of colloidal particles. It is given by

$$a_{\mathrm{sf}}\left(R, R_{\mathrm{P}}, z\right) = \frac{1}{z!}\left(\frac{z+1}{R_{\mathrm{P}}}\right)^{z+1} R^{z}\exp\left(-\frac{z+1}{R_{\mathrm{P}}}R\right), \tag{5.1}$$

where z is a parameter describing the width of the distribution. It is related to the particle size polydispersity $\tilde{P}$ by

$$\tilde{P} = \frac{\Delta R}{R_{\mathrm{P}}} = \sqrt{\frac{1}{z+1}}. \tag{5.2}$$

Here, R_{P} represents the mean value of the particle radii. Incorporating a_{sf}, the particle form factor in equation 4.19 becomes

$$F\left(q, R_{\mathrm{P}}, \tilde{P}\right) = \int\limits_{0}^{\infty}\left(\frac{R^3}{R_{\mathrm{P}}^3}\right)^2 \tilde{F}\left(q, R\right) a_{\mathrm{sf}}\left(R, R_{\mathrm{P}}, \tilde{P}\right) \mathrm{d}R. \tag{5.3}$$

---

[1] The Schulz-Flory distribution describes the parameter spreading in polymer condensation reactions such as the chain length or the molecular weight. For details see: Nakamura, K. et al. (2003). *Powder Technology* **131**, 120.

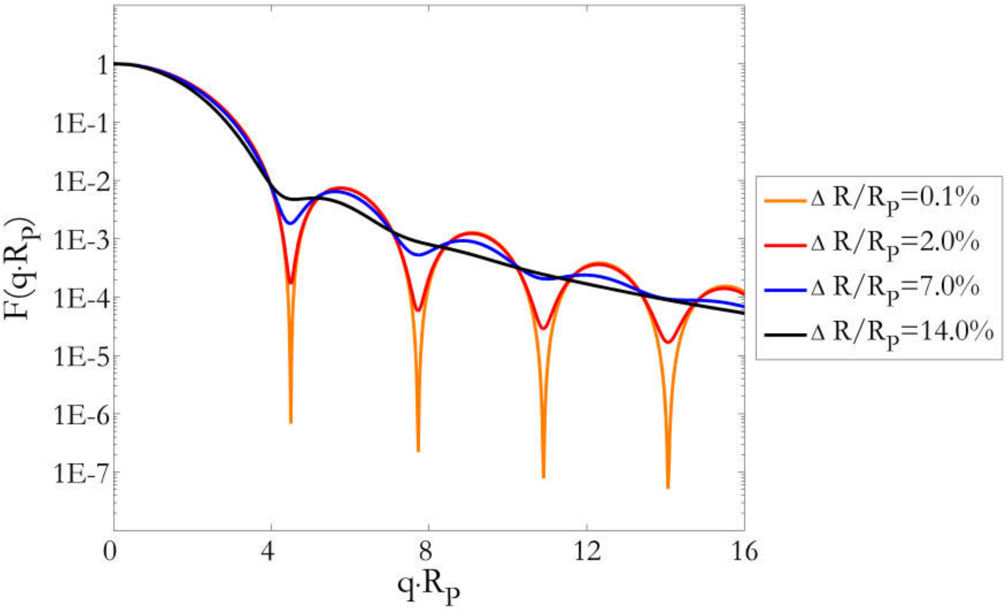

Figure 5.1: Particle form factor F illustrated for different polydispersities.

A solution of this integral can be found in literature[2] and is used in this thesis to model the scattering from colloidal particles in dilute solutions. Calculated form factors of colloidal particles at different $\tilde{P}$ are shown in Figure 5.1. For small $\tilde{P}$ the form factor exhibits sharp minima which are smeared out for larger $\tilde{P}$.[3]

5.2 The static structure factor

The particle form factor F of dilute samples can be used to measure the static structure factor of more concentrated samples by using $S(q) \propto \frac{I(q)}{F(q,R_{\mathrm{P}})}$ (equation 4.20 for spherical particles). In the following, inter-particle interactions are assumed to be described by a Yukawa potential (equation 3.5). Considering the correlation function $h(r)_{ij}$ between two particles i and j as a sum of the direct correlation $c(r)_{ij}$ and the indirect correlations $c\left(\left|\vec{r}-\vec{r}'\right|\right)_{ij}$ involving other particles, one obtains[4]

$$h(r)_{ij} = g(r)_{ij} - 1 = c(r)_{ij} + \sum_k \rho_k \int c\left(\left|\vec{r}-\vec{r}'\right|\right)_{ik}\left(g\left(r'\right)_{ik} - 1\right) \mathrm{d}^3 r. \tag{5.4}$$

---

[2] Aragon, S. R. and Pecora, R. (1976). *J. Chem. Phys.* **64**, 2395.

[3] The model works good for $\tilde{P} < 15$ % since the particle form factor reveals explicit minima. For larger $\tilde{P}$ the model is not sensitive to the particle form factor.

[4] The expression is derived by applying the Ornstein-Zernike relation. See: Ornstein, L. S. and Zernike, F. (1914). *KNAW Proceedings* **17**, 793.

This equation can be solved iteratively by using the mean spherical approximation[5] (MSA) for electrolyte suspensions at moderate to high particle concentrations.[6] With the closure-relations of the MSA given by

$$h(r)_{ij} = -1 \qquad r < (R_i + R_j), \tag{5.5}$$

$$c(r)_{ij} = -\tfrac{1}{k_B \cdot T} \cdot u(r)_{ij} \qquad r > (R_i + R_j), \tag{5.6}$$

one can obtain the pair distribution function $g(r)$. The method can be extended to arbitrary low particle densities by using the rescaled mean spherical approximation (RMSA).[7] A method to calculate the static structure factor obtained within the RMSA model for particles with a Yukawa potential was found by Ruiz-Estrada et al.[8] and was used to model the static structure factor of concentrated solutions throughout this thesis. Parameters of the model are the mean particle radius R_P, the volume fraction $\phi = \frac{\sum V_\mathrm{P}}{V_\mathrm{System}}$, the effective charge Z_eff, the temperature T, and the relative permittivity ϵ_r of the solvent.[9] In Figure 5.2(a) the dependence of the static structure factor $S(q)$ on Z_eff is shown for a volume fraction of $\phi = 20$ vol.% and a relative dielectric permittivity $\epsilon_r = 5$ at room temperature. With increasing Z_eff the first maximum of $S(q)$ increases and narrows. Figure 5.2(b) illustrates the effect of ϕ on $S(q)$ for $Z_\mathrm{eff} = 100e^-$, $\epsilon_r = 5$ at room temperature. With increasing ϕ the first peak of $S(q)$ shifts to larger momentum transfers, indicating a decrease of the next neighbor distances. Furthermore, its height also increases as shown in Figure 5.2(a), indicating in both cases an increased ordering of the system.

5.3 Dynamics of colloidal particles

If one considers the inter-particle interactions to be negligible, the particles' mean squared displacement $\left\langle \Delta\vec{r}_n(\tau)^2 \right\rangle = \left\langle |\vec{r}_n(0) - \vec{r}_n(\tau)|^2 \right\rangle$ is governed only by thermal fluctuations described by Brownian motion. These dynamics are characterized by free diffusion (section 3.3), given by[10]

$$\left\langle \Delta\vec{r}_n(\tau)^2 \right\rangle = 6 D_0 \tau, \tag{5.7}$$

---

[5] Lebowitz, J. L. and Percus, J. K. (1966). *Phys. Rev.* **144**, 251; Percus, J. K. and Yevick, G. (1964). *Phys. Rev.* **136**, 290.

[6] Blum, L. and Hoye, J. S. (1978). *J. Stat. Phys.* **19**, 317.

[7] For details see: Hansen, J. P. and Hayter, J. B. (1982). *Mol. Phys.* **46**, 651.

[8] Ruiz-Estrada, H. et al. (1990). *Physica A* **168**, 919.

[9] Typically, additional screening of the particle interaction is a further parameter. As no salt was added, this parameter was set to zero.

[10] Berne, B. J. and Pecora, R. (2000). *Dynamic Light Scattering: With Applications to Chemistry, Biology, and Physics.* 1st Edition. Dover Publications, New York, USA.

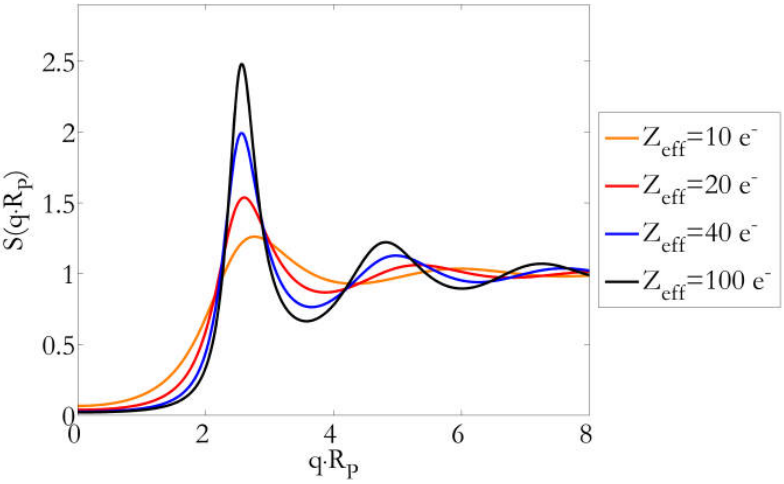

(a) S as a function of the effective charge Z_{eff}.

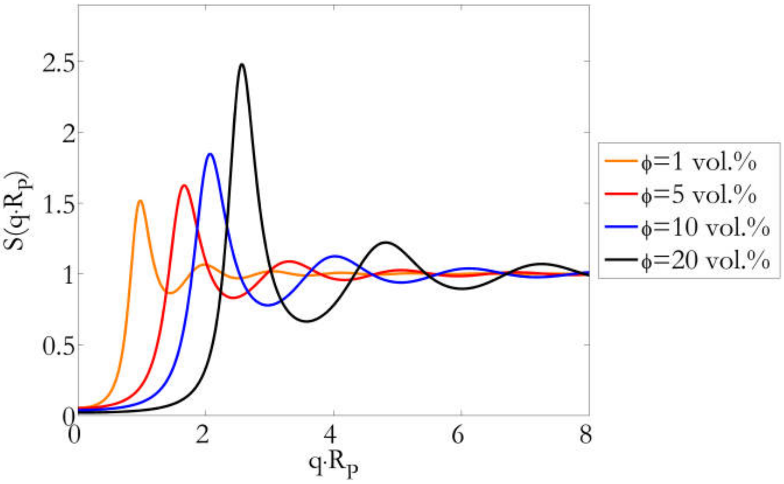

(b) S as a function of the volume fraction ϕ.

Figure 5.2: Static structure factors S calculated by the RMSA model for charge-stabilized particles suspended in a medium with $\epsilon_r = 5$ at room temperature as a function of qR_{P}: (a) Evolution of S as function of Z_{eff} at $\phi = 20$ vol.%. (b) Evolution of S as function of ϕ for $Z_{\text{eff}} = 100e^-$.

where D_0 is the diffusion coefficient of the particles given by the Stokes-Einstein relation[11]

$$D_0 = \frac{k_\mathrm{B} T}{6\pi\eta R_\mathrm{H}}, \tag{5.8}$$

where R_H is the hydrodynamic radius of the particles. In addition, $S\left(q\right)$ is unity in this case. Thus, the normalized field correlation function g_1 (equation 4.32) simplifies to

$$g_1\left(\vec{q}, \tau\right) = \frac{1}{N} \sum_{n=1}^{N} e^{i\vec{q}\cdot\left[\vec{R}_n(0) - \vec{R}_n(\tau)\right]}. \tag{5.9}$$

This can be rewritten as

$$g_1\left(\vec{q}, \tau\right) = e^{\frac{-|\vec{q}|^2}{6}\cdot\left\langle \Delta\vec{r}_n(\tau)^2 \right\rangle} = e^{-D_0 |\vec{q}|^2 \tau}, \tag{5.10}$$

assuming that the displacement of the particles is a Gaussian variable. As a result, the normalized intensity autocorrelation function g_2 is given by

$$g_2\left(\vec{q}, \tau\right) = 1 + \beta\left(\vec{q}\right) \left|g_1\left(\vec{q}, \tau\right)\right|^2 = 1 + \beta\left(\vec{q}\right) e^{-2\Gamma\tau}, \tag{5.11}$$

where $\Gamma = D_0 \left|\vec{q}\right|^2$ is the relaxation rate of the particles, with $\tau_c = \Gamma^{-1}$ defining the characteristic relaxation time of the particle dynamics.

In this context, the possibility to probe τ_c depends on the accessible time window of the experiment. This is given at the lower limit by the detector acquisition time t_a and at the upper limit by the maximal experimental time t_e. To measure the intensity with a detector requires t_a in order to record and read-out the scattering pattern. Therefore, the intensity is a temporal integrated observable $\bar{I}\left(\vec{q}, t\right) = \int\limits_0^{t_a} I\left(\vec{q}, t\right) \mathrm{d}t$.[12] For $t_\mathrm{a} \ll \tau_\mathrm{c}$ this average is sensitive to the particle dynamics, whereas for $t_\mathrm{a} \gg \tau_\mathrm{c}$ it is equal to an ensemble average that is dominated by time independent correlations. This is the same result as obtained in an incoherent X-ray scattering experiment, where the scattering volume is much larger then the coherence volume. That is illustrated in Figure 5.3, where the azimuthal average and a line cut of a speckle pattern are compared. The azimuthal averaging in Figure 5.3(b) causes the disappearance of speckles similar to a temporal average, whereas the intensity of the line cut along a solid angle region ψ, with a width smaller than the speckle size, fluctuates around it. Thus, the lower limit to access τ_c is given by t_a. The upper limit is given by t_e, which is restricted due to the beam stability or the available beam time. These limitations are illustrated in Figure 5.4. There, the normalized intensity

---

[11] Einstein, A. (1905). *Ann. Phys.* **322**, 549.

[12] Given that ergodicity of the system can be assumed.

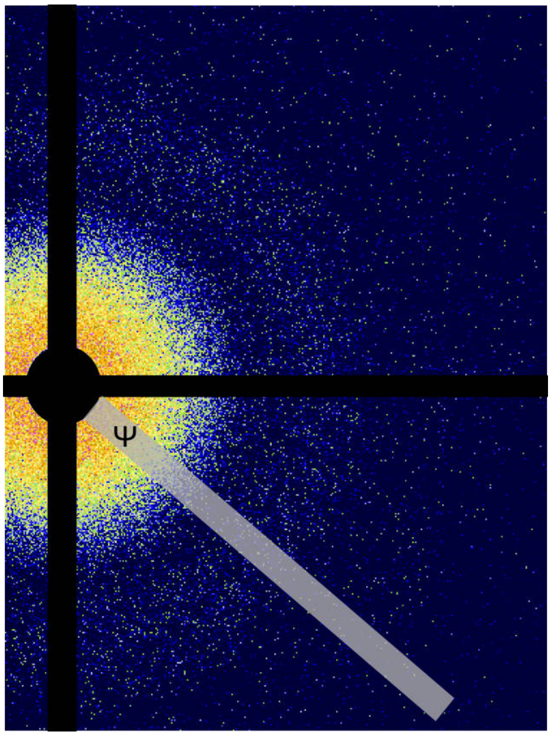

(a) Typical scattering pattern from colloidal particles in solution.

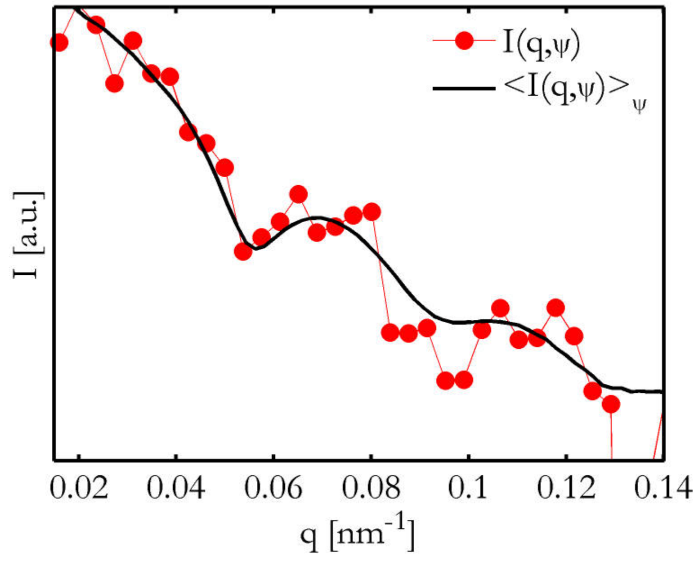

(b) Azimuthal averaged intensity along the cut ψ (red) and for the full angle (black solid line).

Figure 5.3: Difference between coherent and incoherent illumination illustrated by using azimuthal averaging of a single scattering pattern shown in (a). In plot (b) the azimuthal averaged intensity of the full pattern is compared to a line cut with a width smaller than the speckle size.

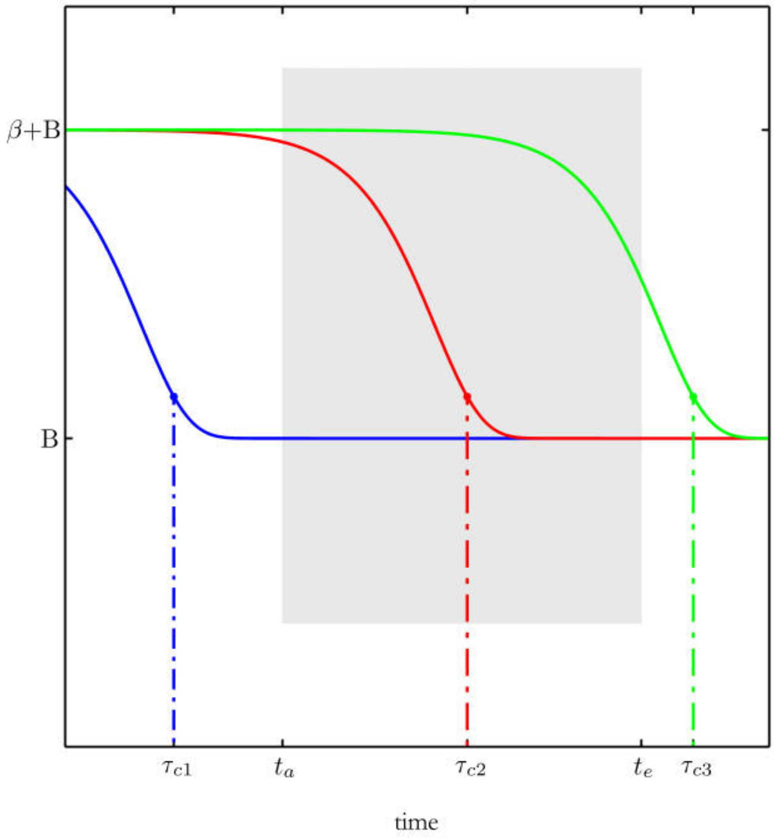

Figure 5.4: The experimental time window (indicated by the gray box) and the limitation to measure τ_c.

autocorrelation function g_2, according to equation 5.11, is shown for three different τ_cx at the same contrast β. In general, g_2 decreases from $\beta + B$ to B around τ_cx, where B is the so-called baseline[13]. The characteristic times τ_cx of g_2 were chosen to be below (τ_c1), above (τ_c3) and within (τ_c2) the limits of the experimental time window $[t_\mathrm{a} \leq t \leq t_\mathrm{e}]$. For $\tau_\mathrm{c} \ll t_\mathrm{a}$, as illustrated for τ_c1, g_2 has reached B during the measurement of the first scattering pattern and cannot be used to determine τ_c1. For $\tau_\mathrm{c} \gg t_\mathrm{e}$, as illustrated for τ_c3, g_2 has not decayed fully and cannot be used to quantify τ_c3. Only for $t_\mathrm{a} < \tau_\mathrm{c2} < t_\mathrm{e}$, g_2 can be evaluated to determine τ_c2 with high accuracy.

In the case of inter-particle interactions, the decay of g_1 is in general non-exponential. Then, g_1 can be expressed by a cumulant expansion[14]

$$g_1\left(\vec{q}, \tau\right) = e^{\left(\sum\limits_{n=1}^{\infty} \frac{\Gamma_n(\vec{q})}{n!}(-\tau)^n\right)}. \tag{5.12}$$

---

[13] This is a parameter according to the offset of the Siegert-relation which is typically close to one.

[14] Kubo, R. (1962). *J. Phys. Soc. Jpn.* **17**, 1100.

For short times τ, the first cumulant term dominates g_1. This yields the effective short-time diffusion coefficient D_{eff} given by[15]

$$\lim_{\tau \to 0} \frac{1}{g_1(\vec{q}, \tau)} \frac{\mathrm{d}g_1(\vec{q}, \tau)}{\mathrm{d}\tau} = \Gamma_1(\vec{q}) = D_{\text{eff}}(q) \cdot |\vec{q}|^2 . \tag{5.13}$$

For small q the effective short-time diffusion coefficient becomes the short-time collective-diffusion $D_{\text{c,short}} = D_{\text{eff}}(q \to 0)$, which describes the first decay caused by large scale density fluctuations. In the opposite case of large wave vector transfers, the effective diffusion coefficient becomes q-independent and is dominated by the self-diffusion of the particles leading to the short-time self-diffusion coefficient $D_{\text{s,short}} = D_{\text{eff}}(q \to \infty)$. The expression for the q-dependence of the effective short-time diffusion follows from the generalized Smoluchowski-equation, and is given by the ratio[16]

$$D_{\text{eff}}(q) = D_0 \cdot \frac{H(q)}{S(q)}, \tag{5.14}$$

where H denotes the hydrodynamic function describing the influence of hydrodynamic interactions with the dispersion medium to the particle dynamics. At low volume fractions of the samples and small effective charge of the particles, the hydrodynamic function can be assumed as $H \equiv 1$ in the probed q-range of $2.5 \leq qR_{\text{P}} \leq 6$.[17] For this case of hydrodynamically non-interacting particles, the effective short-time diffusion becomes $D_{\text{eff}}(q) = \frac{D_0}{S(q)}$, and the diffusion of the system decreases at length scales where $S(q)$ peaks. This phenomenon is known as de Gennes narrowing.[18] It is interpreted as a reduction of particle dynamics caused by a caging of the next-neighbor particles.

---

[15] Altenberger, A. R. (1976). *Chem. Phys.* **15**, 269.

[16] Nägele, G. (1996). *Physics Reports* **272**, 215.

[17] An expression for the hydrodynamic function which verifies the assumption is given in appendix A.2.

[18] De Gennes, P. G. (1959). *Physica* **25**, 825.

6 Experimental details

In the first part of this chapter, the synthesis of the colloidal particles is presented in addition to an overview of the solvent properties of the investigated glass formers polypropylene glycol (PPG) and dibutyl-phthalate (DBP). In the second part, the description of the experimental set-ups and procedures are given.

6.1 Colloidal sample system

In order to investigate solvent dependent tracer dynamics, the particles should be highly monodisperse, offer sufficient repulsion to ensure an adequate distribution inside the solvent, and possess a large electron density contrast with respect to the solvent. This leads to the choice of tracer particles consisting of SiO_2 cores which are synthesized with the Stöber-method.[1] This method produces well defined and highly monodisperse particles. Silica particles exhibit in addition a large electron density contrast compared to the investigated solvents PPG[2] and DBP. The particles were coated with 3-(trimethoxysilyl) propylmethacrylate (TPM) resulting in a steric stabilization and a electrostatic stabilization due to the residual charge of the coating. This ensures a stable and homogeneous dispersion of the particles in the solvent.

6.1.1 Particle synthesis

Colloidal silica particles were synthesized following the Stöber-method. It has become a standard procedure to synthesize highly monodisperse silica particles with a controlled radii in the range between $10-1000$ nm. The process can be sub-divided into two major reaction steps, the hydrolysis of silicon tetra alkoxides (equation 6.1) and the polycondensation (equation 6.2) of silicon tetra hydroxide, both under alkaline conditions in alcohols:

$$\mathrm{Si(OR)_4 + 4\,H_2O \xrightarrow[\text{pH 11-12}]{\text{alcohol}} Si(OH)_4 + 4\,ROH} \tag{6.1}$$

$$\mathrm{Si(OH)_4 \xrightarrow[\text{pH 11-12}]{\text{alcohol}} SiO_2 + 2\,H_2O} \tag{6.2}$$

---

[1] Stöber, W. et al. (1968). *J. Coll. Int. Sci.* **26**, 62.

[2] Here polypropylene glycol with an average molecular weight of 4000 atomic mass units was investigated.

However, the complete reaction is still not completely understood, because there are numerous reaction intermediates and possible reaction pathways.[3] The phenomenon of uniform particle formation was first discovered by Kolbe[4] and later systematically utilized to produce monodisperse particles by Stöber and coworkers. Their approach includes enough water to hydrolyze the silane precursors and uses an alcohol-ammonia system at high pH-values as catalyzer to promote the synthesis of uniform particles.

Since silica nano-particles offer many applications as carriers for catalyst materials or therapeutic substances, their production on a large scale is explored on the basis of the Stöber-method.[5] In this connection, the method was studied to understand the synthesis[6] and the reasons for the monodispersity of the particles[7]. Up to now, several formalisms have been suggested.

The first model is the monomer addition growth model[8] in analogy to a model according to LaMer and Dinegar[9] (Figure 6.1(a)). Here, the nucleation is described as a fast process which takes place as long the concentration of silica $c_{\mathrm{SiO_2}}$ is above the supersaturation concentration C_{N} ($c_{\mathrm{SiO_2}} > C_{\mathrm{N}}$). The nucleation is followed by growth of the particles characterized by condensation of monomeric silicic acid on the nuclei surface at silica concentrations between the supersaturation and the saturation concentration C_{S} ($C_{\mathrm{S}} < c_{\mathrm{SiO_2}} < C_{\mathrm{N}}$). C_{S} defines the limit for the growth of particles. The model focuses mainly on the hydrolysis and condensation rate and the solubility of the intermediates, e.g. silicic acids.

The second model according to Bogush and Zukoski[10] describes the nucleation and growth of particles by a controlled aggregation mechanism (Ostwald ripening) of sub-nanometer sized particles (Figure 6.1(b)). Within this model it is assumed that C_{N} is so small that $c_{\mathrm{SiO_2}}$ cannot drop fast enough to explain monodisperse particles. Instead, the model uses size-dependent aggregation rates, characterized by particle stability, nuclei size, surface charge, and diffusion to motivate that simultaneous growth and nucleation can result in highly monodisperse particles. It includes the finding that the particle size also depends on other parameters beside the reaction rates, e.g. solubility of the substances and the presence of a catalyzer.

---

[3] Bergna, H. E. and Roberts, W. O. (2005). *Colloidal Silica Fundamentals and Applications.* 1st Edition. Marcel Dekker Inc., New York, USA.

[4] Kolbe, G. (1956). "Das komplexchemische Verhalten der Kieselsäure." PhD thesis. Jena, Germany: Friedrich Schiller University.

[5] Nagao, D. et al. (2013). *J. Col. Int. Sci.* **394**, 63.

[6] Bogush, G. H. et al. (1988). *J. Non-Cryst. Solids* **104**, 95; Van Blaaderen, A. and Kentgens, A. P. M. (1992). *J. Non-Cryst. Solids* **149**, 161; Chen, S. L. et al. (1996). *Ind. Eng. Chem. Res.* **35**, 4487.

[7] Matsoukas, T. and Gulari, E. (1988b). *J. Coll. Inter. Sci.* **145**, 557; Bogush, G. H. and Zukoski, C. F. (1991a). *J. Coll. Inter. Sci.* **142**, 1; Giesche, H. (1994). *J. Eur. Ceram. Soc.* **14**, 189.

[8] Matsoukas, T. and Gulari, E. (1988a). *J. Coll. Inter. Sci.* **124**, 252.

[9] LaMer, V. K. and Dinegar, R. H. (1950). *J. Am. Chem. Soc.* **72**, 4847.

[10] Bogush, G. H. and Zukoski, C. F. (1991b). *J. Coll. Inter. Sci.* **142**, 19.

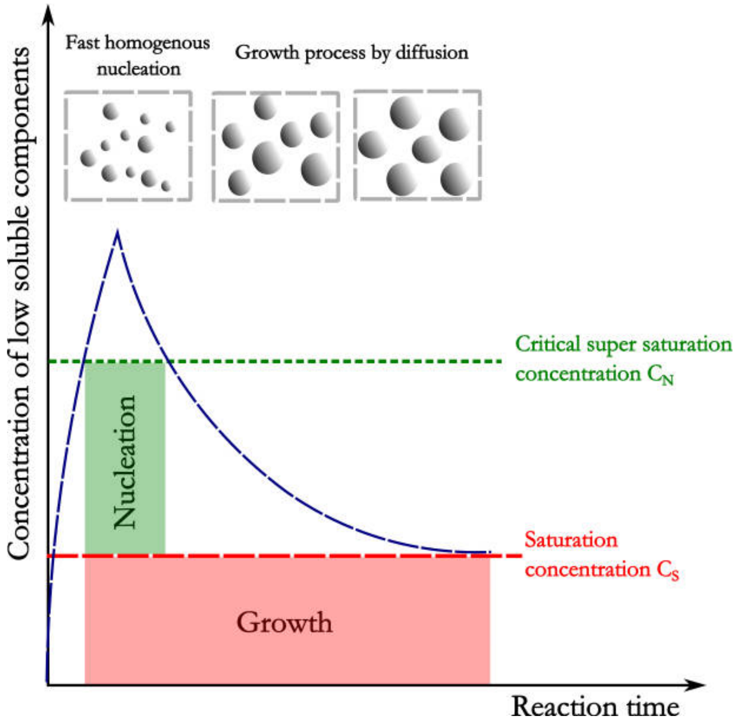

(a) Formation model of monodisperse particles by LaMer and Dinegar.

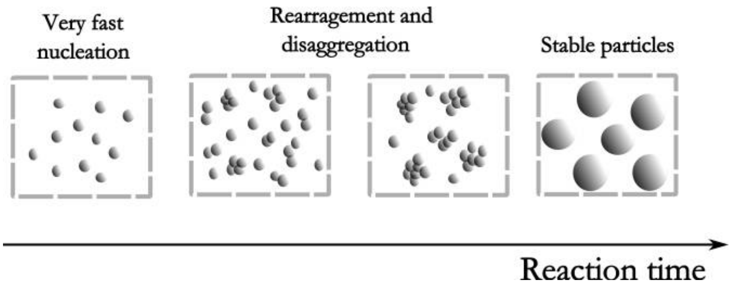

(b) Formation model of monodisperse particles by Bogush and Zukoski.

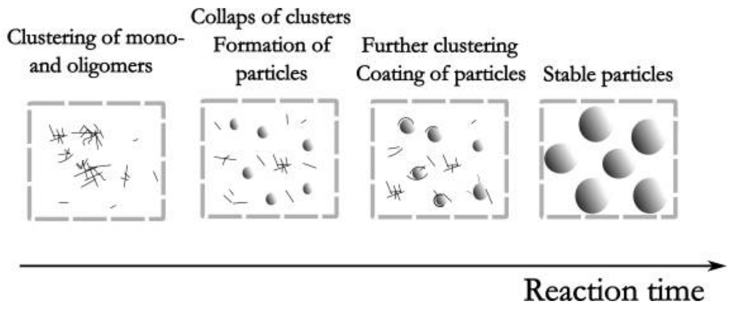

(c) Formation model of monodisperse particles by Bailey and Mecartney.

Figure 6.1: Growth mechanisms describing the formation of monodisperse colloidal silica particles from the condensation of silicon tetra hydroxide.

The third model arose from a cryogenic electron transmission microscopy study on the growth of silica particles by Bailey and Mecartney[11] (Figure 6.1(c)). The study supported a combination of nucleation and growth and suggested a formation where silicon tetra hydroxide polymerizes to larger micro gel clusters until they become insoluble and collapse to stable nuclei. The nuclei grow further by condensation with continuously formed oligomers and polymers or by collisions with other nuclei resulting in stable particles of spherical shape and similar radii. Although this model provides an explanation for the porous nature of Stöber particles[12], a general formation model of monodisperse silica particles has still not emerged.[13]

In general, the particle size obtained within the Stöber-method depends on the composition of the reaction mixture. By using silicon tetra alkoxide as silica source, the particle size and its distribution is highly depending on the silicon tetra alkoxide concentration. Decreasing the silicon tetra alkoxide concentration leads to smaller particle sizes and lower polydispersities. Applying water soluble alcohols as solvent and shorter alkoxides yields smaller particles with larger pores as result of the increased reaction rate. Due the porous nature of Stöber particles the method is limited to prepare silica particles with radii smaller than 50 nm.

To overcome this size limitation, the method was expanded with an additional upstream synthesis step which produce silica nano-spheres serving as seeds for a controlled growth of smooth monodisperse particles with diameters between $10 - 100$ nm.[14] This upstream synthesis is based on the hydrolysis and polycondensation reaction of tetra ethyl orthosilicate (TEOS) in an emulsion containing water and basic amino acids, e.g. lysine, under weak alkaline conditions (pH $\approx 9 - 10$).[15] In the framework of this thesis, the Stöber-method with and without the upstream reaction was applied to produce particles with radii between $10 - 120$ nm.

The Stöber-method using TEOS in ethanol was chosen to synthesize silica particles with radii in the range of $50 - 120$ nm. According to composition specifications given by Bogush et al.[16] $12 - 15$ ml ammonia (25%, Merck, Germany) and 250 ml ethanol (96%, Roth, Germany) are first mixed in a conical flask. Then $3 - 15$ ml TEOS (98%, Sigma-Aldrich, Germany) is added. The mixure is stirred smoothly (500 rpm) with a magnetic stirrer at room temperature ($T \approx 293$ K) during the synthesis. After 24 hours the TEOS is typically

---

[11] Bailey, J. K. and Mecartney, M. L. (1992). *Coll. Surf.* **63**, 151.

[12] Pore depths in the range of $1 - 5$ nm has been found for Stöber particles. See: Fegley, B. and Barringer, E. A. (1984). *Synthesis, Characterization, and Processing of Monosized Ceramic Powders.* Massachusetts Institute of Technology, Cambridge, USA.

[13] Van Blaaderen, A. et al. (1992). *J. Coll. Inter. Sci.* **154**, 481.

[14] Watanabe, R. et al. (2011). *J. Coll. Inter. Sci.* **360**, 1.

[15] Yokoi, T. et al. (2006). *J. Am. Chem. Soc.* **128**, 13664.

[16] Bogush, G. H. et al. (1988). *J. Non-Cryst. Solids* **104**, 95.

exhausted and the growth of particles has stopped.

For the preparation of particles with radii smaller than 50 nm the expanded Stöber-method was utilized. According to Yokoi et al., 0.3 g l-lysine (Sigma, Germany), 20 ml octane (98%, Fluka, Germany) and 200 ml deionized water were mixed and strirred at 450 rpm at $T = 333$ K while 21 ml TEOS is added slowly. The resulting mixture is stirred at $T = 333$ K for 5 hours, before increasing the temperature to 373 K and continue stirring for 20 more hours.

For both methods, $0.5-2$ ml TPM (98%, Sigma-Aldrich, Germany) is added subsequently to the mixture according to the procedure of Philipse and Vrij[17]. Moderated by the mixture of ethanol and ammonia almost all silanol surface groups of the particles are exchanged in a condensation reaction by [γ-(Methacryloxy)propyl]trimethoxysilane groups which cause a low effective charge of the silica particles.[18]

Subsequent to the coating, the particle suspension is purified by evaporation of the ammonia and by removing the remnant of the coating process via a dialysis in pure ethanol (dialysis-membrane, SpectraPor, $MWCO : 6-8K$, Germany) and filtering. Finally, the particles are transfered into PPG ($M_\mathrm{n} \approx 4000$, Sigma-Aldrich, Germany) or DBP (99%, Sigma-Aldrich, Germany) by mixing with the solvent and evaporation of ethanol. The resulting stock solutions were used to prepare series of colloidal solutions with different particle concentrations. Herein, smaller portions of the stock solutions were mixed with multiple amounts of their volume of the corresponding solvent. In this context, solutions with nominal concentrations of $\frac{1}{2}$, $\frac{1}{3}$, $\frac{1}{6}$, and $\frac{1}{9}$ of the stock solution concentration were created. For the investigation of the particle form factor, diluted samples with a nominal concentration of $\frac{1}{49}$ of the stock solution concentration were used.[19]

6.1.2 Polypropylene glycol

Polypropylene glycol (PPG) is a colorless viscous liquid with the chemical composition $\mathrm{H}\left[\mathrm{OCH}\left(\mathrm{CH}_3\right)\mathrm{CH}_2\right]_n\mathrm{OH}$ (Figure 6.2).[20] The composition with a molecular weight of 4000 atomic mass units was investigated which consists of $n \approx 68$ monomers. It has a high lubricity and a low vapor pressure. PPG is partially soluble in water at ambient temperatures and soluble in all proportions with organic liquids except long chain aliphatic hydrocarbons. Thus, it is widely used as a lubricant base, as a cosmetic ingredient, for coatings or as an intermediate for e.g. resin and as plasticizer. PPG at various chain lengths

---

[17] Philipse, A. P. and Vrij, A. (1989). *J. Coll. Inter. Sci.* **128**, 121.

[18] Maranzano, B. J. et al. (2000). *Langmuir* **16**, 10556.

[19] The volume fraction ϕ of this solution can be estimated by using the onset of crystallization in hard-sphere systems (49 vol.% $< \phi <$ 54 vol.%). Since the tracer particles have a repulsive interaction, the stock solution's volume fraction is considerably lower and a dilution of $\frac{1}{49}$ reached $\phi < 1$ vol.%.

[20] For details see: Forkner, M. W. et al. (2004). *Kirk-Othmer Encyclopedia of Chemical Technology: Glycols.* 1st Edition. Wiley-VCH, Weinheim, Germany.

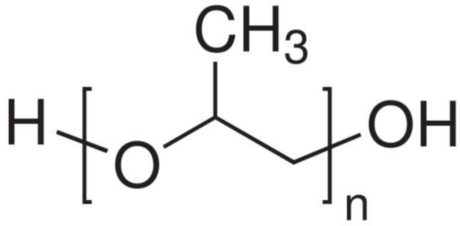

Figure 6.2: Chemical structure of polypropylene glycol which consists of a linear chain of propylene glycol monomers.

can easily be supercooled and is thus well-known as polymer glass former. The supercooled state has been investigated as function of the chain length in studies focusing on the liquid and glassy state[21], in the bulk[22], and at the surface[23]. PPG with a molecular weight of 4000 atomic mass units has a glass transition temperature of $T_\mathrm{g} = 205$ K at a cooling rate of 2 K/min.[24] It was found that its viscosity η follows the Vogel-Fulcher-Tammann (VFT) behavior, given by

$$\ln(\eta) = \ln(\eta_0) + \frac{A}{T - T_0}, \tag{6.3}$$

with a Vogel temperature of $T_0 = 180.1$ K, $\eta_0 = 7.678 \cdot 10^{-4}\mathrm{Pa} \cdot \mathrm{s}$ and $A = 817.2$ K.[25]

Between its melting temperature $T_\mathrm{m} = 330$ K and T_g the translational and rotational relaxation times of the molecules show a complex crossover behavior. Its scaling is still very controversial.[26] However, all reported results state that the α-relaxation can be empirically described by the stretched exponential KWW function.[27]

6.1.3 Dibutyl phthalate

Dibutyl phthalate (DBP) has a molecular weight of 278.34 atomic mass units and is a colorless viscous liquid with the chemical composition $C_{16}H_{22}O_4$ (Figure 6.3). It is an

---

[21] A review to studies on PPG can be found in: Rzoska, S. J. and Mazur, V. A. (2007). *Soft Matter under Exogenic Impacts.* 1st Edition. Springer, Dordrecht, Netherlands.

[22] Ye, J. Y. et al. (1996). *Phys. Rev. B* **53**, 8349; Andersson, S. P. and Andersson, O. (1998). *Macromolecules* **31**, 2999; Bergman, R. et al. (1998). *J. non-cryst. sol.* **235**, 225; Park, I. S. et al. (1999). *JTAC* **57**, 687; Moon, I. K. et al. (2001). *Thermochimica Acta* **1**, 2001; Kaminski, K. et al. (2013). *Macromolecules* **46**, 1973.

[23] Sprung, M. et al. (2004). *Phys. Rev. E* **70**, 51809; Chushkin, Y. et al. (2008). *EPL* **83**, 36001; Streit-Nierobisch, S. et al. (2008). *Phys. Rev. B* **77**, 41410.

[24] This was determined by calorimetric and dielectric investigations. See: Park, I. S. et al. (1999). *JTAC* **57**, 687.

[25] Cochrane, J. et al. (1980). *Polymer* **21**, 837; Schönhals, A. (2001). *Europhys. Lett.* **56**, 815.

[26] Ngai, K. L. (2000). *J. Non-Cryst. Sol.* **275**, 7; Bendler, J. T. et al. (2005). *Phys. Rev. E* **71**, 31508; Ngai, K. L. et al. (2005). *Macromolecules* **38**, 4363.

[27] Schwartz, G. A. et al. (2003). *Eur. Phys. J. E* **12**, 113.

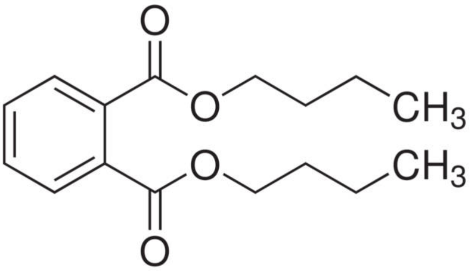

Figure 6.3: Chemical structure of dibutyl phthalate which consists of a phthalic ring with two attached hydrocarbon tails.

organic solvent widely used in industry as a plasticizer.[28] DBP is a well-known glass former of medium fragility ($m = 69$) that was studied as ideal organic liquid in the supercooled state.[29] Its physical properties have been investigated in various studies focusing on the liquid as well as on the glassy state, in the bulk[30], in confinement[31] and at the surface[32]. It was found that DBP has a glass transition temperature of $T_\mathrm{g} = 179$ K at a cooling rate of 10 K/min and that its viscosity η follows the VFT behavior over a wide temperature range with the Vogel temperature $T_0 = 151.3$ K, $\eta_0 = 2.2 \cdot 10^{-4}\mathrm{Pa \cdot s}$ and $A = 966.7$ K.[33] Acoustic studies of the viscoelastic properties of DBP above its melting temperature ($T_\mathrm{m} = 238$ K) revealed low-frequency shear elasticity behavior indicating collective interactions of large groups of molecules.[34] Complementary studies of DBP and its viscoelastic properties in the bulk were performed at different length and time scales using X-rays, light scattering and nuclear forward scattering. The relaxation rates of DBP were found to be depending on geometrical constraints and do not follow the scaling of the mode coupling theory (MCT).[35] In particular, DBP injected into nanoporous silica matrices exhibits an increase of the relaxation time at pore diameters smaller than 250 nm which is assumed to corresponds to the size of cooperative rearranging regions in DBP below T_g. Dielectric[36] and quasi-

---

[28] Cadogan, D. F. and Howick, C. J. (2000). *Ullmann's Encyclopedia of Industrial Chemistry: Plasticizers.* 1st Edition. Wiley-VCH, Weinheim, Germany.

[29] Wang, L. et al. (2002). *J. Chem. Phys.* **117**, 10184.

[30] Cook, R. L. et al. (1994). *J. Chem. Phys.* **100**, 5178; Barlow, A. J. et al. (1967). *Proc. R. Soc. B* **298**, 467; Paluch, M. et al. (1997). *J. Phys.: Condens. Matter* **9**, 5485; Meyer, A. et al. (1997). *Zeitschrift für Physik B Condensed Matter* **103**, 479; Menon, N. et al. (1994). *Phys. Rev. Lett.* **73**, 963.

[31] Asthalter, T. et al. (2003). *Eur. Phys. J. E* **12**, S9–S12; Wellenreuther, G. et al. (2005). *Hyperfine Interactions* **165**, 141.

[32] Sikorski, M. (2008). "Glass transition near the free surface studied by synchrotron radiation." PhD thesis. Hamburg, Germany: University of Hamburg.

[33] Sergueev, I. et al. (2002). *Phys. Rev. B* **66**, 184210.

[34] Badmaev, B. B. and Damdinov, B. B. (2001). *Acoustical Physics* **47**, 487.

[35] Brace, D. D. et al. (2002). *J. Chem. Phys.* **116**, 1598.

[36] Paluch, M. et al. (1997). *J. Phys.: Condens. Matter* **9**, 5485; Schönhals, A. (2001). *Europhys. Lett.* **56**, 815.

elastic nuclear forward scattering[37] studies on fast and slow relaxations in supercooled and glassy DBP reported that the α-relaxation follows the stretched exponential KWW form. However, the reported stretching exponents are not consistent.[38]

6.2 Experimental method

In the framework of this thesis, XPCS measurements in SAXS geometry were performed to study the solvent properties of the molecular glass formers PPG and DBP near T_g in the bulk with the help of silica tracer particles. Since the viscosity changes dramatically within a small temperature range near T_g, the design of the sample environment demands an accurate and very stable temperature control. In addition, active cooling is required to reach T_g of the glass formers. Therefore, the measurements were performed with special cryogenic sample cells for temperatures ranging from room temperature down to T_g. The cooling of the sample is accompanied by an increase of the solvent viscosity which causes an increase of the particle relaxation times. Thus, experiments require increasing waiting times between temperature changes in order to avoid transition effects, for example aging. Such waiting times were chosen to exceed the particle relaxation time by an order of magnitude which consumed an essential portion of the experimental time. XPCS experiments require a source with a high coherent X-ray flux which is provided by the ID10 beamline at the European Synchrotron Radiation Facility (ESRF) in Grenoble (France) and the P10 beamline at the PETRA III synchrotron (DESY) in Hamburg (Germany), where all experiments in the framework of this thesis were carried out. The corresponding beamline set-ups, sample environments and the experimental procedures are presented in this section. Special attention is payed on the XPCS set-up at the P10 beamline including the sample environment as it was commissioned in the context of this work.

6.2.1 Experimental set-up at the ID10 beamline

Various experiments were performed at the ID10 beamline at the ESRF. Due to an upgrade of ID10 in 2011, the experiments were carried out at two different beamline configurations. Before the upgrade the experiments were performed at the ID10A XPCS set-up (experimental hutch EH1) shown in Figure 6.4(a).[39] ID10A was one out of three beamline endstations (ID10A-ID10C) that shared the same source. The source was an

---

[37] Wellenreuther, G. et al. (2005). *Hyperfine Interactions* **165**, 141; Wellenreuther, G. (2005). "Glass dynamics in confinement examined with quasi-elastic nuclear resonant forward scattering." PhD thesis. Hamburg, Germany: University of Hamburg; Sergueev, I. et al. (2002). *Phys. Rev. B* **66**, 184210; Asthalter, T. et al. (2001). *Eur. Phys. J. B* **22**, 301.

[38] Phillips, C. J. (1996). *Rep. Prog. Phys.* **59**, 1133.

[39] Details can be found in: Abernathy, D. et al. (1998). *J. Synch. Rad.* **5**, 37.

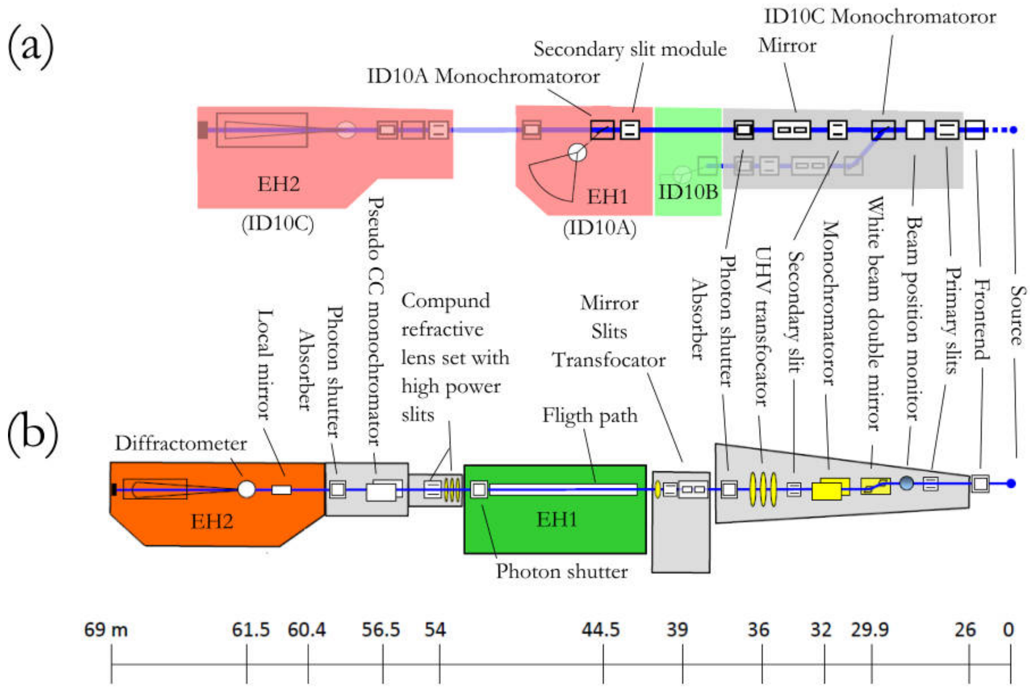

Figure 6.4: ID10 beamline layouts of the XPCS instrument before the upgrade (a) showing the endstations ID10A-ID10C and after the upgrade (b) showing the single multi-purpose endstation. (Picture taken from: ESRF (Oct. 2013). *ID10 - Soft interfaces and coherent scattering beamline @ONLINE*. URL: `http://www.esrf.eu/UsersAndScience/Experiments/SoftMatter/ID10/`.)

array of three undulator[40] segments, one with a 27 mm period (U27), another with a 35 mm period (U35) and a so-called revolver undulator which allows for both periods.[41] It was designed as a high-β source with a low divergence (25 µrad $(H) \times$ 17 µrad (V)) at the expense of a larger source size (928 µm $(H) \times$ 23 µm (V)). While the undulators remained after the upgrade, the multi-station design was dismissed in favor of a single multi-purpose station hosting instruments for high-resolution scattering at surfaces (EH1), and for coherent X-ray diffraction imaging (CDI) and XPCS in various geometries (EH2). The basic components of the beamline layouts before (a) and after (b) the upgrade are shown in Figure 6.4. In both designs, the X-rays emitted by the source pass through the frontend that includes a photon shutter and compound refractive lenses (CRL) for focusing the beam to a size of 670 µm $(H) \times$ 15 µm (V). The beam passes primary slits, a beam position monitor and is further defined and deflected by a double mirror and secondary slits

---

[40] An undulator is an array of periodic alternating dipole magnets. The static magnetic field along the length of the undulator is characterized by its period.

[41] Grübel, G. et al. (1994). *Journal de Physique IV* **4**, 27.

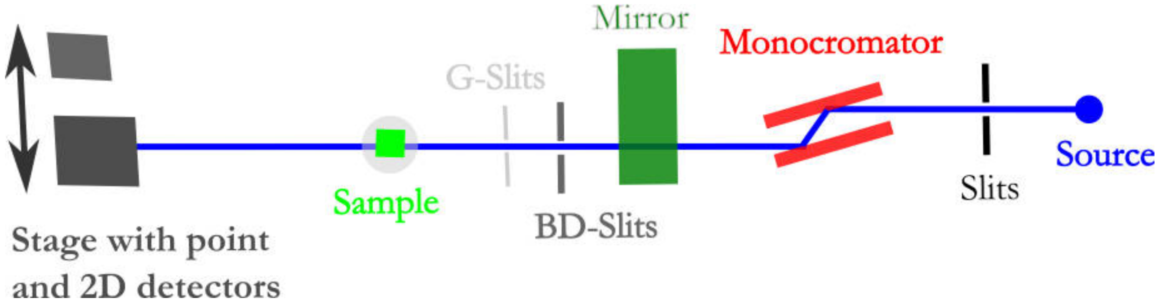

Figure 6.5: Schematic sketch of the XPCS set-up at ID10: The predefined X-ray beam from the source is monochromatized by a Si(111) monochromator. Higher harmonics are suppressed by a mirror. Behind the mirror, the beam size is reduced to its transversely coherent part by a set of beam defining slits (BD-slits). Guarding slits (G-slits) placed before the sample block the Fraunhofer pattern arising from the BD-slits. Finally, the beam is scattered by the sample mounted in a cryo-SAXS sample chamber and the scattered photons are detected subsequently either by an avalanche photo diode (APD) or by a 2D-detector mounted on a horizontal detector translation stage.

before passing through an absorber and shutter system whereupon the beam is entering the section with the experimental instrumentation. The multi-purpose design (b) has a white beam double mirror (enabling white beam operation) and a monochromator for the instruments in EH1 instead of the ID10B monochromator which selected the beam for the ID10B beamline. Furthermore, additional focusing lenses and mirrors were installed in the former ID10B endstation to enable horizontal and vertical scattering geometries in EH1. Before the upgrade, the XPCS instrument was located at EH1, where the beam was further defined by secondary slits and monochromatized by a single-bounce, multi-crystal monochromator placed at 44.2 m distance to the source. The monochromator included a diamond(220), diamond(111) and Si(111) crystal, operable at energies between $7-20$ keV with an intrinsic energy resolution between $0.2 \cdot 10^{-4} - 1.4 \cdot 10^{-4}$. This results in a longitudinal coherence length of about 1 µm and a transverse coherence length of about 10 µm at 8 keV. After the upgrade the XPCS instrument is located in the extended EH2 (former ID10C) which offers additional focusing in combination with an extended sample-detector distance of $D \approx 5$ m. Here, the X-rays are monochromatized by a pseudo channel-cut Si(111) monochromator placed at 56.5 m distance to the source.[42]

All experiments at ID10 were carried out at the undulator configuration $2 \times \mathrm{U27}/1 \times \mathrm{U35}$ optimized for a photon energy of 8 keV, corresponding to a wavelength of $\lambda = 0.154$ nm. The general XPCS set-up for both beamline configurations is shown in Figure 6.5, where the energy is selected by the monochromator. A mirror placed downstream of the

---

[42] For details of the updated ID10 beamline see: ESRF (Oct. 2013). *ID10 - Soft interfaces and coherent scattering beamline @ONLINE*. URL: `http://www.esrf.eu/UsersAndScience/Experiments/SoftMatter/ID10/`.

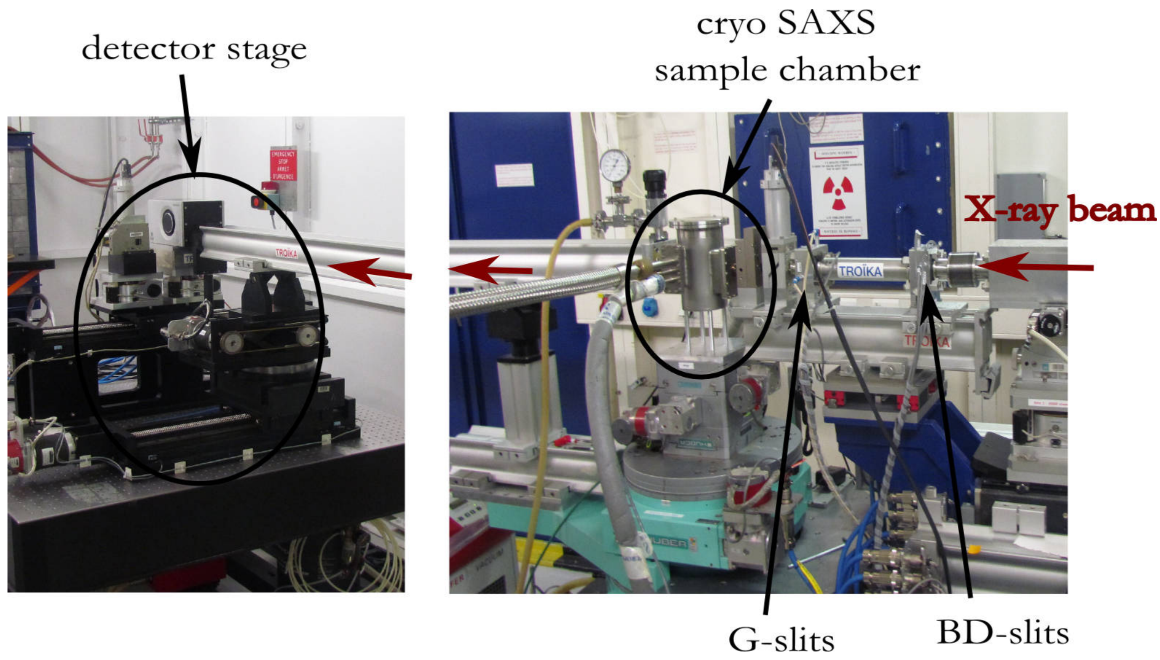

Figure 6.6: Photographs of the ID10 XPCS set-up after the upgrade. The sample chamber is placed onto a 4-circle diffractometer. The beam enters from the right side, passes the BD- and G-slits, is scattered by the sample in the ID10 cryo-SAXS sample chamber and detected by a detector mounted on a detector stage.

monochromator is used to suppress higher order harmonics. Then, the transversely coherent part of the beam is defined by an aperture of slit blades (BD-slits) typical of 20 µm × 20 µm size. A set of guard slits (G-slits) placed upstream of the sample blocks the parasitic scattering from the BD-slits. The scattering from the sample is recorded either by an Andor[43] charge coupled device at a sample-detector distance of about 2 m (layout in Figure 6.4 (a)) or by a Maxipix 2x2 detector[44] at a sample-detector distance of 5.2 m (layout in Figure 6.4(b)). The detectors were mounted on a horizontal translation stage with an additional avalanche photo diode (APD) used for sample alignment and to measure the transmission of the samples. Photos of the XPCS set-up at ID10 are shown in Figure 6.6. The beam enters from the right side, passes the BD- and G-slits and is scattered by the sample in the cryo-SAXS sample chamber that is placed onto a 4-circle diffractometer. The scattered radiation is detected with the APD or the Maxipix 2x2 detector mounted on the detector stage. The evacuated flight-path is segmented and covert by Kapton windows of 50 µm thickness in front of the detector and on both sides of the cryo-SAXS sample chamber. The samples filled in 1 mm thick quartz capillaries (0.01 mm

---

[43] The Andor (iKon-M SY series) detector is a commercial X-ray sensitive camera with a readout time for a full image around 1 s which is detected with a total area of 1024 × 1024 pixels and a pixel size of 13 × 13 µm^2.

[44] The Maxipix 2x2 is a fast readout ($t_a \approx 3.5$ ms) photon-counting pixel detector based on an array of four Medipix2 chips, each consisting of 256 × 256 pixels at a size of 55 × 55 µm^2. For details see: Ponchut, C. et al. (2007). *Nucl. Instr. and Meth. A* **576**, 109.

wall thickness) were placed in the cryo-SAXS sample chamber in vacuum. The sample chamber was developed at the ESRF and offers a highly stable ($\Delta T = 1$ mK) temperature control in the temperature range of $110 - 330\ K$.[45] Its temperature is controlled by a cold gaseous nitrogen flow in combination with impedance heaters monitored by a temperature controller device (Lakeshore, model 340).

6.2.2 The P10 beamline

The P10 beamline[46] is located at the PETRA III synchrotron at DESY[47] and takes advantage of its high brightness. It uses a low-β source configuration. The source of P10 is a 5 m long undulator (U29) which provides a 1-sigma beam size of 36 μm $(H) \times 6$ μm (V) with a divergence of 28 μrad $(H) \times 4.0$ μrad (V) suitable for photon energies of $3.8 - 25.0$ keV. It has an energy gap between $10.5 - 11.5$ keV. The scope of the beamline are applications for coherent X-rays, such as XPCS and CDI. P10 is composed of an optics hutch followed by two experimental hutches facilitating various experimental set-ups. The second experimental hutch (EH2) hosts additional optics enabling focusing ($< 5 \times 5$ μm^2) with compound refractive lenses (CRL)[48] and a beam deflection unit (BDU) which uses two Ge(111) crystals to tilt the beam downwards allowing for measurements in grazing incidence geometry.[49] Subsequent to the optical elements in EH2, either the GINIX set-up[50] or the standard P10 XPCS sample environment (Figure 6.9) can be placed. The first experimental hutch (EH1) hosts a second sample environment to study systems at large sample-detector distances (≈ 20 m). For this purpose, the scattered beam is detected in EH2 allowing for measurements in a q-range up to 2 nm^{-1} at 8 keV. Furthermore, a set-up for rheology experiments plus a 6-circle diffractometer is installed in EH1.

Various experiments were performed at the P10 beamline using the standard XPCS sample environment for which the beamline layout is shown in Figure 6.7. It illustrates the beam defining elements for the P10 XPCS set-up including optical elements of the optics

---

[45] A detailed description can be found in: Steinmann, R. et al. (2011). *Rev. Sci. Instr.* **82**, 25109.

[46] DESY, Photon Science (Oct. 2013). *P10: Beamline layout/specifications.* URL: `http://photon-science.desy.de/facilities/petra_iii/beamlines/p10_coherence_applications/index_eng.html`.

[47] Balewski, K. et al. (Feb. 2004). *PETRA III: a low emittance synchrotron radiation source Technical Design Report.* URL: `http://petra3-project.desy.de/general/tdr/index_eng.html`; Bilderback, D. H. et al. (2005). *J. Phys. B-At. Mol. Opt. Phys.* **38**, 773; Balewski, K., ed. (2010). *Comissioning of Petra III.* International Particle Accelerator Conference 1. Kyoto University. Kyoto: IPAC'10/ACFA.

[48] Zozulya, A. V. et al. (2012). *Optics Express* **20**, 18967.

[49] Prodan, M. (2008). "Entwicklung eines Doppelkristallmonochromators zur Untersuchung von dynamischen Prozessen an Flüssigkeitsoberflächen." MA thesis. Lübeck, Germany: University of Applied Science Lübeck.

[50] GINIX is an acronym for the Göttingen Instrument for Nano-Imaging with X-rays. It enable a nanofocus achieved by KB-mirrors (focal size $< 200 \times 200$ nm^2) in combination with waveguides (focal size $< 10 \times 10$ nm^2) for tomography and holographic imaging experiments. For details see: Kalbfleisch, S. et al. (2010). *AIP Conference Proceedings* **1234**, 433.

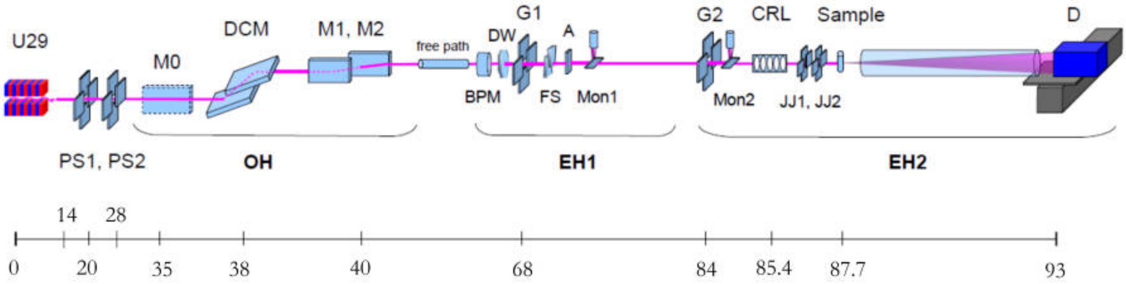

Figure 6.7: Layout of the optical elements at P10 including the standard XPCS set-up. The scale bar is showing the distances of the elements from the source in meters. (Figure was taken from: DESY, Photon Science (Oct. 2013). *P10: Beamline layout/specifications*. URL: `http://photon-science.desy.de/facilities/petra_iii/beamlines/p10_coherence_applications/index_eng.html`.)

hutch (OH) and certain apertures and focusing elements in both experimental hutches (EH1 & EH2). The beam produced by the undulator is predefined by high-power slits (PS1, PS2), before being monochromatized by a standard PETRA III high heat load monochromator[51] (DCM) at 38 m distance to the X-ray source. The monochromator is followed by a pair of horizontally reflecting, flat (R > 100 km) mirrors (M1, M2). They are equipped with two additional stripes coated with Rhodium and Platinum to suppress higher harmonics of the undulator spectrum for energies up to 27 keV. In preparation for pink beam option, the beamline is equipped with cooled pink beam compatible in-vacuum slit systems (G1, G2).[52] After a beam position monitor (BPM) which provides a feedback signal to the DCM, the beam passes a 60 μm thick diamond-window (DW) which separates the storage ring vacuum section from the beamline vacuum section. The beam passes further through a fast shutter (FS) and absorber system (A) installed on a table with optical elements in EH1. Several intensity monitors (Mon1, Mon2) are installed along the beamline. In EH2 additional beam defining elements, such as a CRL transfocator (Figure 6.8(a)), can be used to focus the beam before it reaches the section hosting the experimental set-up. The set-up section is separated by two gate valves on both sides which enable the handling of the set-up vacuum independent from the beamline vacuum. Subsequent to the standard P10 XPCS set-up, which was used in the experiments, a 5 m long and rotate able flight-path is installed. It allows to continue the beamline vacuum up to the detector position. The flight-path is connected to a movable detector table on a 3.5 m long translation axis mounted on a granite block. This allows scattering angles up to $2\theta \approx 30°$ at a 5 m sample-detector distance ($q_{\max} \approx 20\ \mathrm{nm}^{-1}$ at 8 keV). A movable

---

[51] It is a liquid nitrogen cooled double crystal (Si(111) crystal pair (and an unpolished Si(111) channel-cut crystal) high heat load monochromator described in: Horbach, J. et al. (2011). *Diamond Light Source Proceedings* **1**, E35.

[52] A high heat load mirror (M0) is foreseen to enable the pink beam capability at P10.

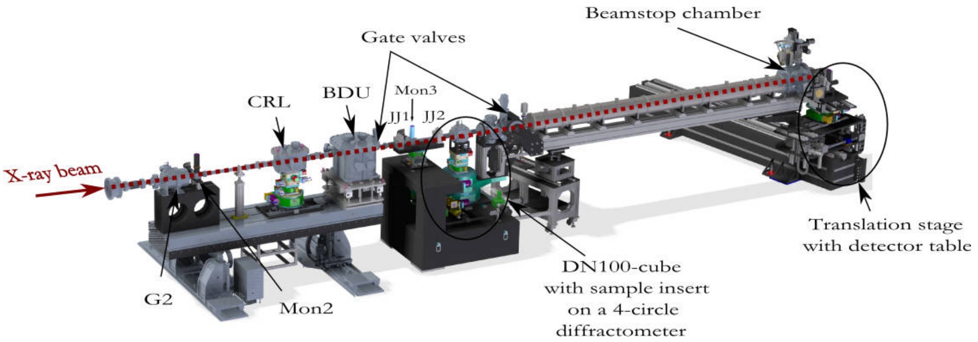

(a) Schematical drawing of the XPXS set-up at P10.

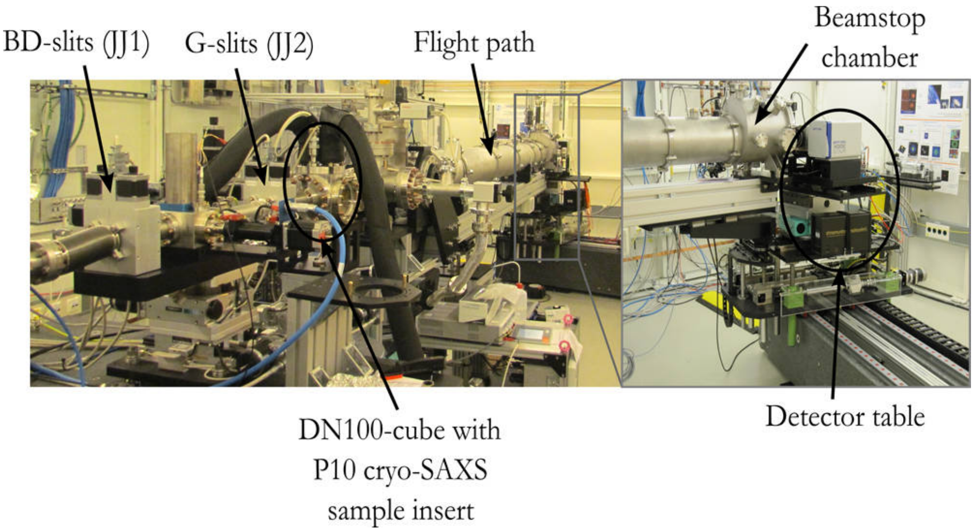

(b) Photographs of the XPXS set-up at P10.

Figure 6.8: XPCS set-up at P10 (EH2): (a) Schematical drawing and (b) photographs.

detector table is mounted on this translation stage which can carry multiple detectors at the same time. In particular, a Pilatus 300K detector (Dectris), a Maxipix 2x2 and 1x5 detector (ESRF), a PI-LCX and PI-PIXIS detector (Roper-Scientific) are available at P10 for multi-speckle XPCS experiments. At the end of the flight-path an in-vacuum beamstop chamber is mounted with several tungsten based bars which are used to block the primary beam from reaching and overexposing the detector. The exit of the flight-path is covered by a large Kapton window of 75 µm thickness and 180 mm in diameter. The typical XPCS configuration of P10 is shown in Figure 6.8. In the pictures the beam is entering from the left and passes a table with optical elements equipped with a pink beam slit (G2), an intensity monitor (Mon2), a CRL transfocator and a beam deflection unit (BDU). The beam enters the gate valve separable section with the standard XPCS sample environment of P10. It consists of BD-slits (JJ1) and G-slits (JJ2), a DN100-cube on a 4-circle diffractometer which can be equipped with various inserts to manipulate the samples, followed by a 6-way cross with interfaces to an intensity monitor, a vacuum pump, and a gate valve which bridges the flight-path. All elements are mounted on granite. The photographs show the standard XPCS sample environment while operating the cryo-SAXS sample insert. The end of the flight-path with a beamstop changer and the detector stage mounted on the fight path translation stage are highlighted.

6.2.3 Experimental set-up at the P10 beamline

The standard XPCS sample environment, shown in Figure 6.9, is placed at a distance of about 87.8 m from the X-ray source in EH2 of P10 and operates usually with a sample-detector distance of 5 m. It consists of a combination of Huber 440 and 430 goniometers sitting on a y-z-translation which is mounted on a granite support.[53] For most experiments the Huber 440 goniometer is used as a rotational bearing for the 5 m long flight-path and the Huber 430 acts as z-rotation for an adaptable tower of Huber translation and rotation stages with a surface area of 170×170 mm^2 on top of the goniometers. The typical configuration offers x-y-z-translation as well as rotations around the x- and y-axis. The X-ray beam (coaxial with the x-axis) is aligned to pass the center of rotation of the 2-circle segment, which is 170 mm above its top surface.[54] On top a vacuum integrated DN100-cube (6 inch outer diameter) is mounted. It can be equipped with the P10 cryo-SAXS sample insert for tempering the samples. On the upstream part of the XPCS sample environment a pair of JJ X-ray slits (IB-C30-HV) is mounted on a Huber y-z-stage. It allows free positioning of the BD-slits and G-slits in a distance of 800 mm, respectively 250 mm, before the sample. They are integrated in the beamline vacuum. The intensity can be monitored at a position between the BD-slits (Mon3). At the downstream part, a 6-way cross connects the standard XPCS sample environment to the flight-path.[55] The hole sample environment can be separated from the beamline vacuum by a DN100 gate valve after the 6-way cross and an additional DN40 gate valve upstream of the JJ X-ray slits. This allow to break and restore the vacuum for a sample change without venting sensitive beamline components.[56] The main benefit of using a DN100-cube as sample chamber on top of the Huber tower is given by its flexibility to design sample inserts. Four sides are accessible with multiple inserts to adapt many possible experimental requirements. The DN100-cube can be evacuated while connected along the beam direction by two

---

[53] The standard XPCS sample environment can be easily exchanged by other set-ups while operating air pads below the granite.

[54] The space on top of the Huber components can be used flexible and allows for many different sample environments.

[55] The 6-way cross also allows the implementation of additional monitors as well as to connect vacuum pumps near the sample region.

[56] It takes approximately 2 min to restore the vacuum at 10^{-4} mbar in the sample section during a typical sample change.

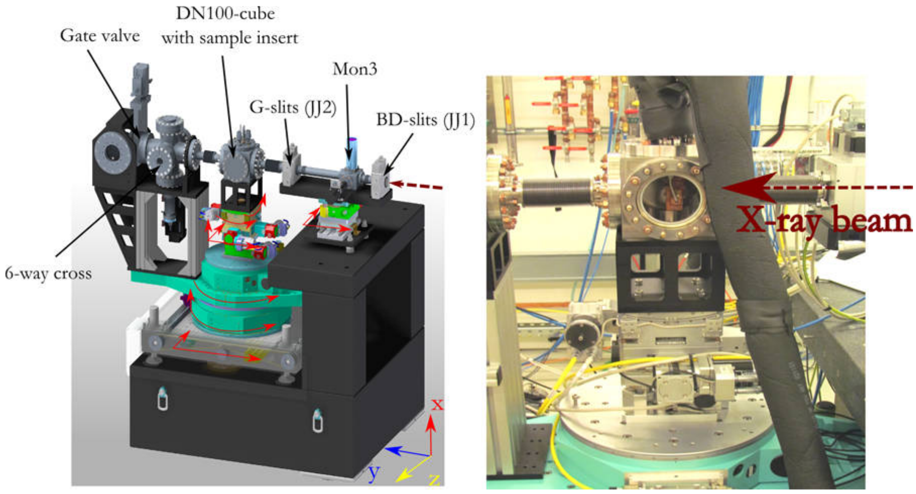

Figure 6.9: The standard XPCS sample environment at P10 as schematic drawing (left) and as photograph (right). The photograph shows the operation with the cryo-SAXS insert mounted. The isolated nitrogen supply pipes are clearly visible on the top.

DN40-bellows (2.75 inch flange diameter) to the beamline vacuum. The bellows decouple the positioning of the sample from those of the JJ X-ray slits and the flight-path.

In the framework of this thesis, multiple inserts were commissioned to study glassy materials.[57] For all experiments at P10 the cryo-SAXS sample insert (Figure 6.10), developed for low temperatures ($120 - 350$ K), was used to place and temper the samples. The insert is based on a CF100-flange holding a copper block. The copper block has two immersed impedance heaters and tubes which allow for temperature control with a gaseous nitrogen flow as cooling. For this purpose, the CF100-flange has a vacuum compatible 9-pin sensor cable connector for up to two 4-point temperature sensors and a high current connector which supplies up to two heaters and a high current device. In order to enable gaseous nitrogen flow, the flange has also two vacuum isolated tube connections. The copper holder is thermally decoupled from the CF100-flange by ceramic isolations. A Lakeshore controller is used to control the heater with the reference from the Pt100 temperature sensors immersed in the copper holder. The nitrogen for the cooling is provided by a pressure stabilized dewar and is controlled in combination with a remotely controlled nitrogen flow meter at the exit of the cryo-SAXS sample insert tube connection. In addition, the flow meter is followed by a membrane pump to create a laminar gas flow. This design allows stable flow rates of nitrogen gas up to 25 $\frac{\mathrm{l}}{\mathrm{min}}$ suitable for temperature changes up to 10 $\frac{\mathrm{K}}{\mathrm{min}}$ down to 120 K within a short term stability of $\Delta T = 3$ mK and a long term term stability of $\Delta T = 1$ mK. A temperature homogeneity of up to $\frac{\Delta T}{\Delta d} = (15 \pm 2)\ \frac{\mathrm{mK}}{\mathrm{mm}}$ at $T = 200$ K is achieved by the symmetric positioning of the

---

[57] An overview of sample inserts developed for different temperature regimes and scattering geometries are given in appendix A.3.

heaters and the cooling around the capillary mount. The copper block has a 4.5×9.5 mm^2 rectangular opening (Figure 6.10(b)) to allow studies in transmission geometry. The beam side of the opening is shielded with a 4 mm tick tungsten plate, in order to prevent fluorescence for $E > 9$ keV when the X-ray beam hits the copper holder. A copper capillary mount for up to three capillaries can be mounted at the opposite side which has the same opening as the copper block.

6.2.4 Experimental procedure

The experiments were carried out at the XPCS set-ups of ID10 and P10 at a photon energy between $7.9 - 8.0$ keV, at beam sizes between 10×10 µm^2 and 25×25 µm^2, and at sample-detector distances between $2 - 5$ m. For all measurements, the samples were filled in 1 mm thick quartz capillaries (0.01 mm wall thickness), vacuum sealed and mounted in the sample cells. The measurements were carried out after establishing vacuum and passing an adequate equilibration time after reaching the designated temperature. In the beginning, the samples prepared as described in section 6.1 had an unknown particle volume fraction.

For the investigation of the static structure factor of these samples, up to 200 SAXS pattern were recorded at $T = 300$ K with an exposure time of up to 0.3 s. The scattering patterns of empty capillaries and the pure solvents were also recorded in order to estimate the scattering background. For these measurements, the detector was positioned to an off-beam center position to exploit the maximal possible q-range, typically in the range of $0.01\ \mathrm{nm}^{-1} < q < 0.25\ \mathrm{nm}^{-1}$. In contrast, for XPCS measurements the detectors were beam-centered in order to use the full angle increment to enhance speckle statistics.[58] The measurements of the most dilute samples ($\phi < 1$ vol.%) were used to determine the particle form factors which were subsequently applied to specify the volume fraction of the more concentrated samples.

The suspensions in each sample series were measured beginning with the highest concentration down to the concentration where the scattering signal was insufficient to be analyzed with the instantaneous intensity correlation function C_{I}. Temperatures from 300 K down to T_{g} were investigated with XPCS at intervals of 20 K to 1 K. The measurements were started after the temperature has stabilized at the target temperature and after an equilibration time which ranged from 100 s (at 300 K) to more than 6000 s (near T_{g}).[59] A series of up to 500 images using the Andor/PI-LCX detector or up to

---

[58] This is essential to resolve higher order correlation functions, since they require sufficient statistics in a single scattering pattern. The detectors typically cover a q-range of $0.01\ \mathrm{nm}^{-1} < q < 0.15\ \mathrm{nm}^{-1}$.

[59] As an adequate equilibration time the tenfold of τ_{c} (at the smallest q) was assumed. The restriction of the equilibration time ($t_{\mathrm{w}} \leq 6000$ s) led to conditions of $t_{\mathrm{w}} \approx 2 - 5\ \tau_{\mathrm{c}}$ close to T_{g}. The samples were not measured much below T_{g} because they are considered as out of equilibrium for infinite t_{w}.

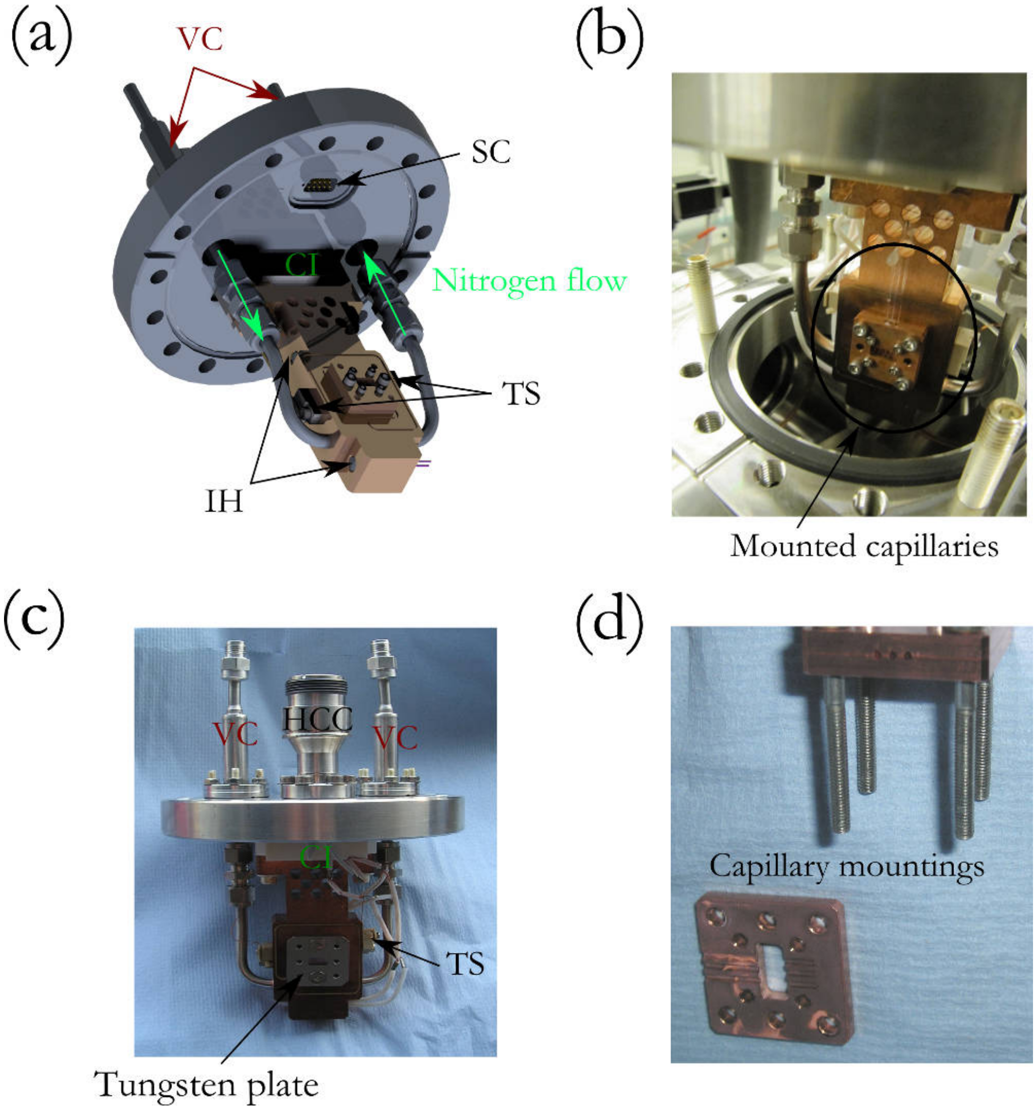

Figure 6.10: P10 cryo-SAXS sample insert: (a) Sectional view of the insert showing the cold gaseous nitrogen cooling, two impedance heaters (IH), two temperature sensors (TS), vacuum isolated couplings (VC), a 9-pin sensor cable connector (SC). (b) Detector-side photograph of the insert with a capillary mount. (c) Beam-side photograph of the insert. The tungsten plate and the high current connector (HCC) are highlighted. (d) Photograph of the capillary mountings. The capillaries are clamped to the cooling surface of the insert, thermal conductivity is enhanced by vacuum compatible grease.

5000 images using the Maxipix 2x2 detector were recorded at each temperature.[60] After changing the temperature, the delay time between scattering patterns was adapted. Delay times ranged from $0 - 12$ s in order to increase the experimental time window and to match the relaxation time at the particular temperature while the exposure time was kept constant. As result, the overall beam exposure was kept below $50 - 80$ s which was identified as beam damage threshold for most of the samples.[61] In addition, the sample was moved 50 μm vertically between measurements at different temperatures to prevent X-ray beam induced damage. Due to the limitations of the long term beam stability, the measurements were not continued beyond 7000 s.[62] In some cases, X-ray absorbers were used to balance the endurance of samples and the optimum of the photon statistics. Focusing of the beam intensified the beam damage and was therefore not used. By using slow read-out detectors (Andor and PI-LCX), slow dynamics ($\tau_c > 1$ s) can be studied. These are measurable typically at temperatures below 250 K in case of PPG, respectively below 210 K in the case of DBP. In contrast, fast read-out detectors such as the Maxipix 2x2 allow to study faster dynamics, but became available only for the last experiments. The measurements of colloidal particles in PPG benefited from the better temporal resolution. Typical set-up configurations are given in Table 6.1.

Parameter	**Andor**	**PI-LCX (1)**	**PI-LCX (2)**	**Maxipix 2x2**
sample-detector distance	2.2m	2.2m	5.2m	5.2m
pixel size	$(13\ \mu m)^2$	$(20\ \mu m)^2$	$(20\ \mu m)^2$	$(55\ \mu m)^2$
frame rate	1.0 s	1.5 s	1.5 s	0.0035 s
accessible temperatures (PPG)	$T < 250$ K	$T < 240$ K	$T < 240$ K	$T < 300$ K
beam size	$(20\ \mu m)^2$	$(15\ \mu m)^2$	$(15\ \mu m)^2$	$(15\ \mu m)^2$
wave length	0.154 nm	0.154 nm	0.154 nm	0.154 nm
speckle size	$(15\ \mu m)^2$	$(22\ \mu m)^2$	$(54\ \mu m)^2$	$(54\ \mu m)^2$

Table 6.1: Overview of typical experimental set-up configuration parameters.

---

[60] Note that in the first experiments at P10 a PI-LCX detector was used. The detector has a read-out time of approximately 1.5 s and detects photons with a direct illumination CCD of 1340 × 1300 chipsize with a pixel size of $20 \times 20\ \mu m^2$. In later experiments, a Maxipix 2x2 detector could be used that allowed to resolve dynamics also at higher temperatures.

[61] For details see section 7.4.

[62] Tests measurements of static samples at ID10 and P10 verified that the beam is not causing decorrelation of the speckle intensity within experimental times of 10000 s and more.

7 Structural properties of colloidal particles in supercooled liquids

In this chapter, results of the time averaged small angle X-ray scattering (SAXS) measurements on colloidal tracer particles suspended in the glass former dibutyl-phthalate (DBP) and poly-propyl glycol (PPG) are presented. All suspensions were first investigated at $T = 300$ K. Furthermore, SAXS results in the temperature range $T_{\mathrm{g}} < T \leq 300$ K were analyzed to quantify a possible temperature dependence. In order to estimate beam damage effects and thresholds for the investigation of the particle dynamics, the structural properties of the particles were also studied as a function of the exposure time.

7.1 Characterization of the samples

The samples were composed of silica particles suspended in a glass forming liquid. The samples are characterized by the particle radius R_{P}, the polydispersity $\tilde{P} = \frac{\Delta R_{\mathrm{P}}}{R_{\mathrm{P}}}$ and the volume fraction ϕ of the particles in the solvent. These properties can be determined via the investigation of the particle form factor $P(q)$ and the static structure factor $S(q)$ (see chapter 5).

Typically, series of 100 images with an exposure time between 0.1 s and 1 s per image were taken with a 2D detector. The images were corrected for bad pixels[1] and dark counts, in addition to a masking of regions contaminated by parasitic slit and beamstop scattering. The images were summed and azimuthally averaged. The result is equal to the averaged scattered intensity $I(q)$ in equation 4.20 incorporating the averaged background intensity of the dispersion medium, the capillary and the window materials in the beam path.

In the following, the samples are labeled according to their radius, solvent (D for DBP and P for PPG), and volume fraction (in vol.%).[2]

---

[1] Bad pixels are not performing as expected, e.g. dead or hot pixels depending upon whether the output is too low or too high.

[2] For example, the sample ${}^{71}\mathrm{P}_{<1}$ characterizes particles with a mean radius of $R_{\mathrm{P}} = 71$ nm suspended in PPG with a volume fraction $\phi < 1$ vol.%.

7.2 Particle form factors

The samples with the lowest concentration of the stock solutions (samples with a dilution of $\frac{1}{49}$) were measured to determine $P\left(q\right)$. Their nominal volume fractions were small ($\phi < 0.5$ vol.%) and $S\left(q\right)$ was unity. In this case, $I\left(q\right)$ depends only on $P\left(q\right)$ and one can obtain information on R_{P} and $\tilde{P}$. $P\left(q\right)$ was modeled by an expression for spherical particles with a size distribution, given by

$$P\left(q\right) \propto \int\limits_{0}^{\infty} \frac{R^6}{R_{\mathrm{P}}^6} F\left(q,R\right) a_{\mathrm{sf}}\left(R, R_{\mathrm{P}}, \tilde{P}\right) \mathrm{d}R + I_{\mathrm{BG}}\left(q\right), \tag{7.1}$$

where $I_{\mathrm{BG}}\left(q\right)$ refers to the experimental background. Here $F\left(q,R\right)$ is the form factor of a sphere, given by Aragon et al.[3] where the Schultz-Flory size distribution $a_{\mathrm{sf}}\left(R, R_{\mathrm{P}}, \tilde{P}\right)$ is applied.

$I_{\mathrm{BG}}\left(q\right)$ was determined from measurements of pure DBP and PPG. Figure 7.1 shows the measured scattered intensity of both solvents which is parameterized by[4]

$$\begin{aligned} I_{\mathrm{BG}}\left(q\right) &= I_{\mathrm{noise}} + I_{\mathrm{B}}\left(q\right) \\ &= I_{\mathrm{noise}} + \frac{1}{q^{\alpha}}, \end{aligned} \tag{7.2}$$

with the results $\alpha_{\mathrm{DBP}} \approx 3.5$ and $\alpha_{\mathrm{PPG}} \approx 2.5$.

The temporal and azimuthal averaged scattered intensity $I\left(q\right)$ is shown in Figures 7.2 and 7.3 for the two diluted samples ${}^{53}\mathrm{D}_{<1}$ and ${}^{71}\mathrm{P}_{<1}$. $I\left(q\right)$ decreases with increasing q and exhibits a modulation which is governed by $P\left(q\right)$, while the visibility of the minima in $I\left(q\right)$ is determined by $\tilde{P}$. The background intensity $I_{\mathrm{BG}}\left(q\right)$ was taken into account according to equation 7.2 via equation 7.1 weighted by the statistical error to the data. The obtained polydispersities were very sensitive to the background while the mean particle radii R_{P} proved to be independent of the detailed background situation.

In comparison to sample ${}^{71}\mathrm{P}_{<1}$, the positions of the minima for ${}^{53}\mathrm{D}_{<1}$ are shifted towards larger q-values, which indicate that the particle radius is smaller. It is furthermore observed that the minima are more pronounced for ${}^{71}\mathrm{P}_{<1}$ indicating a smaller polydispersity. This is confirmed by the $P\left(q\right)$-model fitted to the data. For ${}^{53}\mathrm{D}$ the fits yield $R_{\mathrm{P}} = (53.3 \pm 0.4)$ nm with $\tilde{P} = (12.5 \pm 0.7)$ %, and $R_{\mathrm{P}} = (70.7 \pm 0.1)$ nm with $\tilde{P} = (5.2 \pm 0.3)$ % for ${}^{71}\mathrm{P}$, respectively.

The results of the particle form factor evaluation are summarized in Table 7.1. Therein,

---

[3] Aragon, S. R. and Pecora, R. (1976). *J. Chem. Phys.* **64**, 2395.

[4] The q-independent part of the background I_{noise} refers to the scattering of the solvent at q-values far away from its molecular static structure factor, whereas the q-dependent part of the background $I_{\mathrm{B}}\left(q\right)$ originates from the X-ray beam which is significant only at weak sample scattering.

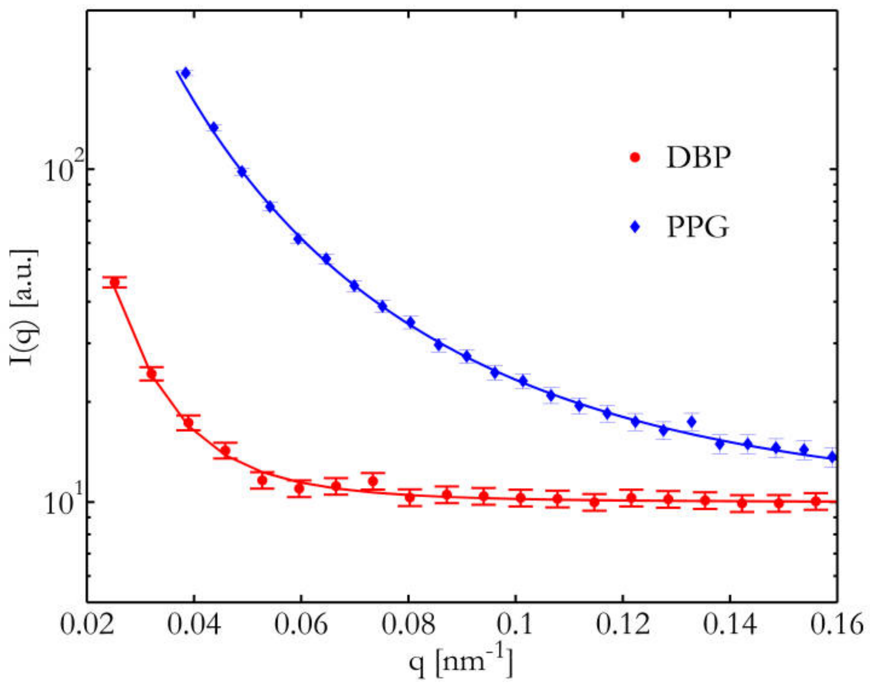

Figure 7.1: Measured background intensity of DBP and PPG. The solid lines are fits of equation 7.2 to the data.

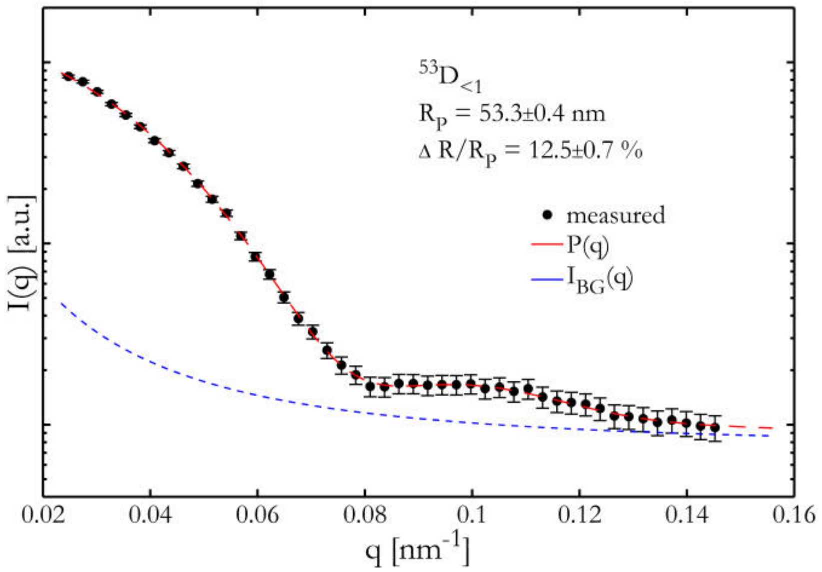

Figure 7.2: Particle form factor of ^{53}D. The red line is the statistical error weighted fit of equation 7.1 to the data using $I_{\mathrm{BG}}(q)$ (blue line) as background.

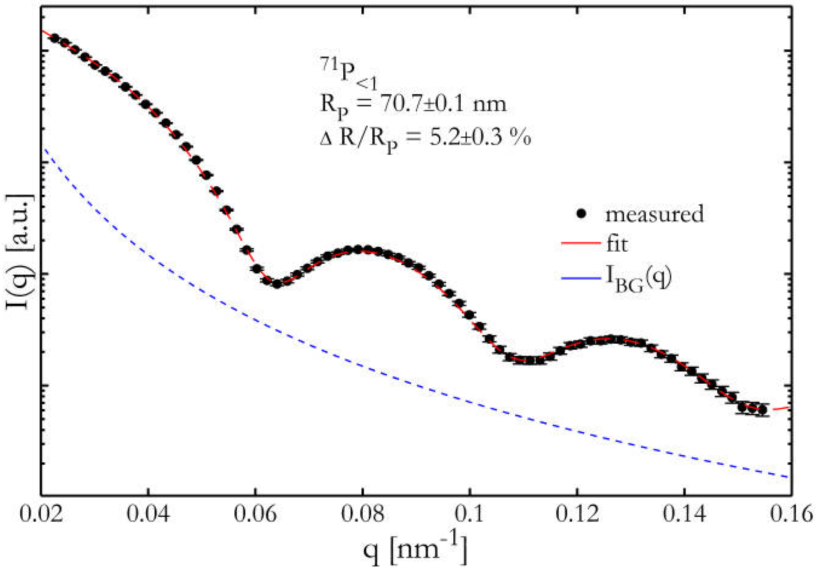

Figure 7.3: Particle form factor ^{71}P. The red line is the statistical error weighted fit of equation 7.1 to the data using $I_{\mathrm{BG}}(q)$ (blue line) as background.

the mean particle sizes, polydispersities and the information on the used synthesis are given.

It is remarkable that the polydispersity for Stöber particles synthesized according to Yokoi et al.[5] (YO) was found in general much smaller than for particles obtained within the Stöber method according to Bogush et al.[6] (BO) (see Table 7.1). This suggest a more uniform growth of particles with smaller pores when using silica nano-particles as seeds. For both particle production methods, it was found that the polydispersity is enhanced at smaller particle sizes which is in agreement with the observation that smaller particles are more affected by pores.

7.3 Static structure factors

According to equation 4.20, the static structure factor $S(q)$ of the concentrated samples can be obtained from the scattering intensity $I(q)$ via division by the particle form factor $P(q)$:

$$S(q) = \frac{I(q)}{P(q)}. \tag{7.3}$$

---

[5] Yokoi, T. et al. (2006). *J. Am. Chem. Soc.* **128**, 13664.

[6] Bogush, G. H. et al. (1988). *J. Non-Cryst. Solids* **104**, 95.

Solvent	**Synthesis**	**Stock solutions**	**Mean particle radius in nm**	**Polydispersity in %**
DBP	BO	^{82}D	82.3 ± 0.7	10 ± 1
	BO	^{53}D	53.3 ± 0.4	12.5 ± 0.7
	BO	^{45}D	45.0 ± 0.3	12 ± 1
	BO	^{38}D	37.9 ± 0.4	13.2 ± 0.6
	YO	^{28}D	28 ± 3	7 ± 4
PPG4000	YO	^{71}P	70.7 ± 0.1	5.2 ± 0.3
	BO	^{27}P	27 ± 1	13 ± 1
	YO	^{18}P	18 ± 1	9.9 ± 0.1

Table 7.1: Particle properties of the samples series. The errors reflect statistical error and q-resolution of the measurements. YO (Yokoi et al.) and BO (Bogush et al.) refer to the applied synthesis methods.

Thus, the results of the $P(q)$-analysis are used to fit the data of the concentrated samples. This is presented in Figure 7.4(a), where $I(q)$ of the sample $^{53}\mathrm{D}_{3.8}$ is shown with $P(q)$ (red line) assuming the background intensity $I_{\mathrm{BG}}(q)$ (blue dotted line). $I(q)$ shows a pronounced peak at small q-values indicating inter-particle interactions. The result of $S(q)$ for $^{53}\mathrm{D}_{3.8}$ obtained via equation 7.3 is shown in Figure 7.4(b), where $S(q)$ exhibits a peak at $q_{\max} = 0.029\ \mathrm{nm}^{-1}$ and equals unity at large q-values. The peaking of $S(q)$ indicate the next neighbor distance via $r_{\mathrm{P}} = \frac{2\pi}{q_{\max}}$. For small q-values the system is probed over large length scales, thus $S(q)$ decreases for $q < q_{\max}$ and is being related to the isothermal compressibility for $S(q \to 0)$.[7] The red line in Figure 7.4(b) represents the results of the error weighted fit of the rescaled mean spherical approximation (RMSA)[8] to the measured $S(q)$. The RMSA model uses the effective charge Z_{eff} of the particles and the volume fraction ϕ as free parameters. The nominal temperature $T = 300\ K$, the relative permittivity of the dispersion medium $\epsilon_r = 5$, and R_{P} as result of the $P(q)$-analysis were fixed parameters of the model.[9] The data was fitted for $0.01\ \mathrm{nm}^{-1} < q < 0.06\ \mathrm{nm}^{-1}$. The fit describes the measured $S(q)$ within the first and second maximum.

Common to all samples is the shifting of the static structure factor peak to larger q-values with increasing ϕ. In addition, an increase of the amplitude $S(q_{\max})$ with increasing ϕ (Figure 7.5) was found which indicates an increase of positional correlations at larger particle concentrations.[10] The shift of $q_{\max}$ to larger q-values is equivalent to a decrease of the inter-particle distances r_{P}. The normalized inter-particle distance $\frac{r_{\mathrm{P}}}{R_{\mathrm{P}}}$ as function of

---

[7] Due to the lack of data at small q-values, $S(0)$ could not be determined.

[8] Ruiz-Estrada, H. et al. (1990). *Physica A* **168**, 919.

[9] The applied RMSA model also uses the salt-concentration as parameter which was set to zero since no salt were added.

[10] It is suggested that this can be attributed to the increase of the direct inter-particle interactions due to a reduction of the particle charge screening at shorter inter-particle distances. See Westermeier, F. et al. (2012). *J. Chem. Phys.* **137**, 114504.

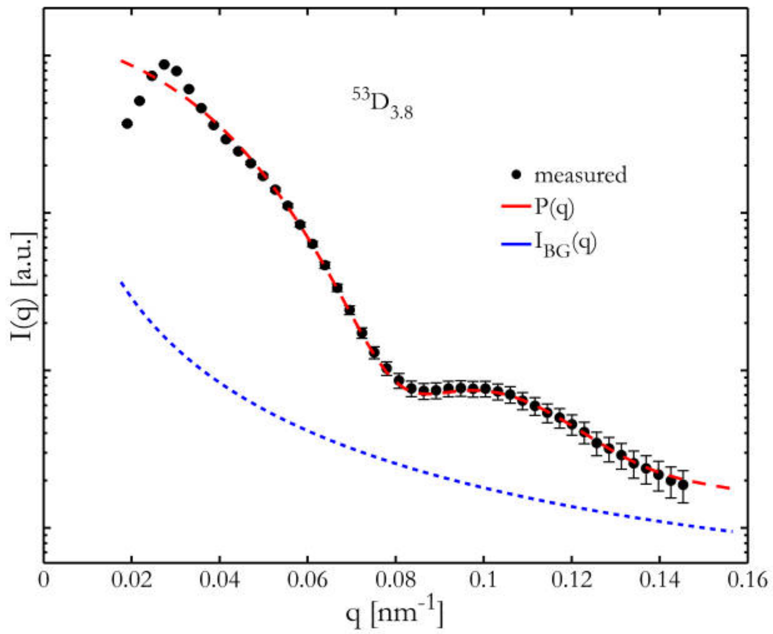

(a) $I\left(q\right)$ measured for ^{53}D at $\phi = 3.8$ vol.%.

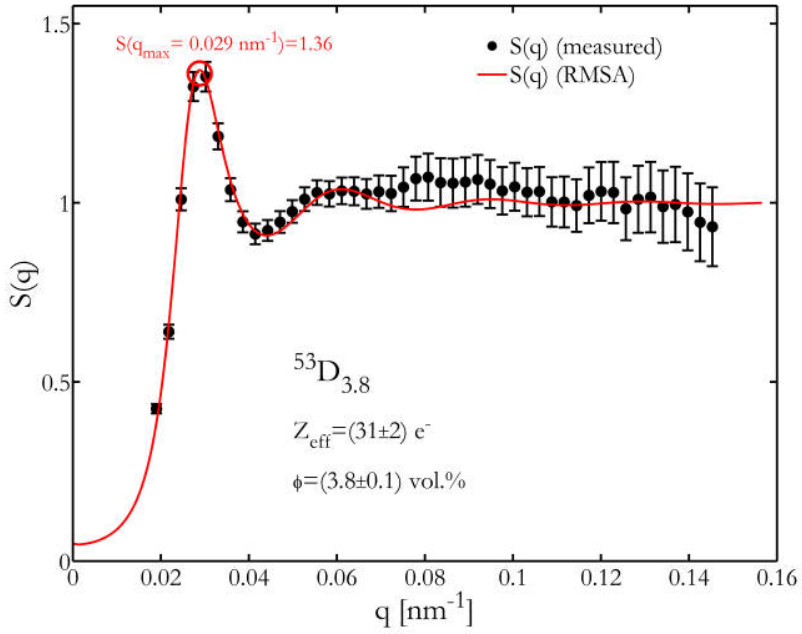

(b) $S\left(q\right)$ as a function of the momentum transfer q for $^{53}\mathrm{D}_{3.8}$.

Figure 7.4: Static structure factor analysis for $^{53}\mathrm{D}_{3.8}$: (a) $I\left(q\right)$ as function of q (b) Result of $\frac{I(q)}{P(q)}$ as function of q. $S\left(q_{\mathrm{max}}\right)$ is denoting the height of the first static structure factor peak.

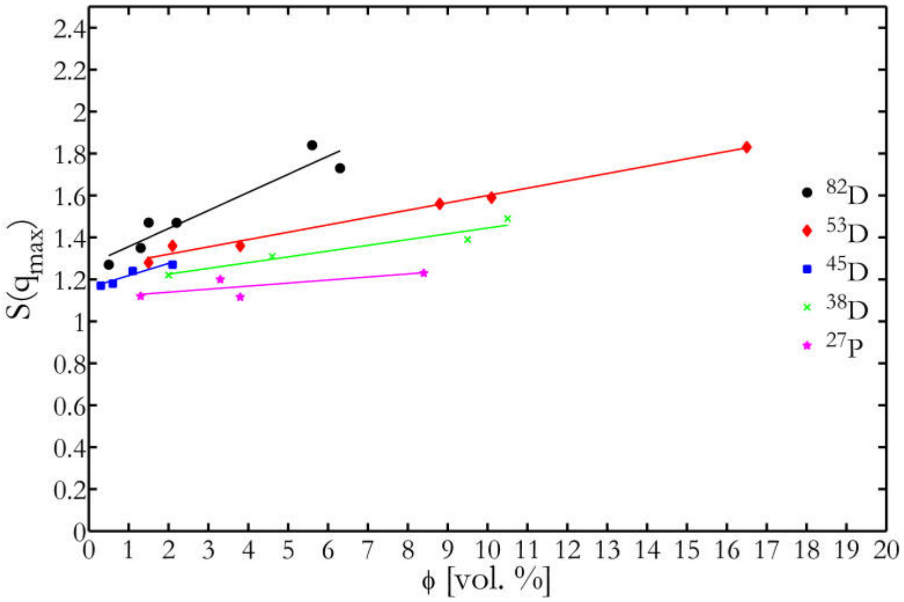

Figure 7.5: Amplitude of $S\left(q_{\max}\right)$ as function of ϕ.

ϕ is shown in Figure 7.6. For all measured samples, the distances are above the particle contact distance $\left(\frac{r_{\mathrm{P}}}{R_{\mathrm{P}}}=2\right)$. Moreover, the amplitude of $S\left(q\right)$ is for all samples well below the onset of crystallization which for charge-stabilized colloidal systems is expected to occur at $S_{\mathrm{c}}\left(q_{\max}\right)\approx 3.1$.[11]

In the following the results of the static structure factor analysis are discussed for three stock solutions of silica particles in DBP: ^{38}D, ^{53}D and ^{82}D (Figures 7.7-7.9).[12]

The static structure factors for the shown sample series correspond to particle suspensions at different volume fractions with nominal volume fractions ϕ_{s}, $\phi_{\frac{\mathrm{s}}{2}}\approx\frac{1}{2}\phi_{\mathrm{s}}$, $\phi_{\frac{\mathrm{s}}{3}}\approx\frac{1}{3}\phi_{\mathrm{s}}$, $\phi_{\frac{\mathrm{s}}{6}}\approx\frac{1}{6}\phi_{\mathrm{s}}$ and $\phi_{\frac{\mathrm{s}}{9}}\approx\frac{1}{9}\phi_{\mathrm{s}}$ where ϕ_{s} is the volume fraction of the stock solution.[13] The RMSA fits to the static structure factors of ^{38}D (Figure 7.7) yield an effective charge of $Z_{\mathrm{eff}}=(22\pm2)$ e^{-} and volume fractions of $\phi_{\mathrm{s}}=9.5$ vol.%, $\phi_{\frac{\mathrm{s}}{2}}=4.6$ vol.% $\left(\frac{1}{2.1}\phi_{\mathrm{s}}\right)$ and $\phi_{\frac{\mathrm{s}}{6}}=2.0$ vol.% $\left(\frac{1}{4.8}\phi_{\mathrm{s}}\right)$. These are in a good agreement with the nominal volume fractions.[14] The small discrepancies can be explained by the difficulties in the preparation of such highly viscous samples. The RMSA fits describes the peak region of $S\left(q\right)$ very well, in particular for $^{38}\mathrm{D}_{2.0}$. For $^{38}\mathrm{D}_{4.6}$ and $^{38}\mathrm{D}_{9.5}$ the fits are slightly different in the q-region of the second static structure factor peak.[15] Although these differences are more

---

[11] Gapinski, J. et al. (2010). *J. Chem. Phys.* **136**, 24507.

[12] The results of the static structure factor analysis for all samples are presented in Table 7.2. The corresponding figures can be found in appendix A.4.

[13] Details are given in section 6.1.

[14] Because of low scattering intensities, $S\left(q\right)$ could not be obtained for ^{38}D at $\phi_{\frac{\mathrm{s}}{3}}$.

[15] This can be related to limitations of the model to describe systems with volume fractions $\phi>10$ vol.%. See Nägele, G. (1996). *Physics Reports* **272**, 215.

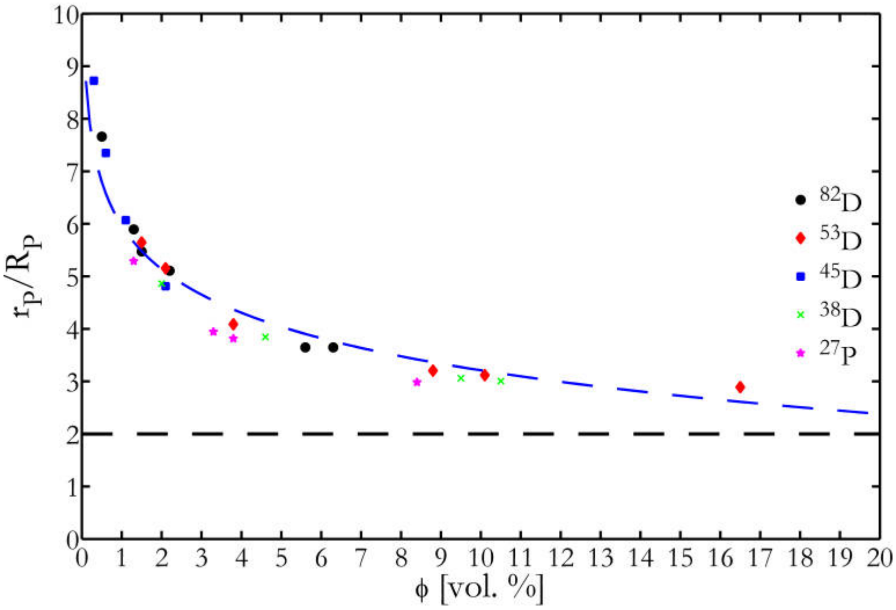

Figure 7.6: Normalized inter-particle distance $\frac{r_\mathrm{P}}{R_\mathrm{P}}$ as function of ϕ.

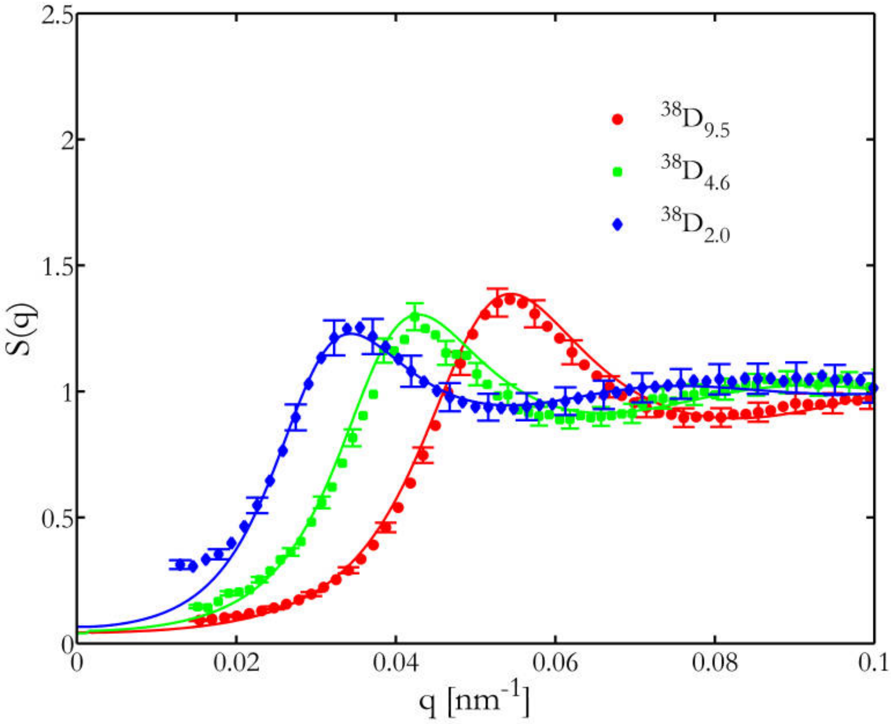

Figure 7.7: Measured static structure factors of ^{38}D at different concentrations. The lines are error weighted RMSA fits to the data.

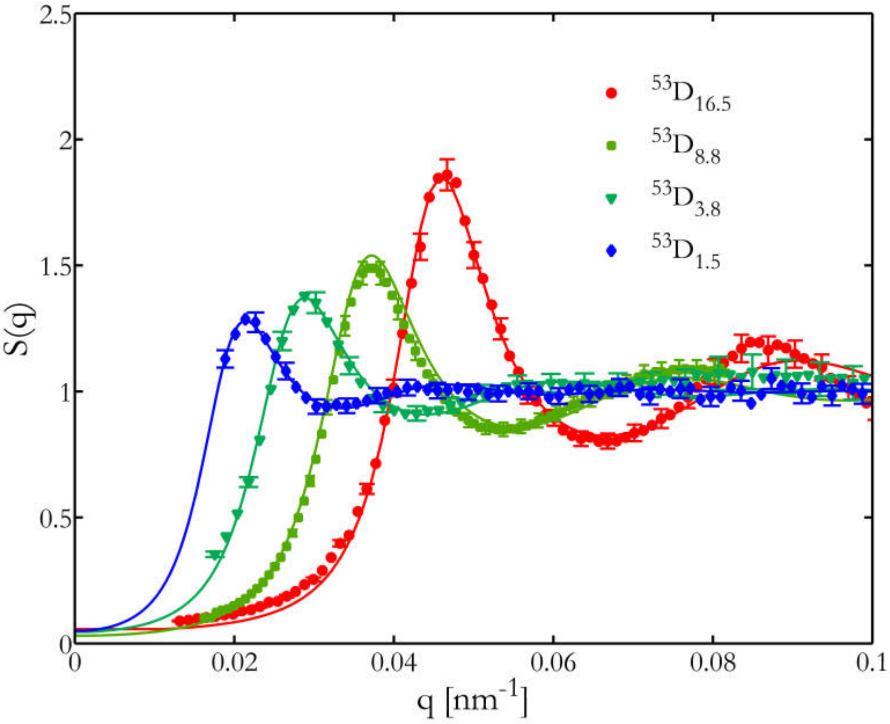

Figure 7.8: Measured static structure factors of ^{53}D at different concentrations. The lines are error weighted RMSA fits to the data.

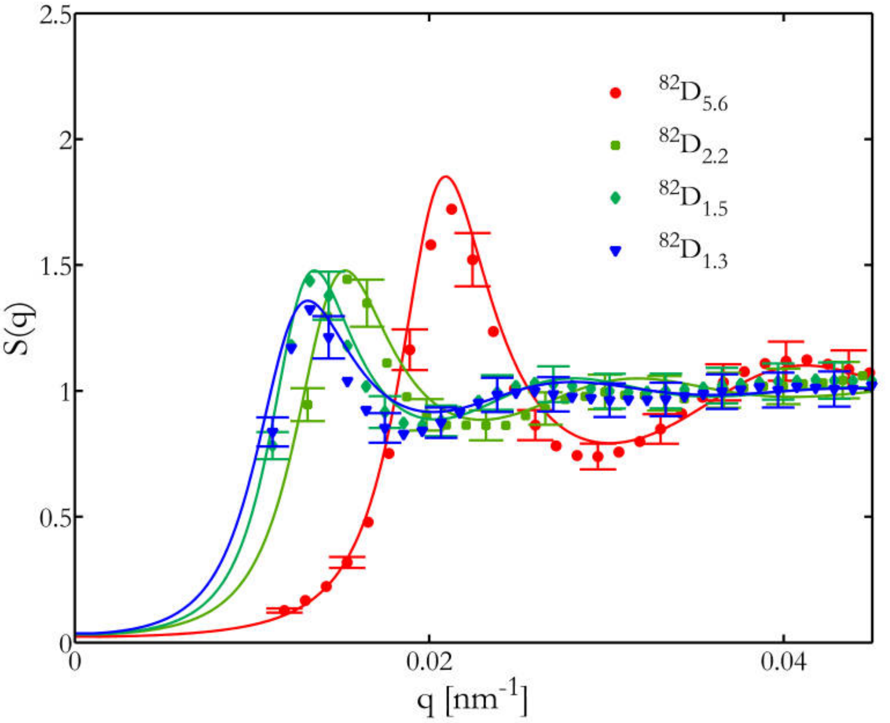

Figure 7.9: Measured static structure factors of ^{82}D at different concentrations. The lines are error weighted RMSA fits to the data.

pronounced in the case of $^{53}\mathrm{D}_{16.5}$ (Figure 7.8), the obtained volume fractions for the lower concentrated samples $^{53}\mathrm{D}$ are in good agreement with the nominal ones. The RMSA fit yield volume fractions of $\phi_{\mathrm{s}} = 16.5$ vol.%, $\phi_{\frac{\mathrm{s}}{2}} = 8.8$ vol.% $\left(\frac{1}{1.9}\phi_{\mathrm{s}}\right)$, $\phi_{\frac{\mathrm{s}}{3}} = 3.8$ vol.% $\left(\frac{1}{4.3}\phi_{\mathrm{s}}\right)$ and $\phi_{\frac{\mathrm{s}}{9}} = 1.5$ vol.% $\left(\frac{1}{11.0}\phi_{\mathrm{s}}\right)$ for $Z_{\mathrm{eff}} = (35 \pm 4)\ \mathrm{e}^{-}$. The RMSA fits for $^{82}\mathrm{D}$ (Figure 7.9) are describing the data adequately. Here, volume fractions of $\phi_{\mathrm{s}} = 6.5$ vol.%, $\phi_{\frac{\mathrm{s}}{3}} = 2.2$ vol.% $\left(\frac{1}{3.0}\phi_{\mathrm{s}}\right)$, $\phi_{\frac{\mathrm{s}}{6}} = 1.5$ vol.% $\left(\frac{1}{4.3}\phi_{\mathrm{s}}\right)$ and $\phi_{\frac{\mathrm{s}}{9}} = 1.3$ vol.% $\left(\frac{1}{5}\phi_{\mathrm{s}}\right)$ were obtained for $Z_{\mathrm{eff}} = (58 \pm 25)\ \mathrm{e}^{-}$. Notice that the first static structure factor peak appears very close to the beam masked q-region for the lowest ϕ which limits the significancy of the fits and could be the reason for the discrepancy to the nominal volume fractions. In this case, the obtained volume fractions can be considered as upper limit of ϕ.

7.4 Considerations to the stability of the sample properties

When performing scattering experiments with X-rays, the interaction of the photons with the sample might cause changes in the sample due to ionization of atoms in the material, e.g. by breaking of polymer chains or heating due to secondary electron cascades dissipating in the sample. Such ionization effects can influence the sample dynamics, e.g. via changing the particle size or the effective charge. To avoid these effects, the experiments were performed without focusing the X-ray beam and at short exposure times. While the particle form factors of dilute samples were found to be independent of exposure times and temperature, important changes were observed for the static structure factor of the concentrated samples.

In order to estimate beam damage effects, test measurements were performed at $T = 200\ \mathrm{K} \approx 1.08\ T_{\mathrm{g}}$, where 500 scattering images were recorded, each with an exposure time of 2.0 s.[16] The effect of beam exposure to $S\left(q\right)$ is shown for $^{38}D_{10.5}$ in Figure 7.10, by comparing $S\left(q\right)$ for different total exposure times t_{e} after 10 s, 50 s, and 90 s respectively. The lines are RMSA model fits to the measured $S\left(q\right)$. A continued decrease of the static structure factor amplitude $S\left(q_{\mathrm{max}}\right)$ with t_{e} is clearly visible while the position at q_{max} does not change. The RMSA modeling suggests a decrease of the effective charge from 25 to 10 elementary charges.[17] The effect becomes significant for $t_{\mathrm{e}} \approx 50 - 80$ s when the decrease of the amplitude exceeds 10% of the initial value. Thus, the absolute exposure time was limited to a value arround 50 s, in order to ensure the invariance of the sample properties during a measurement.

---

[16] An estimation of the energy absorbed by the sample is given in appendix A.5.

[17] It can be speculated that heating by the X-ray beam induce a restructuring of the particles which also cause a decrease of the static structure factor amplitude. This is supported by the finding that

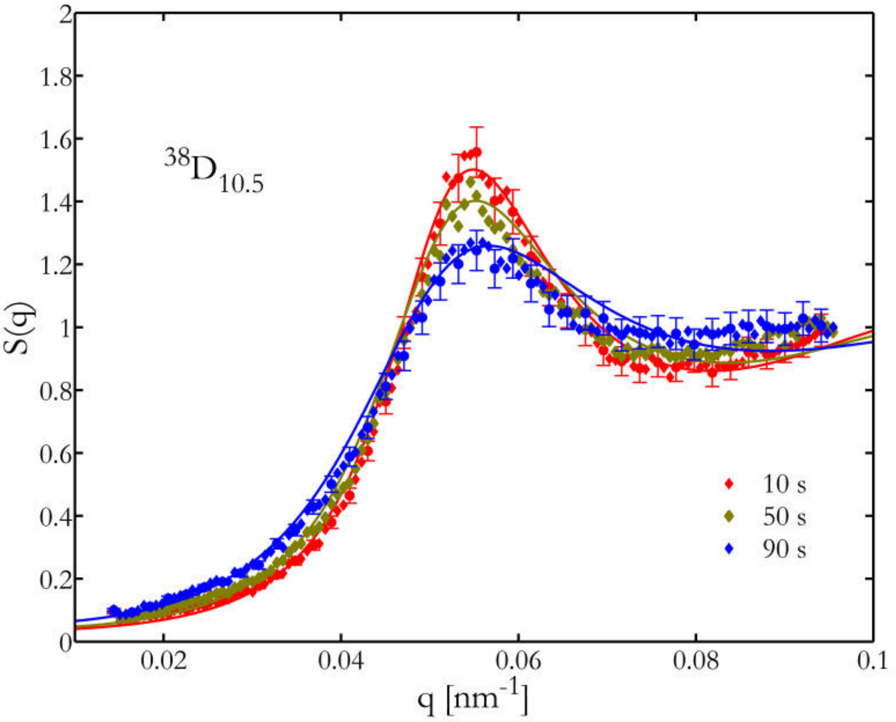

Figure 7.10: Beam exposure effect on $S(q)$ illustrated for $^{38}D_{10.5}$ at 200 K.

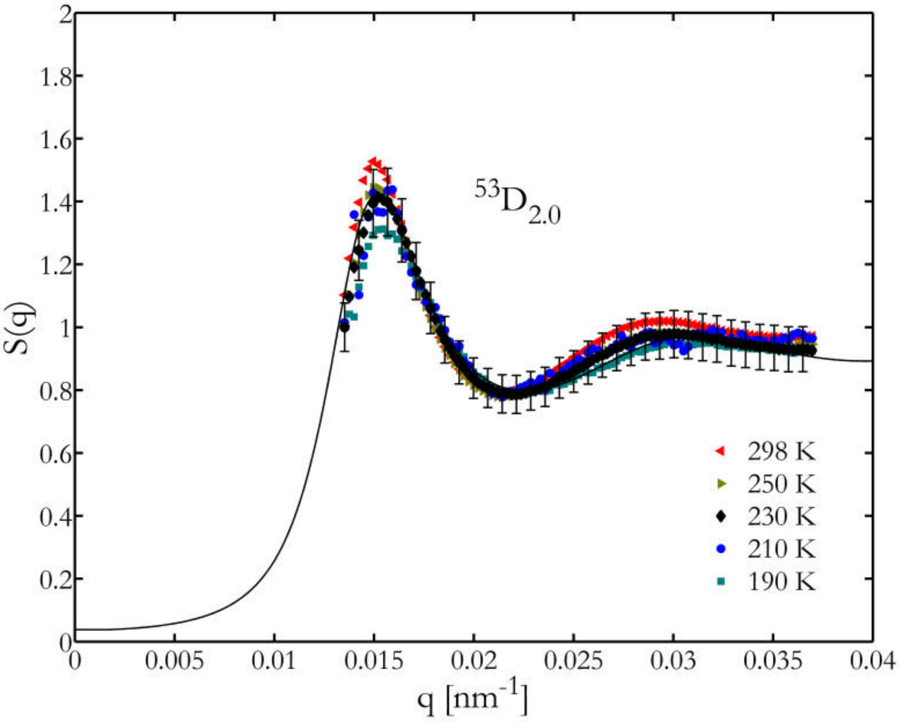

Figure 7.11: $S(q)$ for $^{53}D_{2.0}$ measured at different temperatures. The black line is the RMSA fit to $S(q)$ for $^{53}D_{2.0}$ at $T = 230$ K.

In Figure 7.11 static structure factors obtained at different temperatures between 190 K $< T <$ 300 K for ${}^{53}D_{2.0}$ are compared. As result, $S(q)$ can be described within its uncertainty by the same RMSA model at different temperatures, although the static structure factor peak height slightly decreases with decreasing temperature. In summary, the structural properties obtained via the static structure factor can be assumed as independent of the temperature.

7.5 Summary of structural properties

The particle radius R_p and the polydispersity $\tilde{P}$ of the samples were obtained during the investigation of the particle form factor $P(q)$. The results are summarized in Table 7.1. The particle radii were found to be in the range of $18 - 83$ nm which is in good agreement to the desired range intended during the synthesis. The obtained polydispersities were between 5.2% and 13.2%. The polydispersities achieved in case of the YO synthesis were in general smaller then these obtained via the BO synthesis. Furthermore, $P(q)$ and $S(q)$ were found to be temperature independent. In addition, the invariance of $S(q)$ for exposure times $t_\mathrm{e} < 50$ s was verified.

The static structure factor was investigated in terms of its height and position of its first maximum. RMSA modeling yields the effective charge Z_eff and the volume fraction ϕ. The results are summarized in Table 7.2.[18] The results for ϕ are in good agreement with the nominal concentrations intended during the preparation of the concentration series. The results of Z_eff indicate a small increase with increasing ϕ. Moreover, Z_eff (averaged for ϕ between 1 vol.% $< \phi <$ 10 vol.%) increases linearly with the particle radius R_P (Figure 7.12). This is in contrast to $Z \propto R_\mathrm{P}^2$ as expected if the charge of the particle coating is determined only by Z_eff. This implicates that a complex screening $\left(\propto \frac{1}{R\mathrm{P}}\right)$ is already present at small volume fractions $\phi <$ 10 vol.%.

For dilute samples, the volume spanned by the normalized particle distance $\frac{r_\mathrm{P}(\phi)}{R_\mathrm{P}}$ is directly proportional to the volume fraction ϕ. This volume as function of ϕ is shown in Figure 7.13 for all samples. The blue dashed line indicates the simple relation obtained for dilute samples. Since deviations from this behavior occurs for $\phi >$ 3 vol.%, $\phi \leq$ 3 vol.% can be used as threshold for the dilute case.

---

different delay times between exposures has an effect on the relaxation times near T_g.

[18] In case of ${}^{71}D$ and ${}^{18}P$, the stock solutions were too dilute. Only upper limits for ϕ could be obtained. The restrictions of the measurements at small q-values and the limits of the RMSA model for larger q-values are the reason for the uncertainties of the effective charge for ${}^{81}D$, ${}^{71}D$ and ${}^{18}P$.

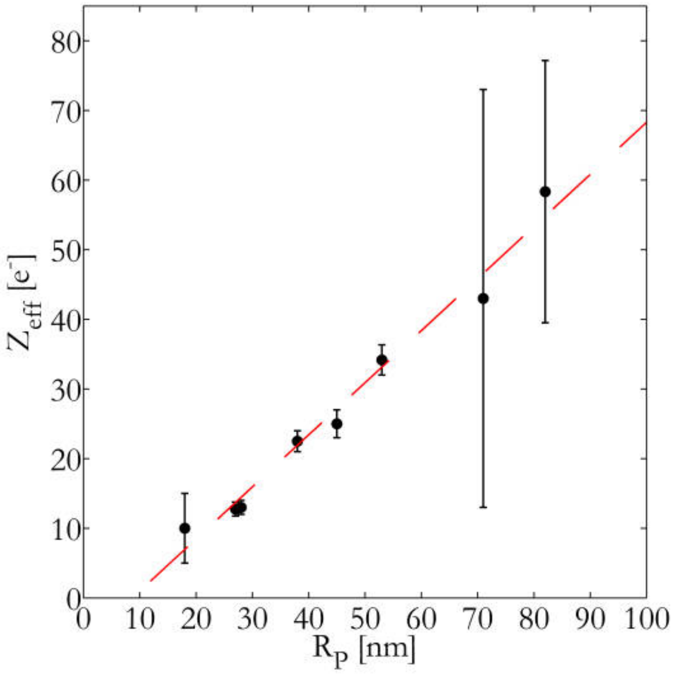

Figure 7.12: Averaged effective charge Z_{eff} as function of the particle radius R_{P}. The averages were obtained for concentrations of 1 vol.% $< \phi <$ 10 vol.%.

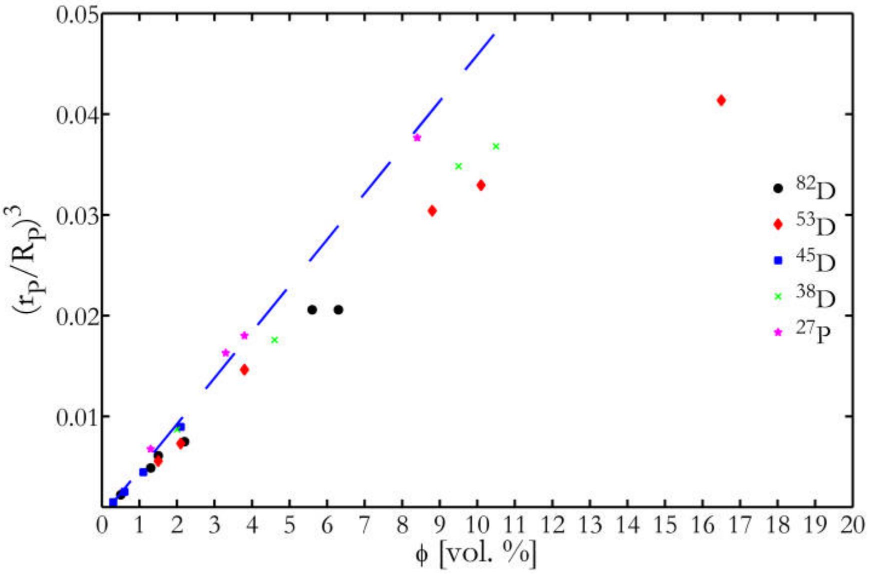

Figure 7.13: Volume spanned by the normalized particle distance $\frac{r_{\text{P}}}{R_{\text{P}}}$ as function of ϕ.

Sample	**Effective charge in e^-**	**Volume fraction in vol.%**	**$q_{\max}$ in nm^{-1}**	**$S\left(q_{\max}\right)$**
$^{82}\mathrm{D}_{6.3}$	66 ± 25	6.3 ± 0.4	0.021	1.73
$^{82}\mathrm{D}_{5.6}$	94 ± 30	5.6 ± 0.2	0.021	1.84
$^{82}\mathrm{D}_{2.2}$	52 ± 14	2.2 ± 0.2	0.015	1.47
$^{82}\mathrm{D}_{1.5}$	55 ± 9	1.5 ± 0.1	0.014	1.47
$^{82}\mathrm{D}_{1.3}$	42 ± 13	1.3 ± 0.2	0.013	1.35
$^{82}\mathrm{D}_{0.5}$	41 ± 22	0.5 ± 0.1	0.010	1.27
$^{53}\mathrm{D}_{16.5}$	39 ± 2	16.5 ± 0.2	0.043	1.83
$^{53}\mathrm{D}_{10.1}$	37 ± 3	10.1 ± 0.2	0.038	1.59
$^{53}\mathrm{D}_{8.8}$	35 ± 3	8.8 ± 0.2	0.037	1.56
$^{53}\mathrm{D}_{3.8}$	31 ± 2	3.8 ± 0.1	0.029	1.36
$^{53}\mathrm{D}_{2.1}$	34 ± 1	2.1 ± 0.1	0.023	1.36
$^{53}\mathrm{D}_{1.5}$	29 ± 2	1.5 ± 0.1	0.021	1.28
$^{45}\mathrm{D}_{2.1}$	25 ± 2	2.1 ± 0.1	0.029	1.27
$^{45}\mathrm{D}_{1.1}$	25 ± 2	1.1 ± 0.1	0.023	1.24
$^{45}\mathrm{D}_{0.6}$	25 ± 2	0.6 ± 0.1	0.019	1.18
$^{45}\mathrm{D}_{0.3}$	25 ± 2	0.3 ± 0.1	0.016	1.17
$^{38}\mathrm{D}_{10.5}$	25 ± 2	10.5 ± 0.2	0.055	1.49
$^{38}\mathrm{D}_{9.5}$	22 ± 1	9.5 ± 0.2	0.054	1.39
$^{38}\mathrm{D}_{4.6}$	23 ± 2	4.6 ± 0.2	0.043	1.31
$^{38}\mathrm{D}_{2.0}$	20 ± 1	2.0 ± 0.1	0.034	1.22
$^{28}\mathrm{D}_{0.9}$	13 ± 1	0.9 ± 0.1	0.037	1.14
$^{71}\mathrm{P}_{<1.0}$	43 ± 30	< 1.0	-	-
$^{71}\mathrm{P}_{<0.5}$	43 ± 30	< 0.5	-	-
$^{27}\mathrm{P}_{8.4}$	12 ± 1	8.4 ± 0.2	0.078	1.23
$^{27}\mathrm{P}_{3.8}$	12 ± 1	3.8 ± 0.2	0.061	1.16
$^{27}\mathrm{P}_{3.3}$	14 ± 1	3.3 ± 0.1	0.059	1.20
$^{27}\mathrm{P}_{1.3}$	13 ± 1	1.3 ± 0.1	0.044	1.12
$^{18}\mathrm{P}_{<1.0}$	10 ± 5	< 1.0	-	-
$^{18}\mathrm{P}_{<0.5}$	10 ± 5	< 0.5	-	-

Table 7.2: Results of the static structure factor analysis for all samples.

8 Dynamics of colloidal particles in supercooled liquids

In this chapter, the results of the X-ray photon correlation spectroscopy study on colloidal particles in polypropylene glycol (PPG) and dibutyl phthalate (DBP) are presented. At the beginning, the discussion focuses on a concentration series of 71 nm sized silica particles in PPG. For these measurements a fast read-out detector could be used that allowed the investigation of faster dynamics at higher temperatures and thus offers the most complete picture of the temperature behavior of all samples ($0.9\ T_\mathrm{g} < T < 1.5\ T_\mathrm{g}$). Since the dynamics of particles without inter-particle interactions are easier to characterize, the results for the dilute suspensions are discussed first. In this context, it will be shown that a distinct change in the particle dynamics is found in a temperature regime well above the glass transition temperature of the solvents. Afterwards, the results of the more concentrated suspensions are discussed in order to determine the effect of the tracer particle concentration on this change in the dynamics. Finally, all results are interpreted in the context of changing solvent properties.

8.1 Comments to the data evaluation

During the experiments, the samples were investigated at different temperatures between $T = 300$ K and T_g. At each temperature, a series of scattering patterns was recorded. The patterns were corrected for background and bad pixels, and evaluated via the normalized intensity autocorrelation function g_2 and the instantaneous intensity correlation function C_I. An overview of the acquired data is given in Table 8.1. Due to limitations to resolve g_2 and C_I, as discussed in sections 4.2 and 5.3, some data taken at the lower and upper limits of the temperature range could not be analyzed. In particular, the signal-to-noise ratio (SNR) of suspensions with smaller particles at low concentrations, e.g. ^{38}D and ^{45}D, was not sufficient to resolve C_I. In addition, the q-range and time scale that allows an evaluation differs for different temperatures. At higher temperatures ($T > 250$ K) the evaluation of larger q-values is limited due to the minimum detector frame spacing t_a, whereas the evaluation of small q-values is limited by the shadowing effects of the beamstop.

Sample	**Detector**	**Read-out time in s**	**Temperature range in K**	**Temperature points**
$^{82}\mathrm{D}_{6.3}$	PI-LCX CCD	1.5	186-205	6
$^{82}\mathrm{D}_{5.6}$	PI-LCX CCD	1.5	187-298	9
$^{82}\mathrm{D}_{2.2}$	PI-LCX CCD	1.5	186-205	5
$^{82}\mathrm{D}_{1.5}$	PI-LCX CCD	1.5	187-298	9
$^{82}\mathrm{D}_{1.3}$	PI-LCX CCD	1.5	187-298	9
$^{82}\mathrm{D}_{0.5}$	PI-LCX CCD	1.5	187-298	9
$^{53}\mathrm{D}_{16.5}$	PI-LCX CCD	1.5	186-205	6
$^{53}\mathrm{D}_{10.1}$	PI-LCX CCD	1.5	186-205	6
$^{53}\mathrm{D}_{8.8}$	Andor CCD	1	186-298	10
$^{53}\mathrm{D}_{3.8}$	Andor CCD	1	187-300	9
$^{53}\mathrm{D}_{2.1}$	PI-LCX CCD	1.5	186-298	9
$^{53}\mathrm{D}_{1.5}$	Andor CCD	1	186-298	10
$^{45}\mathrm{D}_{2.1}$	PI-LCX CCD	1.5	185-298	8
$^{45}\mathrm{D}_{1.1}$	PI-LCX CCD	1.5	185-298	8
$^{45}\mathrm{D}_{0.6}$	PI-LCX CCD	1.5	185-298	6
$^{45}\mathrm{D}_{0.3}$	PI-LCX CCD	1.5	185-298	6
$^{38}\mathrm{D}_{10.5}$	PI-LCX CCD	1.5	200-230	4
$^{38}\mathrm{D}_{9.5}$	PI-LCX CCD	1.5	184-200	6
$^{38}\mathrm{D}_{4.6}$	PI-LCX CCD	1.5	184-200	6
$^{38}\mathrm{D}_{2.0}$	Andor CCD	1	183-300	8
$^{28}\mathrm{D}_{0.9}$	PI-LCX CCD	1.5	180-300	7
$^{71}\mathrm{P}_{<1.0}$	Maxipix 2x2	0.0035	192-300	28
$^{71}\mathrm{P}_{<0.5}$	Maxipix 2x2	0.0035	217-300	18
$^{27}\mathrm{P}_{8.4}$	Andor CCD	1	216-290	7
$^{27}\mathrm{P}_{3.8}$	Andor CCD	1	219-290	7
$^{27}\mathrm{P}_{3.3}$	Maxipix 2x2	0.0035	235-300	6
$^{27}\mathrm{P}_{1.3}$	Maxipix 2x2	0.0035	230-300	7
$^{18}\mathrm{P}_{<1.0}$	Andor CCD	1	222-290	5
$^{18}\mathrm{P}_{<0.5}$	Andor CCD	1	212-290	10

Table 8.1: Overview of the acquired XPCS datasets.

Dynamics above $T = 250$ K was accessible exclusively with the Maxipix 2x2 detector. It had to be operated at different illumination modes to cover short as well as very long experimental times.[1] Thus, for dynamics with characteristic relaxation times τ_c in the range of $1 - 10$ s, only small q-values are accessible with this detector. The limitation to access large q-values is given by either the SNR or the requirement of $\tau_\mathrm{c} \ll t_\mathrm{e}$, while τ_c can be very large in particular for slow dynamics near T_g.

8.2 The normalized intensity autocorrelation function

As shown in sections 4.2 and 5.3, the dynamics of colloidal particles can be described by the normalized intensity autocorrelation function g_2 obtained by the multi-speckle technique. g_2 is related to the field autocorrelation function g_1 via the Siegert-relation

$$g_2\left(q,t\right) = 1 + \beta \cdot \left|g_1\left(q,t\right)\right|^2,$$

which can be interpreted via the Kohlrausch-Williams-Watts (KWW) function as

$$\frac{1}{\beta}\left(g_2\left(q,t\right) - B\right) = \exp\left(-2\left[\frac{t}{\tau_\mathrm{c}}\right]^\gamma\right). \tag{8.1}$$

In this equation, the experimental observables (left), given by the speckle contrast[2] β, the normalized intensity autocorrelation function g_2 and the so-called baseline[3] $B \approx 1$, are separated from the properties of the particle dynamics (right), given by the Kohlrausch exponent γ, and the characteristic particle relaxation time τ_c which is connected to the relaxation rate Γ via $\tau_\mathrm{c} = \Gamma^{-1}$. Γ characterizes the diffusion properties of the particles.

Different particles dynamics can be distinguished by the q-dependence of Γ. On the one hand, $\Gamma \propto q^2$ identifies a path-time[4] relation of $W\left(t\right) \propto t^{\frac{1}{2}}$ which is characteristic for particles undergoing random walks due to collisions with solvent molecules (free diffusion). On the other hand, $\Gamma \propto q$ implies $W\left(t\right) \propto t$ which describes an undisturbed motion of particles in one direction similar to a ballistic flight (hyper-diffusion).[5]

The obtained KWW exponent γ is connected to a nontrivial distribution $G\left(\tau\right)$ of

---

[1] Notice that a reliable beam shutter synchronization was only available for $t_\mathrm{a} > 0.1$ s resulting in two camera modes, one with a continuous illumination for an experimental time up to $t_\mathrm{e} \approx 5$ s for $t_\mathrm{a} < 0.1$ s and one with a shutter controlled illumination suitable for an infinite $t_\mathrm{e} > 10$ s with $t_\mathrm{a} > 0.1$ s.

[2] For the various experimental set-ups the contrast β is ranging between $0.3 - 0.6$.

[3] This is a fit parameter according to the offset of the Siegert-relation which is typically close to unity.

[4] Here, W denotes the mean square particle displacement. See section 5.3.

[5] See Dhont, J. K. G. (1996). *An Introduction to the Dynamics of Colloids.* 1st Edition. Elsevier, Amsterdam, Netherlands.

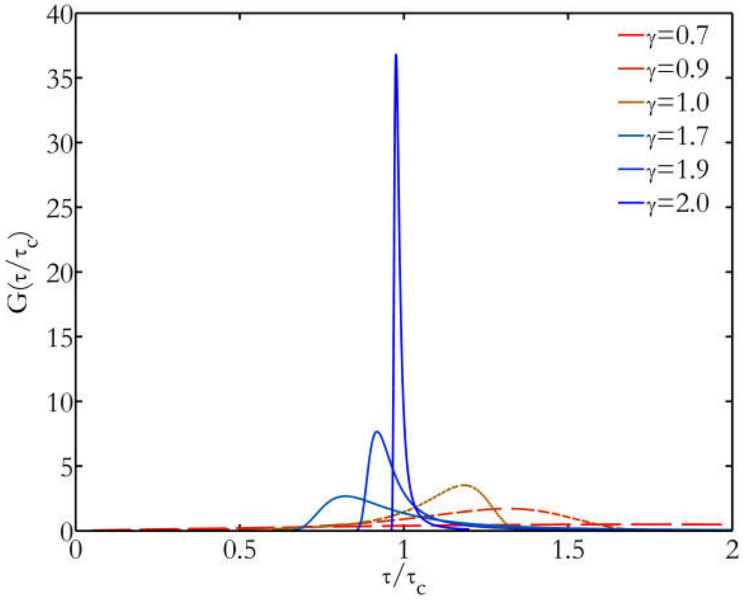

Figure 8.1: Distribution $G\left(\frac{\tau}{\tau_c}\right)$ for different γ-values.

relaxation times τ in the system, which is implicitly defined by

$$\exp\left(-t\right)^{\gamma} = \int G\left(x\right)\exp\left(-t/x\right)\mathrm{d}x. \tag{8.2}$$

$G\left(\frac{\tau}{\tau_c}\right)$ can be computed from a series expansion[6], for which the results are shown in Figure 8.1 for different values of γ. In this context, $\gamma < 1$ is associated to a distribution of τ broader than a Gaussian indicating dynamical heterogeneities, e.g., found for molecular dynamics in supercooled liquids, while $\gamma \approx 2$ represents a Gaussian distribution implying a higher dynamical uniformity which is indicative for correlated particle motion.[7]

The parameters Γ and γ were investigated for dilute and concentrated suspensions of silica particles in PPG and DBP. According to section 7.5, the dynamics of the dilute samples (volume fraction $\phi < 3$ vol.%) are considered to be determined by particle-solvent interactions only. This allows to draw conclusions about the dynamical properties of PPG and DBP, contrary to the concentrated samples ($\phi > 3$ vol.%) where the dynamics is influenced by inter-particle interactions.

---

[6] Lindsey, C. P. and Patterson, G. D. (1980). *J. Chem. Phys.* **73**, 3348; Hansen, E. W. et al. (2013). *Macromolecular Chemistry and Physics* **214**, 844.

[7] Philipse, A. P. and Vrij, A. (1989). *J. Coll. Inter. Sci.* **128**, 121.

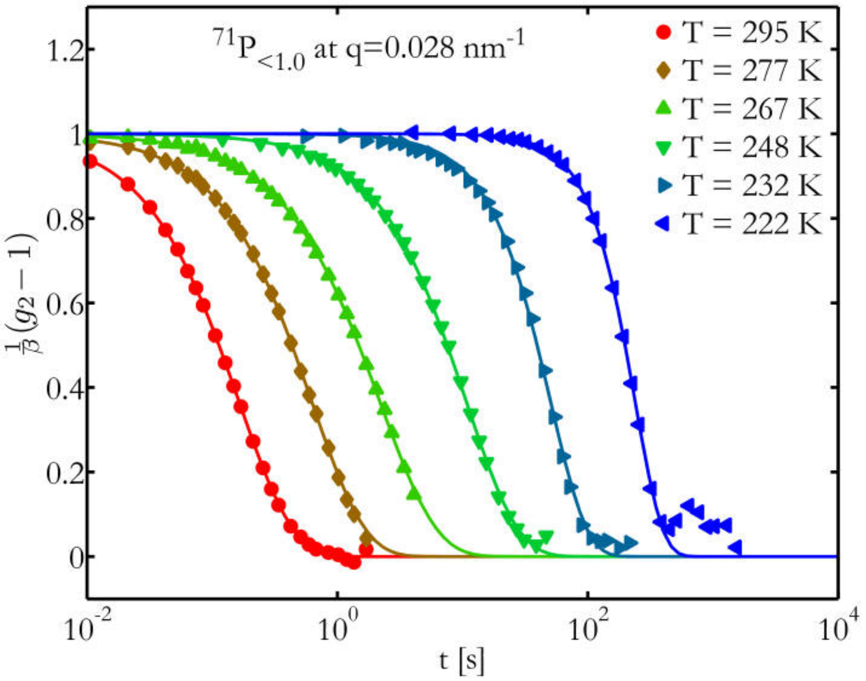

Figure 8.2: g_2 measured for $^{71}\mathrm{P}_{<1.0}$ at $q = 0.028\ \mathrm{nm}^{-1}$ for temperatures $222\ \mathrm{K} \leq T \leq 295\ \mathrm{K}$. Solid lines are KWW fits (equation 8.1) to the data. For clarity, not all measured temperatures are shown.

8.2.1 Dilute samples

In the following, the results for the dilute samples, $^{71}\mathrm{P}_{<1.0}$, $^{71}\mathrm{P}_{<0.5}$, $^{27}\mathrm{P}_{1.3}$, $^{18}\mathrm{P}_{<1.0}$, $^{18}\mathrm{P}_{<0.5}$, $^{53}\mathrm{D}_{1.5}$ and $^{82}\mathrm{D}_{2.2}$, are discussed with special emphasis on $^{71}\mathrm{P}_{<1.0}$.

The general temperature trend of g_2 for $^{71}\mathrm{P}_{<1.0}$ is illustrated in Figure 8.2, where g_2 is plotted as $\frac{1}{\beta}(g_2-1)$ at $q = 0.028\ \mathrm{nm}^{-1}$, for temperatures between $222\ \mathrm{K} \leq T \leq 295\ \mathrm{K}$. The curves show an increase of τ_c with decreasing temperature. This is accompanied by a change of the slope of g_2 that indicates a change from normal ($\gamma \approx 1$) to compressed ($\gamma \approx 2$) exponential decay. In this temperature regime the KWW fits are suited to describe g_2 over the full experimental time t_e. Only small deviations (below 10% of the contrast) in the long time behavior of g_2 close to the baseline are detectable. At temperatures below $T = 222$ K (see Figure 8.3) this cannot be neglected. Since the decay of g_2 is different at large time scales, the KWW fit was limited to the region of the first strong decay. The fits yield $\gamma \approx 2$ for all temperatures in this temperature regime. Remarkably, the obtained τ_c does not increase with decreasing temperature, instead it varies around $\tau_\mathrm{c} \approx 100$ s. The modeling of the second decay at $t \gg \tau_\mathrm{c}$ with the KWW function did not provide reliable results. However, it seems that this decay becomes more pronounced as the temperature decreases.

For $T \geq 222$ K, the increase of τ_c implies a slowing down of the particle dynamics with

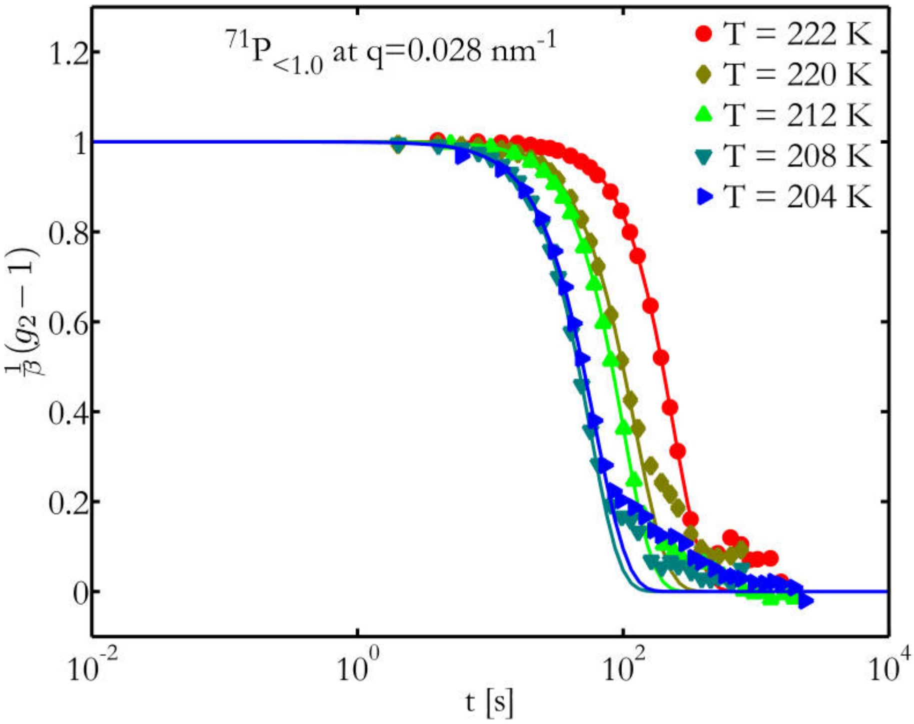

Figure 8.3: g_2 measured for $^{71}\mathrm{P}_{<1.0}$ at $q = 0.028\ \mathrm{nm}^{-1}$ for temperatures $222\ \mathrm{K} \geq T \geq 204\ \mathrm{K}$. Solid lines are KWW fits (equation 8.1) to the fast decay portion of g_2.

decreasing temperature. As described by equation 3.7, this is connected to the free diffusion of particles in the solvent while the viscosity η of the solvent increases with decreasing temperature. According to dielectric measurements[8], the molecular relaxation times τ in the pure solvent should follow the Vogel-Fulcher-Tammann (VFT) law $\left(\tau \propto \mathrm{e}^{-(T-T_0)}\right)$. Such behavior was indeed observed for the particle relaxation times at temperatures $T \geq 222$ K indicated by a linear decrease in Figure 8.4, where the obtained values of τ_c are plotted on a logarithmic scale as function of temperature. For temperatures below 222 K, a different behavior was found where τ_c decreases slightly with decreasing temperature.

A deviation from the VFT behavior for τ_c at low temperatures was observed also for other samples, though at slightly different starting temperatures. Since a conclusive interpretation can not be given at this point, temperatures where τ_c was not following the VFT law were excluded from the further analysis.[9] An exception was made for $^{71}\mathrm{P}_{<1.0}$ in order to discuss the implications on the particle dynamics.

The g_2 results for $^{71}\mathrm{P}_{<1.0}$, are shown in Figures 8.5-8.7 for the three temperatures $T = 295$ K, $T = 267$ K and $T = 222$ K, for accessible q-values. The lines in the figures are fits of equation 8.1 to the data. Since dynamics on short length scales is faster, g_2 at large

---

[8] Cochrane, J. et al. (1980). *Polymer* **21**, 837.

[9] In consequence this implies that the temperature dependence of τ_c will follow the VFT law (equation 2.5).

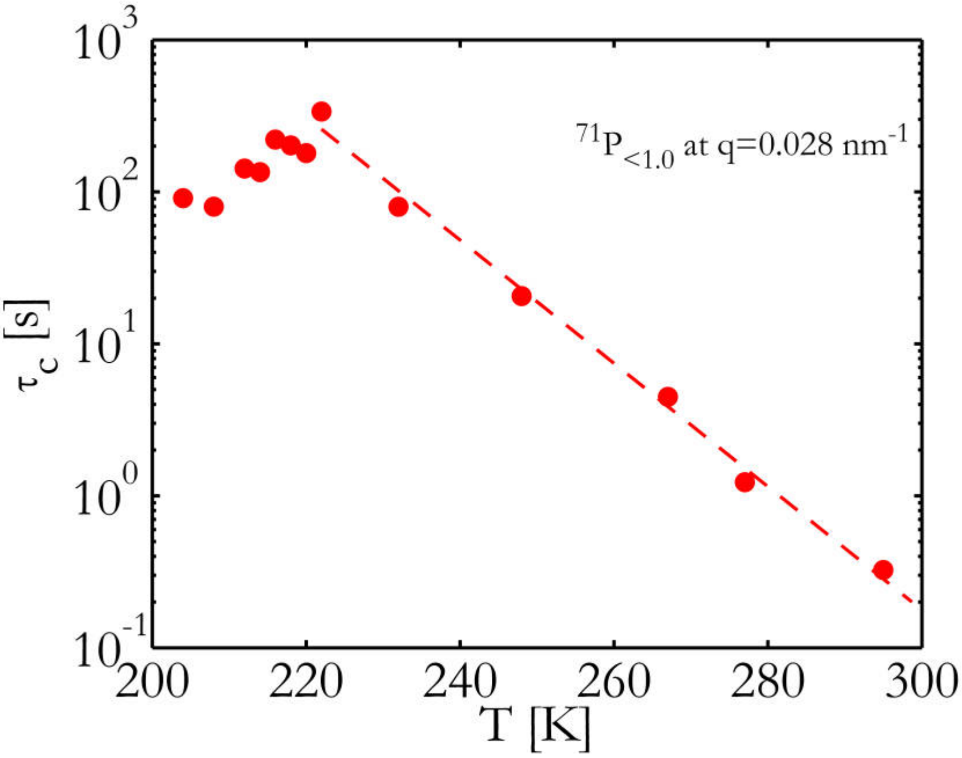

Figure 8.4: τ_c measured for $^{71}\mathrm{P}_{<1.0}$ at $q = 0.028$ nm^{-1} for temperatures 204 K $\leq T \leq$ 295 K. The dashed line is discussed as a guide to the eye reflecting a VFT behavior.

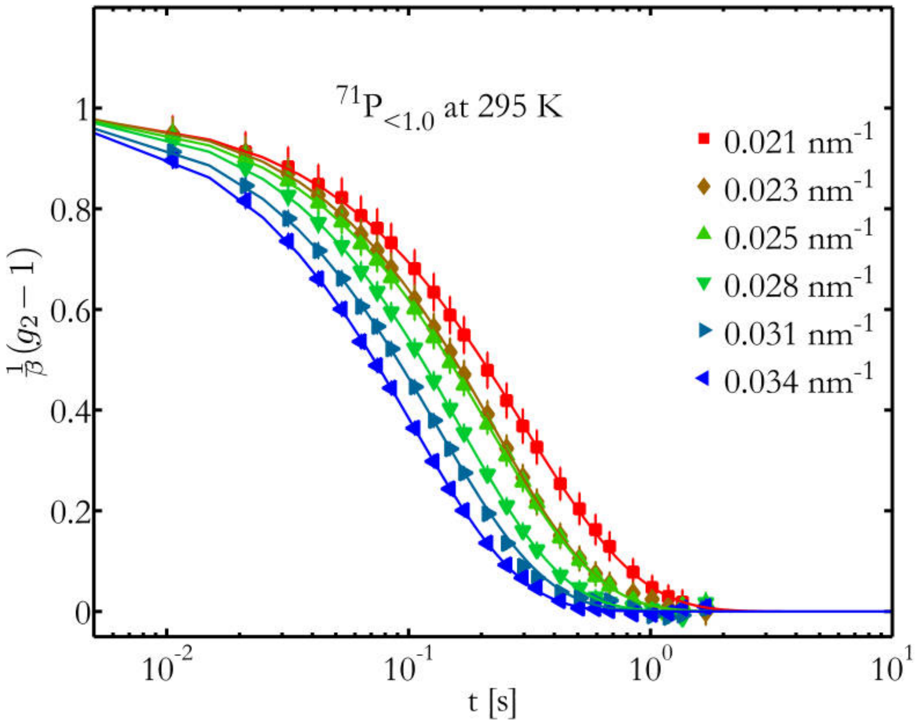

Figure 8.5: g_2 measured for $^{71}\mathrm{P}_{<1.0}$ at $T = 295$ K for different q.

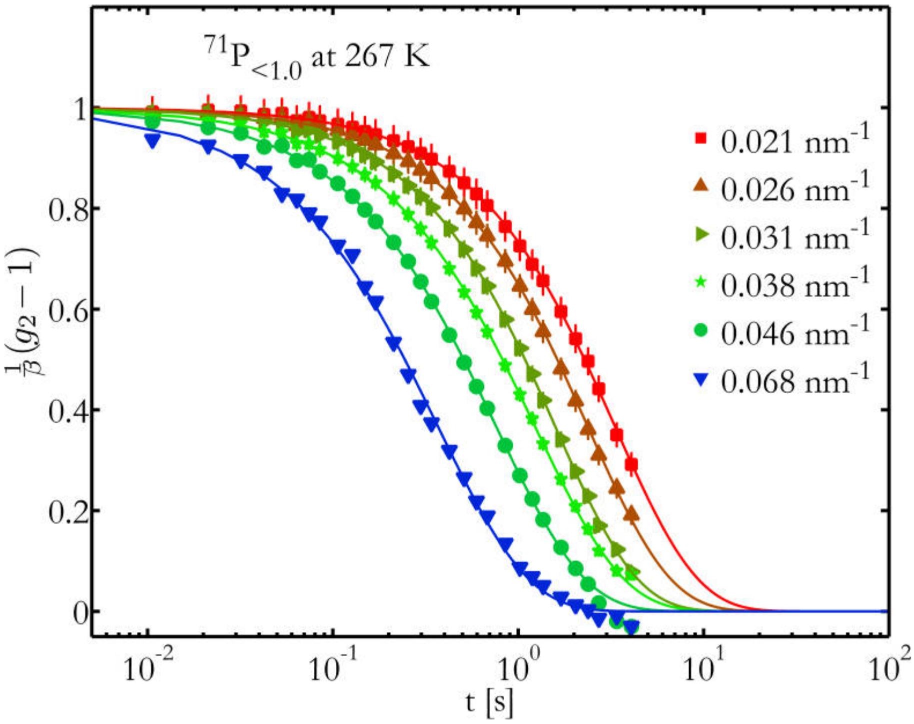

Figure 8.6: g_2 measured for $^{71}\mathrm{P}_{<1.0}$ at $T = 267$ K for different q.

q-values corresponds to short τ_c and decays at shorter times when q increases. This trend is observed for all shown temperatures and was found also for the temperature region $T < 222$ K. For $T = 295$ K and $T = 267$ K, the fits with the KWW function describe g_2 over the full experimental time t_e for all accessible q. This is not the case at $T = 222$ K where g_2 does not follow a single exponential decay. Here, g_2 exhibits a strong first decay followed by a weaker second decay. Although the SNR was not sufficient to fit the second decay, the KWW function adequately describes the first decay for all q-values. Its physical interpretation provides information on the fastest observable dynamical process. For all q the decay is compressed ($\gamma \approx 2$) and it seems that the second decay becomes more pronounced with decreasing q. This can be a sign of increasingly heterogeneous dynamics. For all temperatures similar values of $\mathrm{B} = 1.00 \pm 0.02$ and $\beta = 0.55 \pm 0.05$ were obtained. Reduced values of β were only found for $q \approx 0.056$ nm^{-1}, where the particle form factor of ^{71}P has a minimum (see also Figure 7.3). For q-values for which β or B were not covered by data points, they were assumed to be constant for all q.

The obtained fit parameters are summarized in Figure 8.8. The Kohlrausch exponent γ, the contrast β, and the baseline B are shown for the three temperatures in the right figures, whereas the relaxation rate $\Gamma(q) = \tau_c^{-1}(q)$ is shown in the left figures. The lines

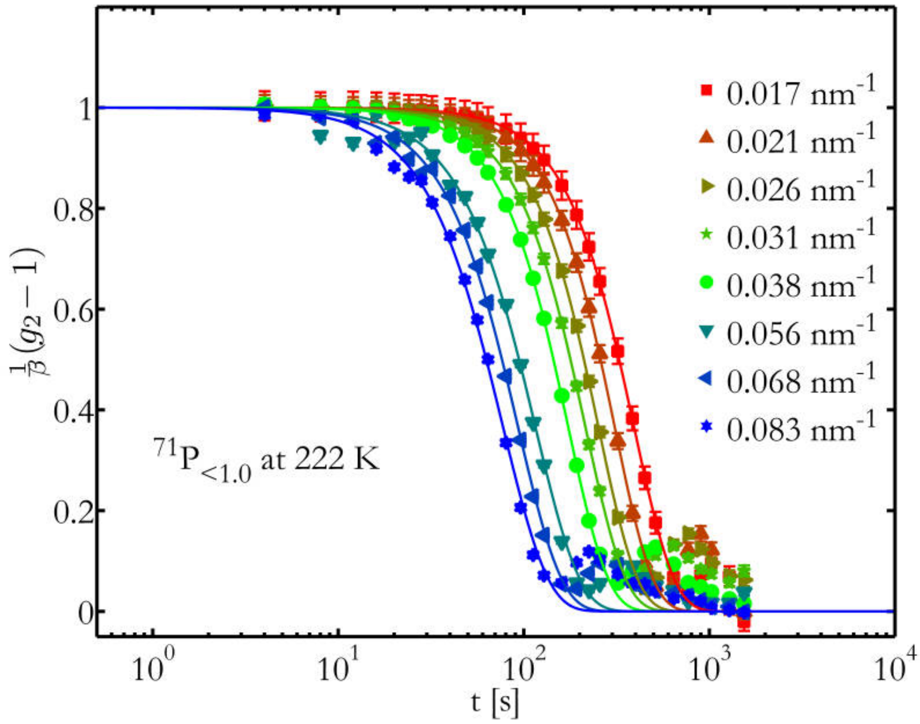

Figure 8.7: g_2 measured for $^{71}\mathrm{P}_{<1.0}$ at $T = 222$ K for different q.

in the left figures are fits with a power law given by

$$\Gamma(q) = D \cdot q^p, \tag{8.3}$$

where the parameter D is equal to the diffusion rate of the particles in the case of free diffusion ($p \approx 2$).

The best fits at $T = 295$ K were obtained for $\gamma \approx 1$ and $\Gamma \propto q^{2.2}$, where the exponent p has a larger uncertainty due to the small evaluated q-range. The corresponding particle dynamics can be identified as free diffusion. This is characterized by a simple exponential decay of g_2 ($\gamma = 1$) with $p = 2$ related to the particle displacement $W \propto t^{\frac{1}{2}}$. The best fits at $T = 267$ K yield values of $\gamma \approx 0.9$ and $\Gamma \propto q^{1.74}$. This can be also related to free diffusion of particles.

The best fits at $T = 222$ K were obtained for $\gamma \approx 1.9$ and $\Gamma \propto q^{1.08}$. This case is similar to $p = 1$ which corresponds to a particle displacement $W \propto t$ and describes hyper-diffusion dynamics of particles. Moreover, the compressed exponential decay ($\gamma \approx 2$) indicate a Gaussian distribution of the relaxation times which is much sharper as found for $\gamma \approx 1$.

In summary, the evaluation of g_2 for the dilute sample $^{71}\mathrm{P}_{<1.0}$ showed that the dynamics of the particles suspended in PPG becomes slower with decreasing solvent temperature. Moreover, the dynamics of the particles at higher temperatures can be characterized as

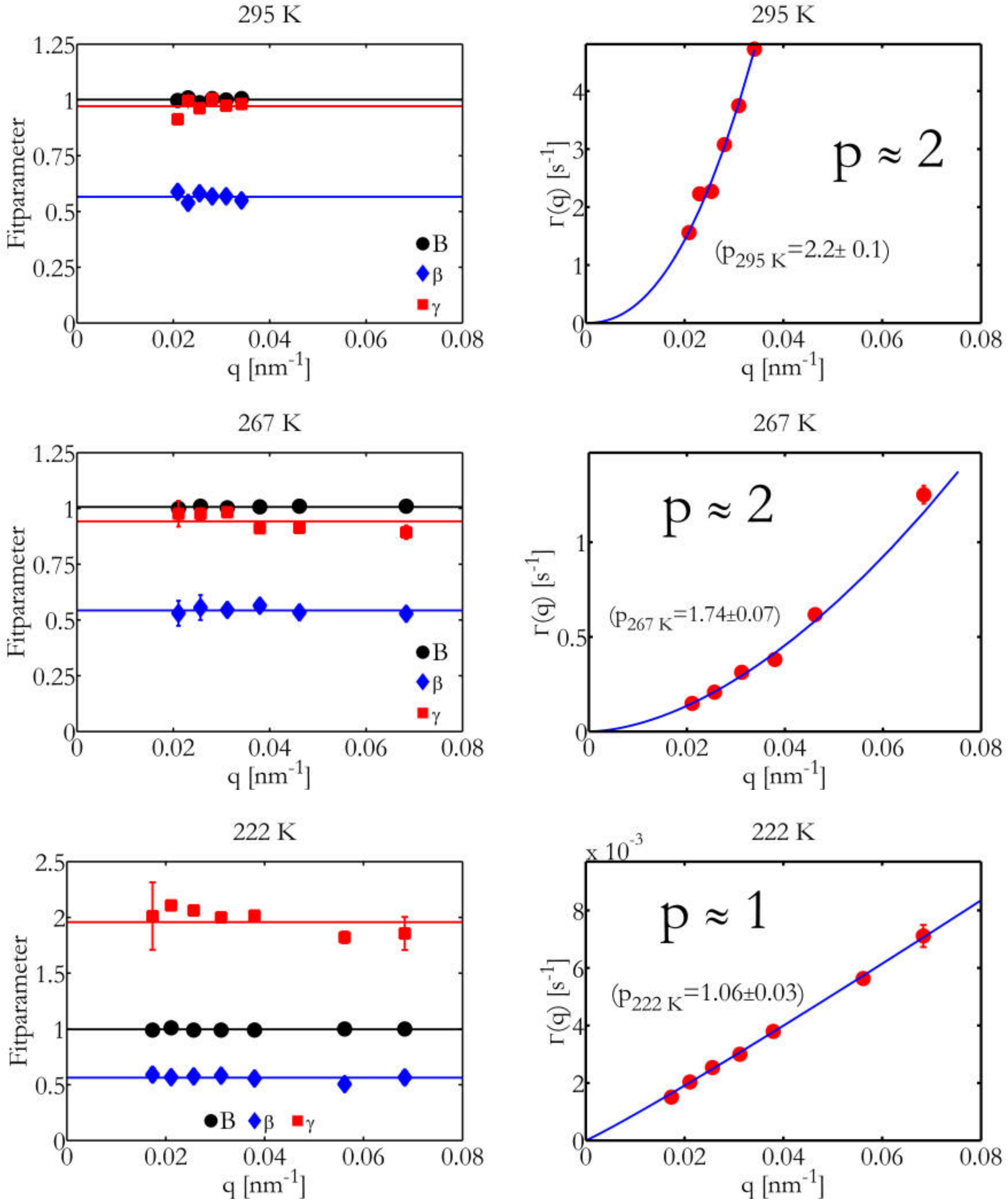

Figure 8.8: Analysis of g_2 for $^{71}\mathrm{P}_{<1.0}$ at $T = 295$ K, $T = 267$ K and $T = 222$ K. Shown are B, γ and β (left) as parameters of the KWW fit and Γ described by $\Gamma = D_0 \cdot q^p$ (right).

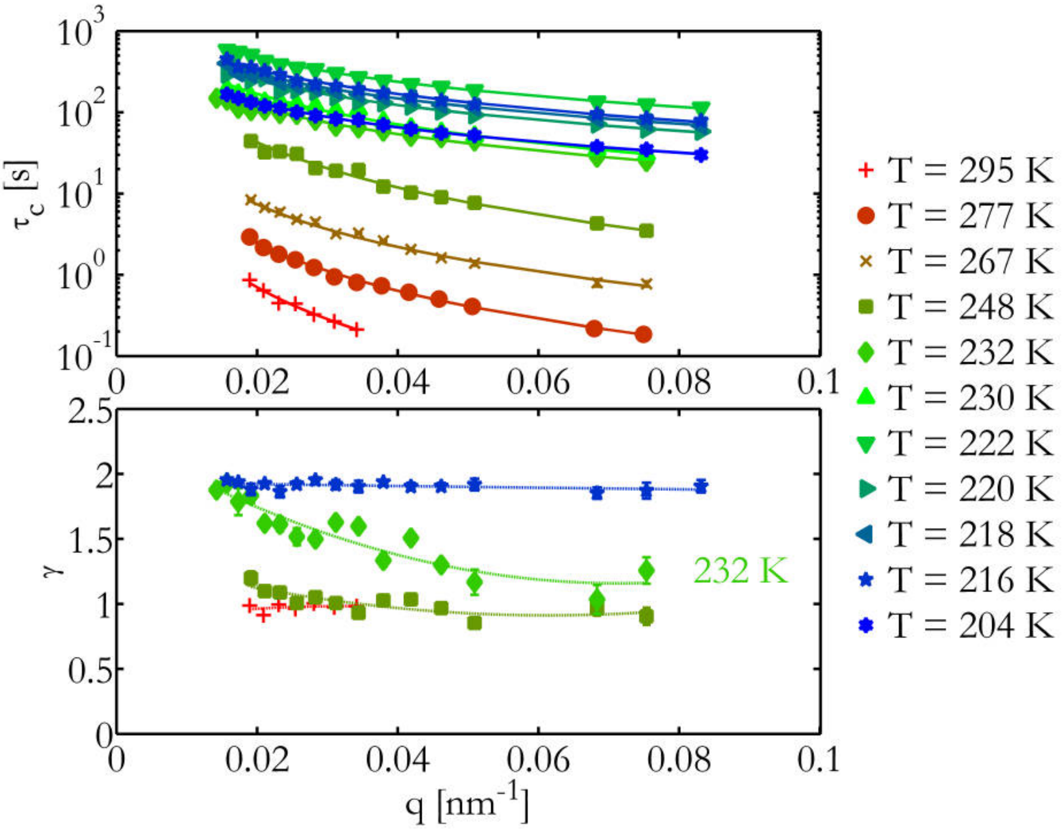

Figure 8.9: Top: $\Gamma(q)$. Bottom: $\gamma(q)$ obtained from the fits of equation 8.1 to the data of $^{71}P_{<1.0}$. For clarity, $\gamma(q)$ is shown only for selected temperatures. Solid lines are fits of $\Gamma(q)$ with equation 8.3, dashed lines for $\gamma(q)$ are guides to the eye.

free diffusion while around $T = 222$ K the dynamical behavior changes.

For the sake of completeness, the obtained values for τ_c and γ for all temperatures are shown in Figure 8.9. In the top Figure 8.9, the general temperature trend of τ_c is illustrated. As described above, τ_c increases with decreasing temperature for $300\text{ K} > T \geq 222$ K. Below $T = 222$ K, τ_c seems to become temperature independent. Simultaneously, the q-averaged value of γ increases from a value around $\gamma \approx 1$ to $\gamma \approx 2$ in the vicinity of 230 K. In this temperature region, γ has a distinct q-dependence and decreases slightly with increasing q. At higher and lower temperatures γ is q-independent.

In Figure 8.10, the parameter D obtained within the evaluation of Γ by equation 8.3 is shown as function of temperature. Here, D decreases exponentially with decreasing temperature but becomes temperature independent below $T = 230$ K. An analogous representation of this dependence is given in Figure 8.11, where the viscosity η obtained from D by using the Stokes-Einstein relation (equation 5.8) is compared to results of dielectric measurements[10]. While the parameter D cannot be treated as diffusion rate

---

[10] Cochrane, J. et al. (1980). *Polymer* **21**, 837.

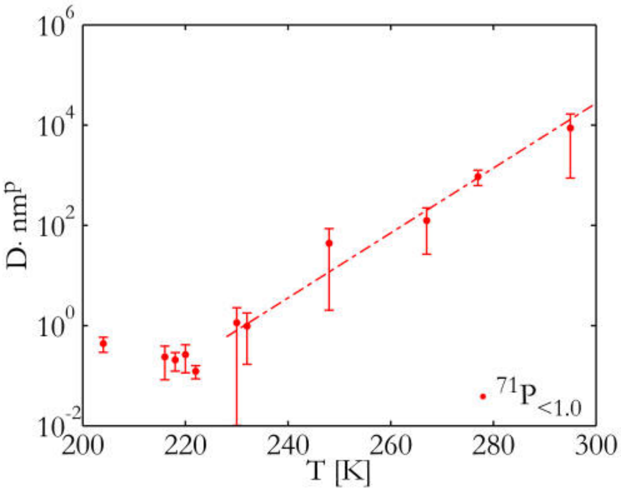

Figure 8.10: Parameter D obtained with power law fits to $\Gamma(q)$ for all measured temperatures. The line is a guide to the eye for temperatures where D can be treated as diffusion rate ($p \approx 2$).

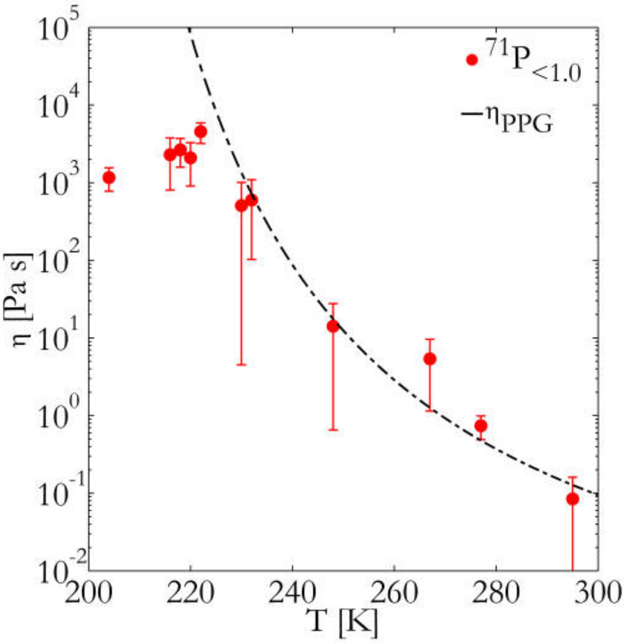

Figure 8.11: Viscosity η obtained for $^{71}\mathrm{P}_{<1.0}$ via the Stokes-Einstein relation compared to η_{PPG} as results of dielectric measurements (Cochrane, J. et al. (1980). *Polymer* **21**, 837).

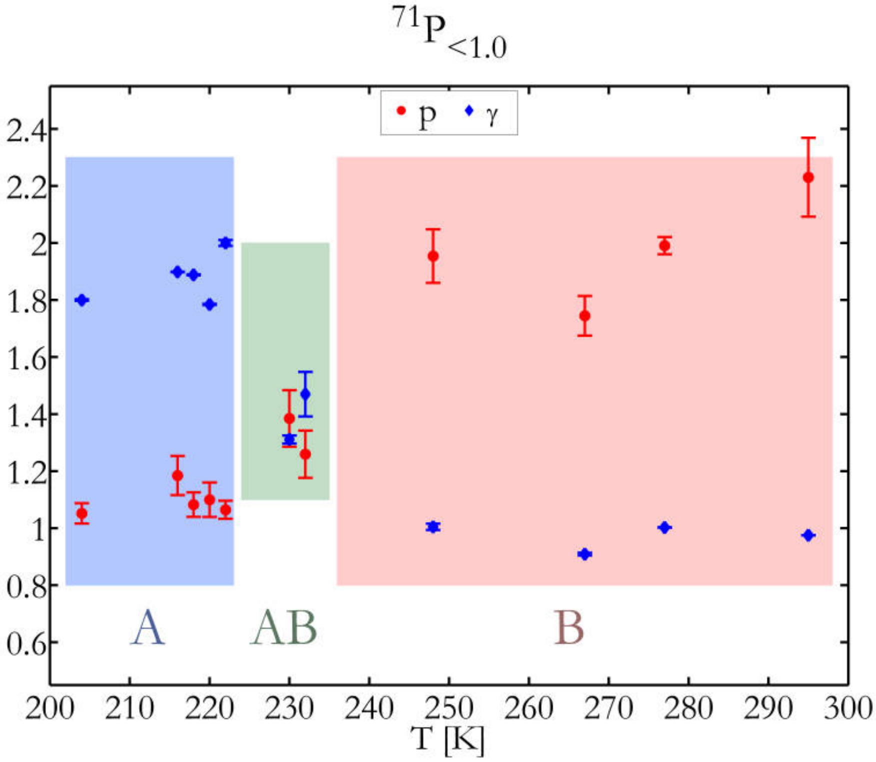

Figure 8.12: Temperature dependence of q-averaged values γ and p of $^{71}P_{<1.0}$.

below 230 K, the obtained viscosity appears lower than expected, indicating a breakdown of free diffusive particle dynamics.

The exponent p and the q-averaged γ-values are shown in Figure 8.12 as function of temperature for $^{71}P_{<1.0}$. The temperature region marked with B, defined by $1.7 < p < 2.3$ ($p \approx 2$) and $\gamma < 1.3$ ($\Rightarrow \gamma < p$) characterizes free diffusion particle dynamics. The temperature region marked with A, defined by $\gamma > 1.5$ and $p < 1.5$ ($\Rightarrow \gamma > p$) characterizes hyper-diffusive and correlated particle dynamics. Altogether, upon supercooling PPG from 295 K to 204 K the particle dynamics changes from free diffusion (B regime) to hyper-diffusion and correlated particle motion (A regime). A more complex dynamics is observed in an intermediate temperature regime around $T = 230$ K $\approx 1.12\ T_g$, which is marked as AB regime. This regime is characterized by the absence of a clear relationship between p and γ. In the following, this differentiation of the dynamical regimes is used to discuss the results of the other samples which will be compared to clarify to what extent the observed change of the particle dynamics is related to the solvent properties. The values of p and γ as function of temperature are obtained analogous to this analysis for the other samples.

Figure 8.13 shows theses values for $^{71}P_{<0.5}$ at temperatures between 223 K $\leq T \leq$ 290 K.[11] Although these results does not cover the same temperature range, the tem-

---

[11] The temperature range was selected due to τ_c in conformity with the VFT law.

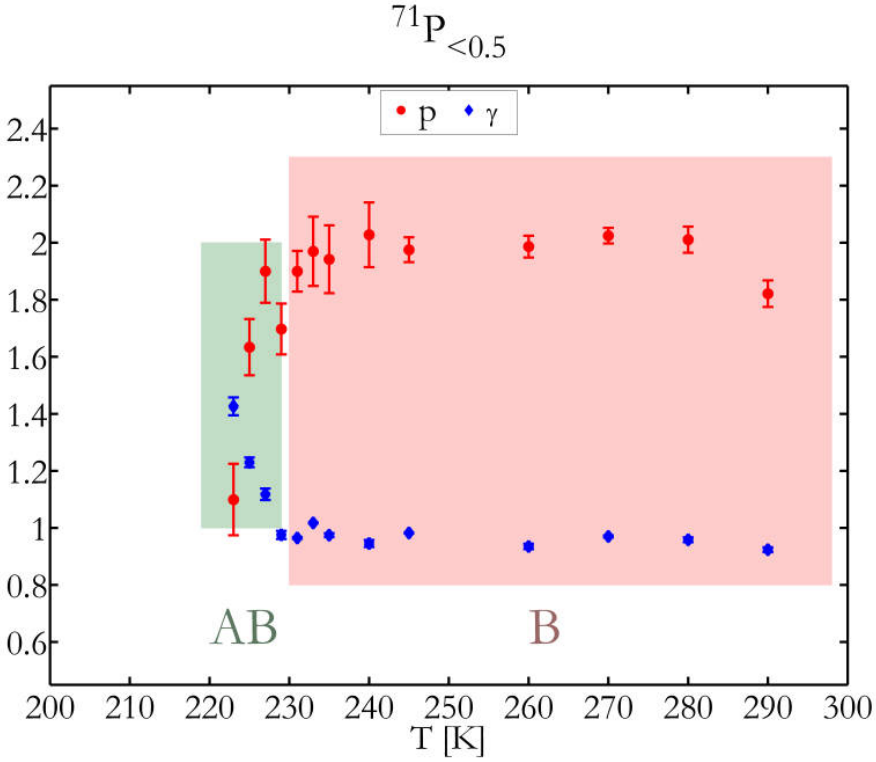

Figure 8.13: Temperature dependence of q-averaged values γ and p of $^{71}P_{<0.5}$.

perature dependence of p and γ is consistent with the change of the particle dynamics found for $^{71}P_{<1.0}$. Here, the dynamics of the B regime is found in the same temperature range (230 K $\leq T \leq$ 290 K), while the temperature range corresponding to the dynamics of the AB regime seems to be shifted to slightly lower temperatures. Due to the limitation of the temperature range, no implications on the existence of an A regime can be made. In addition, it seems that both the decrease of p and the increase of γ with decreasing temperature are continuous in the AB regime when probing smaller temperature intervals. Moreover, the AB regime appears to be smaller indicating a sharper change of the dynamics around $T = 222$ K. However, due to a poor temperature resolution, the influence of the tracer properties to the characteristics of the AB regime could not be classified by the measurements of the other samples. The results of the dilute PPG samples $^{27}P_{1.3}$, $^{18}P_{<1.0}$ and $^{18}P_{<0.5}$ are shown in appendix A.6. They are in agreement with a change of the dynamics above T_g found for $^{71}P_{<1.0}$, although the referring temperatures varies slightly.

The values of p and γ as function of temperature are shown in Figures 8.14 and 8.15 for the dilute samples $^{82}D_{2.2}$ and $^{53}D_{1.5}$. By applying the criteria of the dynamical regimes A, B and AB defined above, an analogous change of the particle dynamics from free diffusion to hyper-diffusion in DBP is found below $T \approx 200$ K $= 1.08\ T_g$. Similar to the results of the PPG samples the temperature range where the change in the dynamics occurs, apparently varies with the particle size. Notably, the γ-values of the A regime obtained

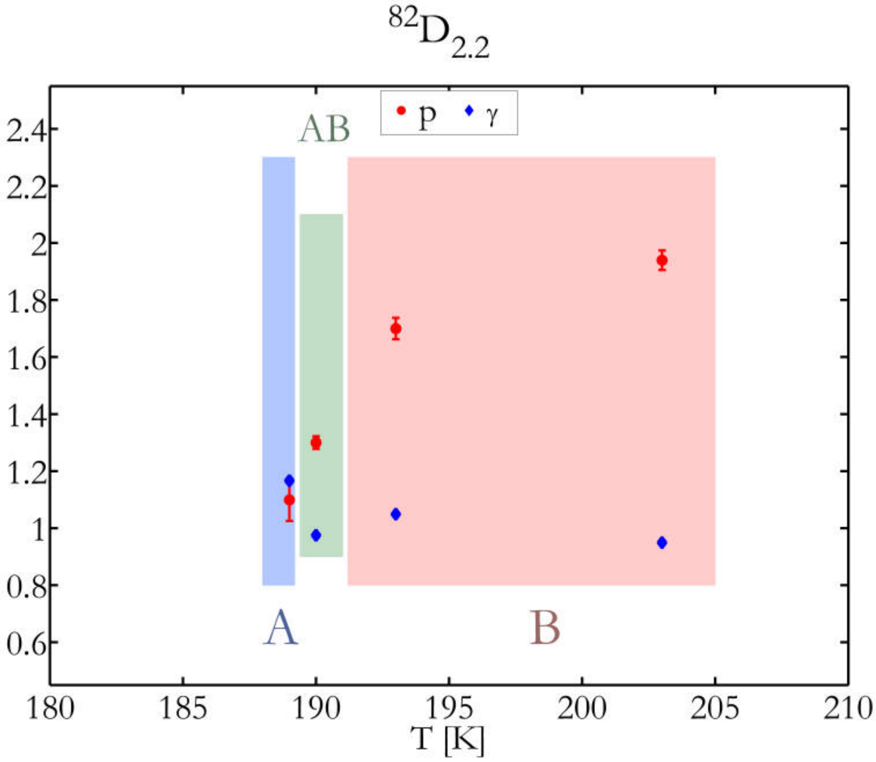

Figure 8.14: Temperature dependence of γ and p for $^{82}\mathrm{D}_{2.2}$.

for the DBP samples are in general smaller than those of the PPG samples.

In summary, the results of the dilute samples $^{71}\mathrm{P}_{<1.0}$, $^{71}\mathrm{P}_{<0.5}$, $^{27}\mathrm{P}_{1.3}$, $^{18}\mathrm{P}_{<1.0}$, $^{18}\mathrm{P}_{<0.5}$, $^{82}\mathrm{D}_{2.2}$ and $^{53}\mathrm{D}_{1.5}$ support an interpretation where the particle dynamics changes at temperatures well above the glass transition temperature of the solvents PPG and DBP ($1.08 - 1.12\ T_{\mathrm{g}}$). The results obtained for $^{71}\mathrm{P}_{<0.5}$ indicate a continuous change of p and γ. In addition, the A regime γ-values obtained for particles in PPG were in general larger as found for particles in DBP. While the results of the dilute samples provide consistent characteristics[12] of the B regime, they differ for the characteristics of the intermediate regime AB and A. However, the differences seem to have no distinct connection to the particle size. Since the inter-particle interactions are weak, the characteristics of the change in the particle dynamics has to be related to changes within the solvents. In this context, the characterization of the A regime dynamics with the feature of $\gamma > 1$, connected to correlated motion, seems to be the key to understand these changes.

---

[12] Here, characteristics of the regime include the temperature limits of the temperature range and the upper and lower limits of p and γ.

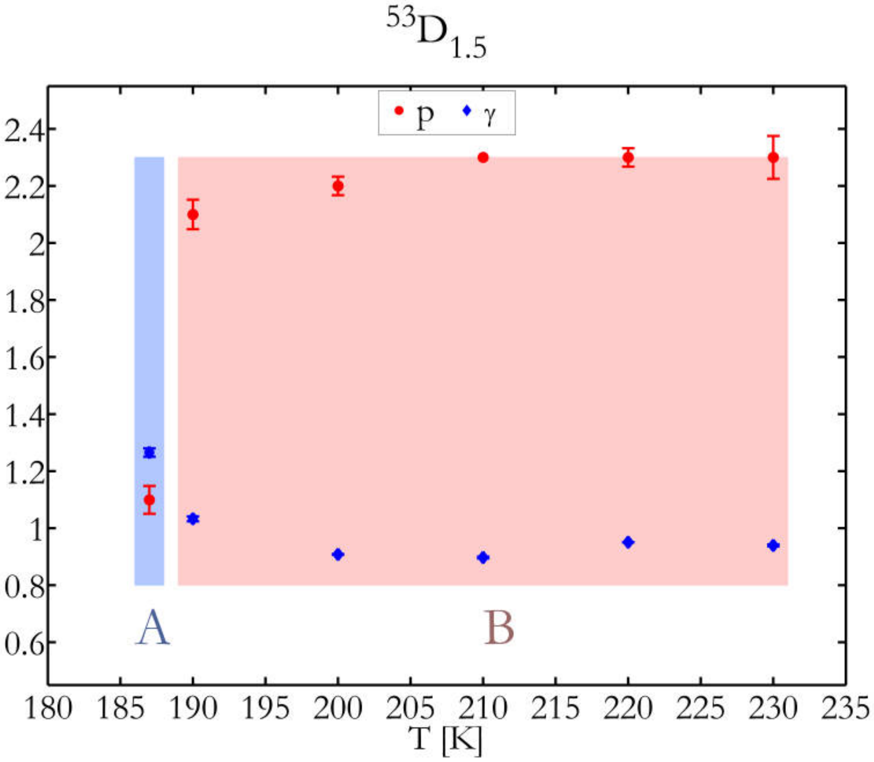

Figure 8.15: Temperature dependence of γ and p for $^{53}D_{1.5}$.

8.2.2 Concentrated samples

Since the interpretation of $\gamma > 1$ towards correlated motion can only be attributed to the solvent if inter-particle interactions as origin can be excluded[13], concentrated colloidal suspensions were investigated to verify such an influence experimentally. In the following, the results of the concentrated samples $^{27}P_{8.4}$, $^{27}P_{3.8}$, $^{27}P_{3.3}$, $^{53}D_{16.5}$, $^{53}D_{8.8}$, $^{53}D_{3.8}$ and $^{82}D_{6.2}$ are discussed. p and γ-values of these samples were obtained analogous to the analysis of g_2 for $^{71}P_{<1.0}$. In addition, the temperature regime where $\tau_c\,(T)$ does not follow the VFT law was excluded. Due to the use of a faster and a slower detector, the temperature ranges differ form sample to sample. The p and γ results as function of temperature are shown in Figures 8.16-8.18 for $^{27}P_{8.4}$, $^{53}D_{16.5}$ and $^{82}D_{6.2}$.[14]

Again, the terms for the dynamical regimes (A, AB and B) defined in the previous section were used. In contrast to the dilute samples, p-values smaller than two ($p < 2$) were already found at higher temperatures for the concentrated samples $^{27}P_{8.4}$ and $^{53}D_{16.5}$. Thus, one rather finds characteristics typical for the AB regime at temperatures where the B regime was found for the dilute samples. Also for the concentrated samples, a change from the B regime to the A regime dynamics was found (see Figure 8.18). This change occurs in the same temperature regime known for the dilute samples but at slightly higher

---

[13] Inter-particle interactions can force neighboring particles to move cooperatively.

[14] The results of the other concentrated samples are provided in appendix A.7.

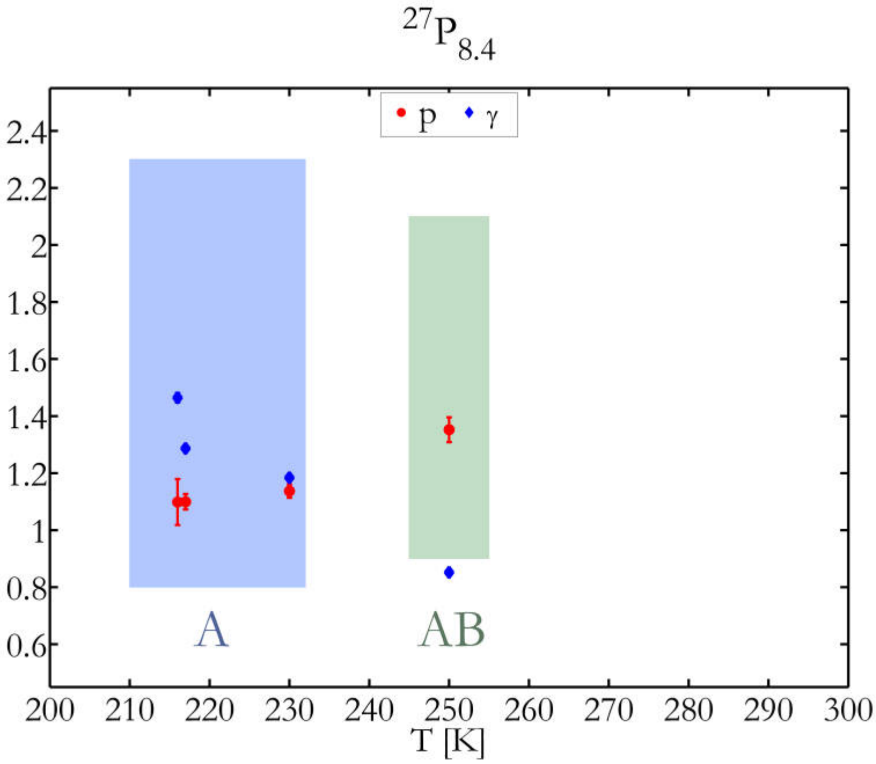

Figure 8.16: Temperature dependence of γ and p for $^{27}P_{8.4}$.

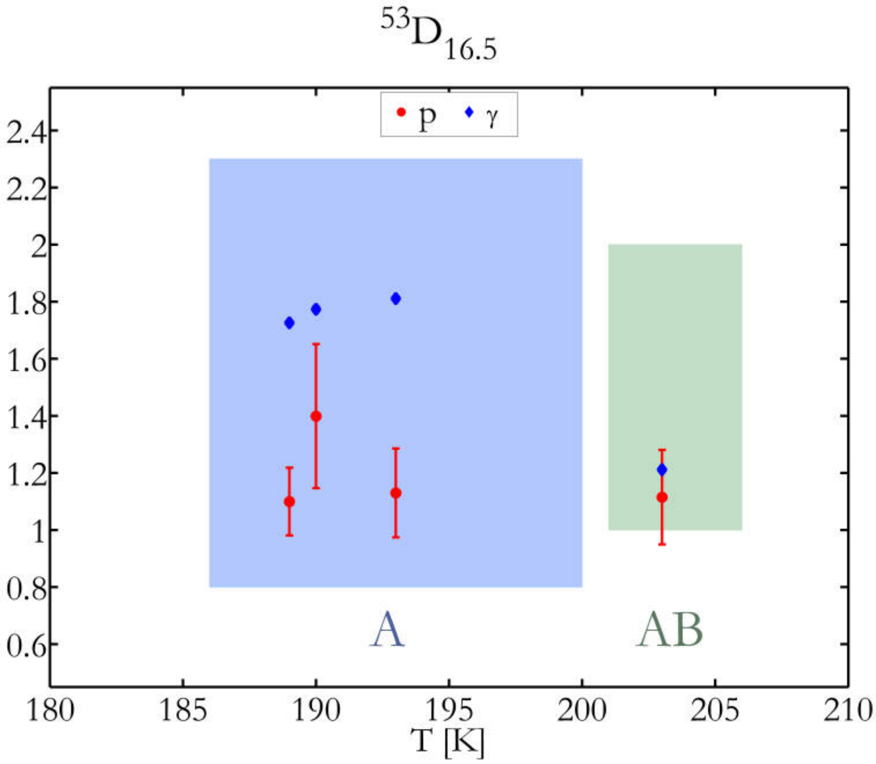

Figure 8.17: Temperature dependence of γ and p for $^{53}D_{16.5}$.

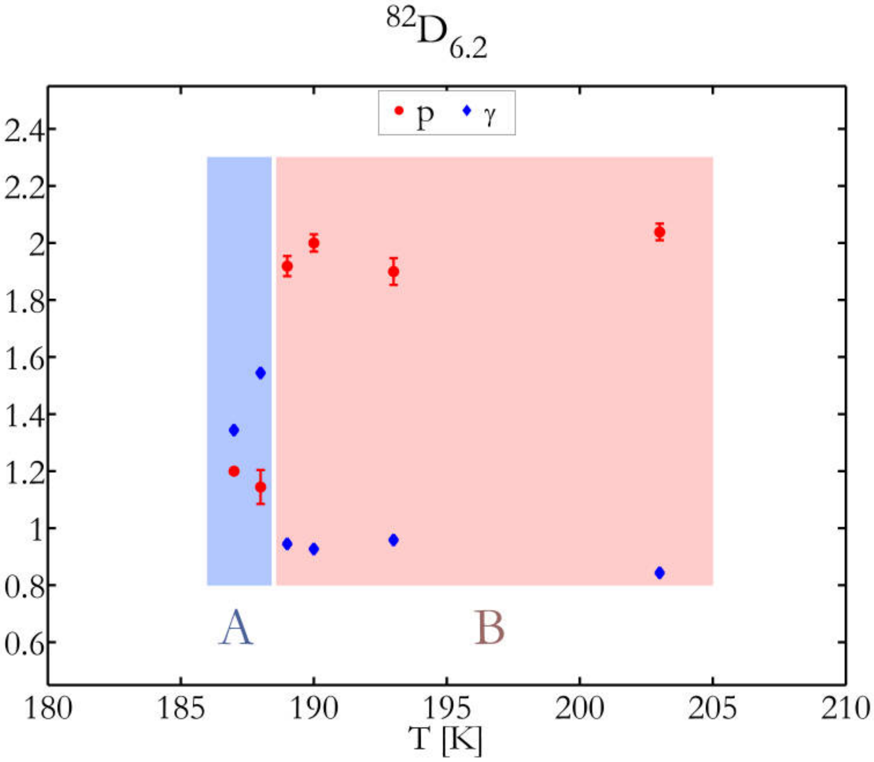

Figure 8.18: Temperature dependence of γ and p for $^{82}\mathrm{D}_{6.2}$.

temperatures. The other concentrated samples (see appendix A.7) indicate also such a change but the temperature dependence is much more complex due to the convolution of inter-particle and particle-solvent interactions.[15] A general finding is that $\gamma_{\max}$ is larger and the change of the dynamics occurs at higher temperatures for PPG samples when compared to DBP samples. The fact that a transition from the B to the A dynamics is found in both, dilute and concentrated systems, indicates that this transition is caused by changes in the particle-solvent interactions. Since the particle properties do not change with the temperature, a scenario involving changing solvent properties at $T \approx 1.08 - 1.12\ T_{\mathrm{g}}$ as indicated by the results of the dilute samples is very probable.

The temperature and q-dependence of γ for the concentrated samples was found to be similar to the dilute samples. Here, the q-averaged γ increases in the A regime with decreasing temperature. In addition, the γ-values of the concentrated samples also exhibit a slight q-dependence (AB regime) which vanishes at lower temperatures (A regime). An additional feature in the q-dependence of γ was found for the most concentrated sample $^{53}\mathrm{D}_{16.5}$. As shown in Figure 8.19, $\gamma(q)$ exhibits a small peak in the q-region where the static structure factor peaks ($q_{\max} \approx 0.043\ \mathrm{nm}^{-1}$). This was observed only for temperatures

---

[15] The complex results of the concentrated samples suggest that the incorporation of inter-particle interactions causes a much more complex realization of dynamical regimes as can be described by $p(T)$ and $\gamma(T)$.

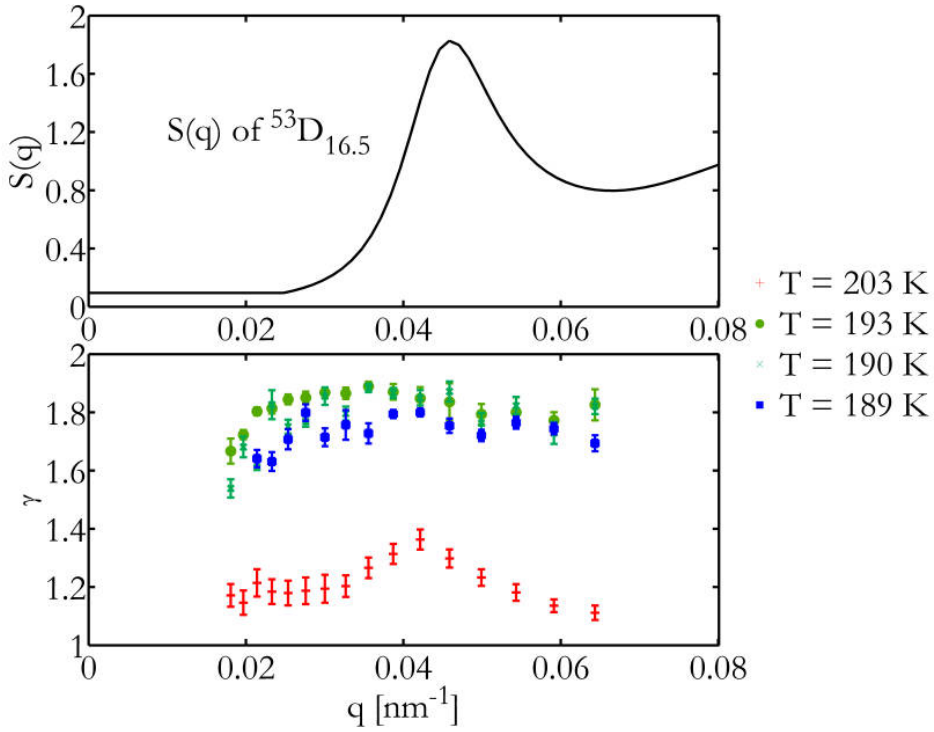

Figure 8.19: Top: $S\,(q)$. Bottom: $\gamma\,(q)$ obtained from the fits of equation 8.1 to the data of $^{53}\mathrm{D}_{16.5}$.

$T \geq 200$ K (AB regime) while the peak disappears for temperatures $T < 200$ K (A regime). However, a clear correlation between $S\,(q)$ and the γ-values could not be established.

Another feature of concentrated samples is the influence of direct particle-interactions characterized via the static structure factor $S\,(q)$ on the decay rates Γ. As a result of the direct interactions, the particle dynamics is slowed down on length scales corresponding to next neighbor distances (de Gennes narrowing). Thus, in the vicinity of the static structure factor peak at q_{max}, $\Gamma\,(q)$ is characterized by $\Gamma_{\mathrm{measured}}\,(q) = \frac{\Gamma_{\mathrm{particles}}(q)}{S(q)}$. This leads to a small dip in the dispersion curve around q_{max} shown in Figure 8.20(a) for $^{27}\mathrm{P}_{8.4}$ at $T = 250$ K ($q_{\mathrm{max}} \approx 0.078\ \mathrm{nm}^{-1}$). A similar behavior was found for the concentrated samples[16] $^{82}\mathrm{D}_{6.2}$ and $^{53}\mathrm{D}_{16.5}$ in the B and AB regimes, respectively, while at the lower temperatures (A regime) this effect seems to disappear (Figure 8.20(b)).

In summary, no distinct relation between $S\,(q)$ and γ was found, except at very high particle volume fractions ($\phi = 16.5$ vol.%) where $\gamma\,(q)$ is peaking in the q-region of the static structure factor peak. This supports the conjecture that the increase of γ found for the dilute samples around $T \approx 1.08 - 1.12\ T_{\mathrm{g}}$ is only related to a change of solvent properties.

---

[16] The influence of the static structure factor was not visible for samples with volume fractions below $\phi < 6$ vol.%.

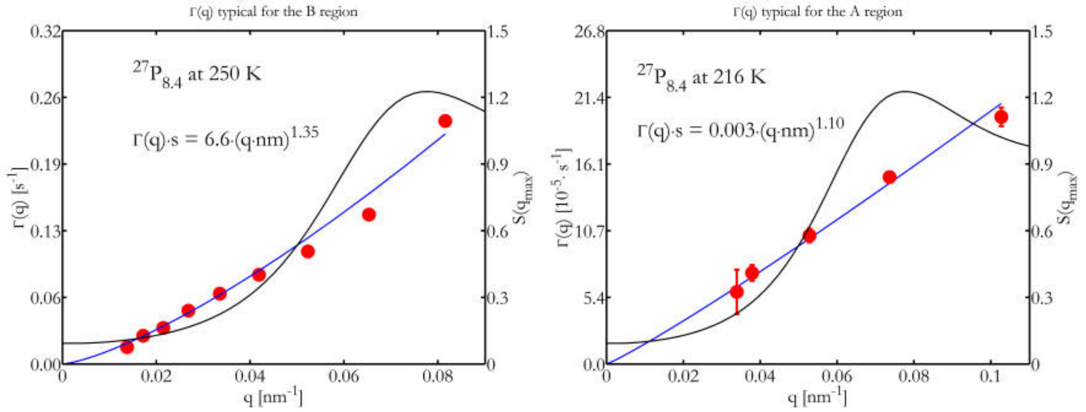

(a) $\Gamma(q)$ for $^{27}\mathrm{P}_{8.4}$ at $T = 250\ K$.

(b) $\Gamma(q)$ for $^{27}\mathrm{P}_{8.4}$ at $T = 216\ K$.

Figure 8.20: $\Gamma(q)$ for $^{27}\mathrm{P}_{8.4}$ at (a) $T = 250\ K$ and (b) $T = 216\ K$. The blue curves are fits with a power law to the data. The static structure factor of $^{27}\mathrm{P}_{8.4}$ is plotted as black line.

8.3 Interpretation of the results

The evaluation of g_2 revealed a transition from a simple exponential ($\gamma \approx 1$) towards a compressed exponential ($\gamma > 1$) decay behavior.[17] Simultaneously, a change of the dynamics from free ($T > 1.12\ T_\mathrm{g}$, B regime) towards hyper diffusive motion ($T < 1.08\ T_\mathrm{g}$, A regime) occurs. The increase of γ above unity indicates that the width of the distribution $G(\tau/\tau_\mathrm{c})$ of the relaxation times τ decreases and becomes a Gaussian at temperatures near T_g.[18] This suggests an increased uniformity of the solvent molecular dynamics which can be a sign of correlated motion. This observation is accompanied by an enhanced visibility of a second g_2-decay indicating that slower dynamical processes are also present in the solvent. A macroscopic flow of the solvent as explanation of these observations was excluded by comparing the analysis results with vertically and horizontally masked scattering patterns. Thus, one may speculate that both observations may be understandable within an interpretation in which at short time scales correlated motion of molecules becomes dominant and the molecular dynamics becomes increasingly heterogeneous with decreasing temperature. This interpretation is supported by the results of the instantaneous intensity autocorrelation function C_I.

The deviation of $\tau(T)$ from the VFT behavior in the A regime implies a temperature

---

[17] $\gamma > 1$ was found in a number of experiments as common feature of jammed (Cipelletti, L. et al. (2000). *Phys. Rev. Lett.* **84**, 2275; Cipelletti, L. et al. (2003). *Farad. Discuss.* **123**, 237), non-diffusive (Kaloun, S. et al. (2005). *Phys. Rev. E* **72**, 011403; Robert, A. et al. (2006). *Europhys. Lett.* **75**, 764; Caronna, C. et al. (2008). *Phys. Rev. Lett.* **100**, 055702) or non-equilibrium aging systems (Leitner, M. et al. (2012). *Phys. Rev. B* **86**, 064202; Ruta, B. et al. (2013). *J. Chem. Phys.* **138**, 054508) and is suggested to characterize a regime of elastic relaxation in media with internal stresses (Bouchaud, J.-P. and Pitard, E. (2001). *Eur. Phys. J.* **E6**, 231).

[18] Hansen, E. W. et al. (2013). *Macromolecular Chemistry and Physics* **214**, 844.

independent dynamics of the molecules with decreasing nominal temperature. This is in contradiction to expectations based on the increase of the solvent viscosity which is experimentally verified. This could on the one hand, be a sign of beam induced heating which could play a crucial role especially at low temperatures near T_g where the heat capacity and conductivity are reduced[19]. Although, this effect seems to be weak[20], it cannot be excluded for data at the lowest temperatures.[21] On the other hand, this observation could be interpreted as an indication that the fastest dynamical process in the solvent becomes temperature independent in the A regime.

Further observations indicated that there may be a connection between the time scales of the observed dynamics and the involved length scales. For example, de Gennes narrowing which was found to be present in the AB and B regime vanishes in the A regime. This could be an indication that the dynamics in the A regime becomes independent from structural rearrangements of molecules. Furthermore, γ increases with decreasing q in the AB regime while this distinct q-dependence also vanishes in the A regime. If one were to speculate that the dynamics becomes more heterogeneous in the AB regime until it becomes temperature independent in the A regime, one way to argue is that this may be related to an increasing length of dynamical correlations with deceasing temperature (AB regime) that become static or exceed the probed length scales in the A regime. Within such a picture the tracer particle size and mean particle distances could affect the temperature range where the A regime can be found which would explain the observed differences, in particular for the concentrated samples.

8.4 The instantaneous intensity correlation function

In order to investigate heterogeneous dynamics, the instantaneous intensity correlation function C_I was determined from a time series of scattering patterns (equation 4.35). This allows the evaluation of the g_2 time evolution and can be used to obtain the dynamic susceptibility χ_T. As described in section 4.2.3, C_I can only be analyzed for q-values with sufficient signal-to-noise ratio (SNR). In addition, conclusions regarding the temporal variance are reliable only when the characteristic time τ_c is much smaller than the experimental time t_e.[22] These constraints were fulfilled only for samples with larger tracer particles at temperatures well above T_g were $t_\mathrm{e} \gg \tau_\mathrm{c}$ could be achieved, for example in the

---

[19] Angell, C. A. (2011). “Glassy, Amorphous and Nano-Crystalline Materials.” 8th Edition. Springer, Amsterdam, Netherlands, 21ff.

[20] For details see appendix A.5.

[21] Thus, for temperatures very close to T_g the interpretation of the data in terms of dynamical heterogeneities must be regarded with caution. In fact, for temperatures close to or below T_g the requirement of $\tau_\mathrm{c} \ll t_\mathrm{e}$ to interpret the dynamic susceptibility χ_T could not be fulfilled.

[22] Consistent results were achieved when t_e was two orders of magnitude larger than τ_c.

case of the samples $^{71}\mathrm{P}_{<1.0}$, $^{71}\mathrm{P}_{<0.5}$, $^{82}\mathrm{D}_{2.2}$ and $^{82}\mathrm{D}_{6.2}$.

In the following, the analysis of C_{I} will be discussed in detail for $^{71}\mathrm{P}_{<1.0}$ at $T = 222$ K. The results of C_{I} are shown in Figure 8.21 for q-values which could be evaluated. The narrowing of $C_{\mathrm{I}}\left(q\right)$ indicates that the corresponding relaxation time $\tau_{\mathrm{c}}\left(q\right)$ decreases with increasing q. In addition, C_{I} exhibits a fluctuation which seems to be more pronounced at small q indicating a distinct time dependence of τ_{c}.

The dynamic susceptibility χ_{T} is given by the variance of C_{I} that is shown for $^{71}\mathrm{P}_{<1.0}$ at $T = 222$ K in Figure 8.22. Typically, χ_{T} exhibits a peak around the time $t = \tau^* \approx \frac{\tau_{\mathrm{c}}^*}{\mathrm{e}}$ that corresponds to the inflection point of g_2. Thus, the peak of χ_{T} quantifies temporal fluctuations of the relaxation time $\left(\chi_{\mathrm{T_{max}}} \propto \frac{\Delta\tau_{\mathrm{c}}}{\tau_{\mathrm{c}}}\right)$ and is a measure for temporally heterogeneous dynamics. Since the measurable q-range changes with temperature, $\chi^*_{\mathrm{T_{max}}} = \chi_{\mathrm{T_{max}}} \cdot \left(\frac{q}{q_0}\right)^p$ (section 4.2.3) is used to compare the results of $\chi_{\mathrm{T_{max}}}$ q-independently. This quantity is shown for $^{71}\mathrm{P}_{<1.0}$ at $T = 222$ K in Figure 8.23, where the peak heights of $\chi^*_{\mathrm{T}}\left(\tau^*_{\mathrm{c}}\right)$ are almost q-independent (Figure 8.24).

The q-averaged values of $\chi^*_{\mathrm{T_{max}}}$ as function of temperature are shown in Figure 8.25 for $^{71}\mathrm{P}_{<1.0}$ and $^{71}\mathrm{P}_{<0.5}$. An intense increase of the peak height around $T = 230$ K is clearly visible for both samples. This suggests that the dynamics becomes increasingly temporal heterogeneous at temperatures below $T = 1.12\ T_{\mathrm{g}}$ for PPG.[23]

Similar results were found for $^{82}\mathrm{D}_{2.2}$ and $^{82}\mathrm{D}_{6.2}$ (Figure 8.26), where the increase of $\chi^*_{\mathrm{T_{max}}}$ was observed in the temperature region around $T = 200$ K. This implies an increase of temporal heterogeneous dynamics for DBP at temperatures between $1.04 - 1.08\ T_{\mathrm{g}}$.

In summary, the results of the C_{I} evaluation support the interpretation of increasing dynamical heterogeneities with decreasing temperature in the AB region for both investigated glass formers DBP and PPG.

---

[23] Cipelletti, L. et al. (2003). *Farad. Discuss.* **123**, 237.

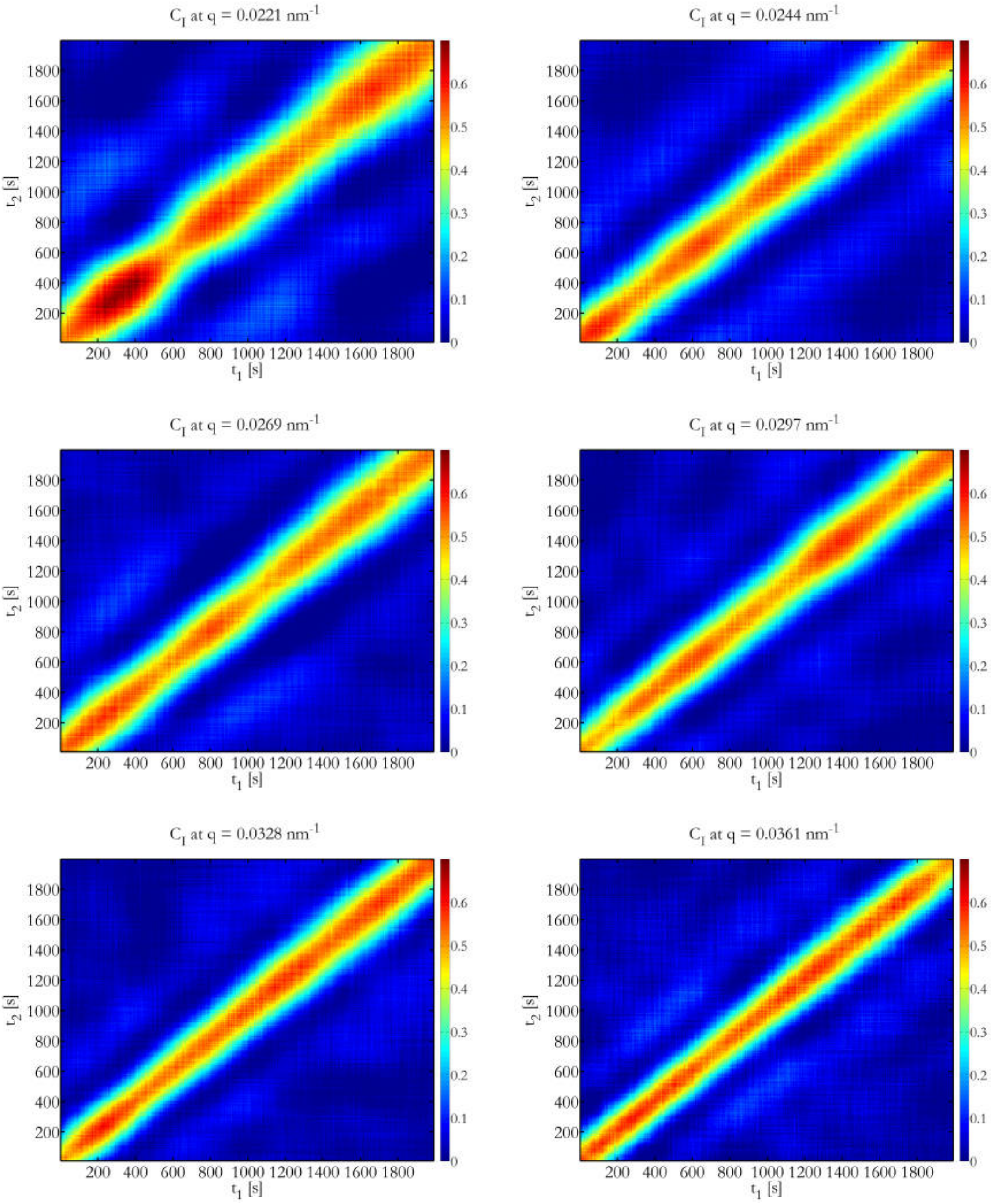

Figure 8.21: C_I for $^{71}\mathrm{P}_{<1.0}$ at $T = 222$ K, shown for q-values with the best SNR. The color illustrates the decay of $\frac{1}{\beta}\left[g_2 - 1\right]$ from 0.7 (red) to zero (blue).

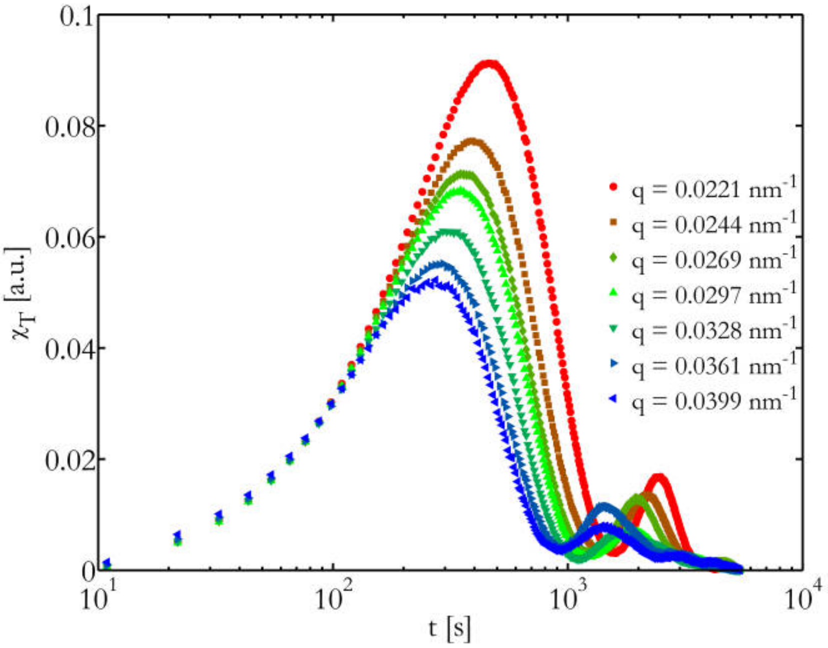

Figure 8.22: χ_{T} for $^{71}\mathrm{P}_{<1.0}$ at $T = 222$ K for q-values with the best SNR.

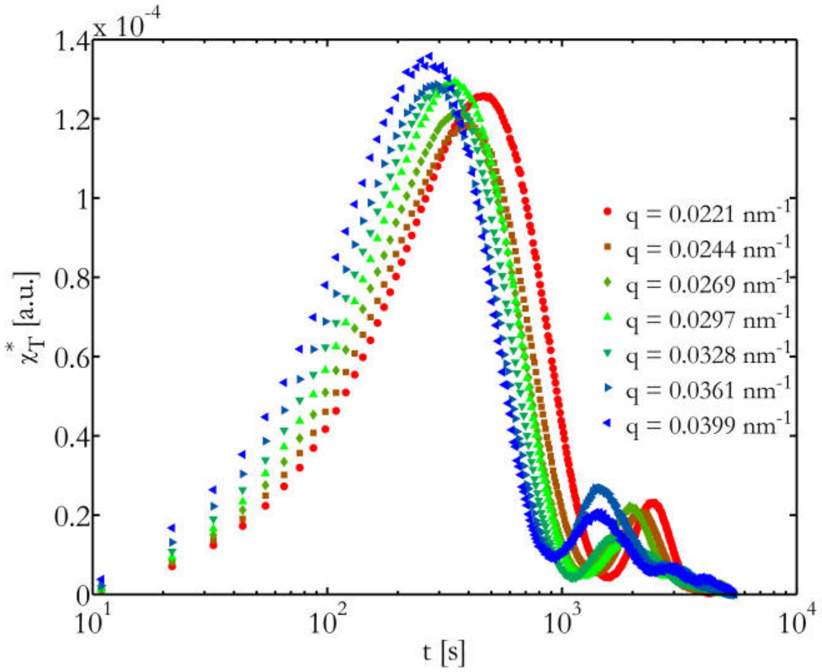

Figure 8.23: χ^*_{T} for $^{71}\mathrm{P}_{<1.0}$ at $T = 222$ K for q-values with the best SNR.

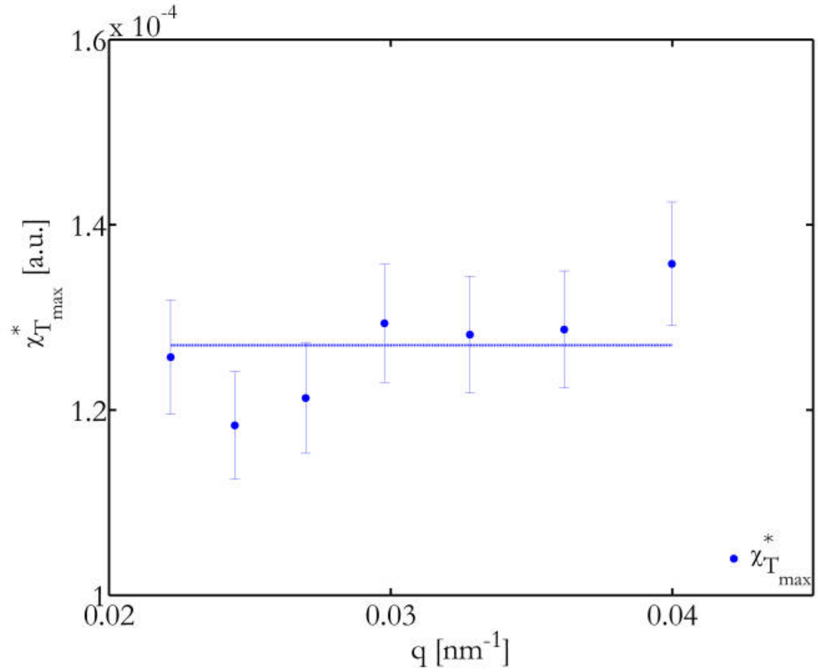

Figure 8.24: $\chi^*_{\mathrm{T_{max}}}$ for $^{71}\mathrm{P}_{<1.0}$ at $T = 222$ K.

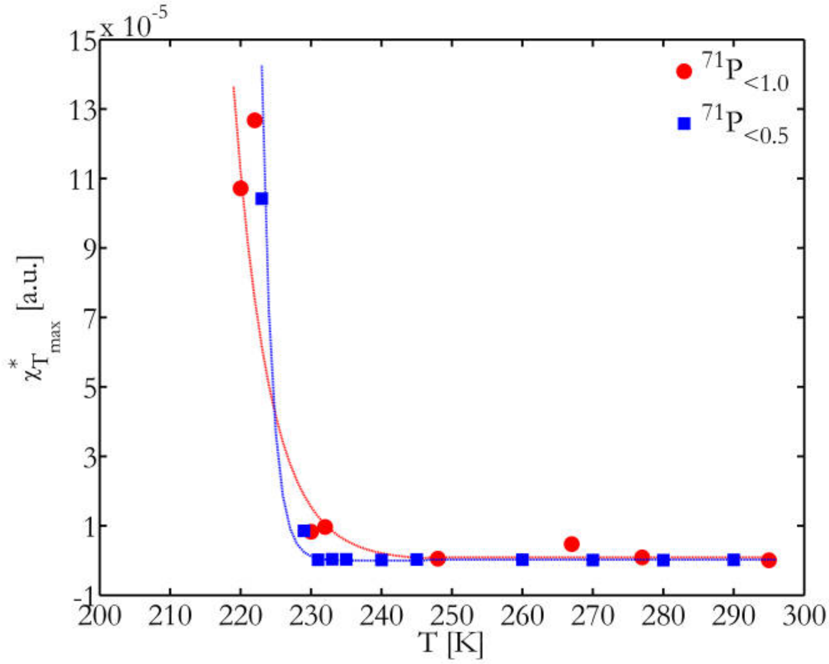

Figure 8.25: $\chi^*_{\mathrm{T_{max}}}$ for $^{71}\mathrm{P}_{<1.0}$ and $^{71}\mathrm{P}_{<0.5}$.

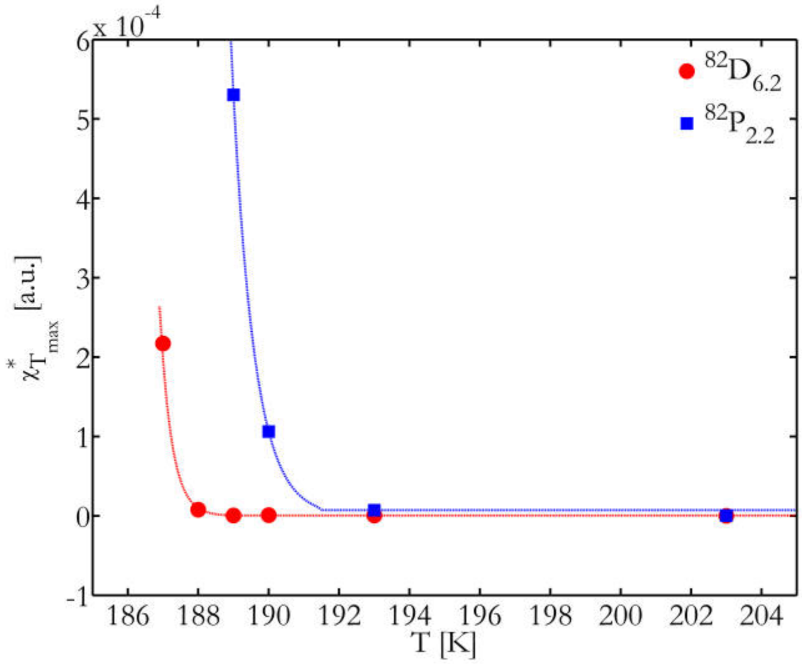

Figure 8.26: $\chi^*_{\mathrm{T_{max}}}$ for $^{82}\mathrm{D}_{6.2}$ and $^{82}\mathrm{D}_{2.2}$.

9 Summary

Weakly-charged silica nano-particles were synthesized using different versions of the Stöber synthesis. The particles were used to create a series of colloidal suspensions with the glass formers polypropylene glycol (PPG) and dibutyl phthalate (DBP). The suspensions were prepared with different particle batches at volume fractions ϕ in the range of $0.3-16.5$ vol.%. The static and dynamic behavior of these colloidal suspensions were studied via X-ray scattering methods.

The time averaged small angle X-ray scattering (SAXS) data on dilute suspension were analyzed, yielding mean particle radii R_p between 18 nm − 83 nm at polydispersities $\tilde{P}$ between 5.2 % − 13.2 %. It was found that $\tilde{P}$ is smaller for particles obtained in a synthesis with seed particles or in a sysntesis of larger particles.

Direct inter-particle interactions were found at higher concentrations for samples with volume fractions of $\phi > 1.3$ vol.% where an ordering of the particles, characterized by the static structure factor $S\left(q\right)$, was observed. The height of the static structure factor peak increases and its position shifts to larger wavevector transfers q with increasing volume fraction, which refects the decrease of inter-particle distances. The measured static structure factors $S\left(q\right)$ were modeled using the rescaled mean spherical approximation (RMSA) which provided independent information on the volume fraction ϕ and the effective charge Z_eff of the silica particles. The computed RMSA structure factors were in good agreement with the measured static structure factors and typically characterizing the first and second maximum of $S\left(q\right)$. The obtained values for the particle volume fraction were in good agreement with the nominal volume fractions of the samples. The effective charge of the particles was found to increase slighly with increasing particle radius. Furthermore, the particle form factors and static structure factors were found to be temperature independent. Beam damage thresholds were established to ensure that the particle dynamics is not affected by the beam during the measurments.

The dynamics of silica nano-particles suspended in the glass formers PPG and DBP were studied via X-ray photon correlation spectroscopy (XPCS). The measurements were performed at different temperatures while supercooling the solvents from 1.3 T_g to T_g. The beam size and exposure time were optimized to allow the evaluation of the normalized intensity autocorrelation function g_2 and the instantaneous intensity correlation function

C_I, while excluding beam damage effects for long experimental times. Although the experiments were performed in the multi-speckle scheme at the lower dose limit of the g_2 and C_I evaluation, X-rays seem to influence the dynamics of the particles at temperatures very close and below T_g.

The q-dependence of the g_2-decay indicate a change of the particle dynamics with decreasing temperature for both investigated glass formers. The dynamics changes from diffusive to hyper-diffusive dynamics around $T = 1.08 - 1.12\ T_\mathrm{g}$. In addition, the decay of g_2 becomes more compressed in the hyper-diffusive regime, which is connected to an increasingly correlated particle motion. It could be verified that both, the transition of the dynamics and the increase of correlated motion, are related to changes of the solvents. Moreover, the evaluation of C_I indicate an increase of temporally heterogeneous dynamics at the onset of hyper-diffusive dynamics. The findings are in agreement with an interpretation of correlated motion domains in the solvent which grow in size with decreasing temperature and exceed the dimensions of probed particle distances around $T = 1.08 - 1.12\ T_\mathrm{g}$.

In this context, the present study extends the findings of a similar study[1] on dilute suspensions of colloidal particles ($R_\mathrm{P} = 250$ nm) in propanediol where a similar change of the particle dynamics was found at 1.26 T_g independent of concentration and particle size. It was speculated that the increasingly heterogeneous solvent potential energy landscape (PEL) predicted by the Potential Energy Landscape Approach (PELA) for temperatures below 1.2 T_g can explain heterogeneous dynamics. It was furthermore speculated that other properties of the supercooled solvent might be involved in the change of the dynamics, e.g. , viscoelastic phase separation[2] or stress-relaxation processes. This study supports the finding that the transition temperature at which the change of the dynamics occurs differs depending on the specific glass former and eventually other parameters. Due to the fact that the results are fragmentary regarding the temperature and the momentum transfer regimes, a quantitative description of the hyper-diffusive regime remains speculative. Thus, the study could not provide further conclusive insights in the observed dynamic behavior but rather confirms our present knowledge.

A combination of XPCS with contemporaneous determination of the viscoelastic solvent properties, for example rheology[3], could be an experimental approach to extend our findings and may allow a conclusion on the origin of the hyper-diffusive regime.

---

[1] Caronna, C. et al. (2008). *Phys. Rev. Lett.* **100**, 055702.

[2] Tanaka, H. (2000). *J. Phys.: Condens. Matter* **12**, 207.

[3] Denisov, D. et al. (2013). *SCIENTIFIC REPORTS* **3**, 1631.

Appendix

A.1 Multiple scattering

The outlined scattering theory (chapter 4) is based on the assumption that a photon is scattered only once before being detected. This is the basis of equation 4.2 which relates the scattered intensity $I(q)$ to the wave vector transfer q. Thus, the single scattering limit is crucial for the analysis. It is characterized by

$$d \ll l_{\mathrm{free}},$$

where d denotes the sample thickness and l_{free} is the mean distance between two scattering events. For a sample with number density ρ_{P}, the free path length l_{free} is given by

$$l_{\mathrm{free}} = \frac{1}{\rho_{\mathrm{P}} \sigma_{\mathrm{P}}},$$

where σ_{P} is the scattering cross section of the particles. Assuming that the scatterers are colloidal particles of radius R_{P}, refractive index n_{P}, suspended in a medium with refractive index n_0, their scattering cross section for visible light ($\lambda = 390 - 700$ nm) is given by[1]

$$\sigma_{\mathrm{P}} = \pi \cdot R_{\mathrm{P}}^2 \left| \frac{n_{\mathrm{P}}}{n_0} - 1 \right| .$$

Hence, the limit of single scattering is realized either in the dilute case ($\rho_{\mathrm{P}} \to 0$), or in the case of index-matching ($n_{\mathrm{P}} = n_0$). This reveals a severe limitation to the investigation of turbid materials in the optical wavelength regime, as the differences in the refractive index can be large. In contrast, in the X-ray wavelength regime the refractive index is very close to unity for all materials. For example, the single scattering limit for a solution of silica particles in dibutyl-phthalate at a volume fraction $\phi = 10$ vol.% $\left(\rho_{\mathrm{P}} \approx (2.5 \cdot R_{\mathrm{P}})^{-3}\right)$ for visible light ($\lambda = 589$ nm) is given by $l_{\mathrm{free}} \approx 100 \cdot R_{\mathrm{P}}$. That corresponds to a sample thickness of $d \ll 0.1\mu$m, which is too small for the investigation of the dynamics in the bulk. For X-rays ($\lambda = 0.15$ nm) one obtains $l_{\mathrm{free}} \approx 5$ mm which is much larger than typical sample dimensions.

---

[1] van de Hulst, H. C. (1957). *Light Scattering by Small Particles.* Wiley, Hoboken, USA.

A.2 Hydrodynamic functions

The hydrodynamic function H describes the influence to the particle dynamics by the interactions with the dispersion medium. It is expressed by

$$H\left(q\right)=\left\langle \frac{k_{\mathrm{B}}T}{N\cdot D_{0}}\sum_{n,m=1}^{N}\hat{q}\cdot\breve{\mu}_{n,m}\left(\hat{R}^{N}\right)\hat{q}\cdot\exp\left(i\vec{q}\cdot\left[\vec{R}_{n}\left(0\right)-\vec{R}_{m}\left(\tau\right)\right]\right)\right\rangle, \tag{A.1}$$

where $\hat{q}$ is the unit vector in the direction of $\vec{q}$. $\breve{\mu}_{n,m}\left(\hat{R}^{N}\right)$ denotes a translational mobility tensor which relates the hydrodynamic force on a particle n to the translational velocity of a particle m depending on the instantaneous positions $\hat{R}^{N}$ of N particles and hydrodynamic boundary conditions. This expression arose from the work of Beenakker and Mazur.[2] They developed the renormalized concentration fluctuation expansion method to derive H for disordered systems at large volume fractions ϕ where higher-order hydrodynamic interactions are important. The method is based on a partial resummation of the many-body hydrodynamic interaction contributions, allowing for separation of the hydrodynamic function into a self-part H_{s} depending on the pair distribution function $g\left(r\right)$ and a distinct q-dependent part H_{d}, yielding

$$H\left(q\right)=H_{\mathrm{s}}\left(g\left(r\right)\right)+H_{\mathrm{q}}\left(q,g\left(r\right)\right). \tag{A.2}$$

For electrostatically interacting charge-stabilized, monodisperse, spherical particles in suspension, an expression of H was derived by Genz and Klein for dilute to moderate particle concentrations ($\phi < 10$ vol.%).[3] They assumed hydrodynamic interactions by a far-field expansion of the two-body hydrodynamic mobility tensors and derived an expression for H via $g\left(r\right)$ with the RMSA method. The result was expanded using the pairwise additive approximation[4] (PA) for the case of polydisperse spheres by Nägele et al.[5], and is given by

$$\begin{aligned}H_{\mathrm{s}}\left(\phi\right)=1&-\frac{15}{8}\phi\int_{1}^{\infty}\mathrm{d}r\frac{g\left(r\right)}{r^{2}}+\frac{17}{64}\phi\int_{1}^{\infty}\mathrm{d}r\frac{g\left(r\right)}{r^{4}}\\&+\frac{253}{1024}\phi\int_{1}^{\infty}\mathrm{d}r\frac{g\left(r\right)}{r^{6}}-\frac{737}{1024}\phi\int_{1}^{\infty}\mathrm{d}r\frac{g\left(r\right)}{r^{8}},\end{aligned} \tag{A.3}$$

---

[2] See: Beenakker, C. W. J. and Mazur, P. (1984). *Physica A* **126**, 349; and Beenakker, Carlo Willem Joannes (1984). "On transport properties of concentrated suspensions." PhD thesis. Leiden, Dutch: Universiteit Leiden.

[3] Genz, U. and Klein, R. (1991). *Physica A* **171**, 26.

[4] For details see: Heinen, M. et al. (2010). *J. Appl. Cryst.* **43**, 970.

[5] Nägele, G. et al. (1993). *Phys. Rev. E* **47**, 2562; Nägele, G. and Baur, P. (1997). *Physica A* **245**, 297.

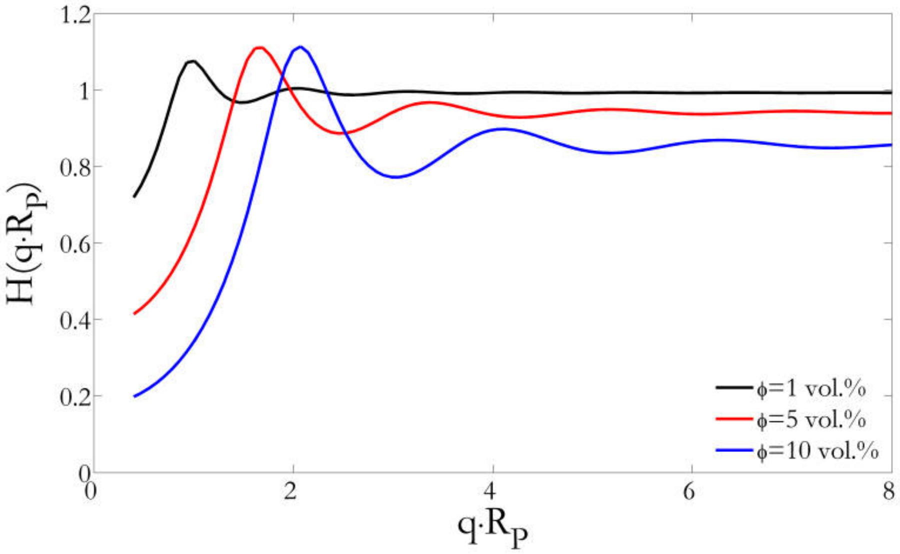

Figure A.1: Hydrodynamic functions H calculated with the PA for different ϕ as function of q. Fixed parameters in the calculation are the effective charge $Z_{\text{eff}} = 50\ e^{-}$, the temperature $T = 293.15$ K, and the relative permittivity of the solvent $\epsilon_r = 5$ without addition of salt.

and

$$H_{\text{q}}\left(q,\phi\right) = 15\phi\frac{J_1\left(q\right)}{q} + 18\phi\int_1^{\infty} \mathrm{d}r\left|g\left(r\right)-1\right|r\left(J_0\left(qr\right) - \frac{J_1\left(qr\right)}{qr} + \frac{J_2\left(qr\right)}{6r^2}\right). \qquad \text{(A.4)}$$

J_n are the spherical Bessel functions of order n. Here, the self-part $H_{\text{s}}\left(\phi\right)$ equals the short-time self-diffusion coefficient $D_{\text{s,short}}$. The PA uses tables of numerically precise values for the two-body mobility tensors and is limited to low volume fractions ($\phi\ <\ 10$ vol.%), where many body interactions can be neglected. Thus, for $\phi\ >$ 10 vol.% the model predicts unphysical behavior for wave vector transfers in the vicinity of the static structure factor peak.[6] In Figure A.1 H calculated for different ϕ as a function of q is shown. H exhibit a strong decrease at small q, where a decrease of the hydrodynamic interactions leads to a slowing down of the collective particles motions. At large q, the hydrodynamic functions oscillates around the short-time self-diffusion coefficient which is equal to unity in the limit of vanishing ϕ. In contrast to an uncharged colloidal system, values of H around the peak of the static structure factor are larger than unity. This indicates an increase of the particles dynamics due to the far-field presence of the hydrodynamic interactions. This increase of particle dynamics as function of ϕ on length scales around the mean inter-particle distance is usually interpreted as back-flow of the displaced solvent caused by collective motions of neighboring particles.

---

[6] Nägele, G. (1996). *Physics Reports* **272**, 215.

A.3 Sample inserts for the P10 XPCS set-up

Different designs were necessary in order to cover various glass transition temperatures T_g, for example the metallic glass former chalcogenide (GeSbTe, $T_\mathrm{g} = 423$ K) or the glass former polyethylene (LDPE, $T_\mathrm{g} = 148$ K). In combination with the demanding requirements of the temperature stability for investigations near T_g, a solution with temperature controls for a low (LT, $120 - 350$ K) and a moderate (MT, $260 - 470$ K) temperature regime is favored. The temperature control of the LT-design is planned as a combination of a nitrogen gas flow and heaters, whereas those of the MT-design is realized as a combination of a Peltier-element and heaters.

The basic designs of the inserts are shown in Figure A.3. Since the LT-design is already described in subsection 6.2.3, an adaptation with an electromagnet mount is presented here (Figure A.3(b)). The MT-design, shown in Figure A.3(a), is similar to the LT-design. Also here a CF100-flange is used as basis. It has the same vacuum compatible 9-pin sensor cable connector and high current connector as the LT-design. The cooling power for the MT-design is delivered by a Peltier-element (PE) which is also used for the thermal decoupling of the CF100-flange and a holder made of copper with pressed-in impedance heaters (IH). The PE is driven by a low noise Kepco power supply through the high current connector. It provides an electrically adjustable temperature offset of up to ± 50 K. The heat load of the PE is transfered flange wise via a water flow within incorporated cooling coils, served by a close cycle chiller operating at a constant temperature ($T_\mathrm{c} = 288$ K). The copper holder has the same opening, shielding and capillary mount as the LT-design. The actual temperature control is analogous to the LT-design arranged with impedance heaters (IH) and Pt100 temperature sensors (TS) symmetrically positioned around the sample mount and controlled by a Lakeshore temperature controller. The MT-type inserts offer a thermal homogeneity up to $\frac{\Delta T}{\Delta d} = 20 \pm 4\ \frac{\mathrm{mK}}{\mathrm{mm}}$ at $T = 350$ K while the temperature can be changed up to $\frac{\Delta T}{\Delta t} = 10\ \frac{\mathrm{K}}{\mathrm{min}}$ within a precision of $\Delta T = 3$ mK and a long term thermal stability of $\Delta T = 1$ mK.

A set of base adaptations were designed to fit special needs of various samples (Figure A.2). For example, the MT-type insert (Figure A.2(a)) can be equipped with clamps on the copper-mount (Figure A.2(b)). The clamps can be used to hold plane surfaces that allow studies in gracing incident geometry. The LT-type insert (Figure A.2(c)) can be equipped with a special electromagnet instead of the capillary mount (Figure A.2(d)). In this configuration one capillary is placed between two electromagnets with a distance of $3 - 4$ mm and rotated to 45° which deliver an adjustable and homogeneous magnetic field of up to 160 mT (homogeneous within ± 2 mT) and a quantified remanence field of 6 mT. The electromagnet mount has a 1.5 mm circular opening for the beam to study magnetic samples in transmission geometry at the presence of a magnetic field. The operation of the electromagnets at full current cause a temperature change of $\Delta T = \pm 50$ mK at the sample position while switching. A temperature stability of $\Delta T = \pm 3$ mK is reached after 10 min which improves to $\Delta T = \pm 1$ mK after 30 min.

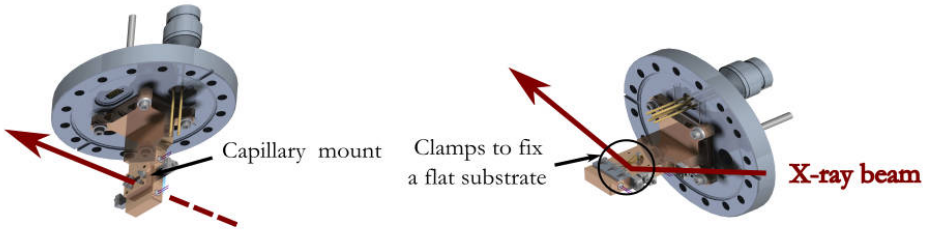

(a) Transmission insert (MT) (b) Reflectivity insert (MT)

(c) Transmission insert (LT) (d) Magnetic insert (LT)

Figure A.2: Sample insert adaptations: (a) The transmission insert (MT-design) enables the study of samples filled in vacuum-sealed capillaries via SAXS. (b) The reflectivity insert (MT-design) allows the study of samples in gracing incident geometry. (c-d) The transmission insert (LT-design) allows the study of samples filled in vacuum-sealed capillaries via SAXS with (c) a multi capillary mount or (d) an electromagnet mount which provides a magnetic field of up to 160 mT.

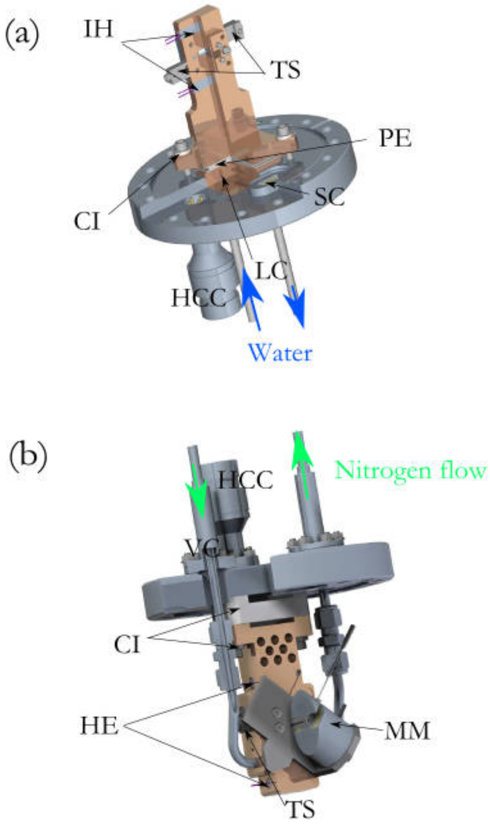

Figure A.3: The two base designs of sample inserts at P10: (a) Upside-down sectional drawing of the MT-type insert for transmission experiments with two impedance heaters (IH), two temperature sensors (TS), a Peltier-element with ceramic surfaces (PE), liquid cooling pipes (LC), a 9-pin sensor cable connector (SC), ceramic isolations (CI), and a high current connector (HCC). (b) Sectional drawing of the LT-type insert with an electromagnet mount (MM) (capable for one capillary) instead of the standard copper mount for up to three capillaries.

A.4 Static structure factors

For completeness, the complement measured static structure factors specified in Table 7.2 are shown in Figures A.4-A.7.

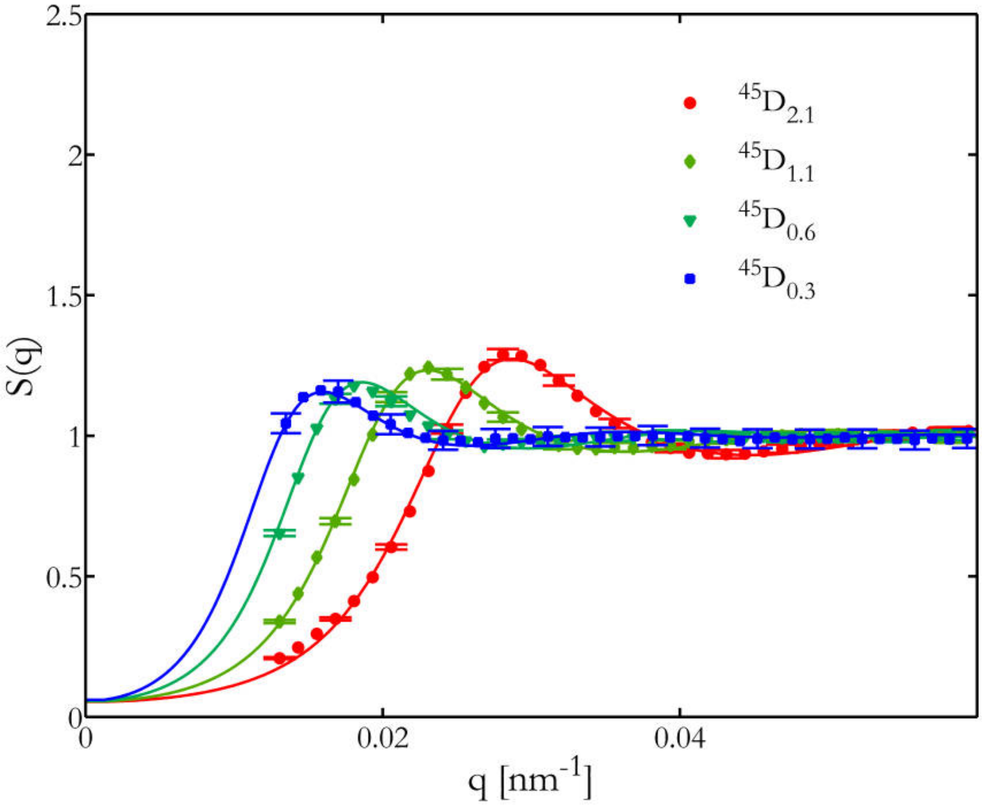

Figure A.4: Measured static structure factors of ^{45}D at different concentrations. The lines are error weighted fits (RMSA) to the data.

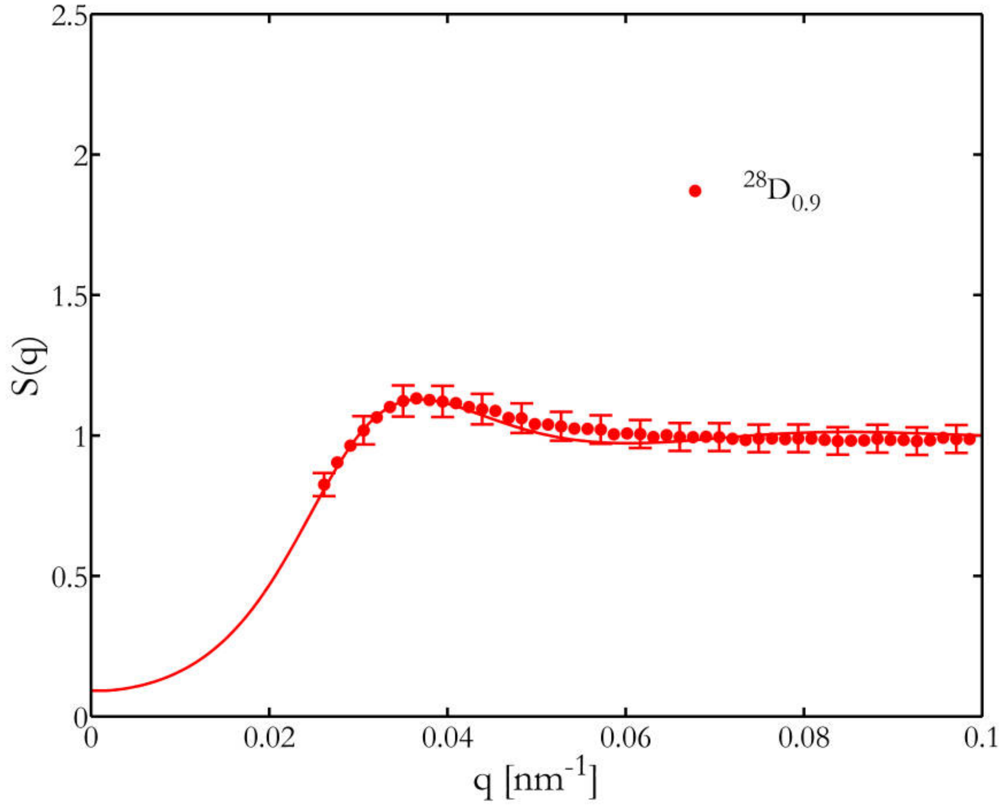

Figure A.5: Measured static structure factors of ^{28}D at different concentrations. The line is the error weighted fit (RMSA) to the data.

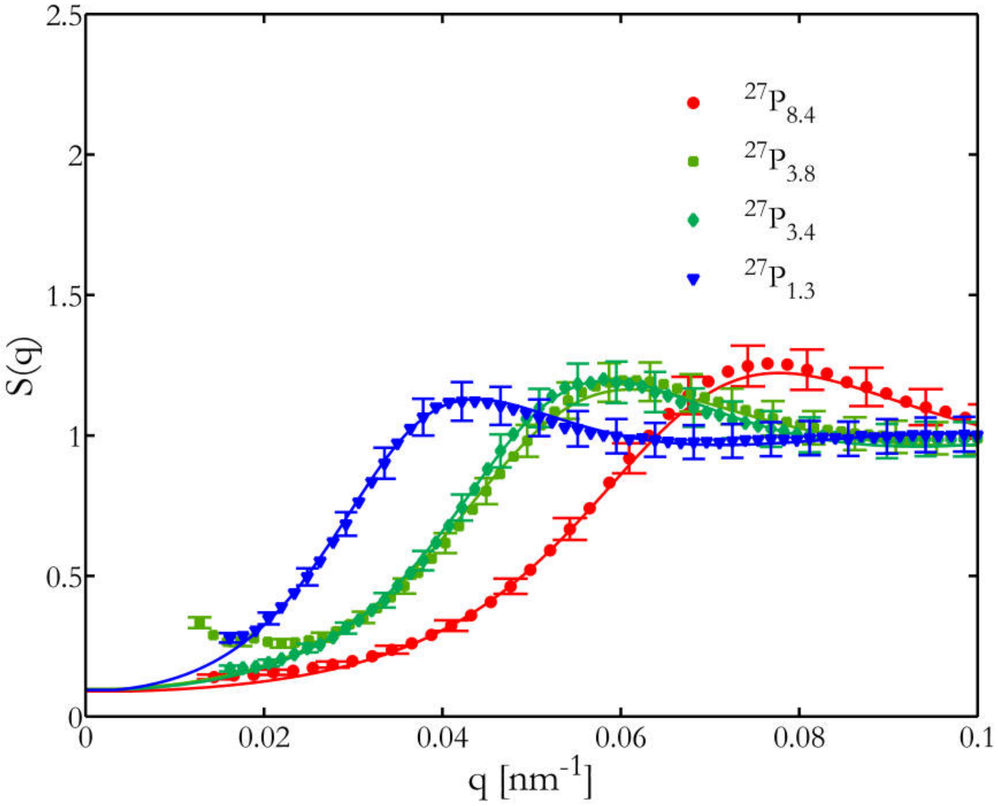

Figure A.6: Measured static structure factors of ^{27}D at different concentrations. The lines are error weighted fits (RMSA) to the data.

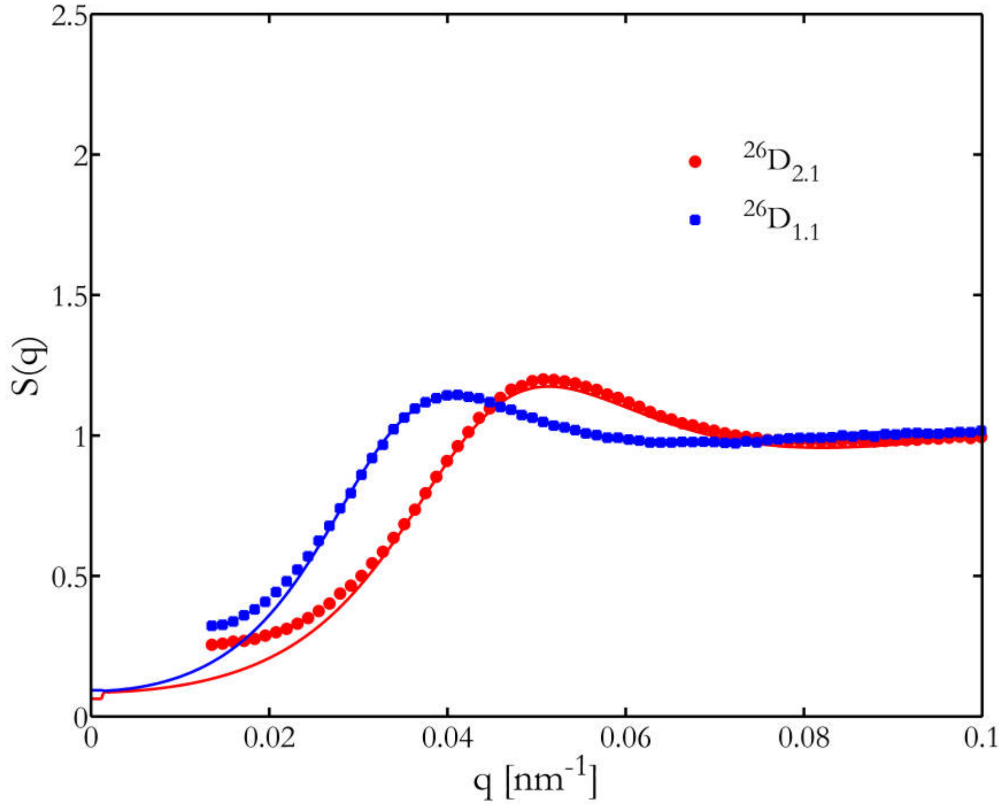

Figure A.7: Measured static structure factors of ^{26}D. The line is the error weighted fit (RMSA) to the data.

A.5 Beam exposure effects at low temperatures

The change of the relaxation time (τ_c) behavior in chapter 8 might be the result of beam induced heating. Because, beam induced heating of the sample would lead to an increasing offset to the nominal temperature with decreasing temperature, while the heat capacity and conductivity decreases. This was observed when comparing the measured relaxation times for different delays between beam exposures.[7] A possible mechanism behind this heating effect could be ionization as result of X-ray exposure followed by cascades of secondary electrons which transform their energy into lattice vibrations via thermalization through multiple collisions in the material.[8]

A simple estimate of the energy absorbed per scattering pattern is given by $0.15\ \mu J$, assuming a sample volume of $V_s = 20 \times 20 \times 800\ \mu\text{m}^3$, with a typical transmission of 30%, exposed to an 8 keV X-ray beam with $4 \cdot 10^9$ photons per second for an exposure time of usually 0.1 s. This leads to an increase of the temperature $\Delta T = 0.3$ K, assuming a typical molar heat capacity $c_m = 0.5\ \text{J} \cdot \text{g}^{-1} \cdot \text{K}^{-1}$. The absorbed energy is usually dispersed between illuminations, if one considers the additional read-out and delay times which typically are in the order of seconds. However, a cumulative threshold exists. For example, it was observed exclusively at low temperatures that the width of the static structure factor peak increases accompanied by a decrease of the peak height (chapter 7) when the sample is exposed continously to the X-ray beam.

---

[7] Since the exposure time for each scattering pattern and the total amount of illuminations were constant, the delay times between illuminations are inverse proportional to the energy absorption rate of the sample.

[8] For details see Ponomarenko, O. et al. (2011). *J. Synchr. Rad.* **18**,4, 580 and references within.

A.6 Dynamics results of the dilute samples

For completeness, the p and γ results of the dilute samples ${}^{27}P_{1.3}$, ${}^{18}P_{<1.0}$ and ${}^{18}P_{<0.5}$ are shown in Figures A.8-A.10. The results for the sample ${}^{27}P_{1.3}$ (Figure A.8) are in agreement with the findings of ${}^{71}P$. The limited number of investigated temperatures do not allow additional statements except that the increase of γ with decreasing temperature seems to be less pronounced for this sample. In the same way the results of ${}^{18}P_{<1.0}$ (Figure A.9) and ${}^{18}P_{<0.5}$ (Figure A.10) can be interpreted. Since these measurements were performed with a low frame rate detector, the relaxation times at temperatures above $T = 250$ K were too short to be analyzed properly. In particular, the data for ${}^{18}P_{<0.5}$ includes temperatures below 222 K which show characteristics of hyper-diffusion and correlated particle motion (A-regime) as observed for ${}^{71}P_{<1.0}$ with the difference that the values do not reach $p = 1$ and $\gamma = 2$.

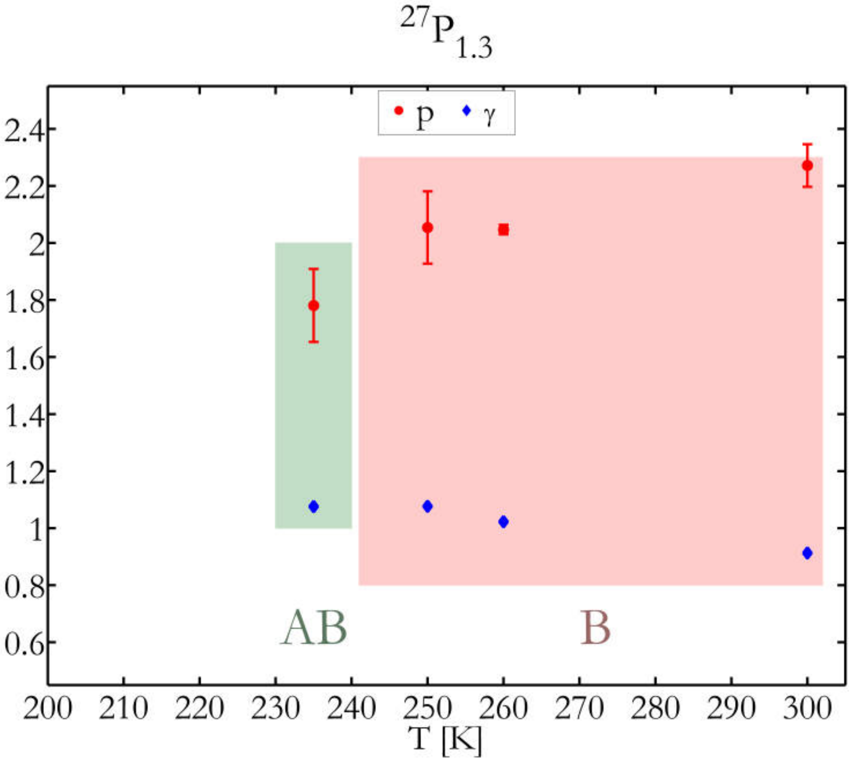

Figure A.8: Temperature dependence of q-averaged values γ and p of ${}^{27}P_{1.3}$.

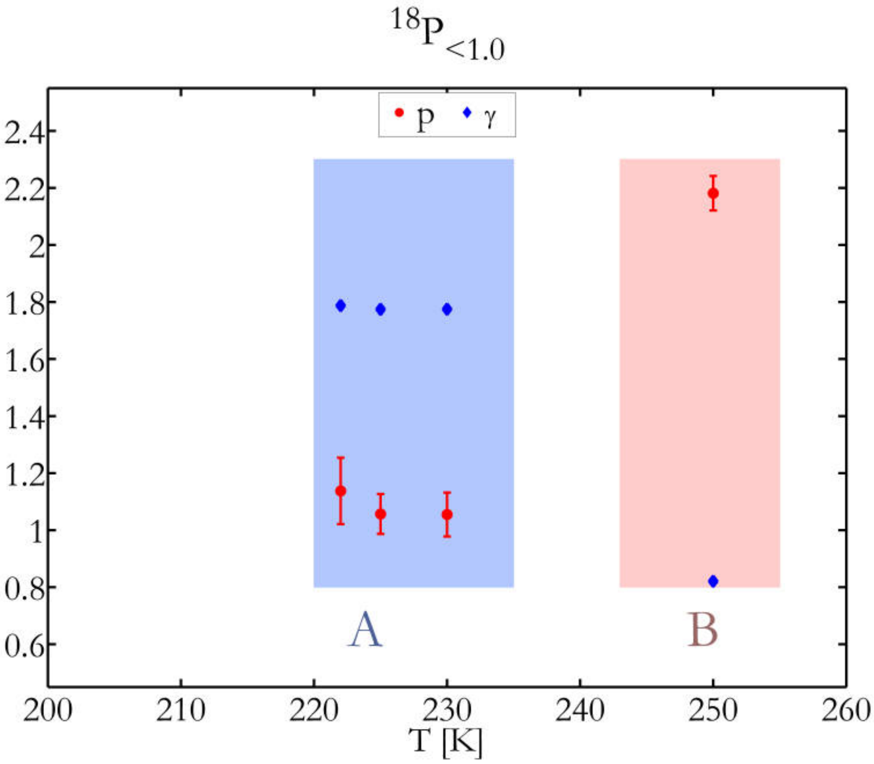

Figure A.9: Temperature dependence of q-averaged values γ and p of $^{18}P_{<1.0}$.

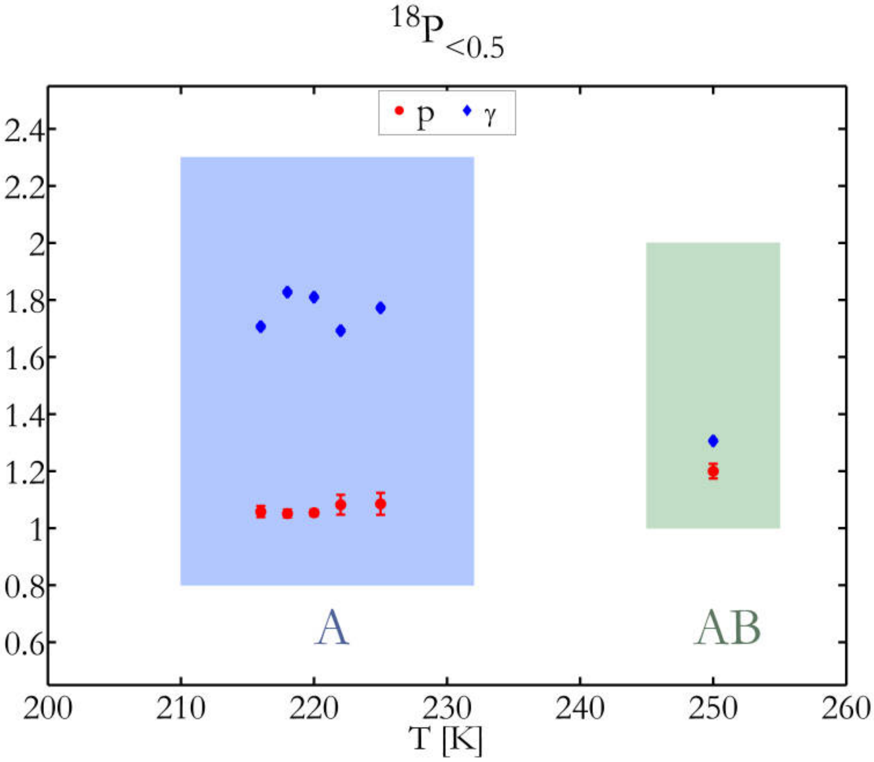

Figure A.10: Temperature dependence of q-averaged values γ and p of $^{18}P_{<0.5}$.

A.7 Dynamics results of the concentrated samples

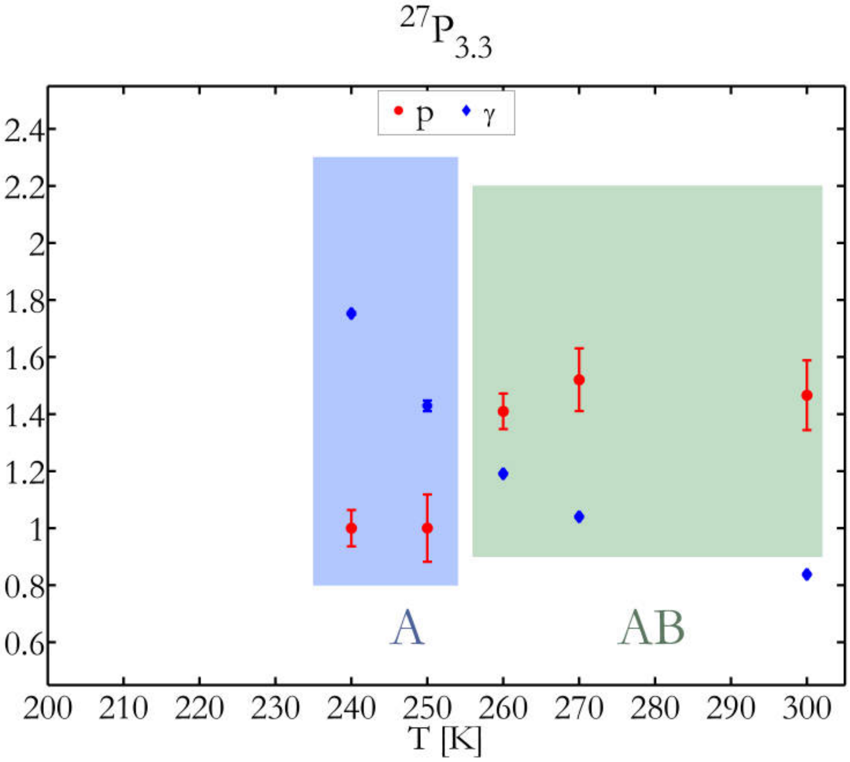

Figure A.11: Temperature dependence of γ and p for $^{27}P_{3.3}$.

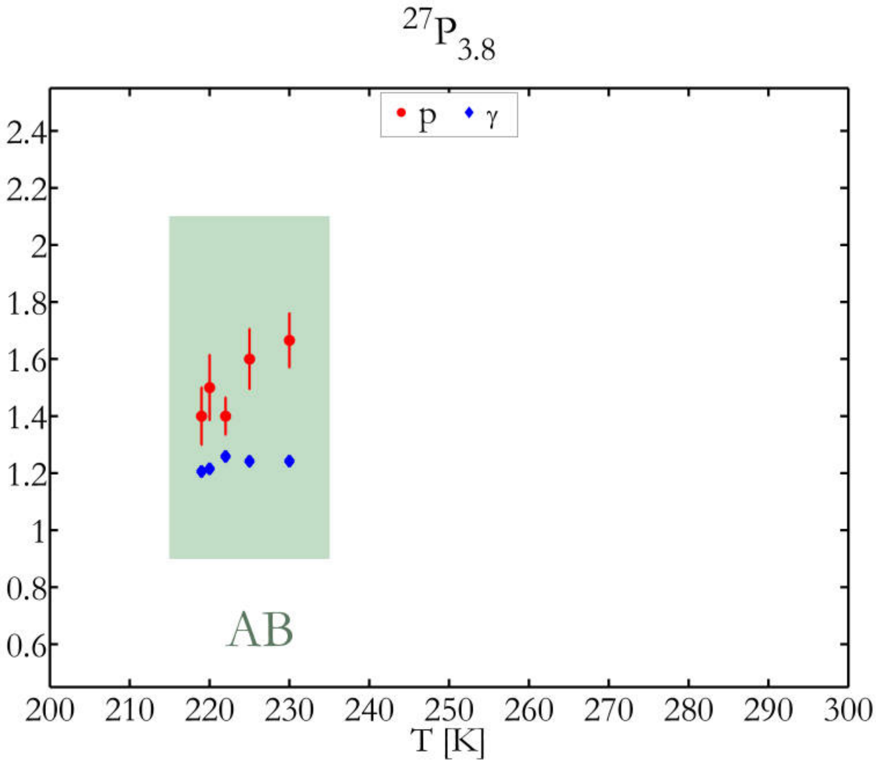

Figure A.12: Temperature dependence of γ and p for $^{27}\mathrm{P}_{3.8}$.

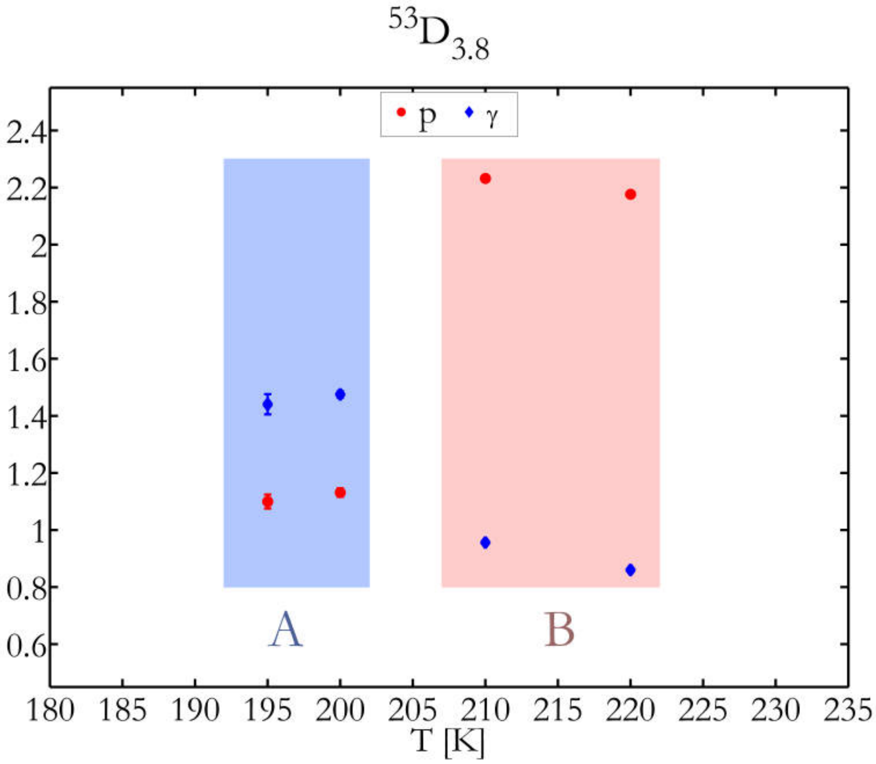

Figure A.13: Temperature dependence of γ and p for $^{53}\mathrm{D}_{3.8}$.

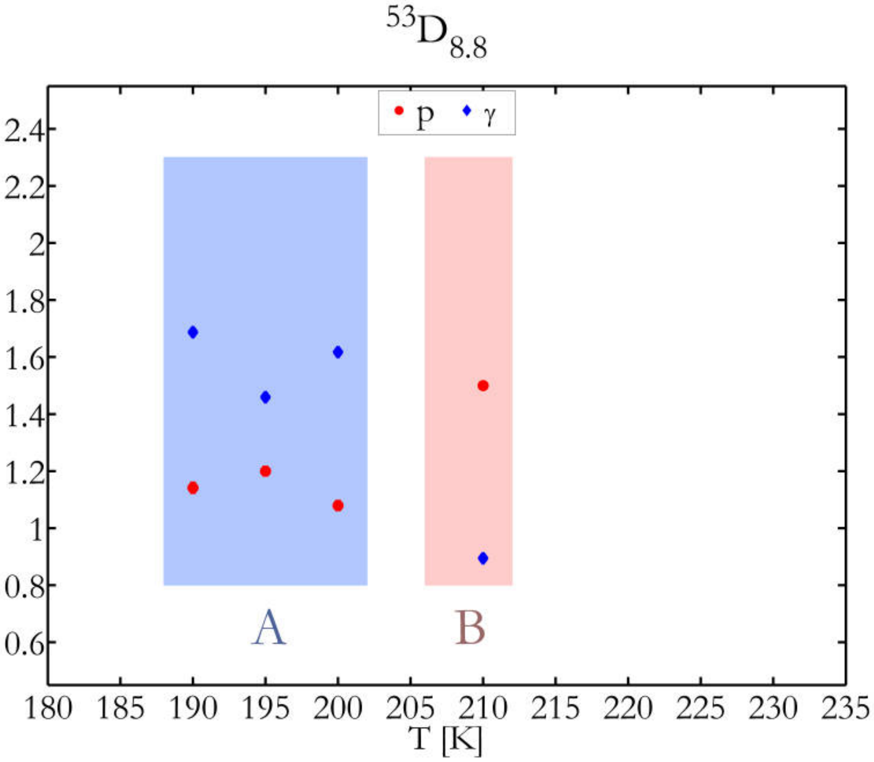

Figure A.14: Temperature dependence of γ and p for $^{53}D_{8.8}$.

List of Figures

List of Tables

Bibliography

Abernathy, D.; Grübel, G.; Brauer, S.; McNulty, I.; Stephenson, G.; Mochrie, S.; Sandy, A.; Mulders, N. and Sutton, M. (1998). *J. Synch. Rad.* **5**, 37.

Adam, G. and Gibbs, J. H. (1965). *J. Chem. Phys.* **43**, 139.

Als-Nielsen, J. W. and McMorrow, D. (2001). *Modern X-Ray Physics.* 2nd Edition. Wiley, Hoboken, USA.

Altenberger, A. R. (1976). *Chem. Phys.* **15**, 269.

Andersson, S. P. and Andersson, O. (1998). *Macromolecules* **31**, 2999.

Angell, C. A. (1988). *J. Non-Cryst. Solids* **102**, 205.

– (1997). *J. Res. Natl. Inst. Stand. Technol.* **102**, 171.

– (2011). "Glassy, Amorphous and Nano-Crystalline Materials." 8th Edition. Springer, Amsterdam, Netherlands, 21ff.

Aragon, S. R. and Pecora, R. (1976). *J. Chem. Phys.* **64**, 2395.

Arndt, M.; Stannarius, R.; Groothues, H.; Hempel, E. and Kremer, F. (1997). *Phys. Rev. Lett.* **79**, 2077.

Asakura, S. and Oosawa, F. (1954). *J. Chem. Phys.* **22**, 1255.

– (1958). *J. Polym. Sci.* **33**, 183.

Asthalter, T.; Sergueev, I.; Franz, H.; Rüffer, R.; Petry, W.; Messel, K.; Härter, P. and Huwe, A. (2001). *Eur. Phys. J. B* **22**, 301.

Asthalter, T.; Bauer, M.; Bürck, U. van; Sergueev, I.; Franz, H. and Chumakov, A. I. (2003). *Eur. Phys. J. E* **12**, S9–S12.

Autenrieth, T.; Robert, A.; Wagner, J. and Grübel, G. (2007). *J. Appl. Cryst.* **40**, 250.

Badmaev, B. B. and Damdinov, B. B. (2001). *Acoustical Physics* **47**, 487.

Bailey, J. K. and Mecartney, M. L. (1992). *Coll. Surf.* **63**, 151.

Balewski, K., ed. (2010). *Comissioning of Petra III.* International Particle Accelerator Conference 1. Kyoto University. Kyoto: IPAC'10/ACFA.

Balewski, K.; Brefeld, W.; Decking, W.; Franz, H.; Röhlsberger, R. and Weckert, E. (Feb. 2004). *PETRA III: a low emittance synchrotron radiation source Technical Design Report.* URL: `http://petra3-project.desy.de/general/tdr/index_eng.html`.

Barlow, A. J.; Lamb, J.; Matheson, A. J.; Padmini, P. R. K. L. and Richter, J. (1967). *Proc. R. Soc. B* **298**, 467.

Beenakker, C. W. J. and Mazur, P. (1984). *Physica A* **126**, 349.

Beenakker, Carlo Willem Joannes (1984). "On transport properties of concentrated suspensions." PhD thesis. Leiden, Dutch: Universiteit Leiden.

Bendler, J. T.; Fontanella, J. J.; Shlesinger, M. F.; Bartoš, J.; Šauša, O. and Krištiak, J. (2005). *Phys. Rev. E* **71**, 31508.

Bergman, R.; Svanberg, C.; Andersson, D.; Brodin, A. and Torell, L. M. (1998). *J. non-cryst. sol.* **235**, 225.

Bergna, H. E. and Roberts, W. O. (2005). *Colloidal Silica Fundamentals and Applications.* 1st Edition. Marcel Dekker Inc., New York, USA.

Berne, B. J. and Pecora, R. (2000). *Dynamic Light Scattering: With Applications to Chemistry, Biology, and Physics.* 1st Edition. Dover Publications, New York, USA.

Berthier, L. (2011). *Rev. Mod. Phys.* **83**, 587.

Berthier, L.; Biroli, G.; Bouchaud, J.-P.; Cipelletti, L.; El Masri, D.; L'Hôte, D.; Ladieu, F. and Pierno, M. (2005). *Science* **310**, 1797.

Bilderback, D. H.; Elleaume, P. and Weckert, E. (2005). *J. Phys. B-At. Mol. Opt. Phys.* **38**, 773.

Binder, K. and Kob, W. (2005). *Glassy Materials and Disordered Solids.* World Scientific Publishing Co., Singapore, Republic of Singapore.

Blum, L. and Hoye, J. S. (1978). *J. Stat. Phys.* **19**, 317.

Bogush, G. H. and Zukoski, C. F. (1991a). *J. Coll. Inter. Sci.* **142**, 1.

– (1991b). *J. Coll. Inter. Sci.* **142**, 19.

Bogush, G. H.; Tracy, M. A. and Zukoski, C. F. (1988). *J. Non-Cryst. Solids* **104**, 95.

Bouchaud, J.-P. and Pitard, E. (2001). *Eur. Phys. J.* **E6**, 231.

Brace, D. D.; Gottke, S. D.; Cang, H. and Fayer, M. D. (2002). *J. Chem. Phys.* **116**, 1598.

Brown, R. R. (1866). *The miscellaneous botanical works of Robert Brown.* 1st Edition. The Ray society, London, UK.

Brumberger, H (1995). *Modern Aspects of Small Angle Scattering.* 1st Edition. Kluwer Academic Publishers, Dordrecht, Netherlands.

Burghardt, W. R.; Sikorski, M.; Sandy, A. R. and Narayanan, S. (2012). *Phys. Rev. E* **85**, 21402.

Cadogan, D. F. and Howick, C. J. (2000). *Ullmann's Encyclopedia of Industrial Chemistry: Plasticizers.* 1st Edition. Wiley-VCH, Weinheim, Germany.

Caronna, C. (2008). "Glassy systems studied by X-ray photon correlation spectroscopy." PhD thesis. Palermo, Italy: University Palermo.

Caronna, C.; Chushkin, Y.; Madsen, A. and Cupane, A. (2008). *Phys. Rev. Lett.* **100**, 055702.

Carpenter, D. K. and Mattice, W. L. (1977). *Biopolymers* **16**, 67.

Carré, A.; Berthier, L.; Horbach, J.; Ispas, S. and Kob, W. (2007). *J. Chem. Phys.* **127**, 114512.

Chen, S. L.; Dong, P.; Yang, G.H. and Yang, J. J. (1996). *Ind. Eng. Chem. Res.* **35**, 4487.

Chushkin, Y.; Caronna, C. and Madsen, A. (2008). *EPL* **83**, 36001.

Cipelletti, L. and Weitz, D. A. (1999). *Rev. Sci. Instrum.* **70**, 3214.

Cipelletti, L.; Manley, S.; Ball, R. C. and Weitz, D. A. (2000). *Phys. Rev. Lett.* **84**, 2275.

Cipelletti, L.; Ramos, L.; Manley, S.; Pitard, E.; Weitz, D. A.; Pashkovski, E. E. and Johansson, M. (2003). *Farad. Discuss.* **123**, 237.

Cochrane, J.; Harrison, G.; Lamb, J. and Phillips, D. W. (1980). *Polymer* **21**, 837.

Colin, R.; Alsayed, A. M.; Castaing, J.-C.; Goyal, R.; Hough, L. and Abou, B. (2011). *Soft Matter* **7**, 4504.

Cook, R. L.; King, H. E.; Herbst, C. A. and Herschbach, D. R. (1994). *J. Chem. Phys.* **100**, 5178.

DESY, Photon Science (Oct. 2013). *P10: Beamline layout/specifications.* URL: `http://photon-science.desy.de/facilities/petra_iii/beamlines/p10_coherence_applications/index_eng.html`.

Dalle-Ferrier, C.; Thibierge, C.; Alba-Simionesco, C.; Berthier, L.; Biroli, G.; Bouchaud, J.-P.; Ladieu, F.; L'Hôte, D. and Tarjus, G. (2007). *Phys. Rev. E* **76**, 041510.

Dawydow, A. S. (1999). *Quantenmechanik.* 8th Edition. Wiley-VCH, Weinheim, Germany.

De Gennes, P. G. (1959). *Physica* **25**, 825.

Debenedetti, P. G. and Stillinger, F. H. (2001). *Nature* **410**, 259.

Debye, P. and Hückel, E. (1923). *Physikalische Zeitschrift* **24**, 185.

Denev, A.; Torquato, S. and Stillinger, F. H. (2005). *Phys. Rev. E* **71**, 11105.

Denisov, D.; Dang, M. T.; Struth, B.; Wegdam, G. and Schall, P. (2013). *SCIENTIFIC REPORTS* **3**, 1631.

Derjaguin, B. and Landau, L. (1941). *Acta Physico Chemica URSS* **14**, 633.

Dhont, J. K. G. (1996). *An Introduction to the Dynamics of Colloids.* 1st Edition. Elsevier, Amsterdam, Netherlands.

Duri, A. and Cipelletti, L. (2006). *Europhys. Lett.* **76**, 972.

Duri, A.; Autenrieth, T.; Stadler, L.-M.; Leupold, O.; Chushkin, Y.; Grübel, G. and Gutt, C. (2009). *Phys. Rev. Lett.* **102**, 145701.

ESRF (Oct. 2013). *ID10 - Soft interfaces and coherent scattering beamline @ONLINE.* URL: `http://www.esrf.eu/UsersAndScience/Experiments/SoftMatter/ID10/`.

Ediger, M. D. (2000). *Annu. Rev. Phys. Chem.* **51**, 99.

Ediger, M. D.; Angell, C. A. and Nagel, S. R. (1996). *J. Phys. Chem.* **100**, 13200.

Einstein, A. (1905). *Ann. Phys.* **322**, 549.

– (1908). *Z. Elektrochem. Angew. Phys. Chem.* **14**, 235.

Ermak, D. R. and McCammon, J. A. (1978). *J. Chem. Phys.* **69**, 1352.

Fegley, B. and Barringer, E. A. (1984). *Synthesis, Characterization, and Processing of Monosized Ceramic Powders.* Massachusetts Institute of Technology, Cambridge, USA.

Feigin, L. A. and Svergun, D. I. (1987). *Structure analysis by small angle X-ray and neutron scattering.* 1st Edition. Plenum Press, London, UK.

Fluerasu, A.; Moussaïd, A.; Madsen, A. and Schofield, A. (2007). *Phys. Rev. E* **76**, 10401.

Forkner, M. W.; Robson, J. H.; Snellings, W. M.; Martin, A. E.; Murphy, F. H. and Parsons, T. E. (2004). *Kirk-Othmer Encyclopedia of Chemical Technology: Glycols.* 1st Edition. Wiley-VCH, Weinheim, Germany.

Gapinski, J.; Nägele, G. and Patkowski, A. (2010). *J. Chem. Phys.* **136**, 24507.

Genz, U. and Klein, R. (1991). *Physica A* **171**, 26.

Giesche, H. (1994). *J. Eur. Ceram. Soc.* **14**, 189.

Glatter, O. and Kratky, O. (1982). *Small-Angle X-ray Scattering.* 1st Edition. Academic Press, London, UK.

Goodman, J. W. (2000). *Statistical optics.* 1st Edition. Wiley, Hoboken, USA.

Götze, W. (2008). *Complex Dynamics of glass forming liquids. A mode-coupling theory.* 1st Edition. Oxford University Press, Oxford, UK.

Götze, W. and Sjögren, L. (1995). *Transp. Theory. Stat. Phys.* **24**, 801.

Grübel, G.; Als-Nielsen, J. and Freud, A. K. (1994). *Journal de Physique IV* **4**, 27.

Grübel, G.; Madsen, A. and Robert, A. (2008). “Soft-Matter Characterization.” 1st Edition. Springer, New York, USA, 954–995.

Gultepe, I. (2007). *Pure and Applied Geophysics* **164**, 1126.

Hamaker, H. C. (1937). *Physica* **4**, 1058.

Hansen, E. W.; Gong, X. and Chen, Q. (2013). *Macromolecular Chemistry and Physics* **214**, 844.

Hansen, J. P. and Hayter, J. B. (1982). *Mol. Phys.* **46**, 651.

Hansen, J. P. and McDonald, I. R. (2005). *Theory of simple liquids.* 3rd Edition. Academic Press, Waltham, USA.

Hansen, J.P.; Levesque, D. and Zinn-Justin, J. *Liquids, freezing and the glass transition.* Elsevier, Amsterdam, Netherlands.

Heinen, M.; Holmqvist, P.; Banchio, A. J. and Nägele, G. (2010). *J. Appl. Cryst.* **43**, 970.

Hemández-Contreras, M.; Medina-Noyola, M. and Vizcarra-Rendón, A. (1996). *Physica A* **234**, 271.

Horbach, J.; Degenhardt, M.; Hahn, U.; Heuer, J.; Peters, H. B.; Schulte-Schrepping, H.; Donat, A. and Lüdecke, H. (2011). *Diamond Light Source Proceedings* **1**, E35.

Hunter, R. J. (2000). *Foundations of colloid science.* 2nd Edition. Oxford University Press, New York, USA.

Ilett, S. M.; Orrock, A.; Poon, W. C. K. and Pusey, P. N. (1995). *Phys. Rev. E* **51**,

James, R. W. (1948). *The optical principles of the diffraction of X-rays.* 1st Edition. Bell and sons, London, UK.

Kalbfleisch, S.; Osterhoff, M.; Giewekemeyer, K.; Neubauer, H.; Krüger, S. P.; Hartmann, B.; Bartels, M.; Sprung, M.; Leupold, O.; Siewert, F. and Salditt, T. (2010). *AIP Conference Proceedings* **1234**, 433.

Kaloun, S.; Skouri, R.; Skouri, M.; Munch, J. P. and Schosseler, F. (2005). *Phys. Rev. E* **72**, 011403.

Kaminski, K.; Kipnusu, W. K.; Adrjanowicz, K.; Mapesa, E. U.; Iacob, C.; Jasiurkowska, M.; Wlodarczyk, P.; Grzybowska, K.; Paluch, M. and Kremer, F. (2013). *Macromolecules* **46**, 1973.

Kauzmann, W. (1948). *Chem. Rev.* **43**, 219.

Kim, K. (1986). *Nuclear Instruments and Methods in Physics Research* **A246**, 71.

Kohlrausch, F. (1863). *Ann. Phys* **195**, 337.

Kolbe, G. (1956). “Das komplexchemische Verhalten der Kieselsäure.” PhD thesis. Jena, Germany: Friedrich Schiller University.

Kotlarchyk, M. and Chen, S. H. (1983). *J. Chem. Phys.* **79**, 2461.

Kubo, R. (1962). *J. Phys. Soc. Jpn.* **17**, 1100.

LaMer, V. K. and Dinegar, R. H. (1950). *J. Am. Chem. Soc.* **72**, 4847.

Lačević, N.; Starr, F. W.; Schrøder, T. B. and Glotzer, S. C. (2003). *J. Chem. Phys.* **119**, 7372.

Lal, J.; Abernathy, D.; Auvray, L.; Diat, O. and Grübel, G. (2001). *Eur. Phys. J. E* **4**, 263.

Langevin, P. (1908). *C. R. Acad. Sci.* **146**, 530.

Lebowitz, J. L. and Percus, J. K. (1966). *Phys. Rev.* **144**, 251.

Leitner, M.; Sepiol, B.; Stadler, L.-M. and Pfau, B. (2012). *Phys. Rev. B* **86**, 064202.

Lindsey, C. P. and Patterson, G. D. (1980). *J. Chem. Phys.* **73**, 3348.

Lumma, D.; Lurio, L. B.; Mochrie, S. G. J. and Sutton, M. (2000). *Rev. Sci. Instrum.* **71**, 3274.

Madsen, A.; Konovalov, O.; Robert, A. and Grübel, G. (2001). *Phys. Rev. E.* **64**, 61406.

Madsen, A.; Seydel, T.; Tolan, M. and Grübel, G. (2005). *J. Synchotron Rad.* **12**, 786.

Madsen, A.; Leheny, R. L.; Guo, H.; Sprung, M. and Czakkel, O. (2010). *New Journal of Physics* **12**, 55001.

Malik, A.; Sandy, A. R.; Lurio, L. B.; Stephenson, G. B.; Mochrie, S. G. J.; McNulty, I. and Sutton, M. (1998). *Phys. Rev. Lett.* **81**, 5832.

Maranzano, B. J.; Wagner, N. J.; Fritz, G. and Glatter, O. (2000). *Langmuir* **16**, 10556.

Matsoukas, T. and Gulari, E. (1988a). *J. Coll. Inter. Sci.* **124**, 252.

– (1988b). *J. Coll. Inter. Sci.* **145**, 557.

Medina-Noyola, M. (1987). *Faraday Discuss. Chem. Soc.* **83**, 21.

– (1988). *Phys. Rev. Lett.* **60**, 2705.

Menon, N.; Nagel, S. R. and Venerus, D. C. (1994). *Phys. Rev. Lett.* **73**, 963.

Meyer, A.; Franz, H.; Wuttke, J.; Petry, W.; Wiele, N.; Rüffer, R. and Hübsch, C. (1997). *Zeitschrift für Physik B Condensed Matter* **103**, 479.

Moon, I. K.; Jeong, Y. H. and Furukawa, T. (2001). *Thermochimica Acta* **1**, 2001.

Nagao, D.; Nakabayashi, H.; Ishii, H. and Konno, M. (2013). *J. Col. Int. Sci.* **394**, 63.

Nägele, G. (1996). *Physics Reports* **272**, 215.

Nägele, G. and Baur, P. (1997). *Physica A* **245**, 297.

Nägele, G.; Kellerbauer, O.; Krause, R. and Klein, R. (1993). *Phys. Rev. E* **47**, 2562.

Nakamura, K.; Kawabata, T. and Mori, Y. (2003). *Powder Technology* **131**, 120.

Ngai, K. L. (2000). *J. Non-Cryst. Sol.* **275**, 7.

Ngai, K. L.; Casalini, R. and Roland, C. M. (2005). *Macromolecules* **38**, 4363.

Norde, W. (2011). *Colloids and Interfaces in Life Sciences and Bionanotechnology.* 2nd Edition. CRC Press, Boca Raton, USA.

Ornstein, L. S. and Zernike, F. (1914). *KNAW Proceedings* **17**, 793.

Paluch, M.; Ziołо, J.; Rzoska, S. J. and Habdas, P. (1997). *J. Phys.: Condens. Matter* **9**, 5485.

Papagiannopoulos, A.; Waigh, T. A.; Fluerasu, A.; Fernyhough, C. and Madsen, A. (2005). *J. Phys.: Condens. Matter* **17**, 279.

Park, I. S.; Saruta, K. and Kojima, S. (1999). *JTAC* **57**, 687.

Percus, J. K. and Yevick, G. (1964). *Phys. Rev.* **136**, 290.

Philipse, A. P. and Vrij, A. (1989). *J. Coll. Inter. Sci.* **128**, 121.

Phillips, C. J. (1996). *Rep. Prog. Phys.* **59**, 1133.

Pietsch, U.; Holy, V. and Baumbach, T. (2004). *High resolution X-ray scattering.* 2nd Edition. Springer, Berlin, Germany.

Ponchut, C.; Clément, J.; Rigal, J. M.; Papillon, E.; Vallerga, J.; LaMarra, D. and Mikulec, B. (2007). *Nucl. Instr. and Meth. A* **576**, 109.

Ponomarenko, O.; Nikulin, A. Y.; Moser, H. O.; Yang, P. and Sakata, O. (2011). *J. Synchr. Rad.* **18**,4, 580.

Prodan, M. (2008). "Entwicklung eines Doppelkristallmonochromators zur Untersuchung von dynamischen Prozessen an Flüssigkeitsoberflächen." MA thesis. Lübeck, Germany: University of Applied Science Lübeck.

Pusey, P. N. and van Megen, W. (1986). *Nature* **320**, 340.

Reichman, D. R. and Charbonneau, P. *J. Stat. Mech.* **2005**, P05013.

Richert, R. (2002). *J. Phys.: Condens. Matter* **14**, R703.

Richert, R. and Angell, C. A. (1998). *J. Chem. Phys.* **108**, 9016.

Robert, A. (2007). *J. Appl. Cryst.* **40**, 34.

Robert, A.; Wagner, J.; Autenrieth, T.; Härtl, W. and Grübel, G. (2005a). *Journal of Magnetism and Magnetic Materials* **289**, 47.

– (2005b). *J. Chem. Phys.* **122**, 84701.

Robert, A.; Wandersman, E.; Dubois, E.; Dupuis, V. and Perzynski, R. (2006). *Europhys. Lett.* **75**, 764.

Roshi, A.; Barjami, S.; Iannacchione, G. S.; Paterson, D. and McNulty, I. (2006). *Phys. Rev. E* **74**, 31404.

Ruiz-Estrada, H.; Medina-Noyola, M. and Nägele, G. (1990). *Physica A* **168**, 919.

Russel, W. B.; Saville, D. A. and Schowalter, W. R. (1989). *Colloidal dispersions.* 1st Edition. Cambridge University Press, Cambridge, UK.

Ruta, B.; Baldi, G.; Monaco, G. and Chushkin, Y. (2013). *J. Chem. Phys.* **138**, 054508.

Rzoska, S. J. and Mazur, V. A. (2007). *Soft Matter under Exogenic Impacts.* 1st Edition. Springer, Dordrecht, Netherlands.

Schönhals, A. (2001). *Europhys. Lett.* **56**, 815.

Schroer, M. A. (2011). “Small angle X-ray scattering studies on proteins under extreme conditions.” PhD thesis. Dortmund, Germany: Technical University of Dortmund.

Schurtenberger, P. (2002). “Neutrons, X-ray and light: Scattering methods applied to soft condensed matter.” 1st Edition. Elsevier, Amsterdam, Netherlands, 145ff.

Schwartz, G. A.; Bergman, R.; Mattsson, J. and Swenson, J. (2003). *Eur. Phys. J. E* **12**, 113.

Sciortino, F. (2005). *J. Stat. Mech.* P05015.

Sergueev, I.; Franz, H.; Asthalter, T.; Petry, W.; Bürck, U. van and Smirnov, G. V. (2002). *Phys. Rev. B* **66**, 184210.

Seydel, T.; Madsen, A.; Sprung, M.; Tolan, M. and Grübel, G. (2003). *Rev. Sci. Instrum.* **74**, 4003.

Sikorski, M. (2008). “Glass transition near the free surface studied by synchrotron radiation.” PhD thesis. Hamburg, Germany: University of Hamburg.

Smoluchowski, M. (1906). *Ann. Phys.* **14**, 756.

Snook, I. (2007). *The Langevin and Generalised Langevin Approach to the Dynamics of Atomic, Polymeric and Colloidal Systems.* 1st Edition. Elsevier, Amsterdam, Netherlands.

Sprung, M.; Seydel, T.; Gutt, C.; Weber, R.; DiMasi, E.; Madsen, A. and Tolan, M. (2004). *Phys. Rev. E* **70**, 51809.

Steinmann, R.; Chushkin, Y.; Caronna, C.; Chavanne, J. and Madsen, A. (2011). *Rev. Sci. Instr.* **82**, 25109.

Stern, O. (1924). *Z. Electrochem.* **30**, 508.

Stillinger, F. H. (1995). *Science* **267**, 1935.

Stöber, W.; Fink, A. and Bohn, E. (1968). *J. Coll. Int. Sci.* **26**, 62.

Streit-Nierobisch, S.; Gutt, C.; Paulus, M. and Tolan, M. (2008). *Phys. Rev. B* **77**, 41410.

Struik, L. C. E. (1978). *Physical aging in amorphous polymers and other materials.* 1st Edition. Elsevier, Amsterdam, Netherlands.

Tadros, T. F. (2008). *Colloids in Cosmetics and Personal Care.* 1st Edition. Wiley-VCH, Weinheim, Germany.

Tanaka, H. (2000). *J. Phys.: Condens. Matter* **12**, 207.

Thompson, A. C., ed. *X-ray data booklet.* 3rd Edition. Lawrence Berkeley National Laboratory, Berkeley, USA.

Trachenko, K. (2008). *J. Non-Cryst. Sol.* **354**, 3903.

Trappe, V.; Pitard, E.; Ramos, L.; Robert, A.; Bissig, H. and Cipelletti, L. (2007). *Phys. Rev. E* **76**, 51404.

Uhlenbeck, G. E. and Ornstein, L. S. (1930). *Phys. Rev.* **36**, 823.

Van Blaaderen, A. and Kentgens, A. P. M. (1992). *J. Non-Cryst. Solids* **149**, 161.

Van Blaaderen, A.; Van Geest, J. and Vrij, A. (1992). *J. Coll. Inter. Sci.* **154**, 481.

Van Megen, W. and Underwood, S. M. (1993). *Nature* **362**, 616.

Verwey, E. J. W. and Overbeek, J. T. G. (1948). *Theory of the stability of lyophobic colloids.* 1st Edition. Elsevier, Amsterdam, Netherlands.

Vrij, A. (1976). *Pure and Appl. Chem.* **48**, 471.

Wandersman, E.; Duri, A.; Robert, A.; Dubois, E.; Dupuis, V. and Perzynski, R. (2008). *J. Phys.: Condens. Matter* **20**, 155104.

Wang, L.; Velikov, V. and Angell, C. A. (2002). *J. Chem. Phys.* **117**, 10184.

Watanabe, R.; Yokoi, T.; Kobayashi, E.; Otsuka, Y.; Shimojima, A.; Okubo, T. and Tatsumi, T. (2011). *J. Coll. Inter. Sci.* **360**, 1.

Wellenreuther, G. (2005). “Glass dynamics in confinement examined with quasi-elastic nuclear resonant forward scattering.” PhD thesis. Hamburg, Germany: University of Hamburg.

Wellenreuther, G.; Franz, H.; Bürck, U. van and Sergueev, I. (2005). *Hyperfine Interactions* **165**, 141.

Westermeier, F.; Fischer, B.; Roseker, W.; G., Grübel; G., Nägele and Heinen, M. (2012). *J. Chem. Phys.* **137**, 114504.

Williams, G. and Watts, D. C. (1970). *Trans. Farad. Soc.* **66**, 80.

Ye, J. Y.; Hattori, T.; Inouye, H.; Ueta, H.; Nakatsuka, H.; Maruyama, Y. and Ishikawa, M. (1996). *Phys. Rev. B* **53**, 8349.

Yokoi, T.; Sakamoto, Y.; Terasaki, O.; Kubota, Y.; Okubo, T. and Tatsumi, T. (2006). *J. Am. Chem. Soc.* **128**, 13664.

Zozulya, A. V.; Bondarenko, S.; Schavkan, A.; Westermeier, F.; Grübel, G. and Sprung, M. (2012). *Optics Express* **20**, 18967.

van de Hulst, H. C. (1957). *Light Scattering by Small Particles.* Wiley, Hoboken, USA.

Publications

1. S. Lee, W. Roseker, C. Gutt, B. Fischer, **H. Conrad**, F. Lehmkühler, I. Steinke, D. Zhu, H. Lemke, M. Cammarata, D. M. Fritz, P. Wochner, M. Castro-Colin, S. O. Hruszkewycz, P. H. Fuoss, G. B. Stephenson, G. Grübel, and A. Robert. Single shot speckle and coherence analysis of the hard X-ray free electron laser LCLS. *OPTICS EXPRESS*, **21**, 024647 (2013).

2. C. Gutt, P. Wochner, B. Fischer, **H. Conrad**, M. Castro-Colin, S. Lee, F. Lehmkühler, I. Steinke, M. Sprung, W. Roseker, D. Zhu, H. Lemke, S. Bogle, P. H. Fuoss, G. B. Stephenson, M. Cammarata, D. M. Fritz, A. Robert, and G. Grübel. Single Shot Spatial and Temporal Coherence Properties of the SLAC Linac Coherent Light Source in the Hard X-Ray Regime. *Phys. Rev. Lett.*, **108**, 024801 (2012).

3. A. Sakko, C. Sternemann, Ch. J. Sahle, H. Sternemann, O. M. Feroughi, **H. Conrad**, F. Djurabekova, A. Hohl, G. T. Seidler, M. Tolan, and K. Hämäläinen. Suboxide interface in disproportionating a-SiO studied by x-ray Raman scattering. *Phys. Rev. B*, **81**, 205317 (2010).

4. O. M. Feroughi, C. Sternemann, Ch. J. Sahle, M. A. Schroer, H. Sternemann, **H. Conrad**, A. Hohl, G. T. Seidler, J. Bradley, T. T. Fister, M. Balasubramanian, A. Sakko, K. Pirkkalainen, K. Hämäläinen, and M. Tolan. Phase separation and Si nanocrystal formation in bulk SiO studied by x-ray scattering. *Appl. Phys. Lett.*, **96**, 081912 (2010).

5. **H. Conrad**, F. Lehmkühler, C. Sternemann, A. Sakko, D. Paschek, L. Simonelli, S. Huotari, O. M. Feroughi, M. Tolan, and K. Hämäläinen. Tetrahydrofuran Clathrate Hydrate Formation. *Phys. Rev. Lett.*, **103**, 218301 (2009).

6. Ch. J. Sahle, C. Sternemann, **H. Conrad**, A. Herdt, O. M. Feroughi, M. Tolan, A. Hohl, R. Wagner, D. Lützenkirchen-Hecht, R. Frahm, A. Sakko, and K. Hämäläinen. Phase separation and nanocrystal formation in GeO. *Appl. Phys. Lett.*, **95**, 021910 (2009).

7. **H. Conrad**, F. Lehmkühler, C. Sternemann, O. M. Feroughi, L. Simonelli, S. Huotari, and M. Tolan. A sample cell to study hydrate formation with x-ray scattering. *Rev. Sci. Instrum.*, **80**, 026103 (2009).

Acknowledgments

I would like to thank all the people who have supported, advised and encouraged me during the last years. All of this work would never have been possible without their help. Without the great atmosphere at DESY Photon Science it would not have been such a wonderful experience, thanks to all who have contributed.

Especially, I would like to thank my supervisors Dr. Michael Sprung and Prof. Dr. Christian Gutt for the great support, the ideas and the discussions during the last years.

I am very grateful to Prof. Dr. Winfried Wurth and Prof. Dr. Gerhard Grübel for the possibility to write the thesis on this project. I am indebted to Prof. Dr. Gerhard Grübel especially for welcoming me in his group, for his encouragement, his expertise, guidance and support since the start of my thesis.

I benefited a lot from working together with the people of the Coherent X-ray Scattering Group: Dr. Birgit Fischer who introduced me into the synthesis of colloidal systems and took care of the samples during my first experiments as well as supporting me at most of the beamtimes. Dr. Michael Sprung who advised me in all technical issues at his beamline, shared his great knowledge on data analysis and always took the time to answer my questions. Prof. Dr. Christian Gutt to whom I could always address the problems and questions that occurred in this thesis. Dr. Fabian Westermeier who shared his expertise in colloidal particle dynamics.

I am grateful to all group members for their support at various beamtimes in Grenoble and Hamburg. Without the help of Dr. Louisa Dahbi, Dr. Birgit Fischer, Prof. Dr. Christian Gutt, Dr. Felix Lehmkühler, Dr. Leonard Müller, Stefan Schleitzer, Dr. Martin A. Schroer, Ingo Steinke, and Dr. Fabian Westermeier the experiments would not have been feasible.

Beyond science, I am very grateful for the pleasant atmosphere in the Coherent X-ray Scattering Group. I would like to thank Dr. Wojciech Roseker for his advises and support, and together with Dr. Sooheyong Lee for their wonderful company during the experiments at the LCLS.

In this context, I address special thanks to Martin Dommach, Sergej Bondarenko and Michael Walther for their extraordinary engineering support of my experiments and especially the projects at the LCLS which never have been accomplished in time without their help. In addition, I thank the people of the Photon Science and DESY workshops which realized all our wishes, although the time was often too short.

I thank in particular all my office mates during the last four years, Dr. Louisa Dahbi, Stefan Schleitzer, and Dr. Martin A. Schroer for many fruitful discussions on physics and non-physics.

I thank Dr. Yuriy Chushkin and Dr. Orsolya Czakkel for their great support at the ID10 beamline as well as Dr. Michael Sprung and Dr. Fabian Westermeier for doing the same at the P10 beamline.

I would like to thank Dr. Anders Madsen and Dr. Yuriy Chushkin for discussions and many ideas.

All colleagues are gratefully acknowledged for proof-reading this thesis and helping me to improve my English.

A special thank is dedicated to Dr. Felix Lehmkühler who has become a good friend and whose positive and constructive nature had a great impact on me since my diploma.

I am in dept to my parents, my twin-sister and her family, and my grandparents for all the support they granted to me in the last decade during my studies.

Finally, I am deeply grateful to my wife Daniela for her support in every circumstance in the past years.